University of Nottingham

School of Medicine

Development of Functional Lung ^{1}H Magnetic Resonance Imaging

Author:
Zachary James Terence Peggs MSci

Supervisors:
Prof. Penny Gowland
Prof. Susan Francis
Prof. Charlotte Bolton
Prof. Ian Hall

August, 2024



University of Nottingham
UK | CHINA | MALAYSIA

Thesis submitted to the University of Nottingham for the degree of Doctor of Philosophy

Abstract

The lungs are complex organs that are responsible for gas exchange. Lung function, and the decline in lung function, are primary predictors of the life expectancy of a population. Typical methods of clinical investigation of the lungs include Pulmonary Function Tests (PFTs), which provide no spatial information, and Computed Tomography (CT) for morphology, which employs ionising radiation. The proliferation of personalised therapies in respiratory medicine has created an urgent clinical need for new pulmonary diagnostics that provide highly sensitive measures of regional lung function. Recent advancements in lung Magnetic Resonance Imaging (MRI) methods have led to several promising non-contrast-based approaches.

The work presented in this thesis is on ^{1}H-based, non-contrast lung MRI development, and includes the development of a novel image analysis method for functional assessment termed VOxel-wise Lung VEntilation (VOLVE) analysis. VOLVE compares the signal from each lung parenchyma voxel to a navigator-type signal, enabling computation of correlation and gradient metrics which describe how the local MR signal varies across the respiratory cycle. This technique is applied in healthy volunteers and lung disease cohorts, and is extended to evaluate pulmonary perfusion by replacing the respiratory navigator with a cardiac signal timecourse, and assess local biomechanical expansion by exploiting the Jacobian determinant from the image registration. The sensitivity of the presented approaches to lung disease are demonstrated throughout with statistically significant differences between healthy volunteers and people with lung disease.

Throughout the development of these techniques, the lung MRI data is explored, and the analysis techniques validated and optimised. Computation of lung volume changes, and optimisation of the acquisition parameters (flip angle, temporal resolution and dynamic image series length) are explored. Future work can apply these techniques in multiparametric pulmonary MRI studies, including longitudinal observational studies and assessment of response to targeted therapeutic interventions.

Contents

Abstract i

Contents ii

Acknowledgements v

Abbreviations vi

1 Introduction 1

1.1 Thesis Overview 2

1.2 Scope of Pulmonary MRI 4

1.3 Overview of Pulmonary MRI 8

1.4 Conclusion 21

2 Theory 22

2.1 Lung Anatomy and Physiology 24

2.2 Principles of Magnetic Resonance Imaging 34

2.3 Conclusion 53

3 Respiratory Induced ^{1}H MR Signal Changes 54

3.1 Introduction 56

3.2 MRI Sequence and Standard Data Preprocessing 71

3.3 Application of PREFUL in CF: FV as a Measure to Assess Response to Kaftrio® Therapy [Adapted from Peggs *et al.* Proc. ISMRM; 2022;#1480] 73

3.4 Development of Voxel-wise Lung Ventilation (VOLVE) Image Analysis Methodology 83
3.5 Voxel-wise Lung Ventilation (VOLVE) Pipeline 102
3.6 VOLVE vs. PREFUL FV in the Assessment of Resonse to Kaftrio® Therapy in CF 105
3.7 Conclusion 109

4 Application and Validation of Voxel-wise Lung Ventilation (VOLVE) Assessment in COPD 110
4.1 Introduction 113
4.2 Methods 116
4.3 Results 126
4.4 Discussion 141
4.5 Conclusion 151

5 Investigating Functional Insights from Lung Motion 152
5.1 Non-rigid Image Registration: Implications for Ventilation Measures and Prospects for Functional Assessment via the Jacobian Determinant 154
5.2 Investigating the Relationship between changes in Lung Volume and Lung-Diaphragm Navigator Signal 182
5.3 Conclusion 196

6 Investigation and Optimisation of VOLVE Acquisition 197
6.1 Introduction 199
6.2 Impact of Coil Support and Relative Coil Displacement on Ventilation Signal 200
6.3 Flip Angle Optimisation for Quantitative Assessment of Pulmonary Ventilation and Perfusion 205
6.4 Temporal Undersampling and Length of Dynamic Image Series 212
6.5 Pilot Study: Whole Lung Coverage in Cystic Fibrosis 219
6.6 Conclusion 226

7 Conclusion 228

8 Appendices **234**

2A Determining Lung Volume, Structure and Function via Retrospective 4D Reconstruction 235

4A Quantification of Emphysema via Low Signal Volume Assessment 238

4B All Subject VOLVE Maps 241

4C Pearson Correlation Coefficient 244

5A Impact of Choice of Registration Target Image on Jacobian Measures 247

Bibliography **254**

Acknowledgements

I have been incredibly fortunate to undertake this project over the past three years and am indebted to many people who have supported me along the way. Firstly, I would like to thank my supervisors for their unwavering support. Prof. Penny Gowland and Prof. Sue Francis have provided constant guidance and mentorship, and have encouraged me to persevere whenever I have been in doubt. I thank Prof. Charlotte Bolton for her support and advice in all clinical aspects of the project, and thank Prof. Ian Hall for his oversight and vision which has kept the research on track. Most of all, I thank my supervisors for their belief in me, which has kept me going throughout.

I would like to thank TidalSense (formerly Cambridge Respiratory Innovations Limited (CRiL)) for funding my doctoral studies. I would also like to extend my thanks to all those who have made my time at the Sir Peter Mansfield Imaging Centre productive and enjoyable. The first year of this project was somewhat obstructed by COVID-19 lockdowns, and being surrounded by dedicated colleagues has made completing the scanning in this work possible. In particular I would like to thank Dr. Jonathan Brooke for many insightful conversations, and his enthusiasm at each stage of the developmental work.

Lastly, I would like to thank my family. Their support throughout my academic life has been relentless, and I owe my successes to them. I thank my parents, Anne and Mike, for the constant support with which they have provided me. I thank my partner, Lucy, for her daily support, for listening to me ramble on about my work, and for 'looking at hundreds of graphs'. Finally, I thank my grandma, Denise, who has stoically battled with lung cancer throughout my studies. She has been an inspiration to me, and is a constant reminder of the importance of medical science, and the furthering of respiratory medicine. I dedicate this thesis to her.

Abbreviations

BART	Berkeley Advanced Reconstruction Toolkit
BPM	Beats per Minute
CF	Cystic Fibrosis
CR	Conventional Registration
COPD	Chronic Obstructive Pulmonary Disease
CS	Compressed Sensing
CT	Computed Tomography
DC	Direct Current
DCE	Dynamic Contrast Enhanced
DMD	Dynamic Mode Decomposition
FASTCOPD	Functional And STructural imaging in Chronic Obstructive Pulmonary Disease
FD	Fourier Decomposition
FEV_1	Forced Expiratory Volume in 1 Second
FFE	Fast Field Echo
FID	Free Induction Decay
FOV	Field-of-View
FRC	Functional Residual Capacity
FV	Fractional Ventilation
FVC	Forced Vital Capacity
FVL-CM	Flow-Volume Loop Correlation Map
GE	Gradient Echo
GOLD	Global Initiative for Chronic Obstructive Lung Disease
GOREG	Group-Oriented REGistration
HC	Healthy Control
HCs	Healthy Controls
LCI	Lung Clearance Index

LVR	Lung Volume Reduction
MR	Magnetic Resonance
MRI	Magnetic Resonance Imaging
M2D	Multi-Slice 2D
NMR	Nuclear Magnetic Resonance
PAR	Peak Area Ratio
PFTs	Pulmonary Function Tests
PREFUL	Phase REsolved FUnctional Lung
PFTs	Pulmonary Function Tests
Q	Perfusion
RF	Radio Frequency
ROI	Region of Interest
RV	Residual Volume
RVent	Regional Ventilation
SE	Spin Echo
SENSE	SENSitivity Encoding
SNR	Signal-to-Noise Ratio
SPMIC	Sir Peter Mansfield Imaging Centre
STFT	Short-time Fourier Transform
SVD	Singular Value Decomposition
TLC	Total Lung Capacity
UoN	University of Nottingham
UTE	Ultrashort Echo Time
V	Ventilation
VDP	Ventilation Defect Percentage
VOLVE	VOxel-wise Lung VEntilation
VTTP	Ventilation Time-to-Peak

Chapter 1

Introduction

1.1 Thesis Overview

The aim of the work described in this thesis is to develop ^{1}H magnetic resonance imaging (MRI) techniques for functional lung imaging. This work has involved probing the underlying temporal magnetic resonance signal variations observed in the lung, developing novel image post-processing approaches, validation and evaluation of these approaches in lung disease cohorts, and optimisation/refinement of the developed approaches. This thesis comprises 7 chapters which are outlined below.

An overview of the thesis structure, and a general introduction to lung MRI is provided in **Chapter 1**. A case is made for the need for lung imaging, followed by a description of several imaging modalities used in respiratory medicine. In particular, lung MRI approaches, including structural and functional imaging, are overviewed.

Chapter 2 provides background information relied upon throughout the thesis. This includes a brief description of pulmonary anatomy and physiology, including the key concepts of gas transfer, ventilation, and pulmonary perfusion. In addition, the underpinning physical principles of MRI are briefly described.

Chapter 3 provides an in-depth review of free-breathing ^{1}H MRI analysis methods, followed by the application of the phase-resolved functional lung (PREFUL) technique in a small Cystic Fibrosis (CF) cohort, investigating the potential of the technique as a means to assess response to therapy. This motivated the need for further development of the image analysis methodology, from which a novel image analysis pipeline was developed termed VOxelwise Lung VEntilation (VOLVE) analysis. This pipeline was used to re-analyse the CF data, and an improvement in sensitivity and repeatability was demonstrated using VOLVE.

Chapter 4 reports the extension of the VOLVE pipeline to evaluate perfusion and cardiac-gated ventilation, and to assess regional lung quadrant-

wise variations in VOLVE metrics. Results of a prospective pilot study in which the developed VOLVE pipeline is evaluated in Chronic Obstructive Pulmonary Disease (COPD) and compared against other prominent post-processing techniques, including PREFUL, are presented. The sensitivity, repeatability, and robustness of VOLVE is compared and contrasted with these other techniques.

Chapter 5 explores lung motion and local expansion in the same COPD cohort. This includes use of fast volumetric imaging to determine a correction factor between respiratory phase and measured 3D lung volume. In addition, image registration is investigated, including the assessment of the impact of different registration methods and algorithms on ventilation quantification. The exploitation of the registration for direct assessment of local expansion is also considered, by tailoring the VOLVE analysis pipeline to make use of the local Jacobian determinant from the image registration.

Chapter 6 considers methodological optimisations of VOLVE based on the advances and insights afforded by the findings of Chapters 4 and 5. The impact of the flip angle and temporal resolution used for VOLVE is investigated to inform the optimum image acquisition parameters for future studies. This motivated a small pilot study in a further CF participant group in which the entire lung volume is imaged with multiple slices in a clinically feasible time frame.

Finally, **Chapter 7** summarises the key findings of the thesis, highlighting the potential for scalable, widespread clinical application, and presents suggestions for future work.

1.2 Scope of Pulmonary MRI

Respiratory diseases continue to incur a significant burden on healthcare systems and communities across the globe. Conditions including lung cancer, Chronic Obstructive Pulmonary Disease (COPD), asthma, lower respiratory tract infections and tuberculosis are among the leading causes of mortality and morbidity worldwide, and account for over 10% of all disability-adjusted life years (DALYs) [1]. It is estimated that 65 million people have moderate to severe COPD — 3 million of which die each year, making COPD the third leading cause of death worldwide [2, 3]. Hence, the ability to diagnose and manage respiratory disease is crucial.

A wide array of diagnostic tools are available to inform the care of people with respiratory illness. Routine examinations include stethoscope auscultation, evaluating airflow through the trachea-bronchial tree, and Pulmonary Function Tests (PFTs), which enable quantification of various aspects of lung function. PFTs include spirometry, plethysmography and washout measurements and provide information relating to functional status and disease severity. While PFTs are inexpensive and well-standardised, they possess several drawbacks which limit their utility. In particular, PFTs that require forced expiration are effort-dependent and are less reliable in young children or those unable to comprehend instruction [4]. This effort dependence also limits the repeatability of these PFTs. Lung Clearance Index (LCI) can overcome this, whereby a washout measurement is performed during tidal breathing. LCI is thought to reflect ventilation inhomogeneity and is likely a marker of smaller airways (rather than larger airways in spirometry) and has been shown to be sensitive to early stage disease [5]. However, the functional assessment provided by PFTs is global in nature and so is insensitive to regionally heterogeneous lung disease. These techniques are therefore unable to provide insight into regional functional or pathophysiological mechanisms. Global measures are averages across the entire lung and so these techniques often lack sensitivity to early-stage disease. While PFTs provide a useful baseline assessment, the relatively coarse

assessment provided by PFTs ultimately limits their utility in a personalised precision medicine framework.

To address these pitfalls, several medical imaging modalities are available to assess lung structure and function. Principally, structural imaging is carried out via the plain radiograph (chest x-ray) in which the 3-dimensional lung volume is projected onto a 2D plane, in either the posteroanterior (PA) or anteroposterior (AP) direction. This enables visualisation of pronounced radiological features including rib fracture, vertebral wedge compression, pneumothorax and pneumonia with a low radiation dose, but is generally of less diagnostic value for chronic respiratory disease [6]. At the cost of a larger radiation dose, computed tomography (CT) offers 3D, high-resolution (up to 3 mm isotropic) electron density-weighted imaging. CT remains to be the prevailing workhorse of pulmonary imaging, being fast, cheap and robust, producing high-resolution images of the lung parenchyma and surrounding structures [7].

While CT is considered the clinical gold-standard for structural imaging, it lacks the ability to directly measure lung function. Functional imaging is predominantly performed via nuclear medicine techniques such as planar scintigraphy for ventilation, single-photon emission computed tomography (SPECT) for ventilation/perfusion and positron emission tomography (PET) for metabolic imaging [8, 9]. These techniques rely on ingestion or inhalation of radionuclides (generally ^{133}Xe for ventilation and technetium-99 macro-aggregated albumin (^{99m}Tc-MAA) for perfusion) and generally have low spatial and temporal specificity, often leading to the requirement of further imaging [10].

Much work has been done in reducing the radiation dose for both CT and nuclear medicine approaches, with a standard thoracic CT ranging from equivalent radiation exposure of 4 months to 2 years of UK background radiation, depending on the extent of the exam [11]. Whilst for many patient groups this poses very little danger, this is problematic for patient groups

where exposure to ionising radiation is undesirable — e.g., children, people who are pregnant or patients with conditions necessitating recurrent scans over an extended period. Further, radiation exposure limits the suitability of CT for longitudinal monitoring of disease progression and assessment of response to therapy.

These drawbacks can all be overcome by magnetic resonance imaging (MRI). MRI is a non-invasive, non-ionising imaging modality that makes use of strong electromagnetic fields and radiofrequency waves. In proton (^{1}H) MRI, the magnetic resonance (MR) signal is related to the density and magnetic characteristics of hydrogen nuclei. Both the spin-lattice (T_1) and spin-spin (T_2/T_2*) relaxation times can be exploited to produce excellent soft tissue contrast. MRI acquisition parameters can be tuned in a bespoke manner, enabling myriad biomedical applications across the body, including novel assessment of physiology and quantification of real-time function.

While CT provides better spatial resolution, and is generally cheaper and more widely available than MRI, the opportunity to study both lung structure and function in a single exam, without the need for ionising radiation, with improved soft tissue contrast and improved temporal resolution provides a strong motivation for adopting pulmonary ^{1}H MRI in clinical practice. However, study of lung morphometry and function with MRI has traditionally been limited due to the unique biophysical attributes of the lung, which have until recently hampered the ability to collect diagnostic quality images.

The challenges of imaging the lung are three-fold: relatively low proton density in lungs since the majority of the lung parenchyma comprises of air, susceptibility artifacts caused by magnetic field inhomogeneity at air-tissue interfaces, and motion artifacts due to cardio-respiratory movement [12]. The first two of these issues arises due to the composition of the lung parenchyma, which are made up of alveoli and blood vessels. This results in a sponge-like framework primarily filled with air, resulting in a proton density significantly lower — 5 to 20 times less — than that of other human organs.

Additionally, this sponge-like architecture consists of both large and small air pockets alongside dense tissue and vessels, leading to substantial variations in magnetic susceptibility at air-tissue and air-water interfaces. The lung tissue and blood are generally diamagnetic, whereas the air contains oxygen which is paramagnetic [13]. These differences lead to magnetic susceptibility differences, causing intravoxel magnetic field inhomogeneity (length scale of approximately 1-5 mm), resulting in a spread of Lamor frequencies. This causes intravoxel phase dispersion, leading to rapid decay of the MR signal. Moreover, the constant motion from respiration and cardiac activity, blood circulation, and pulsation further complicates lung imaging, necessitating a fast, gated, or breath-hold acquisition. For these reasons, ^{1}H MRI of the lungs has traditionally not been widely studied. Instead, alternative MRI techniques utilizing inhaled hyperpolarized gases (e.g., ^{3}He/^{129}Xe) have been suggested, showcasing the capacity to gauge diverse functional biomarkers [14, 15]. Nonetheless, the need for highly specialised equipment and trained personnel encumbers these techniques and renders the widespread clinical adoption of hyperpolarized gas MRI impractical.

However, within the last decade, ^{1}H MRI techniques have gained traction given recent technological advancements in the field. Firstly, after the acquisition of high-quality structural images by utilising very short echo times (TE), known as ultrashort echo time (UTE) imaging. This technique, combined with novel k-space trajectories, parallel imaging and deep-learning reconstructions has shown promise in providing high-quality morphological images of the lung, with comparable quality to CT [16]. In addition to advances in structural imaging, much attention has been paid to rapid imaging to extract functional information from the periodic MR signal changes associated with the respiratory and cardiac cycles. Several post-processing techniques have emerged that attempt to quantify regional ventilation and perfusion from these signals [17, 18].

These recent advancements position ^{1}H pulmonary MRI well for fulfilling the role of a safe, one-stop, comprehensive, cost-effective (approx £500 for

research and £100-200 in healthcare setting[1]) modality for the imaging of chronic respiratory disease (such as COPD and CF), for which widespread clinical translation is feasible. The ability to monitor disease, assess response to treatment, and probe distinct pathophysiology, enables unique insights into lung health, disease and function that have previously not been achievable. It is therefore possible that, in some specific cases and with further advancement, lung MRI could provoke a paradigm shift in respiratory medicine management, providing the bedrock on which future novel precision medicine approaches are delivered. Yet, while the potential for ^{1}H lung MRI is great, there remains several technical challenges in image acquisition and analysis that must be overcome before widespread clinical translation is feasible. This will be the focus of this work: the development, implementation, validation, and optimisation of ^{1}H lung MRI techniques for function quantification, with the aim of providing robust, easily translatable methods for obtaining regional ventilation, perfusion, and biomechanical information.

1.3 Overview of Pulmonary MRI

While traditionally the lungs have not been widely studied with MRI due to the inherent challenges relating to the biophysical properties of the lung, substantial progress has been made in the last two decades. Thoracic motion remains to be a challenge for lung MRI, but several promising techniques that make use of rapid imaging or self-navigation are emerging. In addition, the many air-tissue interfaces within the lung that lead to significant intravoxel dephasing, inducing rapid MR signal decay, remains to be a barrier to CT-like, high-resolution imaging.

Much recent pulmonary imaging has been carried out at the clinical field strength of 1.5 T, as this field strength allows for a compromise of relatively large MR signal and low susceptibility effects. While low-field ($\leq$ 0.5 T) MRI affords longer relaxation times, signal-averaging is often needed which

[1] Approximate UK cost at the time of writing according to local research costings and the 2023/2024 NHS payment scheme, respectively.

in turn extends the image acquisition time. Nevertheless, recent work has led to advancements in structural low-field imaging of the lung [19]. Dynamic functional imaging can be carried out at low-field, although high performance low-field clinical scanners remain relatively uncommon. The theoretical advantage of a higher Signal-to-Noise Ratio (SNR) at higher field, such as 3 T, necessitates shorter echo times (TE) to sample the MR signal before it decays. Still, there is growing clinical availability of 3 T MRI, and very limited literature exploring the specific challenges of lung MRI at 3 T. Lung tissue MR relaxation times (see 2.2.1) are shown in Table 1.1 for 1.5 T and 3 T field strengths.

Table 1.1: Lung tissue relaxation times.

Field Strength (T)	T_1 (ms)	T_2* (ms)
1.5	1172 [20]	2.1 [21]
3	1011 [22]	0.74 [21]

^{1}H pulmonary MRI can elucidate several aspects of lung structure and function, with sequences optimised for assessing tissue density, breathing dynamics, ventilation and perfusion. The following subchapter provides an overview of lung MRI techniques used both clinically and in research settings.

1.3.1 Structural Imaging

Generally, functional impairment of the lung is related to alterations in lung structure. Hence, structural imaging is important for visualisation of localised pathology. Examples of typically used sequences including fast field echo (FFE), MultiVane-XD (MVXD) and ultra-short echo time (UTE) are shown in Figure 1.1 (see Section 2.2.3 for details on gradient echo, spin echo and free induction decay mechanisms, respectively). FFE sequences, also known as field echo, gradient echo, gradient-recalled echo and spoiled gradient echo, have been used ubiquitously since the inception of MRI, and rely on RF/gradient spoiling to destroy transverse (T_2) magnetisation to produce T_1-weighted images (controlled by flip angle and repetition time (TR)). T_2*-weighed images (controlled by echo time (TE)) can also be

produced with appropriate parameter tuning [23] — see Section 2.2 for a description of these parameters. Due to the versatility and flexibility of FFE sequences, they have been employed extensively for 2D and 3D acquisitions to study a diverse range of anatomical structures within the body.



Figure 1.1: Example 3 T structural ^{1}H lung images for a healthy subject with a history of smoking for: A) fast field echo (FFE), B) MultiVane-XD (MVXD) and C) ultra-short echo time (UTE).

Recently much attention has been paid to UTE sequences for structural imaging of the lung parenchyma. UTE sequences typically make use of free induction decay (FID) sampling with particularly short TE. The problem of rapidly decaying signal due to the short T_2* of the lung parenchyma can be overcome by sampling k-space as quickly as possible after the RF excitation. Rapid sampling at these so called ultrashort TEs mitigates the detrimental effect of the exponential signal decay on the obtained SNR. This, in combination with signal averaging, allows for the acquisition of high-resolution images of lung structure [13]. Although there is no precise threshold for "ultrashort", echo times shorter than 200 μs are generally thought to be within the domain of UTE (compared to a minimum TE of 500-800 μs for gradient echo), although most modern implementations achieve a TE of less than 100 μs; the minimum achievable TE is dependent on the limitations of the particular MR system's hardware and the efficiency of the k-space trajectory used.

UTE was originally posed in 1991 by Bergin *et al.* as a method by which the parenchyma could be imaged, employing the fastest k-space sampling techniques at the time [24]. In the last decade, radial k-space

sampling schemes have become commonplace, and now allow for even faster sampling of the k-space centre, further reducing the achievable TE. Also, this rapid sampling of the k-space centre enables the possibility of self-gating to minimise the effects of respiratory motion to allow for free-breathing acquisitions, as well as tracking respiratory and bulk motion [25]. Indeed, UTE-MRI is now commonly performed via a 3D-radial "koosh-ball" trajectory [26] whereby a short RF pulse non-selectively excites the entire lung, followed by a centre-out k-space encoding with ramp-sampling. The SNR gained by this rapid sampling enables lung structure to be imaged more accurately and allows for the possibility of exchanging SNR for an even better spatial resolution, with the ability to produce "CT like" image quality. Alternatively, a cylindrical k-space sampling scheme can be employed such as the "stack-of-stars" or "stack-of-spirals" trajectories. These are hybrid radial-Cartesian schemes that use non-cartesian sampling in the kx-ky plane but Cartesian encoding in the kz (slice) dimension [27]. These schemes offer flexibility in the reconstructed resolution and field-of-view (FOV), as well as use of the partial Fourier technique in the slice dimension. In addition, as the slice dimension has Cartesian encoding, the slices can be separated by the fast Fourier transform (FFT), enabling separate reconstruction of each slice which can be parallelised for rapid (and less memory intensive) image reconstruction, which is conducive to clinical translation.

Zero TE (ZTE) is a technique closely related to UTE which utilises very short TE values (<10 μs [28]) to rapidly sample the MR signal as soon as it is created by RF excitation. In contrast to UTE, ZTE sequences employ activation of readout gradients before RF excitation, allowing sampling of the signal at the same time as it is created, resulting in an echo time of almost zero [29]. Strictly, hardware limitations mean it is challenging to acquire at a TE of exactly zero, but such small TEs can be achieved (< 5 μs) that the name ZTE is appropriate. In addition, without the need for rapidly switching gradients between TR intervals, ZTE is afforded the added benefit of producing significantly reduced acoustic noise in comparison to other similar MR modalities [30]. While ZTE has the potential to become a

useful tool in lung MRI, most validation work so far has been in anatomical regions which are not hampered by involuntary motion, such as the brain [31, 32] and musculoskeletal systems [33, 34], with limited work being carried out specifically on ZTE for lung imaging [35, 36].

1.3.2 Functional Imaging

Functional Imaging is generally performed with the use of contrast agents, although non-contrast enhanced functional imaging is also possible, for example via the blood oxygenation level dependent (BOLD) effect for functional neuroimaging or via the periodic lung tissue density changes for functional ventilation assessment. This section will provide an overview of contrast-based and non-contrast-based approaches.

Contrast agents are commonly used in medical imaging and aim to provide additional contrast to images to better delineate regions that would otherwise be obscured — for example if the particular feature of interest is too small and so lost to partial-volume effects, or the tissue properties are too similar to neighbouring tissues. In pulmonary MR imaging, contrast agents fall into one of two categories: intravenous or inhalation. Generally speaking, the contrast agents available in MRI work in an indirect manner. That is, no signal is derived directly from the contrast agent; all the signal originates from the relaxation of hydrogen nuclei. Instead, the contrast agents function by changing the relaxation times of hydrogen nuclei that are nearby to the contrast agent. Hence, the best candidates for MR contrast agents are substances that produce the largest change in relaxation times [37]. For pulmonary MRI, as an exception, some inhaled contrast agents work directly such as ^{19}F MRI and hyperpolarised-gas MRI, considered below.

The magnetic relaxation properties of hydrogen nuclei depend on the magnetic dipole moment of the species used as a contrast agent, which is in turn dominated by the electronic configuration of the contrast agent. MR contrast agents are generally paramagnetic — materials which exhibit magnetic properties when exposed to an external magnetic field due to a net

alignment of their magnetic moments. When this external field is removed, the coherence phenomenon causing the paramagnetism is rescinded and so the magnetic diploes return to a state of random orientation, thereby losing their magnetism. Species with a larger number of unpaired valence electrons tend to exhibit stronger paramagnetic effects. Gadolinium (Gd^{3+}) is a lanthanide metal with seven unpaired electrons in the 4f valence shell and so possesses a strong magnetic moment. In addition to this, Gd is effective at preserving its electron spin along the direction of the external magnetic field for a long enough duration. Thus, Gd is an excellent choice for MR contrast agent, and is used in DCE-MRI, which is discussed in more detail below. Other paramagnetic species can also be used as contrast agents such as oxygen, which is also considered below.

Paramagnetic contrast agents tend to shorten both the T_1 and T_2 relaxation times. It is convenient when discussing the effect of a contrast agent on relaxation times to introduce relaxation rates, which are defined as the inverse of their respective relaxation times: $R_1 = 1/T_1$ and $R_2 = 1/T_2$. Much work was carried out in the mid-twentieth century to develop a comprehensive theoretical framework to predict T_1 and T_2 values using correlation times and spectral densities, known as the Solomon-Bloembergen-Morgan (SBM) theory of relaxation [38]. This framework offers an explanation of the effects of contrast agents on tissue relaxation — a case specifically considered by Bloembergen et al. [39]. The resulting relationship between contrast agent concentration, C, and the observed tissue relaxation rates, $R_{1,observed}$ and $R_{2,observed}$, respectively, is that of direct linear proportionality, given by

$$R_{1,observed} = \frac{1}{T_{1,observed}} = \frac{1}{T_{1,inherent}} + r_1 \cdot C \tag{1.1a}$$

$$R_{2,observed} = \frac{1}{T_{2,observed}} = \frac{1}{T_{2,inherent}} + r_2 \cdot C \tag{1.1b}$$

where inherent relaxation times relate to the relaxation times in the absence of contrast agents, and r_1 and r_2 are the relaxivities of the contrast agent — this is the extent to which T_1 or T_2 change as a function of contrast agent

concentration. That is, a measure of the capability of a given concentration of contrast agent to increase the tissue relaxation rates, or shorten the relaxation times.

The following sections briefly describe how specific contrast agents can produce contrast in pulmonary MRI, using oxygen, gadolinium and hyperpolarised ^{129}Xe. Non-contrast enhanced rapid functional imaging is also introduced.

1.3.2.1 Oxygen-Enhanced MRI

Oxygen-enhanced MRI (OE-MRI) is a proton-based technique for functional lung imaging based on the weak paramagnetism of oxygen. In OE-MRI, 100% oxygen is used as a contrast agent (≤ £1/L [40]). Upon inhalation, a small amount of the oxygen binds with haemoglobin to form oxyhaemoglobin, while the majority dissolves in the blood as molecular oxygen (O_2). Since the molecular oxygen is paramagnetic, the T_1 relaxation times of the parenchyma and blood are reduced [41]. This reduction in T_1 is directly proportional to the local concentration of the oxygen delivered to the lung tissue and dissolved in the blood and can therefore be used as a surrogate for ventilation. In addition to this T_1-based contrast, there exists two T_2*-based contrast mechanisms: 1) a reduction in T_2* caused by an increase in magnetic susceptibility, induced by the oxygen which possess greater magnetic susceptibility than air [42], and 2) a further reduction in T_2* due to a weak BOLD effect [43]. OE-MRI is advantageous in comparison to hyperpolarised ^{129}Xe in that the any potential issues associated with a hypoxic inhalation is avoided, which is an important consideration for application in patients with respiratory failure and in neonates [44].

Generally OE-MRI involves T_1-weighted acquisitions throughout normoxic (21% oxygen) and hyperoxic (100% oxygen) conditions, to deduce the relative difference in T_1 parenchymal signal. This can be parameterised via the percentage signal enhancement (PSE) or relaxometry ($\Delta R_1 = \Delta(1/T_1)$). A typical example acquisition with PSE maps is shown in Figure 1.2. The

T_2* can also be used as a marker for ventilation, where well-ventilated areas produce shorter T_2* values in hyperoxic conditions than in normoxic conditions, due to the heightened susceptibility gradient [42]. This effect tends to dominate at 3 T for gradient echo-based methods, enabling $\Delta R_2^* = \Delta(1/T_2^*)$ relaxometry [45]. Thus, both T_1 and T_2* imaging is useful in assessing ventilation with the techniques providing complementary information. In order to simultaneously measure T_1 and T_2*, a UTE golden-angle radial acquisition was developed [46]. More recently, methods that make use of more time-efficient acquisition schemes have been implemented to image the whole lung in 3D with isotropic resolution, including OE-MRI with twisted projection imaging (TPI) [47] and with optimised UTE acquisitions [48–50].

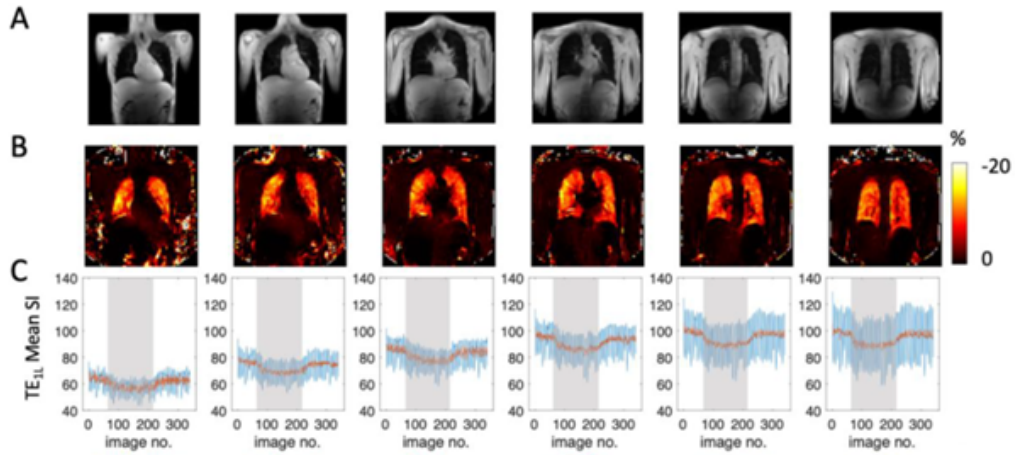


Figure 1.2: Example oxygen-enhanced MRI at 3 T. A) Multi-slice FFE acquisition during normoxic and hyperoxic conditions. B) Example percentage signal enhancement (PSE) maps obtained at TE = 0.71 ms. C) Mean signal time courses for the masked, registered lung data. Adapted from Kim *et al.* [45].

Other recent work has explored the use of OE-MRI at the clinically available field strength of 3 T, exploiting T_1 [51, 52] and T_2* contrast mechanisms [45], with promising initial results on sensitivity and repeatability. In addition, the use of independent component analysis (ICA) has been explored to elucidate the oxygen-enhancement signal from confounding factors (e.g.,

increased magnetic susceptibility effects, respiratory-cardiac motion, etc.), where it was demonstrated that ICA is effective in isolating the oxygen-enhancement signal [53].

1.3.2.2 Dynamic Contrast-Enhanced MRI

Dynamic contrast-enhanced MRI (DCE-MRI) involves the use of an intravenous gadolinium (Gd) contrast agent to measure perfusion and is widely used in vascular and neuro-imaging [54]. Since Gd in free ionic form (Gd^{3+}) is highly toxic to humans, Gd-chelate compounds are used which are not toxic [55]. Gd is used as it is highly paramagnetic and hence is effective in shortening the T_1 relaxation time, thereby generating greater contrast between tissues such that specific pathologies can be identified. Typical DCE-MRI acquisitions involve rapid T_1-weighted 3D spoiled gradient echo imaging during a breath-hold of 15-20 seconds [56]. This allows for visualisation of the transit of the contrast agent within the blood, and subsequent computation of haemodynamic parameters.

It should be noted that this approach is not directly useful for imaging of the lung parenchyma. DCE-MRI is, however, well suited for vascular imaging and can produce high quality perfusion images [57]. This can be particularly instructive when perfusion defects are present in the DCE-MRI images in places where no structural abnormalities are present on an anatomical scan, such as in early-stage CF [58]. A feasible explanation for this is that there is small airways disease on a scale below the resolution of the structural images and so these defects are invisible to this scan, thus sensitive functional measures such as DCE-MRI are needed to provide a diagnostic insight. DCE-MRI can also be used to assess pulmonary embolism, although this is routinely examined via the CT pulmonary angiogram (CTPA) [59].

Although DCE-MRI is a clinically well-established technique, with clinical value being demonstrated in many pulmonary disease groups, including interstitial lung disease (ILD) [60], CF [57, 61], idiopathic pulmonary fibrosis (IPF) [62], COPD [63] and lung cancer [64, 65], work is ongoing to

incorporate newer technological advances in MR physics with the technique. Namely, UTE-MRI and parallel imaging, compressed sensing, and radial acquisition schemes can be utilised to obtain highly accelerated free-breathing DCE-MRI images with high spatiotemporal resolution [66], as well as artifact-free 3D perfusion maps in a single breath-held acquisition [67].

1.3.2.3 Hyperpolarised ^{129}Xe MRI

The use of inhaled hyperpolarised (HP) noble gases as contrast agents has been studied extensively in the last twenty years, with the technique providing a highly sensitive method of imaging pulmonary structure and function. The two predominant noble gases used are ^{3}He and ^{129}Xe, with both gases producing high quality images [68]. While much of the foundational work in the field was carried out with ^{3}He, this approach has been largely eclipsed by ^{129}Xe which is now used in virtually all current research. The switch to ^{129}Xe is largely due to a worldwide ^{3}He scarcity [69]. Although there was some initial hesitation surrounding the anaesthetic properties of, and difficulty in achieving high levels of polarization in, ^{129}Xe, these have since subsided with a favourable safety profile at low alveolar concentrations [44], and advances in polarization technology [70–72].

In disparity to the other contrast mechanisms considered so far, hyperpolarized ^{129}Xe MRI derives an MR signal from the inhaled ^{129}Xe gas directly (≈ £170/L for enriched ^{129}Xe [40]), rather than parenchyma hydrogen protons as in conventional MRI. As a result, ^{129}Xe images the airways and airspaces, as well as characteristics of the parenchyma and red blood cells [14]. In doing so, the usual barriers to pulmonary MRI can be overcome, as external gaseous contrast media do not suffer from inherently short relaxation times or susceptibility artefacts due to air-tissue interfaces. The price of these benefits is the strikingly lower density of ^{129}Xe in comparison to protons, with associated low signal — approximately four orders of magnitude lower. This low density renders elemental ^{129}Xe fruitless in producing an MR signal. To overcome this, a technique known as hyperpolarization is employed, which is used to increase the polarization, and hence the magnetization, by

approximately five orders of magnitude, compensating for the minimal gas density and allowing for imaging to be carried out within a single breath hold [14, 68].

The physics underpinning hyperpolarization came about from advances in atomic physics in the 1960s [73] and 1970s [74]. The technique used, known as spin exchange optical pumping (SEOP), works by using a circularly polarised laser to add angular momentum to an alkali metal atom causing its single valance electron to become polarized/aligned (optical pumping). This is followed by subsequent collisions between the alkali metal atoms and the noble gas, and/or van der Waals complex interactions, where the alignment is transferred (spin temperature equalisation between cold alkali atoms and hot noble gas atoms) from the alkali metal valance electron to the noble gas nuclei (spin exchange) [75]. The result of this is to vastly increase the polarisation of the noble gas, hence the name hyperpolarization. This is of great benefit to the MR signal, and so enhances the obtained SNR and therefore image quality.

To understand how hyperpolarization increases the amount of MR signal generated, we can consider an ensemble of nuclear spins in a sample. In a strong magnetic field B_0 along the z-axis, the orientation of spins in this direction, in thermal equilibrium, is given by the Boltzmann distribution of spin states,

$$P \equiv \frac{n_+ - n_-}{n_+ + n_-} = \tanh\left(\frac{\mu B_0}{k_B T}\right) \approx \frac{\mu B_0}{k_B T} \tag{1.2}$$

where n_+ is the numbers of spins parallel to B_0, n_- is the number of spins antiparallel to B_0, k_B is the Boltzmann constant, T the temperature of the sample and μ the nuclear magnetic dipole moment [68]. It is this proportion of spins, also known as the polarization, which will contribute to the net transverse magnetization ($P \propto M_{0,z}$), and therefore the available MR signal. By increasing the polarization, the population difference of aligned spins is increased, increasing the magnetization of the sample, thus giving an MR signal large enough for imaging to take place (see Chapter 2.2.1). There are

many technicalities relating to imaging with hyperpolarized gases, including achieving enough polarization for sufficient SNR, the fact that the signal strength varies in time and is proportional to dosage (T_1 for hyperpolarized gases relates to the time taken for the polarization to decay back to negligibly small thermal equilibrium values), spatial variation of excitation due to the required dedicated transmit and receive coils fitting differently on different subjects (and further issues associated with coil loading), and others [76].

There are three main assessments that can be carried out with HP ^{129}Xe: static ventilation imaging, diffusion weighted imaging and dissolved phase imaging. This gives HP ^{129}Xe imaging a wide scope for imaging in many different pulmonary diseases, and the ability to detect many different pathologies. Static ventilation imaging infers localised areas of ventilatory defect in areas of reduced ^{129}Xe signal and is usually expressed in terms of a ventilation defect volume (VDV) or a ventilation defect percentage (VDP). Diffusion weighted imaging (DWI) measures the extent to which the HP ^{129}Xe diffuses through the airways and is quantified by the apparent diffusion coefficient (ADC) — a measure of how restricted the diffusion is. Finally, dissolved phase imaging makes use of ^{129}Xe's solubility in the lung (which also gives rise to its anaesthetic properties) and can be used to obtain localised gas transfer information. This is because ^{129}Xe follows the same transfer pathway as oxygen and exhibits a distinctive chemical shift depending on whether it is in the gas phase, dissolved in the barrier tissue, or dissolved in the red blood cells (RBCs). Hence, by selectively exciting a particular resonant frequency, it is possible to image each of these phases [77].

Several disease groups have been studied with HP ^{129}Xe, including asthma [78], COPD [79], CF [80], IPF [81] and pulmonary vascular disease [82]. As well as the proportion of ventilation defect, various pathological features can be probed, including quantification of the extent of emphysema via the ADC [83, 84] and fibrotic thickening of the blood–gas barrier via the ratio of ^{129}Xe dissolved in the tissue and the RBCs [85]. Recently, it was demonstrated that ^{129}Xe was sensitive to impaired gas transfer in non-hospitalised participants

with post-COVID-19 sequelae despite exhibiting no chest CT abnormalities [15]. This highlights the power of HP ^{129}Xe research for improving our understanding of pathology associated with a wide array of disease processes.

1.3.2.4 Fourier Decomposition (FD) & Phase-Resolved Functional Lung Imaging (PREFUL)

While substantial progress has been made in functional lung imaging with contrast-based approaches, this family of techniques are collectively hampered by operational challenges and expensive technical requirements — making the process of clinical translation cumbersome. Hence, the development of ^{1}H non-contrast-based methods, for which clinical translation is much more feasible, is an attractive prospect.

Functional information can be gleaned from small periodic signal changes in the lung parenchyma associated with the respiratory and cardiac cycles. These techniques are discussed in detail in Chapter 3. Briefly, MR signal changes occur in the lung parenchyma, arising from density changes associated with the inflowing and outflowing air during tidal breathing, and from the flow of blood through the imaging slice. These signals can be spectrally separated via Fourier analysis, yielding information relating to ventilation and perfusion, respectively — this is known as Fourier decomposition (FD) [17].

This approach has since been extended and modified in several ways, including via matrix pencil decomposition [86] and non-uniform Fourier transformation [87]. Other methods of extracting ventilation and perfusion information from the acquired dynamic image series have emerged, including Self-gated non-contrast-enhanced functional lung (SENCEFUL) imaging [88], Phase-REsolved FUnctional Lung (PREFUL) imaging [18] and Dynamic Mode Decomposition (DMD) [89]. The technical details of both PREFUL and DMD are detailed in Chapter 3.1.2.

Out of these techniques, PREFUL has been enthusiastically adopted by several sites over the past five years and is the front-running candidate for

clinical translation of regional MRI ventilation/perfusion mapping. PREFUL has been applied in several patient groups, most recently Chronic Thromboembolic Pulmonary Hypertension (CTEPH) in the first large ^{1}H lung MRI multi-centre trial (CHANGE-MRI) across 9 sites across Europe [90].

The excitement garnered by PREFUL has encouraged a flurry of work in the field, including investigation of various image acquisition strategies, novel registration methods and advancements in post-processing techniques [89, 91–93]. This work serves as the groundwork and primary motivation for the methods development and validation conducted in this thesis.

1.4 Conclusion

This chapter has provided an overview to the thesis and broadly outlined the context and scope of pulmonary MRI. There exists a range of MRI techniques that provide structural and functional imaging tools which have great potential for clinical value. Several promising cost-effective, non-contrast based techniques are emerging. Yet, the literature remains scarce in the application and validation of ^{1}H-based lung MRI approaches at 3 T.

Chapter 2

Theory

Abstract

This chapter details background information that is relevant to the work carried out in the remainder of the thesis. This is split into two sections: firstly, lung anatomy and physiology, which gives pertinent details on the structure and function of the lungs; and secondly, principles of NMR and MRI, which serves as a brief overview of the physical principles that underpin the imaging carried out in this thesis.

2.1 Lung Anatomy and Physiology

The following section provides a brief description of lung anatomy and physiology, and largely follows 'Respiratory Physiology: The Essentials (Tenth Edition)', J. B. West (2015) [94], with additional sources as required.

2.1.1 Pulmonary Anatomy

The human lungs are situated within the thoracic cage, enveloped by the sternum anteriorly, the spinal column posteriorly, and laterally by twelve pairs of ribs. The lungs exhibit a conical shape with a slender, rounded apex at the uppermost point. Each lung is separated into lobes via fissures; oblique and horizontal in the right lung, and oblique in the left lung. The respiratory system consists of two tracts: an upper tract consisting of the nose, nasal passage, sinuses and pharynx; and a lower tract encompassing trachea, bronchi, bronchioles, terminal bronchioles, respiratory bronchioles, alveolar ducts, and alveolar sacs, as shown in Figure 2.1.

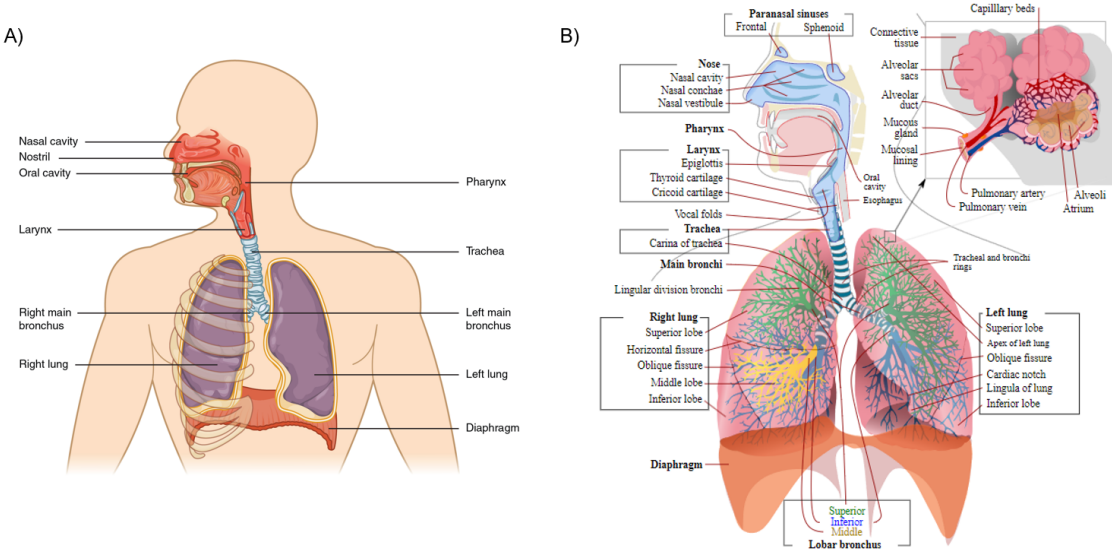


Figure 2.1: A) Schematic of the main human respiratory organs. Reproduced from [95] under Creative Commons license. B) Depiction of the anatomy of the respiratory system. Reproduced from [96] under Creative Commons license.

2.1.2 Pulmonary Function

The primary role of the lungs is to facilitate the process of gas exchange: the transfer of oxygen from inhaled air to the bloodstream, and removal of carbon dioxide produced by cellular respiration from the bloodstream. This process relies upon three key anatomical elements: the pulmonary airways, directing inhaled air towards the alveoli; the alveolar interface, where inspired air traverses the blood-gas barrier into the pulmonary capillaries; and the pulmonary vascular system, which facilitates alveolar perfusion and the transport of exchanged gases [94]. The lungs also perform other secondary functions, including protection from inhalation of dust or harmful microorganisms through mucociliary clearance, as well as supporting regulation of blood pressure and speech [97, 98].

2.1.3 Airways

The pulmonary airways exhibit a bifurcated structure (tracheobronchial tree), starting at the trachea and branching in a dyadic manner into approximately 23 generations, as shown in Figure 2.2. The trachea (generation 0) bifurcates into the left and right main bronchi, initiating a complex branching pattern that continues through subsequent generations. The initial 14-16 generations, ranging from the trachea to the terminal bronchioles, collectively form the "conducting airways" ($Z = 0\text{-}14$). These airways, known as the anatomic dead space, facilitate the transport of air towards the alveolar regions for subsequent gas exchange. Beyond the terminal bronchioles, the transitional bronchioles serve as an intermediary, connecting the conducting airways to the "acinar airways" ($Z' = 0\text{-}8$), where gas exchange takes place, also known as the respiratory zone. The acinar airways encompass the region from respiratory bronchioles, where the initial alveoli form, to the alveolar ducts and sacs, characterised by a complete lining of alveoli [99].

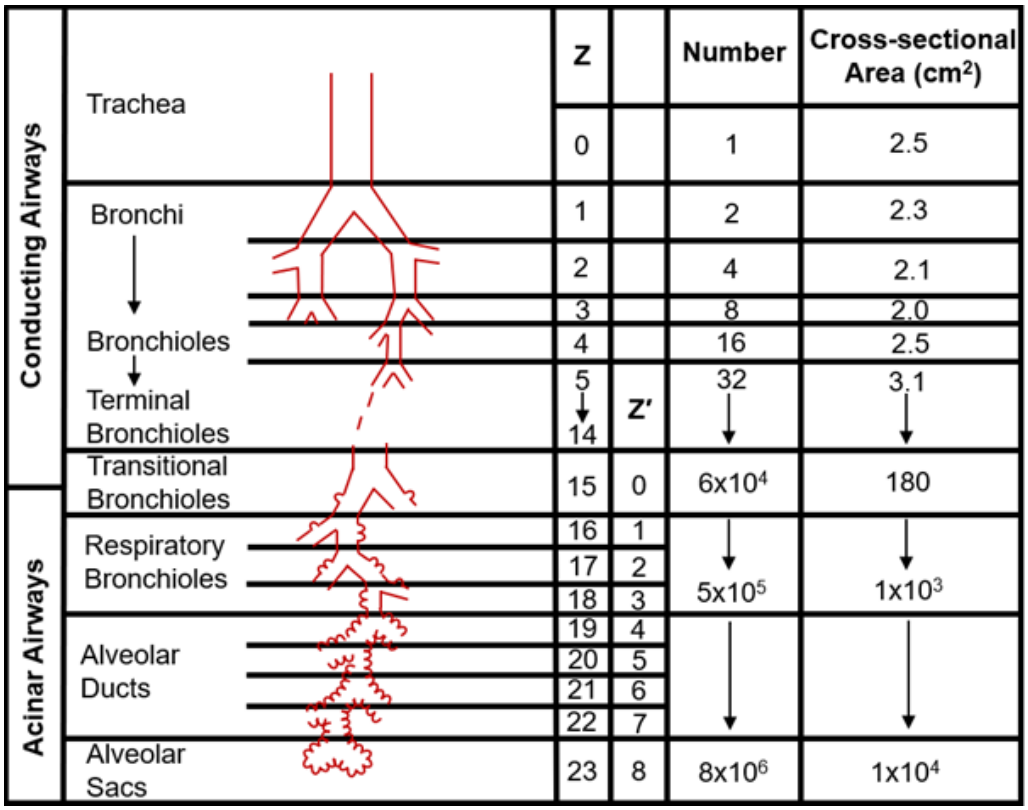


Figure 2.2: Weibel model of airway generations. Dichotomous branching of the tracheobronchial tract of up to 23 generations enables a large alveolar area for gas exchange to take place. Adapted from [94, 99].

The arborized structure of the pulmonary system facilitates a large number of alveoli, and thereby maximises the gas exchange interface. The human lung comprises approximately 500 million alveoli, arranged in a geometry as to maximise the surface available for gas exchange. The cumulative area of the alveolar wall is approximately 70-140 m^2, approximately between the size of a badminton and tennis court [100].

Each alveolus, with a diameter ranging from 100 to 300 microns, is intricately surrounded by capillaries measuring approximately 7-10 microns in diameter, with a width just sufficient to allow the passage of red blood cells. The alveoli and pulmonary capillaries are separated only by an exceptionally thin wall composed of alveolar epithelium and capillary endothelium, known as the alveolar-capillary membrane, spanning 0.5-1 micron [101]. This partition between alveolar air and capillary blood forms the blood-gas barrier

and is the site at which gas exchange via passive diffusion occurs according to Fick's Law: $J = -D\frac{d\phi}{dx}$, where the diffusion flux, J, depends on the diffusion coefficient, D, and the concentration gradient, where ϕ is the concentration and x is position.

2.1.4 Pulmonary Circulatory System

The pulmonary and bronchial circulatory systems collectively contribute to the vascular dynamics of the lung. A schematic illustration of the pulmonary circulatory system is shown in Figure 2.3, depicting the main pulmonary vasculature.

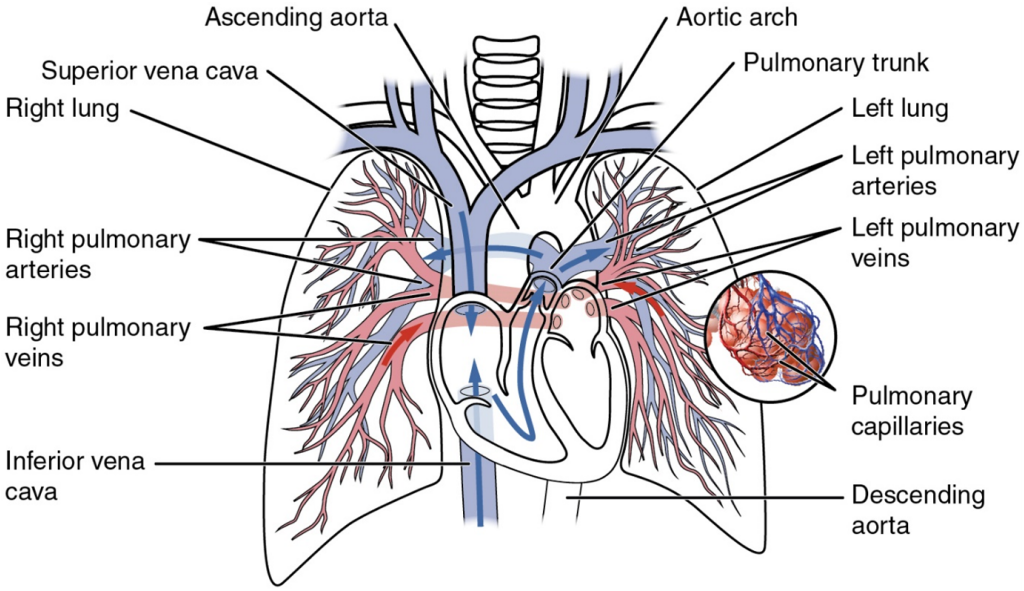


Figure 2.3: Schematic illustration of the pulmonary circulatory system. Reproduced from [102] under Creative Commons license.

The pulmonary circulation is responsible for the reoxygenation of blood, a process initiated by the right ventricular propulsion of deoxygenated blood from the systemic circulation into the pulmonary arteries. Following a branching pattern similar to the tracheobronchial tree, these arteries extend to the level of the respiratory bronchioles. The blood then traverses a highly organised capillary network within the alveolar wall. Within this microvascular bed lies the interface at which deoxygenated blood undergoes oxygenation. This oxygenation occurs through passive diffusion due to the

partial pressure of oxygen being greater in the alveolus than the capillary, and vice versa for carbon dioxide. These partial pressures take approximately 0.25 seconds to reach a state of equilibrium. Following this oxygenation, the newly oxygenated blood is directed back to the left atrium through the pulmonary veins [100].

Simultaneously, the bronchial circulation assumes the role of supporting the metabolic demands of the lung tissue. Originating from the aorta, the bronchial arteries supply oxygenated blood to the bronchi and the connective tissue of the pulmonary parenchyma. This dual-circulatory structure ensures that the lung tissue receives both the necessary oxygen and metabolic nutrients for its optimal function [94].

2.1.5 Pulmonary Ventilation and Perfusion

Gas exchange requires both oxygen-rich air and deoxygenated blood to take place. A sufficient supply of air in the alveoli (ventilation (V)) and blood in the capillaries (perfusion (Q)) is therefore required for efficient gas exchange. The oxygen content in room air, measured at 20.9 mL/100 mL, closely mirrors the oxygen-carrying capacity of the blood, approximately 20.6 mL/100 mL [103]. This congruence means that a V/Q match (i.e., V/Q ratio of unity) is optimum for efficient gas exchange.

2.1.5.1 Ventilatory Mechanics

Generally, ventilation occurs with the respiratory tract directing inspired air towards the alveoli through a branched system of airways. During the respiratory cycle, the respiratory system transports air along pressure gradients created by changing lung volumes induced by the surrounding muscles. These muscles, along with the elastic properties of the lungs facilitate both the inspiration and expiration of ambient air. Inspiration is an active process in which the diaphragm acts as the predominant driving force, aided by the external intercostal muscles. The diaphragm is a dome-shaped muscle that contracts during inspiration, forcing the abdomen

downwards and forwards, increasing the volume of the thoracic cavity. The external intercostal muscles establish connections between neighbouring ribs, exhibiting a downward and forward slope. Upon contraction, these muscles induce an upward and forward movement of the ribs, resulting in an increase of both the lateral and anteroposterior dimensions of the thoracic cavity, facilitating inspiration. In contrast, expiration is passive during tidal breathing. The inherent elasticity of both the lungs and the chest wall facilitates their return to equilibrium positions following the active expansion experienced during inspiration. However, in situations such as exercise or voluntary hyperventilation where expiration is active, expiration is achieved via the abdominal wall muscles. In addition, active expiration is facilitated by the internal intercostal muscles, which contribute by drawing the ribs in a downward and inward direction, thereby reducing the thoracic volume [94].

2.1.5.2 Lung Volumes and Capacities

The volume of air employed during respiration depends on myriad factors, including age, height, weight, gender, and pulmonary health. Lung volumes and capacities relating to lung function can be measured by PFTs and are shown in Figure 2.4. Spirometry uses a forced expiatory maneuver to measure metrics such as the forced expiratory volume in 1 second (FEV_1) and forced vital capacity (FVC). The use of forced respiratory manoeuvres enables computation of flow-volume loops which can give insight into the nature of any potential lung disease. The Tiffeneau-Pinelli index, computed as the FEV_1/FVC ratio, establishes the presence of obstructive lung disease (defined as $FEV_1/FVC<0.7$). FEV_1, expressed as a percentage of a predicted value dependant on patient demographic, grades the severity of airways obstruction [104]. In addition to spirometry, plethysmography can be used to measure total lung capacity (TLC) and functional residual capacity (FRC) [105]. This involves the patient breathing in a sealed chamber and so volumes can be deduced from Boyle's Law (the product of pressure and volume is constant for a given volume of gas for a given temperature).

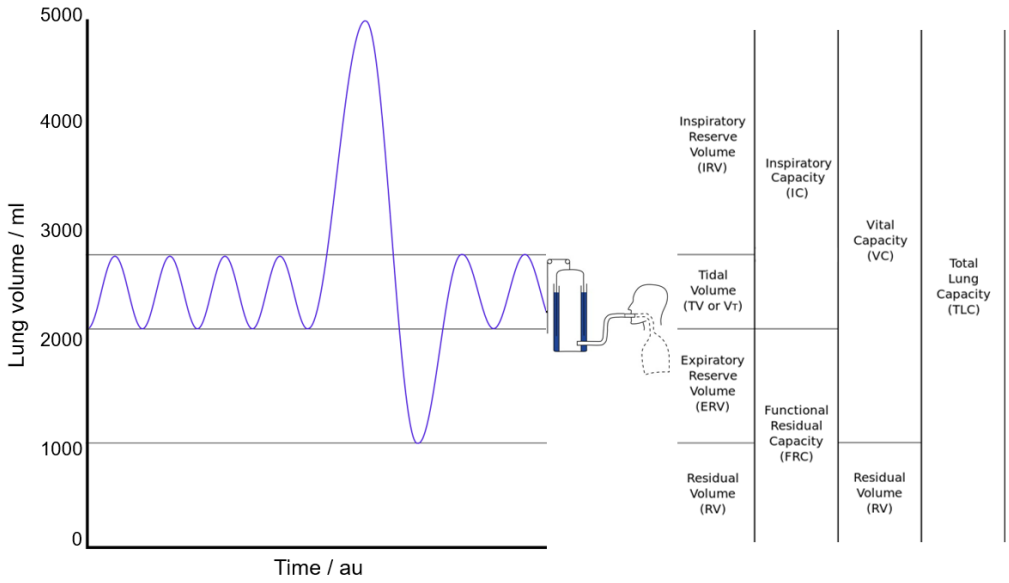


Figure 2.4: Example breathing trace with commonly measured lung volumes and capacities. Adapted from [106] and [107]. A typical volume–displacement spirometer is depicted, whereby air is inspired from a reservoir that is separated from ambient air by a layer of water, and hence the amount of air breathed from the reservoir can be recorded by a measuring device such as a pen which records a breathing trace as shown. After a few normal breaths, the person performs a forced, deep inspiration and deep expiration, enabling computation of the forced expiratory volume in 1 second (FEV_1) and forced vital capacity (FVC).

2.1.5.3 Pulmonary Perfusion

Alveolar perfusion involves the capillaries of the alveolar wall being consistently supplied with deoxygenated blood. The heart pumps blood through the pulmonary artery, maintaining a flow rate of approximately 70 ml per heartbeat for a healthy adult at rest. With a heart rate of 70 beats per minute, this corresponds to a cardiac output of approximately 5 L/min.

Generally, the blood distribution is non-uniform across the lung, especially when upright when the basal regions experience a greater blood flow compared to the apical regions due to gravity. If the capillary pressure at the lung's apex is inferior to the alveolar pressure, the capillaries undergo collapse,

leading to an absence of blood flow in this region. There is therefore a spatially varying lung perfusion distribution depending on physical orientation [108].

This spatial dependence is also evident for ventilation, where the pulmonary parenchyma is also denser in the posterior lung compared to the anterior lung, although the anterior-posterior perfusion gradient is typically larger than the ventilation gradient. Further, imaging examinations are carried out while supine where gravity acts to compress the lung, again influencing regional V/Q differences. This leads to the V/Q ratio of the lung varying at rest between 0.8 and 1.2 [109, 110]. Deviations from a V/Q of 1 also arise due to pathophysiological changes due to lung disease. Different disease processes can impact either the concentration of gases within the lung, the quantity of blood accessible for gas exchange or the thickness of the alveolar-capillary wall. Various pulmonary diseases can impact these pathways through distinct pathophysiological mechanisms.

2.1.5.4 Respiratory Disease

The human lung is susceptible to a multitude of diseases that extend beyond specific pulmonary conditions, including cancer, embolism, and edema. Pulmonary health can also be affected by factors unrelated to the lung itself, such as obesity, scoliosis, and various muscular or nervous system diseases. There are then several pulmonary-specific diseases that impact the architecture of the lungs directly. These respiratory diseases can be categorised into three classes: obstructive, restrictive, and mixed lung diseases [111].

Obstructive lung disease relates to the obstruction of the airways (indicated by a low FEV_1/FVC ratio). This includes several different kinds of pathology, including chronic bronchitis (inflammation of the bronchi leading to obstructed airways), bronchiectasis (dilation of bronchi resulting in narrowing of the airways), emphysema (destruction of alveolar walls) and asthma (narrowing of airways due to inflammation, excess mucus production, hyperplasia, and smooth muscle constriction). Both chronic bronchitis and pulmonary

emphysema are hallmarks of chronic obstructive pulmonary disease (COPD) [112]. Restrictive lung disease generally refers to conditions in which the ability of the lung to expand are compromised, reducing the volume of inspired air (indicated by a low FVC with a preserved FEV_1/FVC ratio). This can be caused by thoracic muscular weakness, disease of the nervous system, skeletal deformity, pulmonary fibrosis, or a pulmonary tumour/lesion [113]. Mixed lung disease involves a combination of the attributes of both obstructive and restrictive disease. In addition to these, diseases affecting the alveolar/capillary membrane also result in poorer gas exchange, such as alveolar capillary dysplasia [114].

Lung pathology takes many forms, and hence it can be convenient when considering MRI examinations to classify these depending on their impact on the density of the lung tissue. Pathophysiological features can generally be characterised as either 'plus' or 'minus' pathologies [115]. Examples of plus-pathologies include fluid accumulation (e.g., mucus) and buildup of cellular tissue (e.g., fibrosis). Examples of minus-pathologies include destruction of airspaces (e.g., emphysema) and reduction in tissue elasticity and/or lung compliance (e.g., leading to hyperinflation).

2.1.5.5 Control and Decline of V/Q

The lung is able to regulate the V/Q ratio to some extent via vasoconstriction and bronchoconstriction which allows for the redirection of blood or air flow, respectively. In the case of alveolar hypoxia, characterised by diminished ventilation (e.g., emphysema), vasoconstriction is initiated in the affected area in order to redirect blood flow to sufficiently ventilated regions of the lung. Similarly, when there is a decrease in perfusion (e.g., pulmonary embolism), bronchoconstriction restricts ventilation in the affected region, redistributing ventilation towards areas that are sufficiently perfused [116].

While these mechanisms can optimise the gas transfer ability of the lungs in the presence of disease, ultimately lung disease leads to a decline in V/Q, leading to impaired gas transfer and hence a reduction in lung function.

The quantification of both ventilation and perfusion is therefore of clinical significance when assessing the extent of lung disease and its impact on lung function. For example, a region that is ventilated but not perfused (e.g., due to emphysema) is known as alveolar dead space, as it does not contribute to gas exchange. Conversely, a region that is perfused but not ventilated (e.g., due to narrowing of the airways) is known as a shunt. For intermediate values of V/Q, where either V or Q is altered in some way, there exists a V/Q mismatch or defect. The ability to assess this V/Q relationship in a regional manner therefore gives pulmonologists insight into the functional and pathophysiological status of the lung.

2.1.5.6 Conclusion

This section has outlined the complex nature of pulmonary anatomy and function. Several mechanisms exist which cause decline in V/Q efficiency and hence pulmonary function, which is relevant for respiratory medicine diagnosis, management and treatment. The work in this thesis aims to make use of Magnetic Resonance Imaging (MRI) to assess localised pulmonary function, feeding into a personalised medicine approach.

2.2 Principles of Magnetic Resonance Imaging

This section provides an overview of the principles of nuclear magnetic resonance (NMR), providing a semi-classical description of nuclear spin states and the process of producing images from these spins. In addition to the overview provided here, further information can be found in [117–120].

2.2.1 Nuclear Magnetic Resonance

2.2.1.1 Nuclear Spin

The phenomenon of Nuclear Magnetic Resonance (NMR) was first discovered by Rabi *et al.* [121], and subsequently advanced by Bloch [122] and Purcell *et al.* [123]. This seminal work was based on the observation that certain atomic nuclei possess the capability to absorb Radio Frequency (RF) energy when placed within a magnetic field, B_0, and exhibit resonance at a frequency dependent on the specific atom and magnetic field strength.

This interaction between the atomic nucleus and external magnetic field relates to the quantum mechanical property of spin, which takes quantised values of half integers or integers. Fermions, such as protons and neutrons, have a spin of either 1/2 or -1/2. Nuclear spin, I, is given by the sum of the spins of the constituent nucleons, and hence only some nuclei possess a non-vanishing I. For nuclei with even numbers of protons and neutrons, pairs of nucleons with opposite spin cancel each other out and hence I=0. All other nuclei possess nuclear spin and so are 'NMR-active', either those with both an odd number of protons and neutrons (odd-odd) and hence integer spin (e.g. ^{2}H, ^{10}B and ^{14}N), or an odd-even/even-odd combination which results in half-integer spin (e.g. ^{1}H, ^{13}C, ^{19}F and ^{23}Na).

A nucleus with spin I has a spin angular momentum, $\boldsymbol{J}$, given by

$$|\boldsymbol{J}| = \hbar\sqrt{I(I+1)} \tag{2.1}$$

where $\hbar$ is the reduced Plank's constant, $h/2\pi$, which gives rise to a nuclear

magnetic moment, μ,

$$\boldsymbol{\mu} = \gamma \boldsymbol{J} \tag{2.2}$$

where γ is the gyromagnetic ratio of the nucleus. The constant γ depends on both the mass and charge of the nucleus, and determines the magnitude of the induced magnetic moment for a given spin angular momentum. ^{1}H (proton) imaging is most widely used due to the large natural abundance of protons in organic tissue, and due to the large NMR response of protons due to their large gyromagnetic ratio (42.6 MHzT^{-1}). Since only ^{1}H MRI data is presented in this thesis, the following sections focus on ^{1}H NMR.

2.2.1.2 Zeeman Splitting

Since I is quantised, with discretised integer/half-integer values, so too is $\boldsymbol{J}$, with a total of $(2I + 1)$ eigenstates. Considering the hydrogen nucleus, for which $I = 1/2$, the two possible eigenstates are $|+1/2\rangle$ and $|-1/2\rangle$ and are often referred to as spin up, $|\uparrow\rangle$, and spin down, $|\downarrow\rangle$. These states are degenerate in the absence of a magnetic field. Upon application of an external magnetic field, the z component of the magnetic moment is given by

$$\mu_z = \gamma \hbar m_I \tag{2.3}$$

where $m_I = -I, -I + 1, \ldots, I$ are the valid spin quantum numbers of the nucleus, and so for a hydrogen nucleus this is given by

$$\mu_z = \pm \frac{1}{2} \gamma \hbar. \tag{2.4}$$

Hence the spins are either aligned with (parallel) or against (anti-parallel) the externally applied magnetic field, B_0. These differences in alignment produce two energy states, $E = \pm 1/2 \gamma \hbar B_0$, where the parallel state, $|\uparrow\rangle$, has lower energy than the anti-parallel state, $|\downarrow\rangle$. The energy difference between these two spin states is given by

$$\Delta E = \gamma \hbar B_0. \tag{2.5}$$

The phenomenon of nuclear energy levels separating in the presence of a magnetic field is known as Zeeman splitting. Combining Eqn. 2.5 with Planck's equation, $\Delta E = h\nu$, gives the Larmor equation,

$$\omega_0 = \gamma B_0. \tag{2.6}$$

which gives the angular frequency, ω_0, of electromagnetic radiation required to induce transitions between the Zeeman energy levels. For a proton at 3 T, the Larmor precession frequency ω_0 = 128 MHz.

2.2.1.3 Precession

While a magnetic moment, $\boldsymbol{\mu}$, tends to align with the B_0 field, it also experiences a torque due to the spin angular momentum, $\boldsymbol{J}$, governed by the cross product of the magnetic moment with the external magnetic field,

$$\boldsymbol{\tau} = \frac{d\mathbf{J}}{dt} = \boldsymbol{\mu} \times \mathbf{B}, \tag{2.7}$$

and, by substitution from Eqn. 2.2, it can be seen that the magnetic moment undergoes precession in a magnetic field according to

$$\frac{d\boldsymbol{\mu}}{dt} = \gamma \boldsymbol{\mu} \times \mathbf{B}. \tag{2.8}$$

The protons therefore precess around the B_0 field at the Larmor frequency, ω_0 (Eqn. 2.6).

2.2.1.4 Net Magnetisation

This section considers an ensemble of spins in an external magnetic field. At absolute zero (0 K) all spins occupy the lowest energy, spin up state, $|\uparrow\rangle$. At temperatures above this, random interactions occur which promote some spins to the higher energy, spin down state, $|\downarrow\rangle$. In addition, spins exhibit a slight tendency to align with the external magnetic field (in the lower energy, spin up, state). There is thus a distribution of spins precessing about B_0 as shown in Figure 2.5. The distribution of spins between the spin up and spin

down energy levels therefore depends on the temperature, T (in Kelvin), and the strength of the external magnetic field, B_0, and is given by the Boltzmann distribution as

$$\frac{N_\uparrow}{N_\downarrow} = \exp\left(\frac{\Delta E}{k_B T}\right) = \exp\left(\frac{\gamma \hbar B_0}{k_B T}\right) \tag{2.9}$$

where k_B is the Boltzmann constant. Given that $k_B T \gg \gamma \hbar B_0$ (high temperature limit), Maclaurin expansion gives the population distribution as

$$\frac{N_\uparrow}{N_\downarrow} \approx 1 - \left(\frac{\gamma \hbar B_0}{k_B T}\right) \tag{2.10}$$

which gives rise to a net magnetisation, M_0, of

$$M_0 \approx \frac{\gamma^2 \hbar^2 N_s B_0}{4 k_B T} \tag{2.11}$$

where N_s is the number of spins per unit volume.

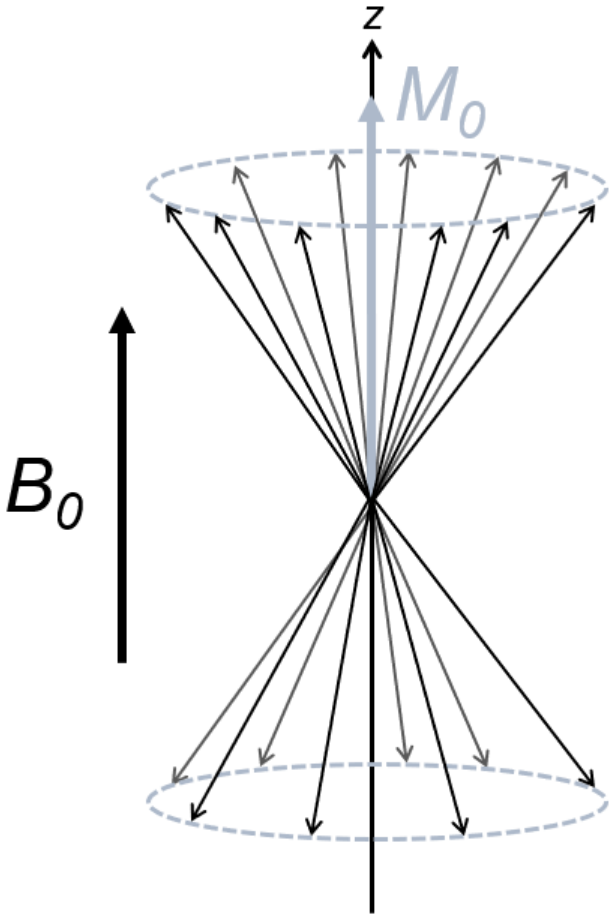


Figure 2.5: Net magnetisation, M_0, (as indicated by the blue arrow) in the direction of the main magnetic field, B_0, is induced by a population difference between the spin-up and spin-down states which precess about B_0.

The population difference that produces the net, bulk, magnetisation, M_0, is inherently small at ambient temperature in organic tissue. For example, biological tissue at typical body temperatures at 3 T exhibits a population difference of approximately 3 parts per million (ppm). Therefore the measurable NMR signal is inherently low, but can still be detected due to the high density of protons. According to Eqn. 2.11, the net magnetisation and therefore the available NMR signal can be increased by applying a stronger external main magnetic field, B_0 [1].

[1]Quantum mechanically the spin states exist in a linear superposition of the two states, but the details of this description are not required for the work presented in this thesis. From here, a classical description of NMR is sufficient.

2.2.1.5 Resonance

To produce an NMR signal, the application of a time varying magnetic field ($B_1(+)$) is required to perturb the spins from their equilibrium state. By applying an RF signal on resonance at the Larmor frequency of precession of the spins, given by Eqn. 2.6, the $B_1(+)$ field acts to tip the net magentisation vector, $\boldsymbol{M_0}$, away from B_0. The extent to which $\boldsymbol{M_0}$ is tipped away from the axis of B_0 (z) and into the transverse (xy) plane is determined by the duration of the RF pulse, τ, and the amplitude of B_1. Typically shaped RF pulses are applied, and by tuning the RF pulse parameters, arbitrary flip angles, α, can be achieved, where $\alpha = \int_0^T \gamma B_1 d\tau$.

2.2.1.6 Relaxation

The tipping of magnetisation, M_0, from along the longitudinal ($\boldsymbol{M_z}$) direction to the transverse ($\boldsymbol{M_{xy}}$) plane is the source of NMR signal — this produces an electromotive force (emf) in a receiver coil in the transverse plane as it precessess and undergoes Free Induction Decay (FID). Both $\boldsymbol{M_z}$ and $\boldsymbol{M_{xy}}$ return to their equilibrium states through a process called relaxation. This relaxation is governed by two independent relaxation mechanisms, known as spin-lattice relaxation with a time constant T_1, and spin-spin relaxation with a time constant T_2.

Relaxation is described mathematically by the full form Bloch equation,

$$\frac{d\mathbf{M}}{dt} = \gamma\,(\mathbf{M} \times \mathbf{B}) - \frac{(M_z - M_0)}{T_1}\hat{\mathbf{z}} - \frac{M_x\hat{\mathbf{x}} + M_y\hat{\mathbf{y}}}{T_2}, \tag{2.12}$$

where the $\gamma\,(\mathbf{M} \times \mathbf{B})$ term represents precession and the relaxation for each axis can be described separately as

$$\frac{dM_z}{dt} = -\frac{M_z(t) - M_0}{T_1}, \tag{2.13}$$

$$\frac{dM_x}{dt} = -\frac{M_x(t)}{T_2}, \tag{2.14}$$

$$\frac{dM_y}{dt} = -\frac{M_y(t)}{T_2}. \tag{2.15}$$

Longitudinal or spin-lattice relaxation describes the process by which the longitudinal magnetisation, M_z, regrows and is restored back to its equilibrium magnetisation, M_0. This is analogous to the damping of a pendulum due to air resistance, but instead is caused by collisions and electromagnetic interactions between the 'lattice' of spins. The rate of M_z regrowth is characterised by T_1, where M_z recovers $(1 - \frac{1}{e})$ of its initial magnetisation, M_0, in the time T_1.

In parallel, we observe the decay of the transverse magnetisation, M_{xy}, occurring due to loss of spin coherence due to spin-spin interactions. Small fluctuations in the magnetic field, for example caused by random dipole-dipole interactions, causes small variations in the Larmor frequency across the spin system. As the spins precess at slightly different rates, they become dephased and hence the transverse magnetisation, M_{xy}, is lost with a time constant T_2.

In addition to this inherent dephasing (described by T_2) additional dephasing can occur due to B_0 field inhomogeneities caused by magnetic susceptibility differences and/or hardware defects (e.g. imperfect shimming). These static B_0 inhomogeneities cause additional decay of M_{xy} with a time constant T_2'. Hence the decay in M_{xy} has contributions from both the 'true' T_2 and T_2', and is given by a decay time constant T_2^*, which is described by

$$\frac{1}{T_2^*} = \frac{1}{T_2} + \frac{1}{T_2'}. \tag{2.16}$$

2.2.1.7 Measuring T_1 and T_2

Solving Eqn. 2.13 for the longitudinal magnetisation, M_z, gives

$$M_z(t) = M_0 \left[1 - \exp\left(-\frac{t}{T_1}\right)\right] + M_z\,(0) \exp\left(-\frac{t}{T_1}\right), \tag{2.17}$$

where $M_z\,(0)$ is the magnetisation at time $t = 0$. This relation is exploited to measure T_1 via the inversion recovery technique. Upon application of an 180° RF pulse, known as an inversion pulse, the longitudinal magnetisation, M_z, is fully inverted, such that $M_z(0) = -M_0$. Hence, after an inversion pulse,

the longitudinal magnetisation recovers according to

$$M_z(t) = M_0 \left[1 - 2\exp\left(-\frac{t}{T_1}\right)\right]. \tag{2.18}$$

By measuring M_z at a number of different inversion times (TI) — the time between the 180° inversion pulse and the start of the readout portion of the sequence — both M_0 and T_1 can be estimated via parametric curve fitting (Figure 2.6A).

Similarly, T_2^* can be measured following application of a 90° excitation RF pulse, with the transverse magnetisation, M_{xy} being given by

$$M_{xy}(t) = M_{xy}(0)\exp\left(-\frac{t}{T_2^*}\right) \tag{2.19}$$

and so T_2^* can be fit (Figure 2.6B) having collected repeated Echo Time (TE) measurements.

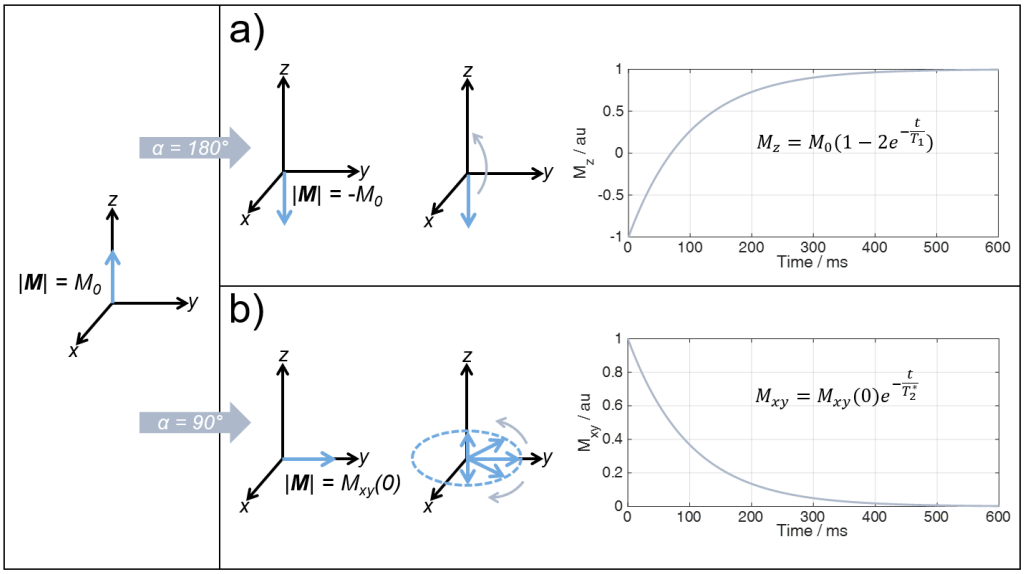


Figure 2.6: a) Recovery of the longitudinal magnetisation, M_z, after application of a 180° inversion RF pulse to fit T_1. b) Decay of the transverse magnetisation, M_{xy}, following the application of a 90° RF pulse to fit T_2^*.

2.2.1.8 Spin Echo

In order to measure the 'true' T_2, as opposed to T_2^*, it is necessary to counteract the influence of static magnetic field inhomogeneities which contribute to T_2^*. The dephasing induced by these inhomogeneities, leading to T_2^*, can be mitigated through the application of a Spin Echo (SE) sequence. In a SE sequence, an initial 90° excitation pulse flips the magnetization into the transverse plane, establishing phase coherence. Subsequently, $T_2^{'}$ effects cause certain spins to precess rapidly while others precess more slowly, resulting in dephasing with T_2^*.

This dephasing can be reversed by applying a 180° refocusing pulse. If a 180° pulse is applied at the midpoint of the TE, t=TE/2, this will reverse the phase shift (spins that previously accumulated the most substantial positive phase shift now exhibiting the most substantial negative phase shift, and vice versa). As the static B_0 inhomogeneities influencing T_2^* are constant in time, they remain consistent for each spin, and hence a spin echo is formed at time t = TE. However, since the processes contributing to T_2 relaxation are time-varying and so not static, they cannot be refocused by the 180° pulse, resulting in signal decay at a rate determined by T_2. This is illustrated in Figure 2.7. Measuring M_{xy} at several different TEs and curve fitting to Eqn. 2.19 yields estimates for T_2 (and M_{xy} (0)).

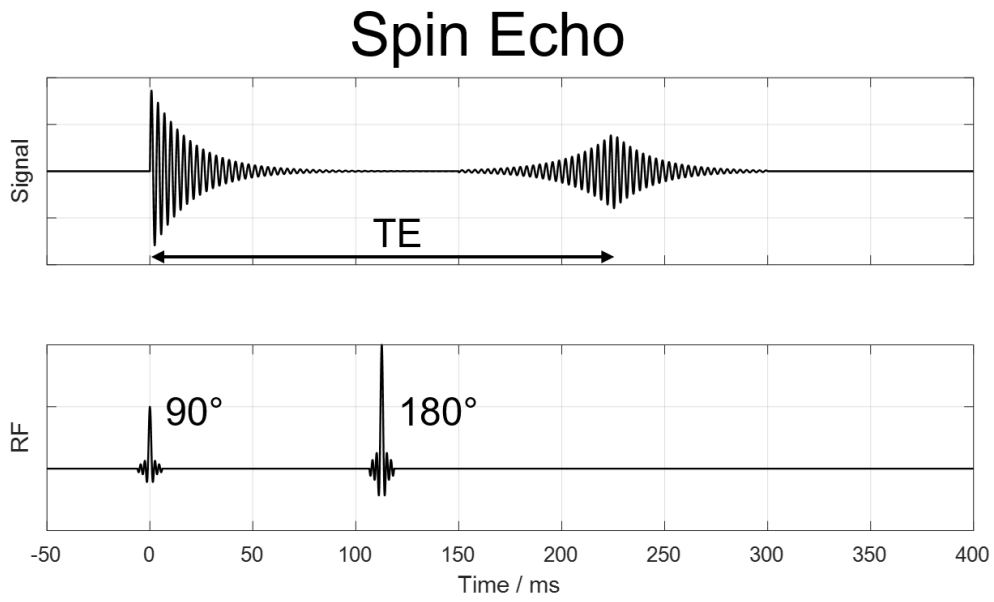


Figure 2.7: Example of a Spin Echo (SE) sequence with an Echo Time (TE) of 225 ms.

2.2.1.9 Gradient Echo

An alternative mechanism for generating echoes is through a Gradient Echo (GE). MRI scanners make use of switchable fields to create spatial variations in the magnetic field for image formation (see 2.2.2), but these gradients will cause additional dephasing, and so a mechanism is needed to produce a gradient echo which depends on the T_2^* of the tissue.

Similarly to a SE pulse sequence, a GE pulse sequence is initiated with a 90° excitation pulse, tipping the magnetization into the transverse plane. Following this, a gradient field is applied, causing rapid dephasing in regions with higher magnetic field strength and slower dephasing in areas with relatively lower field strength. The reversal of the gradient polarity at time TE/2, akin to the effect of a 180° refocusing pulse in SE, leads to rephasing and the formation of a gradient echo at time TE. This is illustrated in Figure 2.8. Details of the spoiled gradient echo sequence, which makes use of this phenomenon, and is the sequence which is predominantly used in this thesis, are given in Section 2.2.3.

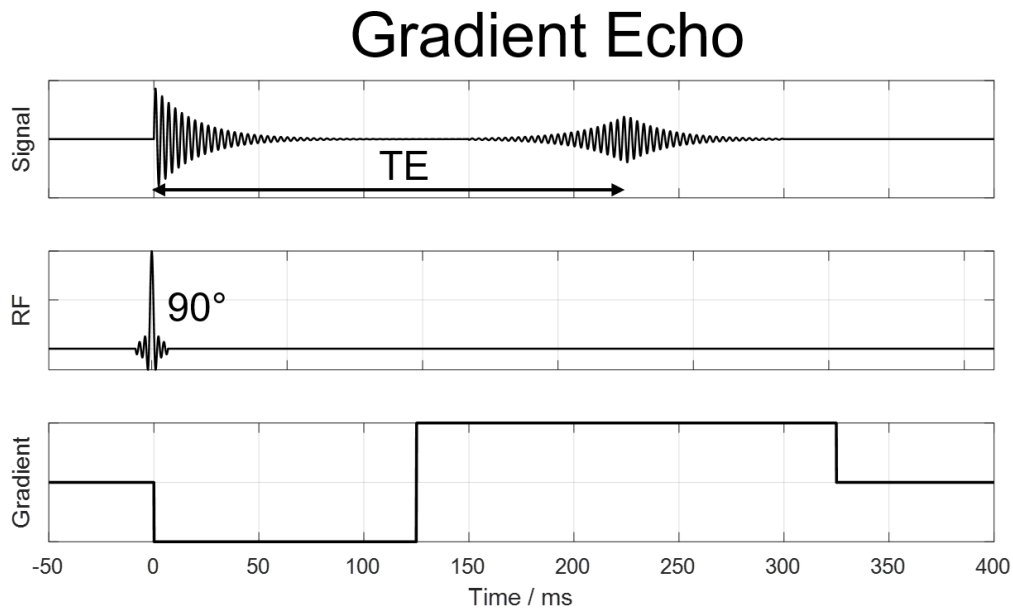


Figure 2.8: Example of a Gradient Echo (GE) sequence with an Echo Time (TE) of 225 ms.

2.2.2 Magnetic Resonance Imaging

2.2.2.1 Spatial Localisation

In order to create an image from NMR signal, we must encode spatial information in the signal such that the location in the body from which the signal originates can be determined. MRI employs spatially varying magnetic fields, known as gradient fields, G_x, G_y and G_z, to encode spins depending on their spatial location. The magnitude of the magnetic field at a given location is then the sum of the main magnetic field, B_0, and the gradient field, which for a G_z gradient, the spatially varying Larmor frequency is given by

$$\omega(z) = \gamma(B_0 + G_z z). \tag{2.20}$$

2.2.2.2 Slice Selection

By applying an RF pulse with a small range of frequencies (bandwidth), a particular 2D slab or slice can be excited, as only those spins precessing with a corresponding Larmor frequency will be on resonance and so emit an NMR

signal. The process is termed slice selection. The thickness of a slice is given by

$$\Delta z = \frac{\Delta\omega}{\gamma G_z}, \tag{2.21}$$

where $\Delta\omega$ is the bandwidth of the RF pulse and the gradient, G_z, is in the slice direction. Since generally a rectangular excitation profile is desired, this is achieved via applying a (truncated) sinc shaped RF pulse, where the excitation profile in frequency space can be determined via Fourier transformation.

2.2.2.3 Frequency and Phase Encoding

After slice selection in z, the in-plane (xy) data is spatially encoded by applying a series of gradients. To encode one dimension, e.g. x, frequency encoding can be used. This is where a gradient field is applied in the x direction, G_x, to make the frequency of precession dependant on the x location. To encode the other in-plane dimension, e.g. y, phase encoding is used. For phase encoding, an additional gradient is applied in the y direction, G_y for a short time, τ. During the application of G_y, spins precess with a frequency dependant on their y position, and hence accrue phase relative to y=0, given by

$$\phi(y) = \gamma\tau G_y y. \tag{2.22}$$

2.2.2.4 k-space and Fourier transformation

By using slice selection, frequency and phase encoding gradients, information can be spatially encoded in 3 dimensions. The acquired signal can be expressed as

$$S(t) = \iiint \rho(x,y) e^{-i\omega_0 t + i\gamma G_x x t + i\gamma G y y t'} dx dy dt' \tag{2.23}$$

where $\rho(x,y)$ is the spin density.

In frequency space, also known as k-space, we can define k_x and k_y as

$$k_x = \gamma G_x t_x \tag{2.24}$$

and

$$k_y = \gamma G_y t_y. \tag{2.25}$$

Substituting Eqns. 2.24 and 2.25 into Eqn. 2.23 gives

$$S(t) = \iint \rho(x, y) e^{-i[k_x + k_y]} dx dy. \tag{2.26}$$

Applying a 2D Fourier transform, the proton density $\rho(x, y)$ is recovered as

$$\rho(x, y) = \iint S(k_x, k_y) e^{-i[k_x + k_y]} dk_x dk_y. \tag{2.27}$$

Hence by sampling the signal in k-space, $S(k_x, k_y)$, an image can be generated which is dependent on $\rho(x, y)$, as shown in Figure 2.9a/d.

There are many different methods for sampling k-space spatial frequencies, and the exact nature by which the sampling is carried out has implications on image quality and any potential artefacts. Various k-space paths or trajectories can be utilised, including Cartesian (rectilinear) sampling, and non-Cartesian (e.g. radial, spiral) sampling. The low spatial frequencies of k_x and k_y at the centre of k-space contain information relating to the gross structural features of the image (low-contrast image features), whilst the high spatial frequencies at the periphery of k-space contain information about the finer image details and edge information, as shown in Figure 2.9. The sampling density, or the distance between k-space samples, Δk, determines the Field-of-View (FOV). The highest frequency sampled (furthest from the k-space origin) determines the image resolution.

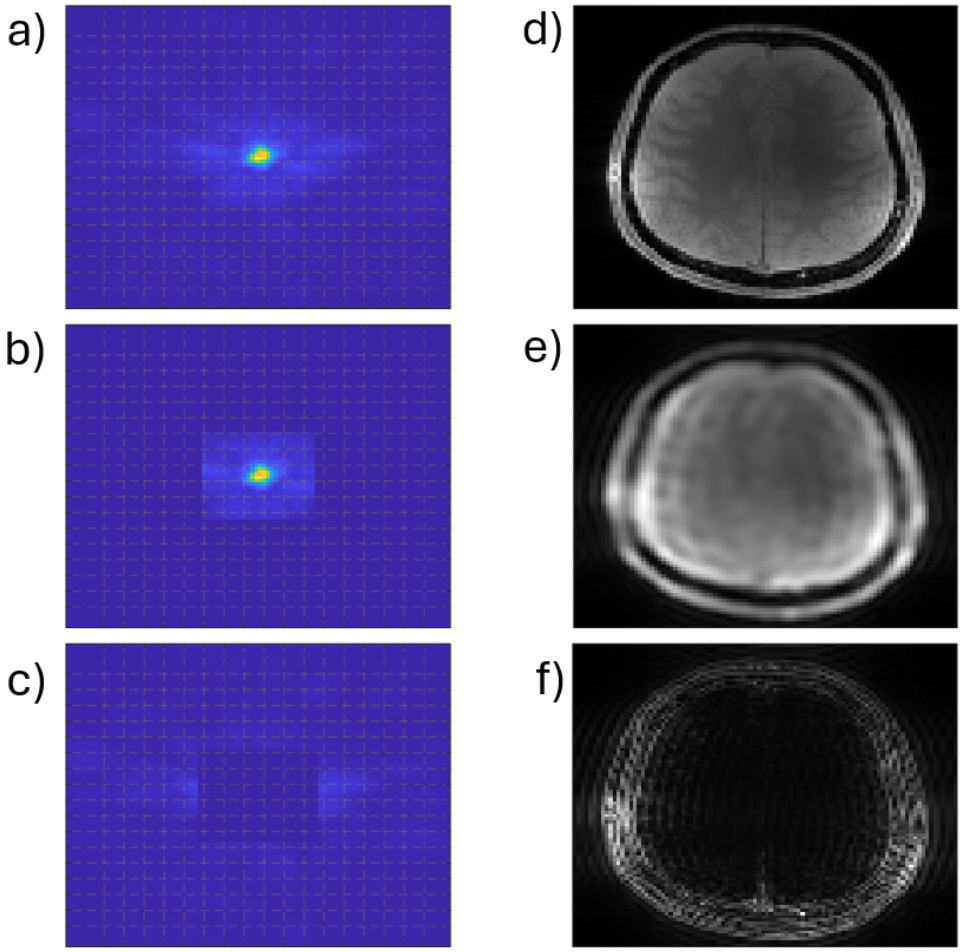


Figure 2.9: Brain example: a) fully sampled k-space with corresponding image d). All but the low spatial frequencies are removed in b), which produces an image e) with lower resolution. c) contains the k-space periphery, which produces an image f) which contains edge information.

2.2.2.5 Parallel Imaging

The acquisition of k-space data can be accelerated to reduce overall acquisition time. This can be achieved by reducing the repetition time (TR) to acquire a k_x line. However, this can impact the contrast, and leads to rapidly changing gradient fields which can induce peripheral nerve stimulation. Alternatively, acceleration can be achieved by reducing the number of phase encoding lines, k_y, by reducing $k_{y,max}$ and keeping Δk_y the same, but this reduces the image resolution. To maintain the image resolution, instead Δk_y can be reduced by undersampling k_y, but this results in spatial aliasing if the

FOV is made smaller than the imaged object. However, parallel imaging techniques can be used to overcome this aliasing, and 'unfold' the aliased images.

Parallel imaging techniques exploit spatial information from a multichannel RF receiver coil array. Coil sensitivity relates to how sensitive a given receive coil is to a given spatial area (see Figure 2.10b), with stronger MR signal intensity measured closer to the receive coil (resulting in regionally varying, spatially dependent hyperintense signal in each coil). Hence additional spatial information is encoded by the multichannel receive coil sensitivities. A common technique used to exploit such coil sensitivity is SENSitivity Encoding (SENSE), which is implemented on Philips scanners. A coil sensitivity map is generated prior to imaging, followed by the acquisition of an undersampled k-space. Each coil measures an aliased image with signal contributions from different spatial locations. Considering two receive coils, the measured signal intensity in each, I_1 and I_2, are a linear combination of signals from locations A and B. Since the coil sensitivity profiles, C_A and C_B, are known, the measured signal intensities can be expressed as

$$I_1 = A \cdot C_{A1} + B \cdot C_{B1} \tag{2.28}$$

$$I_2 = A \cdot C_{A2} + B \cdot C_{B2} \tag{2.29}$$

where solving these simultaneous equations yields the full FOV image, as shown in Figure 2.10.

By using linear algebra and matrix inversion methods, these systems of equations can be efficiently solved for higher acceleration factors. An alternative method for parallel imaging is the Generalised Autocalibrating Partially Parallel Aquisition (GRAPPA), which works in a similar way but utilises the undersampled k-space directly rather than the aliased images. This method is implemented on Siemens scanners. Other more advanced methods combine complex RF-pulses with parallel imaging techniques to achieve simultaneous multi-slice imaging (excite multiple slices simultaneously), also known as

MultiBand imaging.

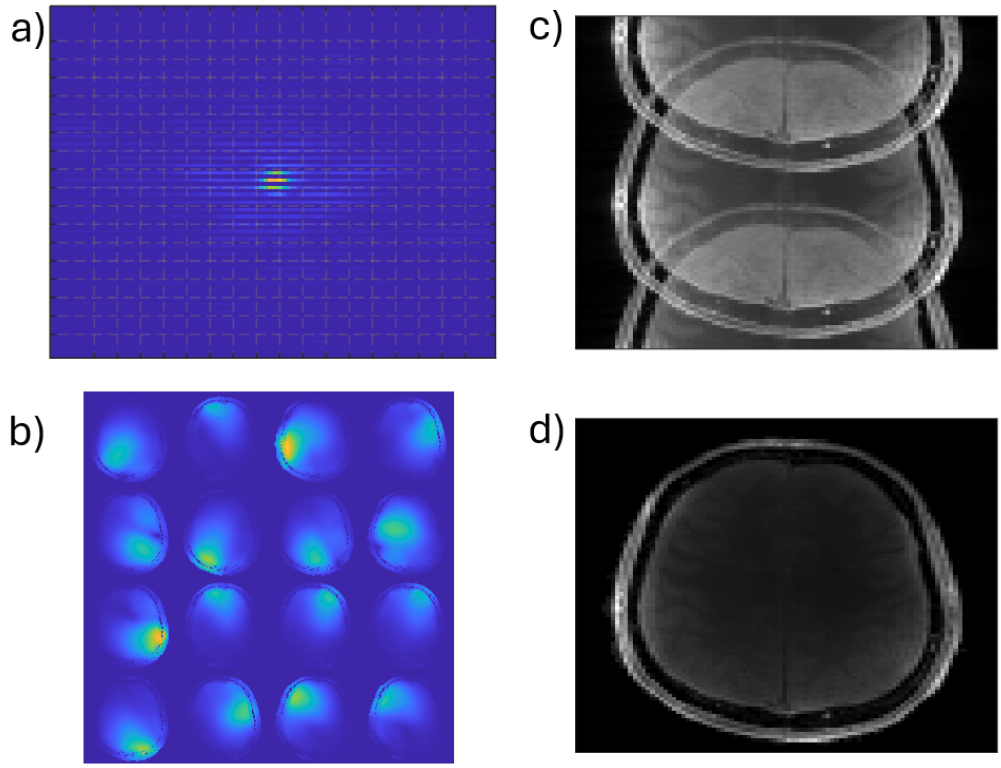


Figure 2.10: Brain example: a) retrospectively undersampled k-space with Δk_y spacing increased by a factor of 2, resulting in c) a reduced FOV and spatial aliasing. To overcome this, SENSE can be exploited by making use of a sensitivity map, b), to recover the unaliased image, d).

2.2.2.6 Compressed Sensing

Another acquisition acceleration technique is Compressed Sensing (CS). This relies on pseudorandom, incoherent k-space sampling, and the fact that the unknown signal should be sparse in some transform domain, i.e. can be represented by a vector with sparse coefficients. Sampling of the k-space centre is somewhat prioritised so as to retain the low spatial frequency information. Then, the image reconstruction reduces to a minimisation problem in which Fourier coefficients (k-space samples) from a subset of k-space can be used to reconstruct an accurate representation of the fully sampled k-space [124]. This involves the following iterative process: 1) reconstruct image from undersampled k-space, 2) low intensity noise

(smoothed across the image) is filtered out via thresholding, 3) inverse Fourier transformation to convert the thresholded image into k-space, 4) comparison of the 'de-noised' k-space with the original k-space, where differences are likely to be due to noise and so can be removed.

This allows for additional undersampling in addition to that enabled by parallel imaging alone. A combination of SENSE and compressed sensing (Philips implementation of Compressed SENSE) is used in this thesis in Chapter 5.

2.2.3 Imaging Acquisition Schemes

The following section provides an overview of the imaging schemes used in this thesis.

2.2.3.1 Fast Field Echo

The primary MRI sequence used throughout this thesis is the Fast Field Echo (FFE), also known as SPoiled GRadient echo (SPGR) or Fast Low Angle SHot (FLASH). The basic principle of the gradient echo was outlined in Section 2.2.1.9. The pulse sequence diagram for a typical 2D FFE sequence is shown in Figure 2.11. In a typical FFE sequence, flip angles $\ll 90^\circ$ are used which enables a short TR between phase encoding steps. For the case where TR $\ll$ T_1, the longitudinal magnetisation M_z does not recover to its initial magnetisation, M_0, before the next excitation is applied. This creates a new steady state magnetisation level, M_{SS}, lower than that of M_0 — this is discussed further in Chapter 6.3. Further to this, if TR<T_2, some residual transverse magnetisation, M_{xy}, remains. This is destroyed via spoiling, which can be achieved by applying an additional gradient field after the frequency encoding gradient (gradient spoiling) or by incrementing the phase of the applied RF pulse (RF spoiling).

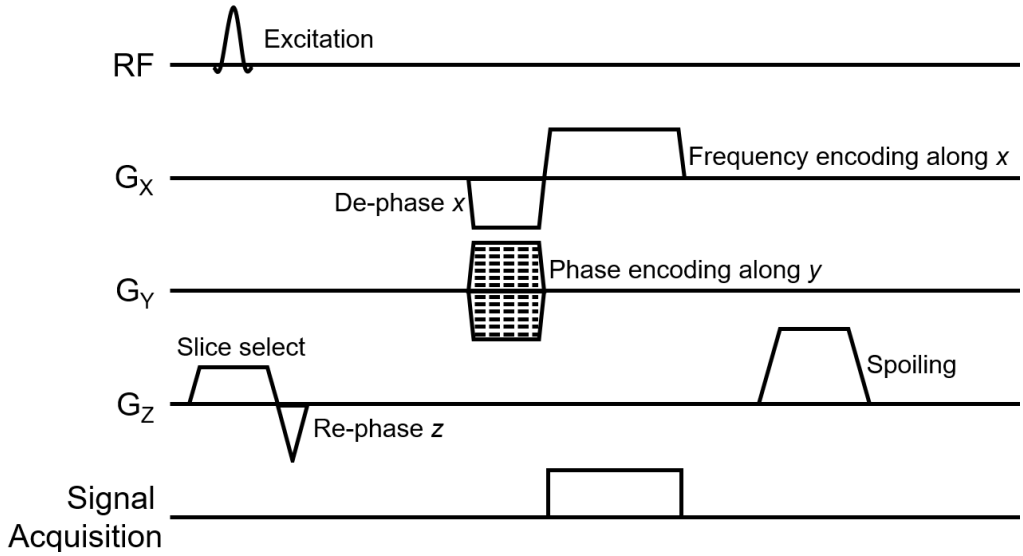


Figure 2.11: Example pulse sequence diagram for a typical 2D FFE sequence. This sequence is repeated after each repetition time (TR) interval with varying amplitudes of the phase encoding gradient, G_Y, with gradient spoiling applied along G_Z.

Upon reaching steady-state magnetisation, and assuming perfect spoiling, the Magnetic Resonance (MR) signal for an FFE sequence is given by

$$S_{FFE} \propto \frac{\sin(\alpha)\left(1 - e^{-TR/T_1}\right)e^{-TE/T_2^*}}{1 - \cos(\alpha)e^{-TR/T_1}}. \tag{2.30}$$

The flip angle, α_E, for which S_{FFE} is maximised is determined by computing the value for which $\frac{dS}{d\alpha} = 0$, giving

$$\alpha_E = cos^{-1}\left(e^{-TR/T_1}\right) \tag{2.31}$$

which is commonly known as the Ernst angle.

By tuning the acquisition parameters, the FFE sequence can be used to produce images with differing contrast, dependant on T_1, T_2^* and the spin density. According to Eqn. 2.30, at long TR and TE, the e^{-TE/T_2^*} relaxation dominates and hence the image is 'T_2^*-weighted'. Moreover, at low flip angles $\cos(\alpha) \approx 1$ and hence the $\left(1 - e^{-TR/T_1}\right)$ terms cancel, removing the effects of T_1, leaving spin density and T_2^* weighting. T_1-weighting is introduced by

increasing α or reducing the TR.

2.2.3.2 Ultrashort Echo Time

An increasingly widely used sequence for lung structural imaging is an Ultrashort Echo Time (UTE), as introduced in Chapter 1.3.1. UTE sequences employ free induction decay (FID) sampling and/or gradient echos with particularly short echo times, which can achieved via RF pulse truncation and ramp sampling. A 2D UTE pulse sequence is shown in Figure 2.12.

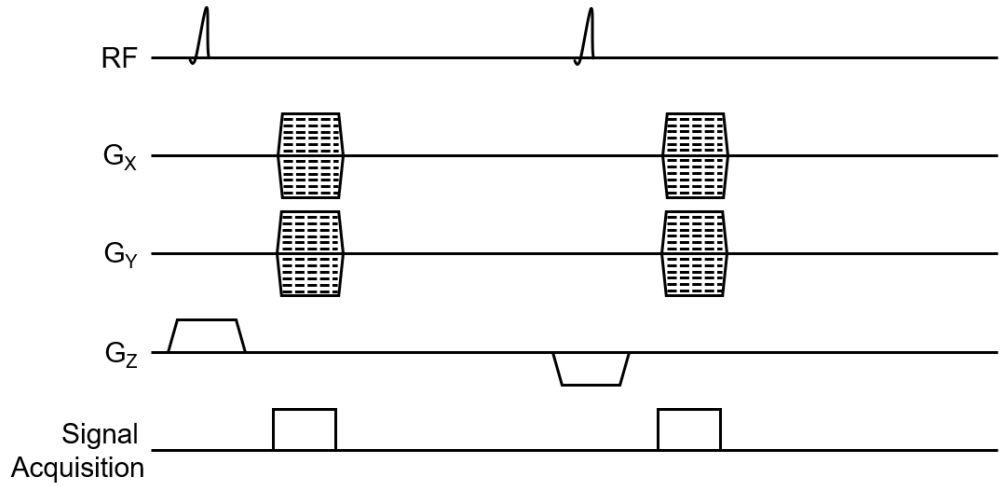


Figure 2.12: Example pulse sequence diagram for a 2D UTE sequence. The excitation RF pulses are truncated allowing signal acquisition to begin almost immediately after excitation (while the readout gradient is ramped on) via radial trajectory. Slice selection gradients with opposite senses are used to acquire half of k-space each, with the sum giving the complete k-space. Adapted from Tyler *et al.* [125]

Non-cartesian trajectories are often used for UTE to more efficiently sample k-space, enabling shorter echo times (acquisition delays). In radial sampling, radial spokes are acquired which each pass through the centre of k-space, oversampling the low spatial frequencies, reducing the sensitivity to motion artefacts. However, these non-uniformly acquired k-space samples must be re-gridded (interpolated) onto a rectilinear grid, which can be challenging when the sampling occurs during gradient ramp and

plateau. Furthermore, the impact of interpolation error accumulation for imaging techniques that require interpolation for re-gridding, registration and respiratory cycle resorting may limit the available SNR. Example radial acquisitions and reconstructions are shown in Appendix 2A.

2.3 Conclusion

This chapter has provided an overview of pulmonary physiology, and of the fundamental MR physics that underpins the subsequent lung imaging experiments performed throughout the thesis.

Chapter 3

Respiratory Induced ^{1}H MR Signal Changes

Abstract

This chapter details the basis of functional ventilation assessment using free-breathing pulmonary ^{1}H MRI. The periodic signal changes associated with the respiratory and cardiac cycle are considered, and several analysis methodologies for ventilation quantification are reviewed, including Fourier Decomposition (FD), Phase-REsolved FUnctional Lung imaging (PREFUL) and Dynamic Mode Decomposition (DMD).

PREFUL-derived Fractional Ventilation (FV) was examined in Cystic Fibrosis (CF) as a marker of response to therapy, where it was found that FV was insensitive to presence of disease, was unable to detect functional change associated with therapy, and lacked an acceptable level of repeatability. This motivated the development of a novel image analysis pipeline termed VOxelwise Lung VEntilation (VOLVE). This pipeline was used to re-analyse the CF data, and an improvement for the sensitivity and repeatability of VOLVE metrics was demonstrated.

A component of this work was presented at the International Society for Magnetic Resonance in Medicine (ISMRM) 31st Annual Meeting (2022) [126, 127].

Statement of Contribution

Zachary Peggs (ZP) performed all data analysis. ZP, Jan Paul (JP) and Christopher Bradley (CB) collected the MR data. Christabella Ng (CN), Helen Barr (HB), Andrew Prayle (AP) and Alan Smyth (AS) contributed to the experimental design for the CF study. ZP, Susan Francis (SF) and Penny Gowland (PG) interpreted the data. SF, PG, Charlotte Bolton (CEB) and Ian Hall (IH) supervised the research.

3.1 Introduction

3.1.1 Variation in Proton Density with Respiration

The motivation for measuring lung function from dynamic ^{1}H Magnetic Resonance Imaging (MRI) first arose from the observation by Zapke *et al.* that in videos of low-field free-breathing Magnetic Resonance (MR) image series, the grey scale values of the lung parenchyma seemed to change throughout the respiratory cycle [128]. At the time, it was hypothesised that this was due to a change in the air/tissue ratio. That is, the local proton density decreases during inspiration, with an associated drop in MR signal intensity, and increases during expiration. Hence, this relative change in signal throughout respiration can be used to measure the change in alveolar density, and therefore the relative change in air content within the lung – this is the ventilation.

After this initial observation, it was shown that a relative change in lung volume produces a relative change in the MR signal intensity of the lung parenchyma in a linear and repeatable fashion. This led to the exciting possibility of assessing local ventilation on the basis of changes in MR signal [129]. For the characterisation of such MR signal changes, non-rigid image registration is required to align the lung boundary (so that signal changes in each voxel can be calculated), developed only a few years prior [130]. This work was initially carried out at low field (0.2T) to minimise T_2* signal decay [128, 131], although studies have now taken place at higher field strength, including 1.5T [17, 18] and 3T [132, 133].

The ability to measure regional ventilation based on relatively straightforward, free-breathing dynamic MRI was a major breakthrough which paved the way for the field of functional pulmonary ^{1}H MRI. Over the last decade, several approaches have emerged which attempt to make use of the variation in proton density with respiration as a functional biomarker relating to lung function. The following chapter provides an overview of the current techniques and potential confounders to the various methodologies, followed

by proposed corrections, improvements, and optimisations. This chapter aims to further develop the methodology used in the analysis of ^{1}H functional pulmonary MRI.

3.1.2 Analysis Methodology for Quantification of Function

3.1.2.1 Fractional Ventilation

The first attempts in the literature to regionally assess ventilation were made by the determination of Fractional Ventilation (FV); the results of which were shown to correlate well with conventional Pulmonary Function Tests (PFTs) for a number of groups including healthy controls, asthma and Cystic Fibrosis (CF) (overall $r = 0.8$; $p < 0.001$ for FV across groups) [128]. The FV parameter has been used extensively in the field since, in particular in Fourier Decomposition (FD)-MRI, and can be understood as follows: consider a two-compartmental model which treats the total lung tissue volume as fixed, and the total volume of air contained inside as variable. During inspiration, there is an increase in the volume of air inside the lung, and hence a decrease in the lung tissue density. This relative decrease in density can be used to infer the relative increase of air, which acts as an indirect measurement of ventilation. This principle is demonstrated schematically in Figure 3.1.

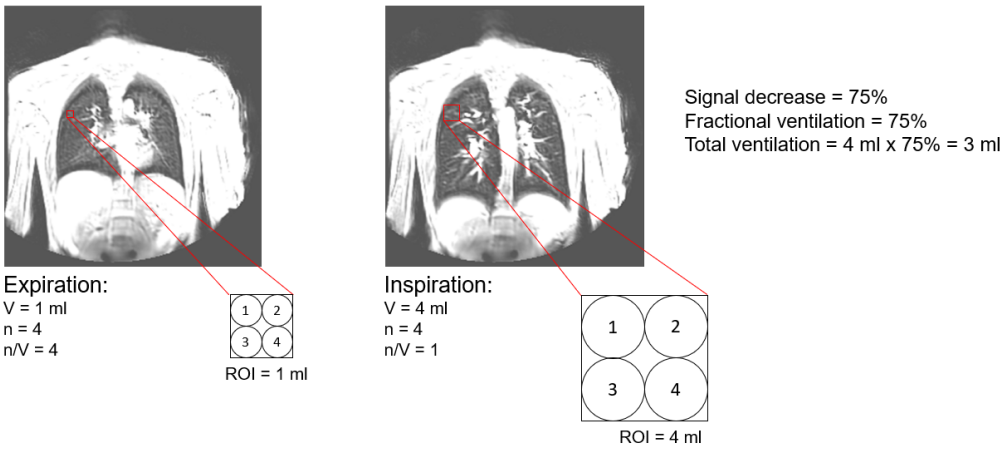


Figure 3.1: Schematic diagram of the FV model. Considering a small group of alveoli in a given volume element or voxel. At the point of full expiration, each alveolus is compressed in space and so occupies only a relatively small volume. During inspiration, the alveoli fill with air and become larger, taking up a larger volume. Since the number of alveoli (or 'mass' of alveoli) is constant, the density must fall for an increasing volume. Since each alveolus now contains more air, with signal equivalent to background noise, there is a corresponding drop in MR signal. Since this reduction in signal is due to a relative increased air content, this gives a measure of ventilation [134].

From this model, assuming that each voxel contains a homogenous distribution of lung parenchyma, Zapke *et al.* state that the total ventilation (ml increased air content per ml lung parenchyma) can be calculated from

$$V_T = \frac{S_{exp} - S_{insp}}{S_{exp} - S_{noise}} \tag{3.1}$$

and so the ventilation at a given point in the respiratory cycle is given by

$$V(t) = \frac{S_{exp} - S(t)}{S_{exp} - S_{noise}}. \tag{3.2}$$

An alternative derivation comes directly from the MRI density equation,

$$\rho(t, x) \cdot V(t, x) = M(x) \tag{3.3}$$

where $\rho(t, x)$ is the proton density, $V(t, x)$ is the finite, local volume centred at position x, and $M(x)$ is the time-invariant 'mass'. Then, we can consider the two key principles involved in dynamic MR measurements:

1. The measured MR signal, S, is proportional to density $\rho(t, x)$.

2. The density $\rho(t, x)$ is inversely proportional to the lung volume.

Hence, S is proportional to the inverse of lung volume. This treatment yields the same equation as proposed by Zapke *et al.* without the noise term [18]:

$$FV = \frac{V_{insp} - V_{exp}}{V_{insp}} = \frac{(1/S_{insp}) - (1/S_{exp})}{(1/S_{insp})} = \frac{S_{exp} - S_{insp}}{S_{exp}}. \tag{3.4}$$

This is the FV definition used throughout this thesis.

There are also other ventilation metrics that use different respiratory cycle phases for ventilation quantification. These including specific ventilation (SV) [135, 136],

$$\text{SV} = \frac{S_{exp} - S_{insp}}{S_{insp}}, \tag{3.5}$$

which is commonly used in exogenous contrast-based approaches (hyperpolarized ^{129}Xe or oxygen-enhanced MRI); and regional ventilation (RVent) [137],

$$\text{RVent} = \frac{S_{mid}}{S_{insp}} - \frac{S_{mid}}{S_{exp}} \tag{3.6}$$

where S_{mid} is the 'average' signal at an intermediate position between inspiration and expiration, introduced for Phase REsolved FUnctional Lung (PREFUL)-MRI. Related analyses have also recently been performed using the Jacobian determinant from the image registration as a measure of local lung expansion — this is explored in Chapter 5.1 of this thesis.

3.1.2.2 Fourier decomposition (FD)

Following on from the initial work by Zapke *et al.*, a significant milestone in ^{1}H pulmonary MRI was the advent of FD. This technique was motivated by the observation that as well as proton density variations during respiration,

there was an additional source of periodic signal variation present in the dynamic image series. The time-of-flight effect, where blood flows into the imaging slice, causes an additional signal variation in the lung parenchyma (discussed in detail in Chapter 6.3), and it was hypothesised that this could be used as an indirect measure of perfusion.

FD-MRI aims to separate signal variations occurring in the lung parenchyma due to the two principle physiological processes driving the oscillatory variations in MR image series signal: respiratory and cardiac cycles. The purpose of this is to use spectral separation to derive both ventilation- and perfusion-related information. This spectral separation process can be visualised with the use of a signal model. Using the model proposed originally by Lujan *et al.* [138] for the apical-basal position of the diaphragm, and then modified by Bauman *et al.* [17] to account for cardiac variations, the parenchymal signal intensity change is given by

$$i(t) = i_0 - A_r \cos^{2n}\left(\frac{\pi t}{\tau_r} - \phi_r\right) + A_c \sin^{2m}\left(\frac{\pi t}{\tau_c} - \phi_c\right) \tag{3.7}$$

where A_r and A_c represent the amplitudes of the respiratory and cardiac cycles, respectively; τ_r and ϕ_r the period and phase of the respiratory cycle, respectively; τ_c and ϕ_c the period and phase of the cardiac cycle, respectively; n and m determine curve shallowness; and i_0 is an offset value. Generation of a simulated signal time-course using this idealised model of signal intensity, along with Fourier analysis to show the spectral lines, is shown in Figure 3.2.

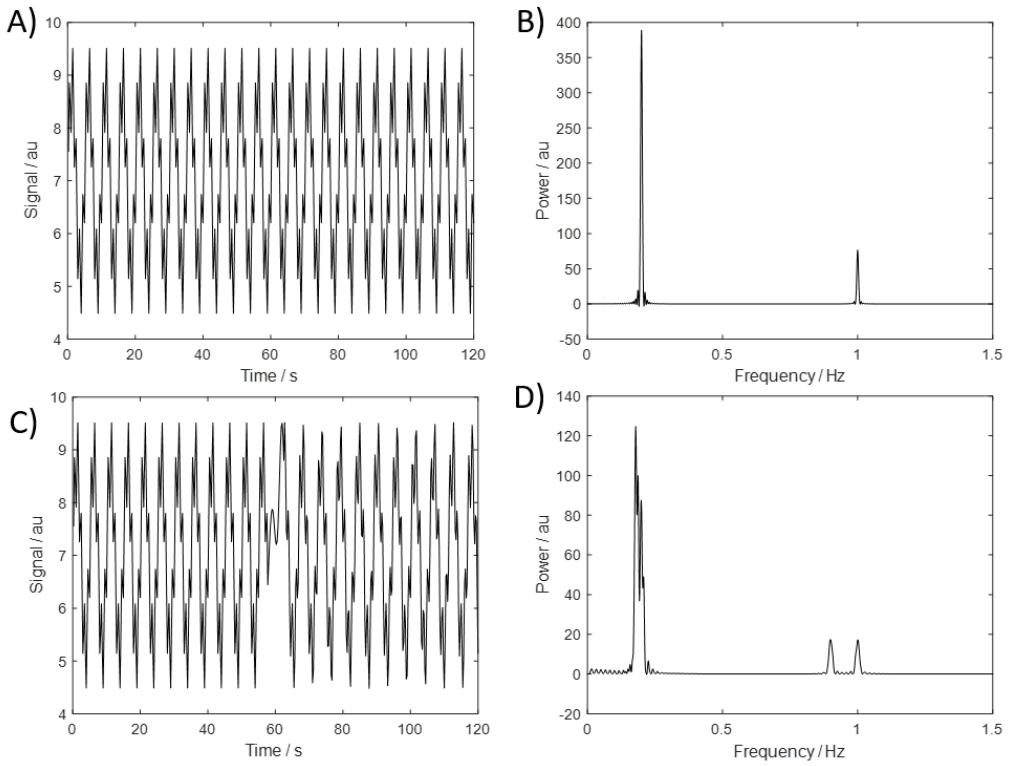


Figure 3.2: A) Simulated lung parenchyma timecourse with signal contributions at both respiratory and cardiac frequencies. Modified Lujan formula used with the following parameters: A_r = 18, A_c = 8, n=1, m=1, τ_r = 5 s, τ_c = 1 s. B) Fourier transform of timecourse in (A) showing spectral peaks at the respiratory and cardiac frequency. C) Altered timecourse with time-varying frequency components. D) Fourier transform of timecourse in (C) showing two overlapping respiratory peaks and two distinct cardiac peaks.

Through this method of Fourier analysis, the signal components from the respiratory and cardiac cycles can be separated. The typical human respiratory rate is between 12 and 20 breaths per minute, with 16 breaths per minute on average (approx. 0.27 Hz) [139]; the typical adult resting heart rate is between 60 to 80 beats per minute (BPM) (approx. 1.17 Hz), although this can vary greatly depending on heart condition and myriad other factors [140]. To achieve this spectral separation in practice, it is a requirement that the images are acquired at a rate of at least double the frequency of the highest frequency component (i.e. the cardiac frequency) in order to satisfy the Nyquist sampling criterion and avoid aliasing of the subsequently generated

signal time course. Hence the minimum temporal resolution required is approximately 3 images/second (90 BPM = 1.5 Hz, hence requiring images to be acquired at 3 Hz).

Once both the Ventilation (V) and Perfusion (Q) frequencies have been identified, voxel-wise calculation of the power spectra is carried out for the masked, registered images, with the area under the respiratory and cardiac peak being calculated for each voxel. This results in ventilation- and perfusion-weighted images, like those produced by Bauman *et al.* [17]. In an initial validation of the FD technique, qualitative ventilation- and perfusion-weighted images were created which showed agreement for instance changes in morphological CT and Dynamic Contrast Enhanced (DCE)-MRI for a patient with a cystic parenchymal defect.

Importantly, these are V/Q-weighted maps, and so these results are dimensionless and non-quantitative in nature. To obtain quantitative FD results for ventilation, Kjørstad *et al.* [134] proposed using the zero-frequency component image to ascertain a baseline from which the signal changes associated with ventilation occur. The zero-frequency component can be found for each voxel by averaging the registered images across time. The establishment of a baseline enables the calculation of the fractional change in ventilation which is a quantified ventilation map, that can be expressed as

$$V_{FD} = \frac{2 \times FD_V}{FD_0 + FD_V} \tag{3.8}$$

where FD_V is the FD ventilation image, FD_0 is the zero-frequency component image and V_{FD} is the quantified FD ventilation. In a similar manner, there is a method of quantifying the FD perfusion maps also put forward by Kjørstad *et al.* [141], where the partially blood-filled voxels are compared with the fully blood-filled voxels in the aorta to calculate quantitative haemodynamic parameters related to pulmonary perfusion.

The principal weaknesses of FD analysis relates to the inherent tendency for the respiratory and cardiac frequency to fluctuate with time. The extent of

frequency variation can be illustrated by the Short-time Fourier Transform (STFT), which involves breaking down a signal into shorter segments of equal length and performing Fourier transformation separately on each segment, as illustrated in Figure 3.3. Examples of stable and unstable respiratory and cardiac frequencies are shown (from a dynamic gradient echo acquisition as described in Section 3.2). As the cardiac and respiratory frequencies are not stationary in time, assumption of a constant frequency leads to an artificial loss in signal. This is due to a mischaracterisation of the spectral profile (height, linewidth, area, etc.) by considering only a single frequency or peak of a multipeak spectrum.

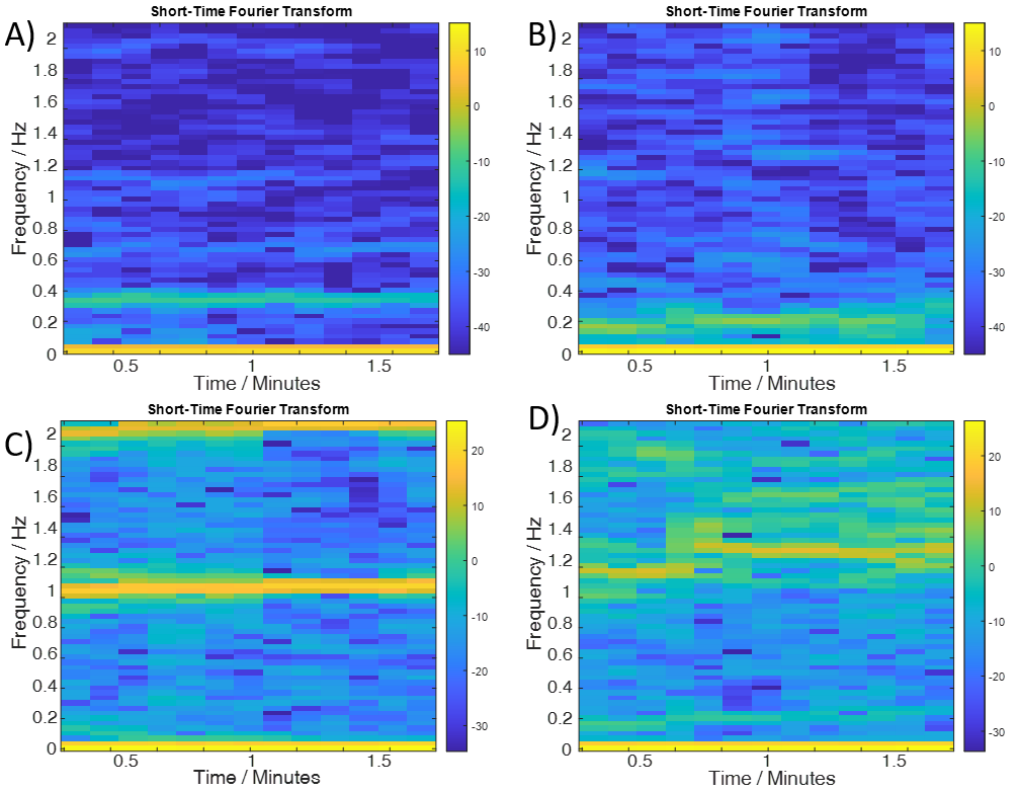


Figure 3.3: Time-frequency spectrograms showing short-time Fourier transforms (STFT) of stable respiratory (A) and cardiac (C) frequencies, and unstable respiratory (B) and cardiac (D) frequencies. Exemplar plots generated from healthy volunteer data acquired according to Section 3.2.

There are some post-processing techniques which could be employed to improve the accuracy of the spectral peak characterisation, such as zero

padding and spline interpolation before Fourier transformation to improve the spectral resolution. However, being able to accurately characterise time-varying frequency components requires a more sophisticated approach. There are broadly three domains of approaches that have been proposed in the literature for lung function quantification: frequency-based, k-space-based and image-based. These techniques are summarised in Table 3.1.

Technique	Domain	Brief description
Non-uniform Fourier transform (NUFFT) [87]	Frequency-space	Evenly sampled signal with variable frequency is converted to a signal with constant frequency with a variable sampling rate.
Matrix pencil decomposition (MPD) [86]	Frequency-space	MPD used to estimate the respiratory and cardiac frequencies, followed by a linear least-squares method to determine the amplitudes.
Dynamic mode decomposition (DMD) [89]	Frequency-space	Eigendecomposition used to pick out dominant spatiotemporal modes.
Self-gated non-contrast-enhanced functional lung (SENCEFUL) [88]	k-space	Self-gating approach (DC gating) to reconstruct respiratory and cardiac cycles for FD-type analysis.
Phase resolved functional lung (PREFUL) [18]	Image-space	Image-based phase estimation and resorting to reconstruct respiratory and cardiac cycles.

Table 3.1: Techniques for lung function quantification.

In the following subsections, the most recent image-space-based (PREFUL) and frequency-space-based (Dynamic Mode Decomposition (DMD)) approaches will be explained in detail.

3.1.2.3 Phase REsolved FUnctional Lung (PREFUL) Imaging

An FD-related method known as Phase REsolved FUnctional Lung (PREFUL) imaging was recently proposed by Voskrebenzev *et al.* [18]. PREFUL is an image-space based approach which sorts the dynamically acquired images into highly temporally resolved respiratory and cardiac cycles, such that the temporal resolution is much higher than that of the rate of image acquisition. By reconstructing full respiratory and cardiac cycles in post-processing, it is possible to obtain PREFUL ventilation and perfusion maps which have shown moderate to good correlation to a number of other more established techniques, including spirometry [Flow-Volume Loop Correlation Map (FVL-CM) and Forced Expiratory Volume in 1 Second (FEV_1) ($r = 0.65$, $p < 0.0001$); Regional Ventilation (RVent) and FEV_1; $r = 0.33$, $p = 0.001$] [93], hyperpolarized ^{129}Xe ventilation maps [133] and dynamic contrast-enhanced (DCE) perfusion maps. Notably, significant agreement between perfusion-weighted PREFUL and perfusion-weighted DCE were found across various disease groups (COPD: $r = 0.79$, $p < 0.01$; CF: $r = 0.77$, $p < 0.01$; CTEPH: $r = 0.73$, $p < 0.01$)[142].

A comprehensive description of the PREFUL framework can be found in [18], with further refinements in [137]. The focus of this work is on the assessment of ventilation, which will be considered here in detail. An overview of the post-processing steps for ventilation are shown in Figure 3.4, and can be broadly broken down into four steps:

1. Lung-diaphragm navigator signal time course generation

    - Segmentation of an Region of Interest (ROI) comprising diaphragm and basal lung parenchyma, followed by averaging of the image ROI signal in the time dimension (before registration) to generate a respiratory/navigator signal time course; end-inspiration points are local minima and end-expiration points are local maxima.

- Extreme outliers in the respiratory signal time course, defined as inspiration points below 10% or expiration points above 95%, are removed from the time course.

2. Respiratory phase calculation and image sorting

- A model function is defined based on the range, R, and offset, C, of the time course,

$$A(t) = R\cos(2\pi f t) + C \tag{3.9}$$

- Each image is classified as either inspiration or expiration based on the instantaneous gradient of the respiratory/navigator time course, m_{tc}, and subsequently the respiratory phase, $\phi_r(t)$, of each image is calculated from the model function according to

$$\phi_r(t) = \begin{cases} \frac{1}{2\pi}\cos^{-1}\left(\frac{A(t)-C}{R}\right) & m_{tc} < 0 \\ 1 - \frac{1}{2\pi}\cos^{-1}\left(\frac{A(t)-C}{R}\right) & m_{tc} > 0. \end{cases} \tag{3.10}$$

- The images are then sorted according to $\phi_r(t)$ and interpolated onto an equidistant time grid, such that the respiratory cycle is reconstructed with high temporal resolution.

3. Filtering, registration and masking

- The image series is registered towards a fixed reference image in the mid-inspiration position, to minimise the overall deformations needed.

- The image series is filtered using edge-preserving guided filtering, where the registered image series is averaged and the resulting highly averaged image (high Signal-to-Noise Ratio (SNR)) is used as the guiding image, increasing the SNR of the entire image series.

- A lung mask is calculated by seeded region growing, with manual corrections if required.

4. Functional parameter calculation

- Various functional parameters can then be determined, such as the FV, FV = $\frac{(S_{exp}-S_{insp})}{S_{exp}}$, and Regional Ventilation (RVent), RVent = $\frac{(S_{exp}-S_{insp})}{S_{exp}} \cdot \frac{(S_{mid})}{S_{insp}}$, or their dynamic analogues, FV(t) = $\frac{(S_{exp}-S(t)))}{S_{exp}}$ and RVent(t) = $\frac{(S_{exp}-S(t)))}{S_{exp}} \cdot \frac{(S_{mid})}{S(t))}$. Additional analysis steps can be carried out on these maps, such as k-means clustering or linear binning [132]. Additional dynamic quantities can be computed such as the Ventilation Time-to-Peak (VTTP).

- Both static (FV, RVent) and dynamic (FV(t), RVent(t), VTTP or, more recently, RVent-CC) functional parameters can be generated as follows:

  – FV can be computed via nonparametric regression (e.g. Nadaraya-Watson regression with a Gaussian kernel), where expiration and inspiration signal values are determined from this fit for each voxel; values at end-expiration are given by the first element of the fit (maximum relative respiratory phase), and end-inspiration are given by the central element of the fit (middle relative respiratory phase) from the phase-sorted data.

  – VTTP can also be computed from this nonparametric fit, given by respiratory phase at which the fit reaches a minimum signal value, with the ideal value equalling middle relative respiratory phase (50% VTTP).

  – RVent-CC can be computed from the first derivative of RVent(t) ($\frac{\Delta \text{RVent}(t)}{\Delta t}$) determined by the symmetric difference quotient — this gives an MRI surrogate for airflow. This 3D

matrix (2D spatial + time) is simplified to a 2D map via cross-correlation comparison to a healthy RVent region.

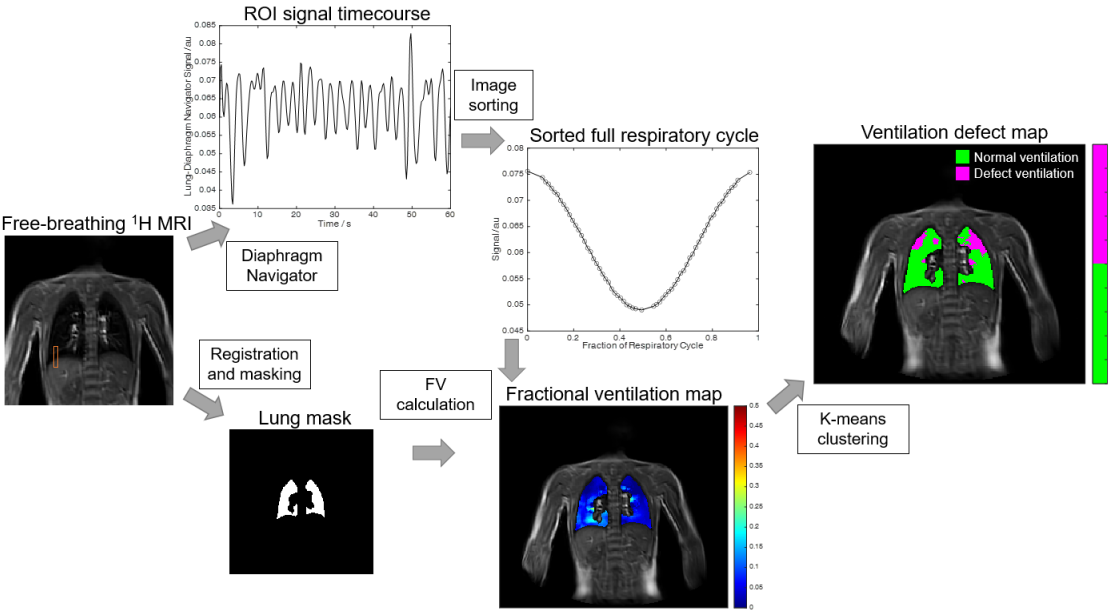


Figure 3.4: PREFUL ventilation pipeline overview. Each image in the free-breathing ^{1}H MRI image series is assigned a respiratory phase value based on a diaphragm navigator signal. The images are then sorted into a canonical respiratory cycle. The images are registered and masked, and subsequent voxel-wise functional parameter computation is performed. Fractional ventilation (FV) — see Eqn. 3.4 —computation followed by k-means clustering can be used to determine regions of ventilation defect.

The PREFUL framework has been widely used by a number of centres and has shown promising preliminary results in several patient groups, including cystic fibrosis (CF) [18, 132, 142], chronic obstructive pulmonary disease (COPD) [18, 142, 143], chronic thromboembolic pulmonary hypertension (CTEPH) [18, 142] and chronic lung allograft dysfunction (CLAD) [144]. However, further validation is required before PREFUL is ready for use in routine clinical assessment of patients. It is especially important that the results produced show an acceptable level of repeatability and reproducibility, which requires further work. This is especially true for use in broader patient groups for which irregular breathing patterns and altered diaphragm

mechanics are observed. These factors are considered in the subsequent subsections — with PREFUL applied in CF in Section 3.3 to determine FV and limitations of this approach discussed in Section 3.3.5.

3.1.2.4 Dynamic Mode Decomposition (DMD)

FD-related techniques aim to derive functional ventilation and perfusion signals from parenchymal proton density change with respiration, and the flow of unsaturated spins in blood, respectively. As discussed in the previous section, this technique is hampered by the instability of the respiratory and cardiac frequency in time. Relatively recently, a data-driven method for extracting the dominant spatiotemporal features from dynamic data known as dynamic mode decomposition (DMD) has been proposed. Initially used in the field of fluid mechanics to decompose complex flow fields, this technique has become widely applied in many different fields, such as fluids dynamics, power systems analysis and medical imaging [145]. The widespread applicability of the techniques owes to the fact that DMD is data-driven and does not require prior information about the nature of the dynamics of the system. In general DMD modes are not orthogonal. DMD has recently been applied to dynamic lung imaging by Ilicak *et al.* with promising initial results [89]. A key advantage to this approach is that all dominant modes are identified via eigen-decomposition and it is therefore robust to time-varying frequencies. A summary of DMD in the application of functional lung imaging follows, with a full treatment of the details of DMD available in [146].

Consider a discrete-time dynamic system in which samples are taken at regular intervals. Each sample or measurement of the system is assumed to be related to the following sample by some linear operator A, and so any pair of sequential samples, x_n and x_{n+1}, can be expressed as $x_{n+1} = Ax_n$. The operator A is known as the linearised dynamics matrix and provides a mapping between successive measurements of the system. It is important to note that while A is a linear operator, it is able to provide the best-fit linear approximation to non-linear dynamics (linear auto-regressive model). The aim of DMD is to use the

eigendecomposition of A to identify dominant spatiotemporal features of the dynamic system. To achieve the eigendecomposition of A, DMD constructs a low-rank approximation of A via Singular Value Decomposition (SVD). This reduced-dimensional representation of the data has the same eigenvalues and eigenvectors as A but is much more computationally efficient to determine. Once the dominant eigenvectors and eigenvalues of A are found, specific modes of interest can be reconstructed via summation over a specified range of frequencies. To apply DMD to functional lung imaging, the following procedure can be followed:

1. Preprocessing: standard preprocessing including non-rigid image registration for dynamic lung data.

2. Data reshaping: represent dynamic data in time-shifted matrices, X and X'.

3. Data stacking: generate multiple time-shifted copies of the measurement matrices to form a larger augmented matrix – increases the rank of the measurement matrix helps improve accuracy of DMD.

4. Dimensionality reduction: apply SVD to generate a low-dimensional representation of the data.

5. Eigendecomposition: perform eigendecomposition of the reduced-dimensional matrix obtained by SVD to yield the DMD modes and eigenvalues: the DMD modes represent the dominant spatiotemporal coherent structures in the data, while the eigenvalues correspond to the oscillation frequencies and amplitudes of each mode.

6. Mode selection: the most dominant DMD modes are identified based on their corresponding eigenvalues. These modes capture the significant respiratory and cardiac frequencies and their associated signal modulations.

7. Signal reconstruction: signal modulations due to ventilation and perfusion can be reconstructed via summation over a both a ventilation and

perfusion frequency range.

While DMD has the potential to overcome the limitations of traditional FD, there is limited published work in this space. In particular, DMD has so far only been applied in healthy cohorts, and so the sensitivity to lung disease is currently unknown. DMD is applied to healthy controls and a Chronic Obstructive Pulmonary Disease (COPD) group in Chapter 4, Section 4.3.4 of this thesis (using the same data used for PREFUL/VOLVE analysis).

3.2 MRI Sequence and Standard Data Preprocessing

This chapter considers image analysis methodology for evaluating lung function using a simple Fast Field Echo (FFE) single slice sequence (see Section 2.2.3). Previous studies have used similar acquisitions [132, 133] and also balanced steady-state free precession (bSSFP) sequences [17, 147].

All images presented in this thesis were acquired using a whole-body 3 T Ingenia MR scanner (Philips Medical Systems, Best, The Netherlands) with flexible ^{1}H abdominal (anterior) coil with 32 channels and in-built posterior receive coils. This acquisition was carried out during free-breathing using a 2D FFE sequence. The sequence parameters are given in Table 3.2 and are matched to the parameters set out in Couch *et al.* [132]. A single coronal slice placed approximately 1 cm posterior to the heart, at the level of the descending aorta, was imaged repeatedly with a temporal resolution of 229 ms. This fast sampling rate was required to avoid aliasing of the cardiac signals. This slice position was chosen to ensure minimal interference from cardiac motion and major pulmonary vessels, whilst capturing a large lung cross-section. A total of 512 dynamic images were acquired in 117 s.

The acquired dynamic, single slice, FFE image time series was analysed using software written in-house in MATLAB R2022b (MathWorks, Natick, MA, USA). Two key steps in the image analysis are 1) image registration and

Parameter	Value
TE (ms)	0.58
TR (ms)	1.9
Flip Angle (degrees)	18
Slice Thickness (mm)	15
FOV (mm^2)	475x475
Resolution (mm^2)	2x2
Bandwidth (Hz/Px)	1500
Dynamic Scan Time (ms)	229
Total Scan Duration (s)	117

Table 3.2: Summary of FFE image acquisition parameters.

2) lung parenchyma segmentation.

Image registration was carried out using a nonrigid demons-based registration algorithm. This technique, first introduced by Thirion [148], matches images by considering object boundaries (in the 'moving' image) as semi-permeable membranes, through which the deformable grid model (from the 'target' image) can diffuse. This framework for nonrigid image registration has been shown to be highly efficient and effective, and has been widely used in medical imaging [149]. The resultant registered image series has lung structures aligned such that the voxels are approximately stationary throughout the respiratory cycle. Image registration is investigated further in Chapter 5 to assess the impact on ventilation measures.

Lung parenchyma segmentation was performed on the registration target image semiautomatically via seeded region growing as described by Kirby *et al.* [150]. Seeds were automatically placed in each lung using predefined seed points, after which region growing is used to iteratively grow the two regions by comparing all unallocated neighbouring pixels to the segmented region; this is done by computing the difference between a pixel's intensity and the segmented region's mean intensity — the pixel with the smallest difference is allocated to the respective region. This process stops when the intensity difference between the region mean and the new pixel become larger than a certain tolerance value. After the initial thoracic cavity mask is generated, a Frangi filter is applied to remove large pulmonary vessels from

the mask [151]. The final thoracic cavity mask was then generated after manual corrections, if required.

After the image series has undergone registration to the target image, and the lung parenchyma has been segmented, the resultant lung tissue signals can be further analysed to quantify lung function.

3.3 Application of PREFUL in CF: FV as a Measure to Assess Response to Kaftrio® Therapy [Adapted from Peggs *et al.* Proc. ISMRM; 2022;#1480]

3.3.1 Introduction

To investigate PREFUL FV as a ventilation measure, a small pilot study was carried out in people with Cystic Fibrosis (CF) and Healthy Controls (HCs). CF is an inherited condition characterised by viscous secretions, especially in the lungs. As a result, people with CF are susceptible to recurrent chest infections and ultimately chronic respiratory disease. New treatments for CF, such as Kaftrio® have recently been licenced in the UK and have been shown to significantly improve lung function [152]. The aim of this pilot study was to study the effect of Kaftrio® therapy on lung function as assessed using PREFUL-MRI at 3T in patients with CF, and to assess repeatability of PREFUL measures in these subjects. It was hypothesised that the proportion of hypointense FV values should be increased in the CF group compared to the Healthy Control (HC) group, and that FV values should increase after commencement of Kaftrio® therapy.

3.3.2 Methods

6 people with CF (12-21 years) and 5 HCs (23-25 years) were recruited to undergo non-contrast enhanced proton MRI on a 3T Philips Ingenia

scanner. PREFUL-MRI was performed with a 2D dynamic Fast Field Echo (FFE) acquisition (TE/TR 0.57/1.9 ms, image acquisition time = 229 ms), as described in Section 3.2. Briefly, a single coronal slice was placed just posterior to the heart (≈ 1cm); 512 images were collected during free breathing over 117 s. In CF participants, scans were collected at baseline (Visit 1), and 12 weeks after commencement of Kaftrio® therapy (Visit 2). Repeated PREFUL datasets were acquired during Visit 2 for CF participants and for the HCs — this was acquired a few minutes after the initial PREFUL scan without the repositioning of the participants. Spirometry was performed for the CF patients at both visits to determine forced expiratory volume in 1 second (FEV_1).

PREFUL analysis was performed using the pipeline of Couch *et al.* [132]. Fractional ventilation (FV) maps were calculated, and k-means clustering [150] was used to distinguish regions of normal ventilation from poorly ventilated areas of the lung. K-means clustering with 5 clusters was used, with the first cluster considered to be ventilation defect (regions of hypointense FV). Ventilation Defect Percentage (VDP) was computed as the number of defect voxels divided by the total number of voxels within the lung mask. Histograms of the FV maps, and the skewness of the histogram and fractional area under histogram for values less than FV=0.2 (%FV<0.2) were calculated. For repeat scans, the standard deviation in VDP was computed along with the coefficient of variation, C_v, of VDP and each histogram metric. A two-sample t-test was performed to compare CF patients (Visit 1) to healthy controls, and to compare CF patients between Visit 1 and 2.

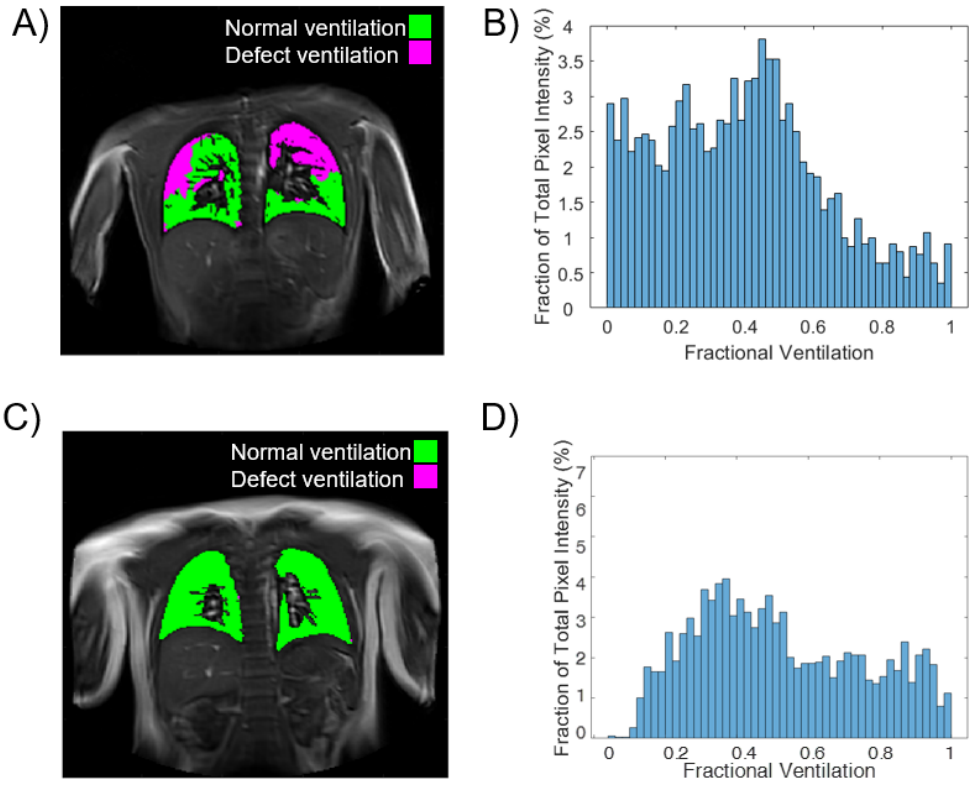


Figure 3.5: K-means clustered FV map from PREFUL analysis in A) a person with CF (FEV_1 of 60%), and C) a healthy control. Regions of normal ventilation (green) and ventilation defect (pink) (VDP = 38% in the CF patient) are shown. B) and D) show FV histograms (anchored using 99th percentile) in CF and HC.

3.3.3 Results

Figure 3.5 shows an example clustered FV map separated into areas of normal ventilation and defect ventilation, and the corresponding FV histogram for a person with CF and a HC. In this CF patient, apical lung regions show ventilation defect (VDP=38%), whereas minimal defect is observed in the HC.

Figure 3.6 shows VDP, skewness and %FV<0.2 of the FV histograms for CF participants plotted against FEV_1 as an assessment of response to therapy for both MRI-based and spirometry-based functional markers. In all but 1 subject, FEV_1 increased at Visit 2 relative to Visit 1. There was generally little

change in VDP between visits in CF. Table 3.3 shows negative correlations that were significant for both VPD and skewness against FEV_1 for the CF patients for both visits, although these correlations may have been strongly influenced by a few data points. Table 3.3 also shows that no change was detected between healthy controls and CF (sensitivity to disease), and no change was observed between visits in CF (all $p>0.05$) (response to therapy).

Figure 3.7 indicates repeated measures for the healthy controls and CF patients (Visit 2 only) and shows the within subject mean, within subject coefficient of variation, $C_{v,w}$ (assessment of repeatability) and between subject coefficient of variation, $C_{v,b}$ (variability within group).

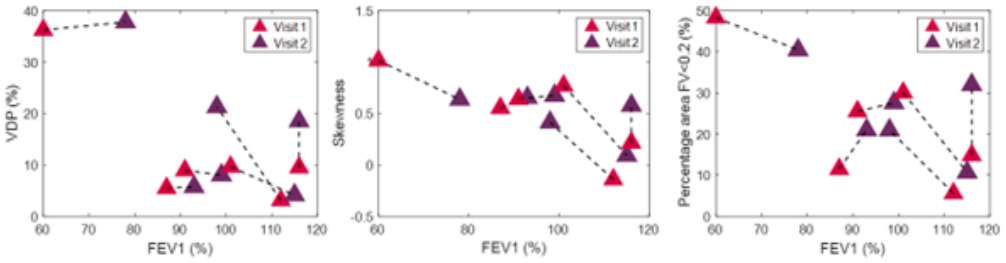


Figure 3.6: CF response to therapy; VDP, skewness and fractional area under histogram for values less than FV=0.2 (%FV<0.2) are shown plot against FEV_1 % predicted values for the CF group.

	HC scan 1 vs CF Visit 1 (sensitivity to disease), p	CF Visit 1 vs Visit 2 scan 1 (response to therapy), p	CF Pearson Correlation against FEV_1 Visit 1, r (p)	CF Pearson Correlation against FEV_1 Visit 2, r (p)
VDP (%)	0.61	0.31	-0.81 (p=0.04)*	-0.79 (p=0.02)*
Skewness	0.50	0.50	-0.83 (p=0.04)*	-0.91 (p=0.01)*
$\%FV_{<0.2}$	0.77	0.36	-0.78 (p=0.07)	-0.50 (p=0.3)

Table 3.3: Assessment of change between HC and CF patients and in CF patients in response to therapy (two-sample, one-tailed, t-test; *=significant)

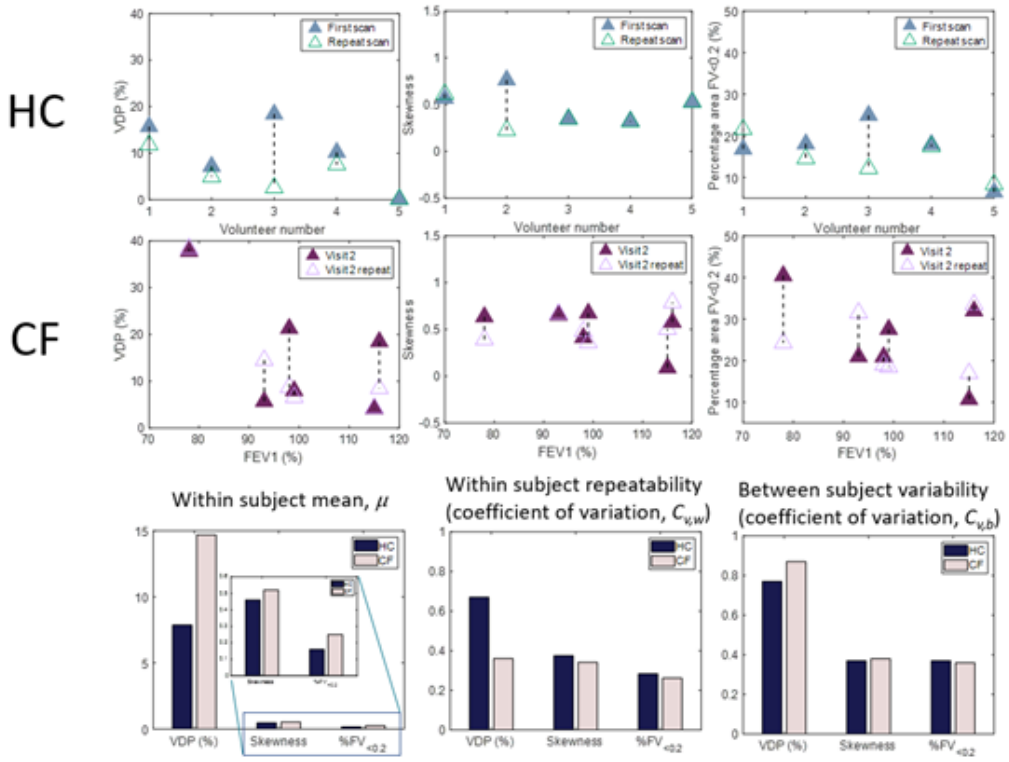


Figure 3.7: Repeat measurements of VDP, skewness and fractional area under histogram for values less than FV=0.2 (%FV<0.2) – top two rows. Within subject mean, within subject coefficient of variation and between subject coefficient of variation are shown – bottom row.

3.3.4 Discussion

In this small study, no significant difference in the PREFUL-derived FV measures used, either between HC and CF patients, or before and after Kaftrio® therapy in CF patients, (t-test or simply comparing changes to C_v for repeated measures) were observed. There was a trend for all measures to be increased in CF visit 1 compared to HC (according to hypothesis), although this was not significant. While FEV_1 (global, bulk measurement) tended to increase between visits, there was no clear trend in the FV metrics.

This may be due to the small sample size in this preliminary study and also lack of age matching. It was notable that repeatability was relatively low in the CF group (up to 40% C_v,w with between-visit changes of 10-80%). This poor repeatability may be because these young subjects tended to move more than

the HCs during scanning. Also, the relatively large C_v values could be due to metrics which have near-zero means, thus small differences between repeats will have a large impact on the C_v. However, upon repeat analysis of HC subject 3 first scan (outlier), a change in the mask threshold and registration target image led to a VDP of 5.7 %; more in line with other HC values and closer to the repeat value. This indicates the sensitivity of the measures to segmentation of the lung-diaphragm ROI, subjective thresholding and arbitrary choice of target for image registration.

The FV histograms exhibited non-Gaussian distributions, which may be related to the omission of a noise term in the computation of FV, although it is not clear how this term would vary between inspiration and expiration. While a trend for an increase in the proportion of hypointense FV values was seen in CF, further investigation into the nature of the FV distribution in health and disease is required. This includes investigating the impact of noise and whether a reduction in FV is related to a reduction in SNR due to a decrease in local proton density such as from air trapping (minus pathology). This may be especially problematic when relying on use of the inspiration state for which the local proton density is further reduced.

A potential limitation in the computation of VDP in this pipeline is the use of k-means clustering. This technique has been widely used for hyperpolarized gas MRI [150, 153] for computing VDP, and so it was assumed that this method of VDP segmentation is viable for PREFUL FV. As suggested by Couch *et al.*, other methods such as linear binning that make use of healthy reference data to define defect thresholds may be more appropriate [132].

Additionally, FV is calculated from the change in the parenchyma MR signal between inspiratory and expiratory phases of respiration as determined from the lung-diaphragm navigator ROI. Hence, the measured value of FV may be affected by irregular breathing patterns (breathing with varying respiratory frequency and amplitude), particularly in patients. This could

partly explain the apparent lack in sensitivity to disease and inability to assess response to therapy. Other metrics such as PREFUL VTTP could be explored, which may be more robust to irregular breathing.

These potential sources of intra- and inter-visit variability require further investigation before PREFUL FV-based approaches are viable for clinical translation or for use as endpoints in further clinical trials, and are explored in the following Section 3.3.5.

3.3.5 Confounders: Breathing Behaviour & Respiratory Cycle Resorting, Diaphragm Dynamics, and Signal Response Linearity

The principal drawback of static FV-related approaches, where calculation of the ventilation parameters involves only two or three respiratory states, is their dependence on the exact breathing behaviour exhibited when the data is acquired. Since FV depends on the signal at end-expiration and end-inspiration (Equation 3.4) then variation in tidal volume inevitably leads to variation in FV [154]. Thus, variability in the amplitude of breathing, especially in different patient groups, makes characterisation of ventilation via FV challenging. An example of the impact of breathing behaviour is shown in Figure 3.8, where PREFUL-derived FV maps are shown for regular tidal breathing and deep breathing in the same healthy subject. It can be seen that the same general distribution is observed, with areas of increased FV in free breathing becoming much more prominent with greatly increased values for heavy breathing. This can be explained by an increased tidal volume producing an increase in the absolute ventilation. Voskrebenzev *et al.* introduced a correction for this effect, utilising a lung area timeseries derived from the inverse deformation fields from image registration to determine a tidal volume adjustment, which was found to improve FV repeatability and reproducibility [155]. However, the production of static ventilation maps still results in inefficient data sampling and introduces bias based on the respiratory cycle phases used in the analysis.

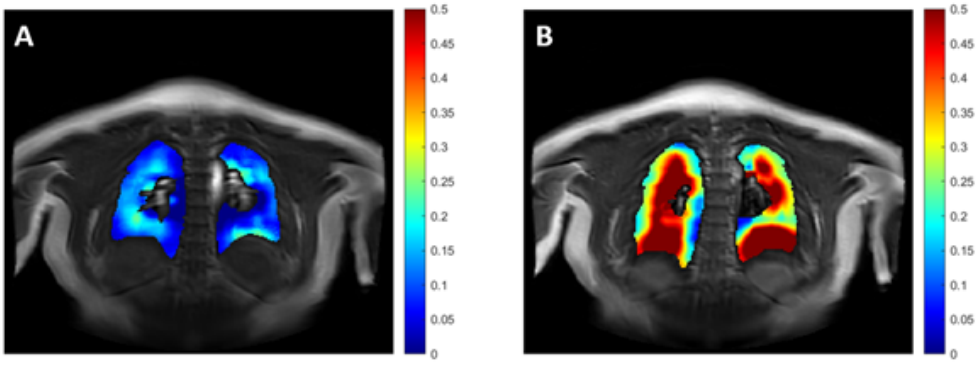


Figure 3.8: PREFUL-derived FV maps for (A) gentle, tidal breathing (median = 0.10) and (B) exaggerated, heavy breathing (median = 0.47). Similar regional patterns are shown, but with greater increased FV values for heavy breathing due to increased total ventilation.

Recently, much work has been done with the PREFUL technique, including the determination of dynamic regional flow-volume parameters as a form of imaging-based spirometry, rather than static ventilation measures derived from traditional FD analysis [93]. These dynamic assessments are achieved by determining voxel-wise the slope of $\mathrm{RVent}(t) = \frac{(S_{exp} - S(t))}{S_{exp}}$, which gives a surrogate for airflow. These regional flow-volume loops can be transformed into functional maps by comparing each loop to a healthy reference loop via cross-correlation. The assessment of ventilation dynamics via regional flow-volume loops has been shown to correlate with FEV_1 in COPD and be more sensitive than static ventilation measures in early chronic lung allograft dysfunction [144]. Additional dynamic ventilation parameters can be calculated such as VTTP, which uses the symmetry of the model function to suggest a healthy VTTP at 50% through the respiratory cycle – i.e., the signal in a given voxel is expected to reach a minimum at end-inspiration (see Section 3.1.2). While a shift away from static measures towards these dynamic measures is encouraging, there remains several confounders in the regional mapping of ventilation with this method.

A key factor in the regional ventilation maps produced by dynamic, free-breathing ^{1}H MRI is the exact nature of the subject's breathing during the

MRI acquisition. Breathing with irregular frequency leads to a broadened spectral linewidth in the Fourier domain and breathing with irregular amplitude/depth leads to difficulty in determining comparable respiratory cycles for signal averaging and a bias towards particularly deep breaths. The impact of deeper breathing resulting in increased total ventilation and a skewed FV map was illustrated in Figure 3.8. In addition, although during PREFUL image resorting extreme respiratory outliers are removed, there is still a potential for bias; for example, if there is a period of substantially deeper breathing during the acquisition, this will bias the threshold for outlier removal to an artificially high value, leaving room for still relatively large amounts of variation in respiration amplitude throughout tidal breathing. Also, this image resorting relies on the instantaneous gradient of the lung-diaphragm navigator timeseries, which is sensitive to signal variations other than respiratory induced density changes, although this can be somewhat compensated for by performing binarization before computing the respiratory phase timecourse, or by lowpass filtering, as shown in Figure 3.9.

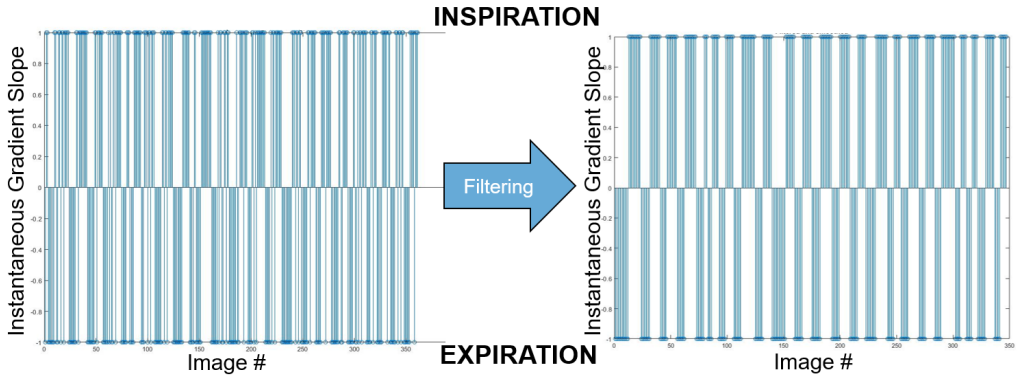


Figure 3.9: Stem plot showing the slope of the instantaneous gradient of the respiratory navigator timecourse. A slope of +1 corresponds to inspiration and -1 to expiration. The navigator signal is corrupted by high frequency signal variations e.g., from the cardiac cycle, and so the instantaneous gradient slope switches between ±1 sporadically on timescales much less than the period of a typical breath (i.e., two images span 0.5s and so an isolated stem point would correspond to an unrealistic expiratory/inspiratory phase of less than 0.5s). This respiratory phase mischaracterisation can be compensated by lowpass filtering and removal of outlying breaths, as shown.

It is reasonable to hypothesise that breathing irregularities will be as common if not more common in patient groups with compromised lung function, and so it is important that any method attempting to quantify lung function is robust to this and so independent of breathing behaviour. There are additional considerations when looking to apply these techniques in certain patient groups with altered or compromised diaphragm mechanics and morphometry. Certain pathology such as air trapping causes hyperinflation, leading to a considerably increased residual volume and an increased tendency to utilise intercostal muscles rather than diaphragm muscles for breathing effort [156]. These altered diaphragm mechanics should be accounted for if the diaphragm is being used to characterise respiratory phase.

Another important consideration when attempting to infer information about ventilation from proton density changes is the nature of the relationship between the respiratory cycle and the evolution of the MR signal in the lung parenchyma. The underlying principle first set out by Bankier *et al.* [129] that MR signal varies linearly with lung volume in healthy individuals should be carefully considered in the presence of pathology and how different pathophysiology may impact this relationship. In addition, this assumption of linearity has not been explicitly explored in the literature, and with the move of several centres from 1.5 T to 3 T there is a growing need for verification that this relationship holds true in the 3 T regime.

The remainder of this chapter details work that aims to address some of the identified confounders in the currently employed ^{1}H MRI image analysis methodologies, and the development of the Voxel-wise Lung Ventilation (VOLVE) technique.

3.4 Development of Voxel-wise Lung Ventilation (VOLVE) Image Analysis Methodology

The aim of this work is to probe the fundamental signal variations that are measured during dynamic ^{1}H imaging, independent of breathing pattern. A fundamental assumption in previous work is that the ^{1}H MRI signal depends on the fraction of lung parenchyma tissue in a given voxel and that the MRI signal varies linearly with the change in lung volume — an assumption that is interrogated in Chapter 5.2. Assuming that linearity holds in health and disease, a framework for quantifying this signal change is proposed making use of the Pearson correlation coefficient, cross-correlation and York regression (introduced by Derek York in 2004 [157]). This framework is termed VOxelwise Lung VEntilation (VOLVE) analysis, and works by comparing the global respiratory state from a navigator signal to the voxelwise lung parenchyma signal timeseries.

3.4.0.1 Fitting Methodology

After standard image post-processing steps including non-rigid image registration and lung parenchyma segmentation (as outlined in Section 3.2), the resulting data consists of approximately 2500-5000 lung parenchyma voxels depending on the size of the person and the slice position. These voxels exhibit complex oscillatory signal variations that depend on several factors, including:

- Major signal fluctuations dominated by the respiratory and cardiac cycles – although this is also impacted by the image acquisition rate which determines the degree of aliasing of the signal from the blood (unsaturated spins) flowing through the imaging slice.

- Additional signal changes associated with the change in blood volume over the cardiac cycle, and the change in vascular space occupancy due to changes in blood pressure and flow velocity.

- Anatomical spatial positioning – apical/basal and anterior/posterior changes in alveolar density, and location of major pulmonary vessels (more vessels at central vs peripheral lung).

- Gravitational effects due to subject orientation, including varying gradients of intrapleural pressures and lung water distribution impacting ventilation in supine verses prone posturing [158]. This is particularly relevant when comparing between lying and seated/standing positioning and when exploring anterior-posterior changes.

- Diffuse and localised lung disease affecting both ventilation and perfusion – some pathology reduces proton density ('minus pathology') such as emphysema and other pathology increases proton density ('plus pathology') such as fibrosis.

- Dynamic range of signal affected by the total ventilation – deep breathing increases dynamic range compared to normal tidal breathing. This can also be affected in disease such as air trapping leading to hyperinflation in COPD, reducing the dynamic range and altering breathing mechanics.

- Signal changes also affected by image registration regularization parameters and registration target choice (see Chapter 5.1).

Assuming that the change in the MR signal in a given voxel varies linearly with the change in lung volume, it is hypothesised that the magnitude of this change can be characterised by a linear regression approach. This relies on the use of a navigator-type signal, which characterises the respiratory phase of each image (i.e., end-expiration, end-inspiration, or somewhere in-between). This navigator signal represents the global respiratory behaviour and gives the expected signal evolution of the lung parenchyma due to proton density changes. This navigator signal can then be regressed voxelwise against the signal timecourse in each lung parenchyma voxel, which represent localised respiratory behaviour.

Various metrics that describe the relationship between these two quantities can then be computed: the Pearson correlation coefficient, gradient, cross-correlation and lag. In the following section, these metrics are applied to an example in vivo dataset which was first registered and segmented, for a healthy volunteer (age 24, male) with no lung disease/symptoms (referred to as 'the illustrative dataset') to illustrate the development of the approaches throughout this chapter.

3.4.1 Pearson Correlation Coefficient

The Pearson product-moment correlation coefficient (PPMCC, or more commonly abbreviated to simply correlation coefficient, CC) is used ubiquitously as a measure of linear correlation between two sets of data and is often denoted as r, where r, ranges from +1 to -1 and indicates the strength of linear relationship between two variables. An r value of 1 corresponds to perfect positive correlation, and an r value of -1 corresponds to a perfect negative correlation. A value of zero indicates no correlation. The correlation coefficient, r, for a sample is defined as the mean of the products of the standard scores, given by

$$r = \frac{1}{N-1} \sum_{i=1}^{N} \left(\frac{A_i - \mu_A}{\sigma_A} \right) \left(\frac{B_i - \mu_B}{\sigma_B} \right) \tag{3.11}$$

where N is the sample size, μ_A and σ_A are the mean and standard deviation of A, respectively, and μ_B and σ_B are the mean and standard deviation of B. In general, it is assumed that there is a linear relationship between the change in MR signal in the lung parenchyma with lung volume. It is therefore hypothesised that in the healthy lung, there exists a strong positive correlation between the lung volume and the parenchyma signal, as the alveoli expand and contract throughout the respiratory cycle, giving rise to MR signal evolution in line with the corresponding density changes. It is assumed that the lung volume change is well characterised by a lung-diaphragm navigator signal, derived from MR signals changes in an ROI across the diaphragm – this assumption is investigated in Chapter 5.2. Given this assumption, it is

expected that the lung-diaphragm navigator signal and healthy lung tissue will have a strong positive correlation.

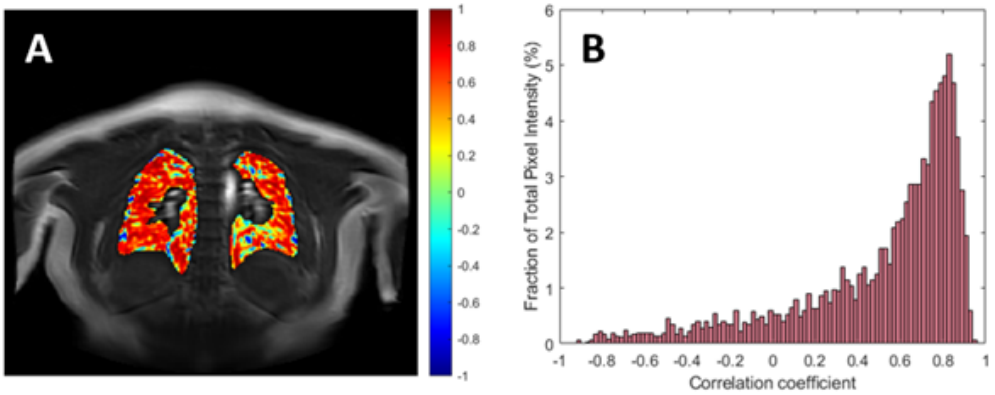


Figure 3.10: Example map (A) of the correlation coefficient (CC) for a healthy volunteer (age 24, male), along with associated histogram (B) which is heavily negatively skewed (skewness = -1.44).

To test this hypothesis, the CC was computed voxelwise for the illustrative dataset. The CC map and histogram are shown in Figure 3.10. As expected, in the healthy lung the CC map was relatively homogenous with CC values > 0.7 (histogram negatively skewed; skewness = -1.44), except for some small regions in, or bordering, vessels. For a given voxel, which provides a local measurement of proton density variation, a strong correlation with the navigator signal, which provides a global measure of proton density variation, indicates signal variations in line with the expected density changes. It appears that the correlation values are lower in the left lung (image-RHS) near the heart and/or main pulmonary vessels, which could be due to interference from pulsatile flow through the slice. Alternatively, this could be explained by bulk tissue motion through the 2D slice or by inaccurate registration. The source of the negative CC values at the lung periphery are not immediately obvious – this could be an artefact from the ribs as they appear to be in localised areas with similar sized vertical gaps – or due to genuine differences in density changes at the lung periphery. Further data collection and analysis is required to determine the nature of these negative regions. It is also reasonable to expect this CC to be impacted by disease, which is investigated

in Chapter 4.

3.4.2 Linear Fitting: York Gradient

3.4.2.1 York Regression, Comparison to Ordinary Least Squares and Validation of Used Algorithm

In addition to the linear correlation, the gradient provides a measure of the magnitude of the local MR signal change, which is physically (and therefore clinically) relevant. There are several regression techniques that can be used to determine the gradient and intercept of a linear model. A brief overview of widely used techniques is provided in Table 3.4. Ordinary least squares (OLS) is commonly used due to it being the most straightforward approach. OLS regression minimises the sum of squares in the dependent variable (Y) residuals. Hence, only errors in the dependent variable are considered, and it is assumed that the independent variable (X) has zero error. There are several approaches for situations where there are errors in both dependent and independent variables. These can be categorised as either bivariate fitting techniques (also known as error-in-variables regression) and total least-squares fitting techniques. Figure 3.11 provides a visual representation of commonly used minimisation schemes.

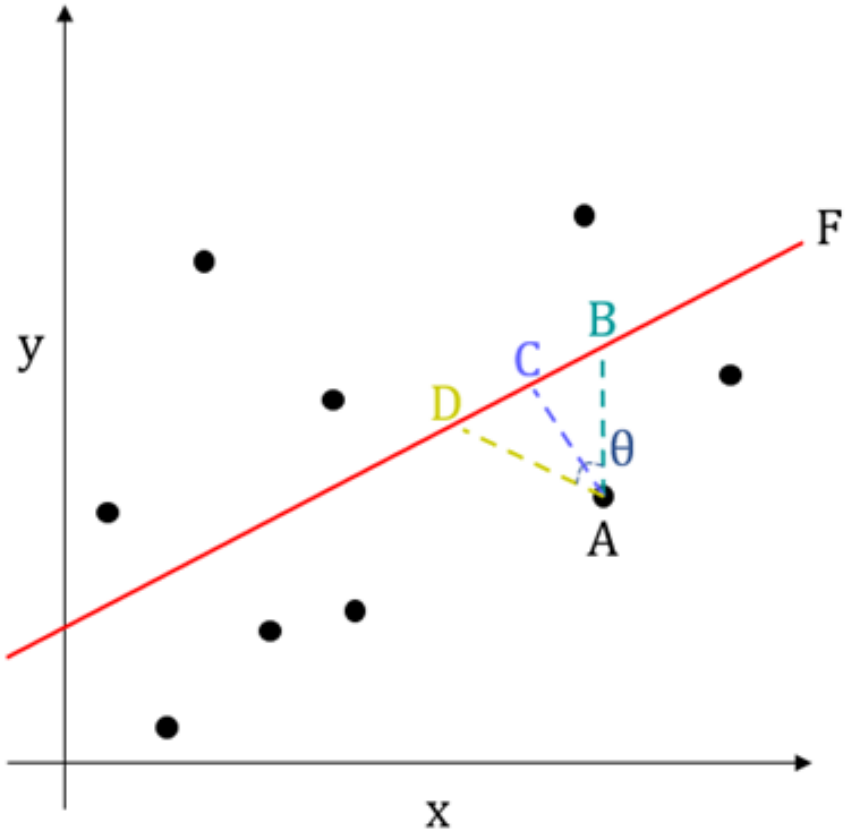


Figure 3.11: Relations between data point A and linear fit line F. Fitting by OLS minimises the distance AB (AB orthogonal to x-axis). Fitting by ODR and DR (λ=1) minimises the distance of AC (AC orthogonal to F). Fitting by DR (λ=$\omega(X_i)/\omega(Y_i)$) , WODR and YR minimises AD. AD is given by AB rotated by angle θ, where θ is determined by the uncertainty in y and x.

Briefly, OLS minimises the sum of squares in Y residuals, orthogonal distance regression (ODR) [159] minimises the sum of squares in Y and X residuals, Deming regression (DR) [160] and weighted orthogonal distance regression (WODR) [161] minimise weighted Y and X residuals, and York regression (YR) [157] introduces the correlation between the errors/weights into the minimisation routine. OLS and DR are closed-form, whereas ODR, WODR and YR are carried out iteratively, although usually converge in ten or fewer iterations given a convergence tolerance for the gradient, b, of $\frac{b_{i+1}-b_i}{bi}$ = $1x10^{-15}$.

YR will be used in this thesis, as it provides the most comprehensive regression scheme as it allows for correlation between the X and Y errors. YR is widely used in the geophysical literature, but practically unknown outside of this field. It provides a general and exact solution to best-fit straight line, where other linear regression methods are special cases of YR that are valid only under specific conditions [162].

YR involves iteratively solving the following system of equations:

$$a = \overline{Y} - b\overline{X} \tag{3.12}$$

$$b = \frac{\Sigma W_i \beta_i V_i}{\Sigma W_i \beta_i U_i} \tag{3.13}$$

$$\overline{x} = \frac{\Sigma W_i x_i}{\Sigma W_i} \tag{3.14}$$

$$\overline{y} = \frac{\Sigma W_i y_i}{\Sigma W_i} \tag{3.15}$$

$$U_i = X_i - \overline{X} \tag{3.16}$$

$$V_i = Y_i - \overline{Y} \tag{3.17}$$

$$W_i = \frac{\omega\left(X_i\right)\omega\left(Y_i\right)}{\omega\left(X_i\right) + b^2\omega\left(Y_i\right) - 2br_i\alpha_i} \tag{3.18}$$

$$\beta_i = W_i\left[\frac{U_i}{\omega\left(Y_i\right)} + \frac{bV_i}{\omega\left(X_i\right)} - \left(bU_i + V_i\right)\frac{r_i}{\alpha_i}\right] \tag{3.19}$$

$$\alpha_i = \sqrt{\omega_{xi}\omega_{y_i}}. \tag{3.20}$$

In practice, this involves assuming a starting value for the gradient, b, then calculating U_i, V_i, W_i, β_i and α_i, then updating the value of b via gradient descent. This process continues iteratively until b changes by a small enough amount, determined by a convergence tolerance parameter. The uncertainty in the intercept, a, and gradient, b, can also be determined in this iterative procedure, given by

$$\begin{aligned} \sigma_a^2 &= \frac{1}{\Sigma W_i} + \overline{x^2}\sigma_b^2 \\ \sigma_b^2 &= \frac{1}{\Sigma W_i u_i^2}. \end{aligned} \tag{3.21}$$

YR was implemented in MATLAB R2022b. This implementation was validated by comparing to two other implementations: 1) published spreadsheet-based implementation by Cantrell [163] and a commercial software implementation (OriginProTM 2022). The dataset chosen for this validation was Pearson's data with York's weights according to York (Pearson-York data — depicted in Figure 3.11) [164]. York's weights were converted to uncertainties by the relation $\sigma_i = \frac{1}{\sqrt{W_i}}$. All three implementations tested produced linear fit coefficients (y=-0.480533407446x + 5.479910224033) in agreement to 12 significant figures.

Table 3.4: Summary of linear regression techniques.

Approach	**Sum of Squared Residuals**
Ordinary least squares (OLS)	$S = \sum_{i=1}^{N} (y_i - Y_i)^2$
Orthogonal distance regression (ODR)	$S = \sum_{i=1}^{N} [\ (x_i - X_i)^2 + (y_i - Y_i)^2\ ]$
Deming regression (DR)	$S = \sum_{i=1}^{N} [\ \omega(X_i)(x_i - X_i)^2 + \omega(Y_i)(y_i - Y_i)^2\ ]$
Weighted orthogonal distance regression (WODR)	$S = \sum_{i=1}^{N} \left[\frac{(x_i - X_i)^2 + (y_i - Y_i)^2}{\eta} \right]$
York regression (YR)	$S = \sum_{i=1}^{N} [\ (\omega(X_i)(x_i - X_i)^2 - 2r_i\sqrt{\omega(X_i)\omega(Y_i)}(x_i - X_i)(y_i - Y_i) + \omega(Y_i)(y_i - Y_i)^2)\ ] \frac{1}{1 - r_i^2}$

3.4.2.2 Robustness to Phase Difference

To investigate the impact of phase shift between two signals on the linear gradient obtained from OLS and YR, a simulation was performed using a

sinusoidal signal model. Two simulated signals were generated from signal equation $S = S_0 \sin(\omega t + \phi) + A + r$, where S_0 is the signal amplitude, ω is the signal frequency, ϕ is the relative phase, A is the signal offset and r is a Gaussian noise parameter. The first generated signal had a reduced noise level and $N = 1$ repeats; this is a model for the respiratory phase signal. The second signal had an increased noise level and $N = 10000$ repeats; this is a model for the MR signal from the lung parenchyma. The phase difference between the signals was then varied from -3π to +3π, as seen in Figure 3.12. For a phase difference of up to $\pm\frac{\pi}{2}$, the York regression can be seen to be robust in determining the gradient. For a phase difference of more than $\frac{\pi}{2}$ (but less than $\frac{3\pi}{2}$), York regression finds a negative gradient. This is significant for two reasons: 1) YR can mitigate against gradient bias in the event of a phase shift of up to $\frac{\pi}{2}$ ($-\frac{\pi}{2} < \phi < \frac{\pi}{2}$), and 2) YR can find a negative gradient of the correct magnitude for phase shift of up to $\frac{3\pi}{2}$ ($\frac{\pi}{2} < \phi < \frac{3\pi}{2}$). Hence, we can determine magnitude signal changes of the lung parenchyma relative to the navigator signal that are robust to phase shifts between the signals.

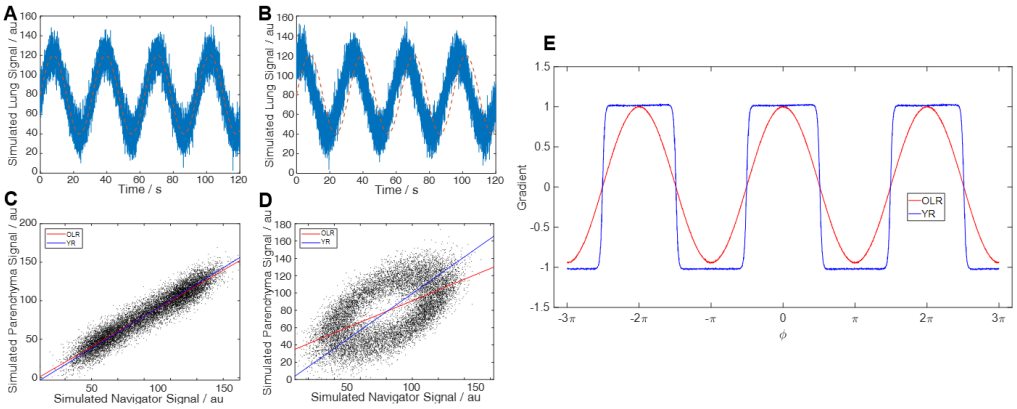


Figure 3.12: Simulated respiratory timecourse with Gaussian noise, without (A) and with (B) a phase shift. (C, D) shows ordinary linear regression (OLR) and York regression (YR) in (A, B), with N=10000 simulated Y signals (simulated lung parenchyma signals) and N=1 X signals (simulated navigator signal). Note that for this phase shift ($\frac{\pi}{3}$ or 60°), the OLR gradient is shallower, while the YR gradient remains the same. (E) shows the relationship between gradient and phase for OLR and YR.

3.4.3 Application of York Gradient to Dynamic Lung Imaging

It is hypothesised that for healthy lung tissue, which expands and contracts and so exhibits variations in density throughout the respiratory cycle, that an equal relative change change will be observed between the respiratory navigator and localised voxel signals. The navigator is expressed as relative/percentage change from the signal median, resulting in an expected average gradient value of approximately +1. Deviation from this implies distortion or asymmetry of the parenchyma signal response to respiration. Details on the determination of the navigator signal are provided in see Section 3.5.

To test this hypothesis, York regression was performed as described for the illustrative dataset. The York gradient map and histogram are shown in Figure 3.13. The York gradient map displays values generally >0.5, except for negative values in the remaining main pulmonary vessels. The gradient histogram displays a primary peak at 1.3, and a small secondary negative gradient peak at -1.

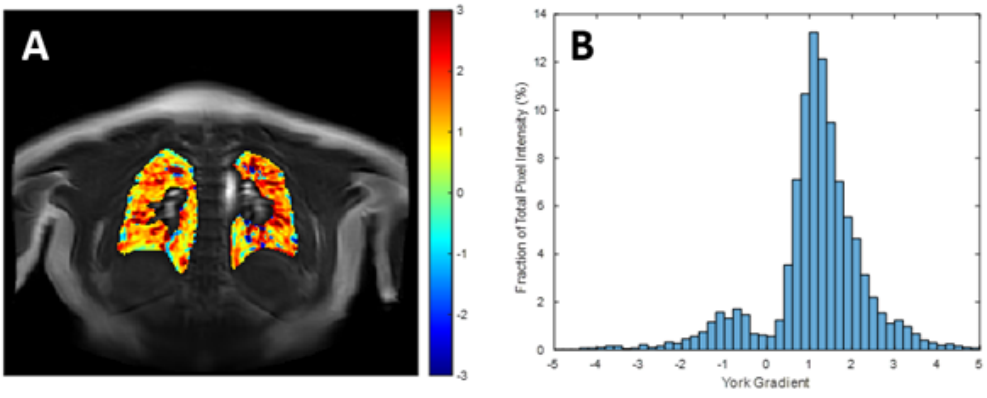


Figure 3.13: Example map (A) of the York gradient for a healthy volunteer (age 24, male), along with associated histogram (B) which displays bimodality with a primary positive peak and secondary negative peak.

There is intrinsic thermal (Johnson-Nyquist) noise in all MR images, where each receiver channel's signal is confounded with white noise (zero-

mean Gaussian). After the raw complex k-space data are transformed into image-space via the Fourier transform (linear and orthogonal operation), the real and imaginary signals zero-mean Gaussian white noise is preserved. The real and imaginary images are combined via the root sum-of-squares (a non-linear operation) to give the magnitude image. This also combines the two Gaussian noise distributions into the asymmetric Rician probability distribution, giving rise to a rectified noise floor [165, 166], as shown in Figure 3.14. This noise floor imposes a minimum signal level below which the measured MR signal of interest cannot be discerned from background noise.

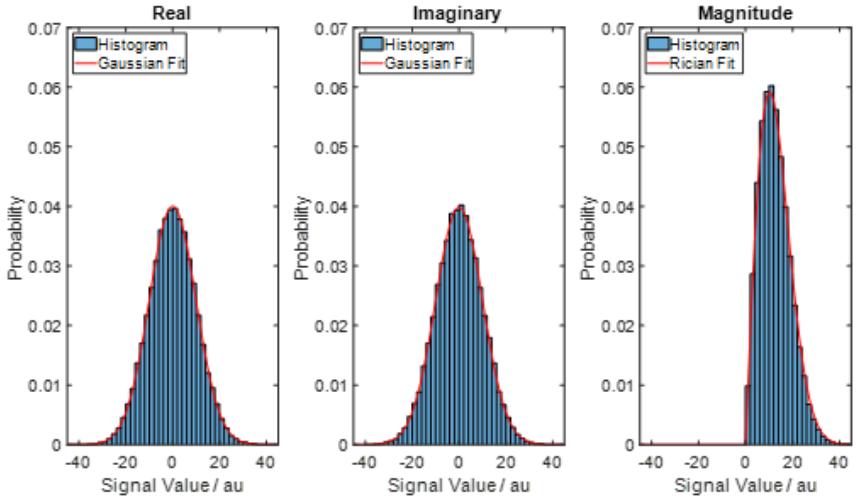


Figure 3.14: Simulated histograms showing noise-only real, imaginary and magnitude image signal intensity distributions. The real and imaginary images exhibit a Gaussian distribution, while the magnitude image exhibits a Rician distribution.

It was hypothesised that the negative gradient values, especially those located outside of the main pulmonary vessels, could be due to lung tissue with low signal. In particular, if the measured MR signal in these regions is near or below the MRI noise floor, this random noise could lead to erroneous gradient values. A simulation was carried out to investigate whether the observed negative gradient histogram peak was related to the MRI noise floor. This involved simulating sinusoidal lung signal timecourses with varying minimum signal intensities and varying the noise floor threshold. The simulated

timecourses were generated with the signal model: $S = S_0 \sin(\omega t + \phi) + A + r$, where S_0 is the signal amplitude, ω is the signal frequency, A is the signal offset and $r = r(\mu, \sigma)$ is a Gaussian noise parameter with mean μ=0 and standard deviation σ. The minimum signal intensity is given by $Smin = A - S_0$, and the noise floor is determined by σ.

These parameters were varied, and the York gradient distribution computed for each variation. A summary is shown in Figure 3.15, with S_{min}=2,5,10 and σ=10,20,30. All computed histograms passed the Kolmogorov-Smirnov test for normality ($p < 0.05$) and did not exhibit bimodality, even in the extreme case of $S_{min} = 2$ and $\sigma = 30$. Hence it can be concluded that the MR noise floor is not the cause of the observed York gradient bimodality.

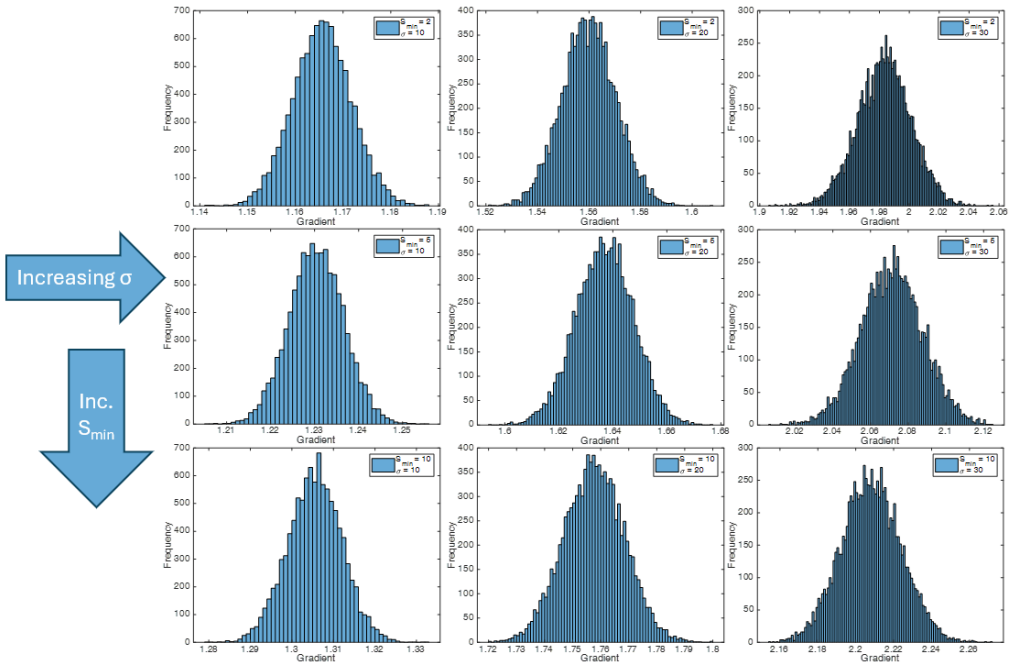


Figure 3.15: York gradient histograms from the signal model $S = S_0 \sin(\omega t + \phi) + A + r(\mu, \sigma)$. Histograms for $A - S_0 = S_{min}$=2,5,10 and σ=10,20,30 are shown. All histograms passed the Kolmogorov-Smirnov test for normality ($p < 0.05$).

To assess the differences in the relative sizes of the two observed peaks, a two-component Gaussian mixture model was fitted to the York gradient histogram. A Gaussian model function was chosen after the data was split

up into positive and negative, and a Kolmogorov-Smirnov test for normality applied to each peak, confirming that each peak was normally distributed. To fit the two-component Gaussian mixture model, the following 6-parameter fitting function was used:

$$y(x) = \frac{A_1}{\sqrt{2\pi\sigma_1^2}} \exp\left(\frac{-(x-\mu_1)^2}{2\sigma_1^2}\right) + \frac{A_2}{\sqrt{2\pi\sigma_2^2}} \exp\left(\frac{-(x-\mu_2)^2}{2\sigma_2^2}\right). \quad (3.22)$$

The fitting routine employed was nonlinear least-squares, which solves $min(\Sigma||F(x_i) - y_i||^2)$, for data y_i where $F(x_i)$ is some nonlinear fitting function. The fit was constrained such that μ_1 was <0 and μ_2 was >0. An example fit can be seen in Figure 3.16.

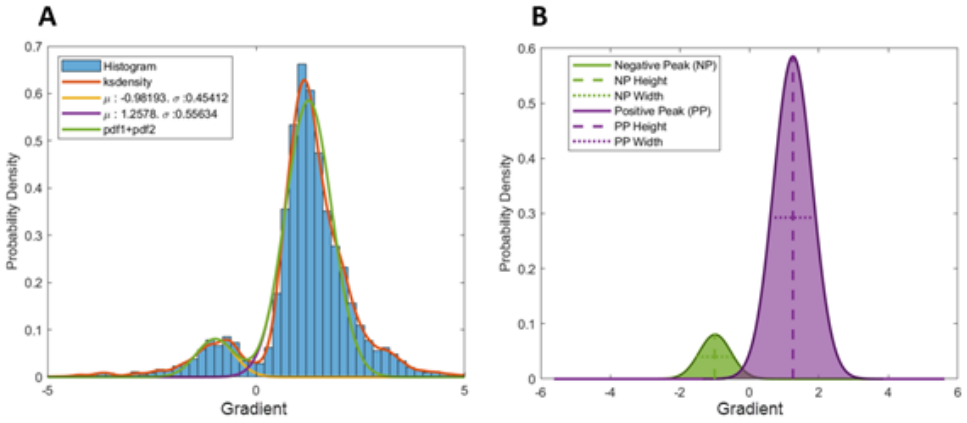


Figure 3.16: York gradient histogram with fitted two-component Gaussian mixture model (A) with the following parameters: μ_1= -0.98, σ_1 = 0.45, μ_2 = 1.26, σ_2 = 0.56; Computed areas (B): $Area_1$ = 0.092, $Area_2$ = 0.82, peak area ratio (PAR) = 8.91.

From this fitted model, there are several parameters that can be used to quantify these peaks. For each peak there is the mean μ and standard deviation σ, as well as the height of the peak at x = μ, given by

$$h = \frac{A}{\sqrt{2\pi\sigma^2}} \quad (3.23)$$

and the full width at half maximum value, given by

$$\text{FWHM} = 2\sigma\sqrt{2\ln 2}. \tag{3.24}$$

The peak area, A, can be computed as

$$A = \sqrt{2\pi}h\sigma = \frac{\sqrt{2\pi}}{2\sqrt{2\ln 2}}(h)(\text{FWHM}) \approx 1.064467(h)(\text{FWHM}). \tag{3.25}$$

Once the peak areas have been determined, the ratio of the area of the two peaks can be computed – this metric is named the Peak Area Ratio (PAR). This metric is used throughout this work to compare the relative sizes of the two observed gradient histogram peaks.

3.4.4 Spatial Distribution of Fitting Error

The standard error in the York gradient, determined iteratively from Eqn. 3.21, ($\sigma_b^2 = \frac{1}{\Sigma W_i u_i^2}$), can also be computed and mapped voxelwise. It is expected that this error will be larger in the pulmonary vessels than in the parenchyma. This error could be used as a weighting factor, or to remove voxels which have a particularly large error. By computing the inverse of the gradient error, a weighting factor can be determined, where large error values are down-weighted. Figure 3.17 shows the gradient, gradient standard error, and the inverse of this error (weights), along with the correlation coefficient map. As expected, the largest error/smallest weights occur at the major pulmonary vessels. There is relatively large error in the central vessels (e.g., pulmonary artery and superior pulmonary vein), smaller error at these vessel borders and smaller subsidiary branched vessels, and much smaller error at the lung periphery. Interestingly, the spatial distribution of the error appears to depend mainly on the pulmonary vasculature, whereas the CC has a more varied distribution – in particular with some clusters of high CC voxels in the central left lung where there is large gradient error.

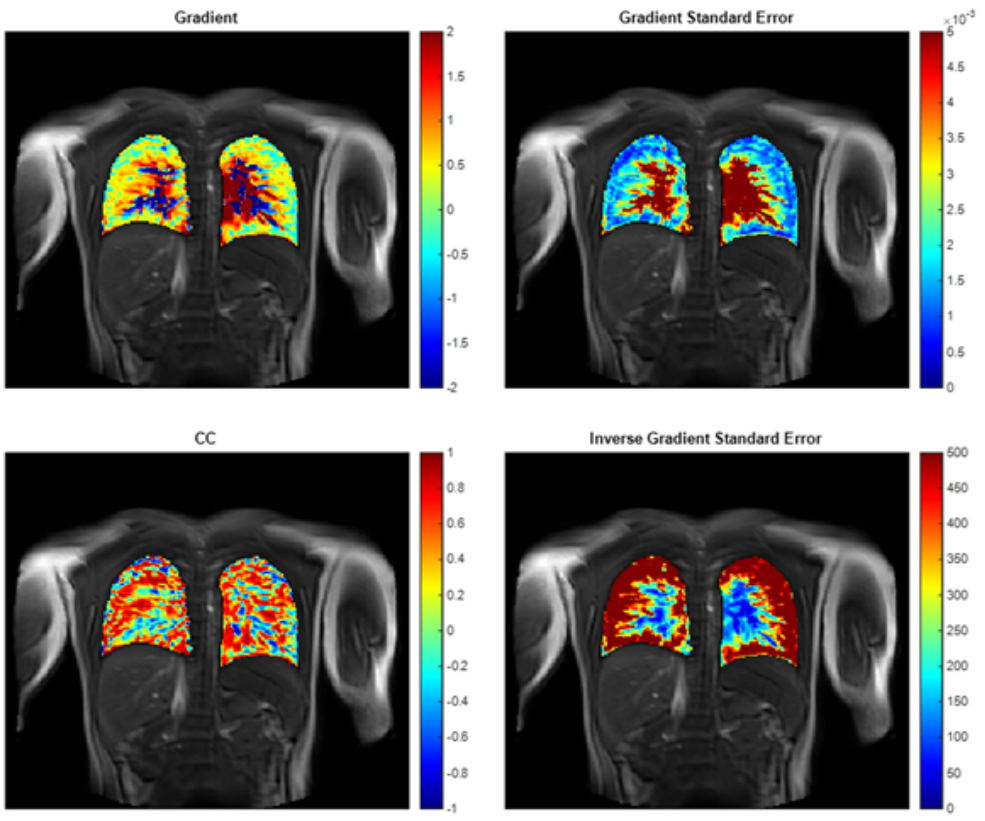


Figure 3.17: Example maps (healthy volunteer, age 23, female) of the York gradient, gradient standard error, correlation coefficient and inverse/reciprocal gradient error (weights).

To visualise the spatial relationship between the CC, gradient and weights in the lung parenchyma, scatter plots are shown in Figure 3.18 after removing the large central vessels. There is no particular relationship between CC and weights. The CC and gradient appear to be piece-wise constant with a discontinuity in gradient at zero CC. The gradient and weights exhibit a positive asymptotic distribution (abs(1/x)), where the larger gradient values are down-weighted compared to the smaller gradient values. This is due to the standard error scaling linearly with the gradient (abs(x)), indicating a constant relative error. The relationship between gradient error and CC for increasingly noisy data is explored in the following subsection.

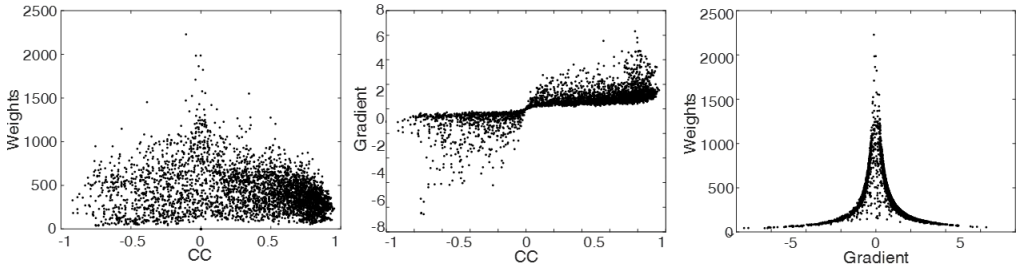


Figure 3.18: Scatter plots showing the relationship between correlation coefficient (CC), gradient and weights (reciprocal of gradient standard error). Note that voxels in the main vessels have been removed to allow for visualisation of the lung parenchyma relationship.

3.4.4.1 Gradient Error and Correlation Coefficient

To investigate the relationship between York and least-squares (LS) gradient with CC, a simulation was performed with the same signal model as used in previous simulations, $S = S_0 \sin(\omega t + \phi) + A + r(\mu, \sigma)$. Noise was added once to a clean sinusoidal signal (representing the navigator signal) with a noise value of σ=5 and regressed against many (N=10000) more noisy signals (representing lung parenchyma voxels). Both the York and LS gradient standard error were determined, as well as the CC, and these quantities plotted against one another, as shown in Figure 3.19. The simulation was repeated for varying noise levels (increasing σ), including σ=10,20,30,40. It was found that for LS gradient, there was a negative linear relationship between LS gradient standard error and CC, which became weaker with increasing noise. Contrastingly, there was no correlation between York gradient standard error and CC, irrespective of noise level. It was found that the standard error for the York gradient was an order of magnitude smaller than the LS gradient error.

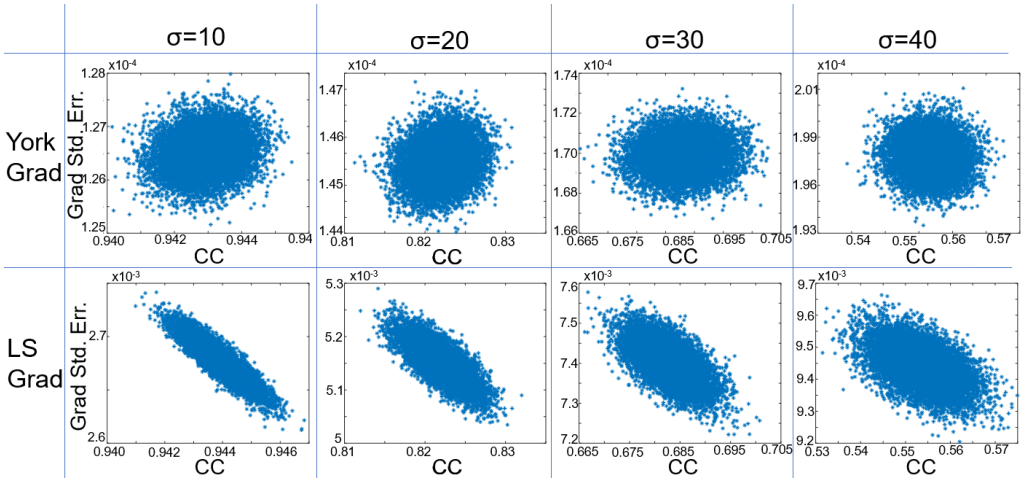


Figure 3.19: Scatter plots showing the York and least-squares (LS) gradient standard error against correlation coefficient (CC) for varying noise levels. The signal model used was $S = S_0 \sin(\omega t + \phi) + A + r(\mu, \sigma)$. σ=10,20,30,40 is shown.

3.4.5 Phase Shift and Cross-Correlation

Given that the error in the gradient and CC are not correlated with one another, do not share an obvious spatial relationship and do not vary significantly with increasing noise, further investigation into the CC is required. In particular, the negative CC values for which the MR signal increases with inspiration. It is hypothesised that these negative CC voxels are due to a phase shift between the navigator signal and the voxel signal. To investigate this, a cross-correlation metric was used to determine the correlation between the signals are different lags or phase shifts.

The cross-correlation is a mathematical operation used to measure the similarity between two sequences of data as a function of their relative displacement. Mathematically this is known as a sliding dot product. For discrete signals, the cross-correlation between two signals is computed by sliding one signal over the other while calculating the sum of element-wise products at each step. The resulting values form a signal that represents the extent of the overlap between the signals as they are shifted with respect to one another. Here, a variation of this technique is used whereby instead

of computing the similarity of the signals by multiplying and summing the overlapping portions, the Pearson correlation coefficient is computed for each lag. The cross-correlation, XCC_x, between two signals A and B at position i at lag j is given by

$$XCC_x = \frac{\sum_i (A_i - \overline{A})(B_{i+j} - \overline{B})}{\sqrt{\sum_i (A_i - \overline{A})^2 \sum_i (B_{i+j} - \overline{B})^2}} \tag{3.26}$$

where $\overline{A}$ is the mean of signal A_i and $\overline{B}$ is the mean of signal B_{i+j}. This provides a normalised measure of cross-correlation that directly measures the impact on linearity as the signals are shifted. This is advantageous as it accounts for the different magnitudes/scales of the signals (navigator signal likely to have larger magnitude) and therefore provides an intuitive measure of cross-correlation. The previously utilised Pearson correlation coefficient can be considered to be a special case of this cross-correlation at zero lag.

To make use of the cross-correlation as a functional metric, a straightforward approach is to use the maximum cross-correlation. This is the cross-correlation at which the Pearson correlation between the signals is at a maximum value within any prescribed lag constraints (i.e. within ±1 respiratory cycle). The lag at which this maximum cross-correlation occurs provides a measure of the phase shift between the two signals. In the context of a dynamic image series, the lag is computed in terms of the number of images or timeseries points that need to be shifted to achieve maximal cross-correlation. This can be converted to a lag time by dividing by the image acquisition frequency or expressed as a percentage of the respiratory cycle by multiplying by the respiratory frequency (as determined by Fourier analysis of the navigator signal). The lag relative to the average respiratory cycle period provides a measure of phase difference that can be compared between individuals.

It is expected that in healthy individuals, lung voxels will mostly be in-phase and so have zero or minimal lag values. It is expected that the negative CC voxels will be able to be shifted such that they will be in-phase and so have

increased XCC (in comparison to their 'unshifted' CC). Figure 3.20 shows four example voxels for a healthy individual with varying CC. Voxels A and B have zero lag (and hence XCC=CC), whereas voxels C and D are lagged by 30% (110° phase shift) and 50% (180° phase shift) of the respiratory cycle, respectively.

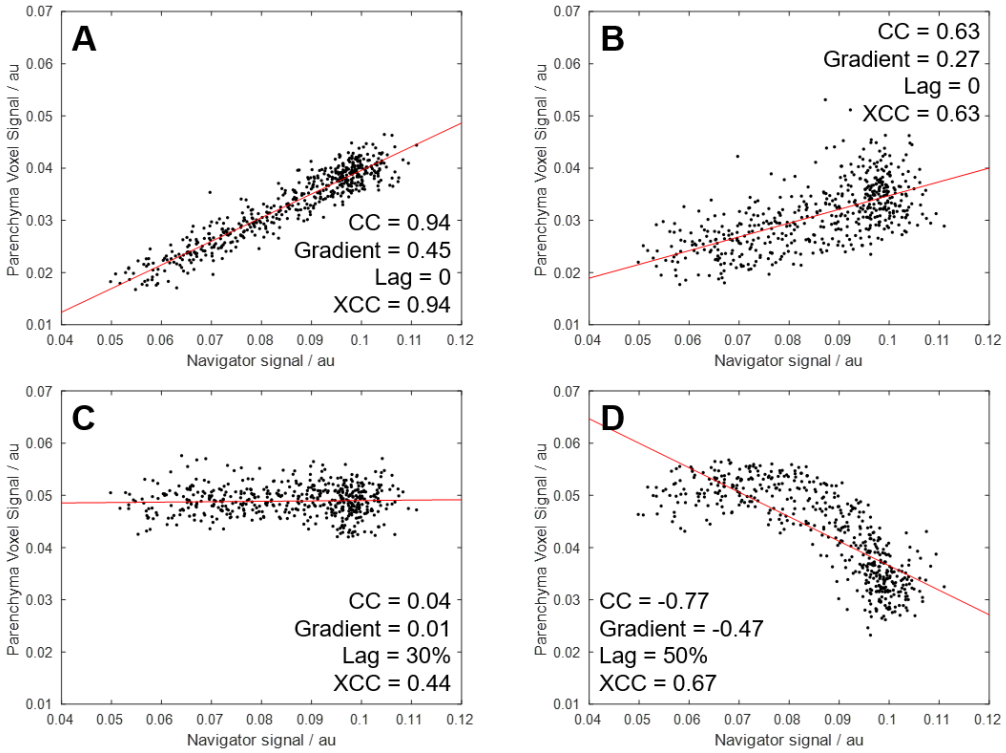


Figure 3.20: Example parenchyma versus navigator signal scatter plots for a healthy individual. Four voxels are shown with varying correlation coefficients (CC), to illustrate strong correlation (A), moderate correlation (B), poor correlation (C) and negative correlation (D). Note that some voxels display nonlinear relationships, as shown in D.

The maximum cross-correlation (XCC) maps are expected to be similar to the CC maps, but with increased (and positive) XCC in voxels with negative CC. The XCC was computed voxelwise for the illustrative dataset. The CC map and histogram, XCC map and histogram, along with a scatter plot of XCC against CC are shown in Figure 3.21. The scatter plot illustrates that there are voxels that do not posses a lag and so the CC and XCC are equal (y=x line on plot), but also many voxels with a larger XCC than CC after

undergoing a lag (XCC always >0). This means that even in the healthy lung, there are some voxels that vary with a delay, and this can be quantified via this method.

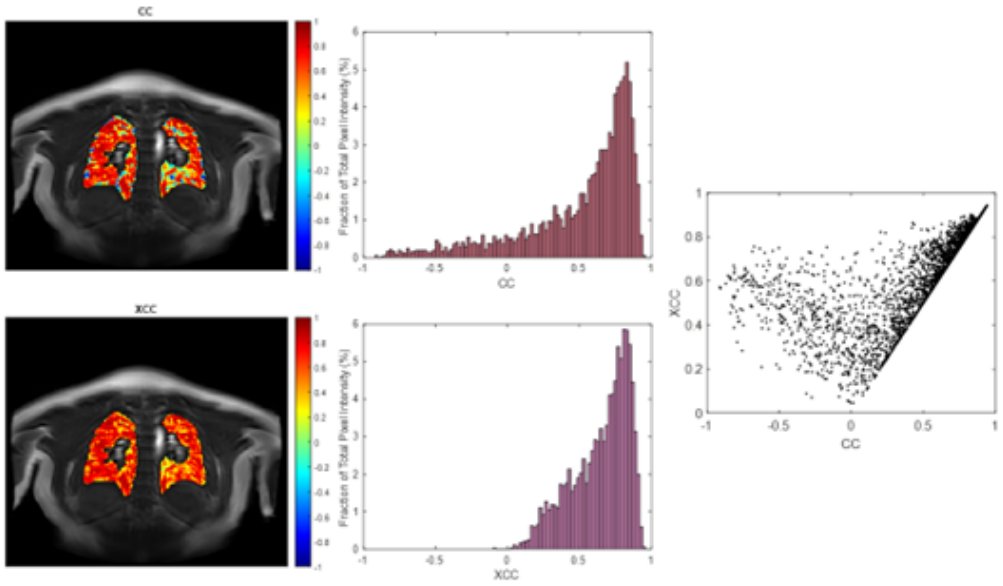


Figure 3.21: Example maps and histograms of the correlation coefficient (CC) and cross-correlation (XCC) for the illustrative data set (healthy individual, age 24, male). The CC varies between -1 and +1, while the XCC varies between 0 and +1 (but both shown on the same scale for comparison). Both histograms are negatively skewed, with the XCC histogram having increased total pixel intensity between 0 and 0.5 as the negative CC values wrap to positive XCC.

3.5 Voxel-wise Lung Ventilation (VOLVE) Pipeline

An image analysis pipeline to perform VOLVE analysis was established in MATLAB R2022b (MathWorks, Natick, MA, USA).

First, the initial 15 images were removed from the data set to ensure the signal had achieved steady-state. The navigator signal was generated by calculating for each time point the mean signal inside a rectangular ROI spanning the right hemidiaphragm to capture the apical-basal diaphragmatic motion; the right lung was used to avoid contamination from cardiac

signals. This ROI (30 voxels in foot-head direction by 5 voxels in right-left direction) was defined automatically for consistency; the right lung was segmented via seeded region growing [150], and the ROI was centred on the right hemidiaphragm at the 1/3 lateral point between the costophrenic and costocardiac angles. The relative navigator signal (percentage of the median navigator signal) was used, as this was a good proxy for relative lung volume (expressed as a percentage change from its median) – see Chapter 5.2. Once the navigator signal was determined, any extreme outliers caused by e.g. coughs or bulk motion (more than three scaled median absolute deviations from its median) were removed, and the navigator signal was then low-pass filtered at 0.6 Hz to remove cardiac signal contributions.

To obtain the voxel-wise lung parenchyma signal time courses, the single coronal slice FFE image time series were registered, using a non-rigid, demons-based registration algorithm [149], to a target image acquired close to the mean respiratory phase (at an intermediate level of lung inflation) to minimise the need for large deformation fields.

Next, a lung mask was created for the registration target/fixed image using automatic segmentation of the thoracic cavity, again via seeded region growing, excluding large pulmonary vessels, and with manual correction if required. The registered parenchyma timeseries for voxels inside the lung mask were low-pass filtered at 0.6 Hz to remove cardiac signal contributions (using the same filter as applied to the navigator signal).

Finally, the lung parenchyma signals were compared to the navigator (respiratory phase) signals across the entire time course for each voxel in turn, computing 1) XCC_V and Lag_V maps of the maximum cross-correlation and lag at which this cross-correlation occurs, and 2) $Grad_V$ maps of the gradient of linear regression via York regression. The Lag_V was computed in terms of the number of images or timeseries points that need to be shifted to achieve maximal cross-correlation, and was expressed as a percentage of the respiratory cycle by multiplying by the respiratory frequency as determined

by Fourier analysis of the navigator signal. An outline of the image processing pipeline is shown in Figure 3.22. Histograms were created from the XCC_V, Lag_V and $Grad_V$ maps. The skewness of the XCC_V histogram was computed, and the bimodal distribution of the $Grad_V$ histogram was fit to a two-component Gaussian mixture model and the Peak Area Ratio (PAR) was computed as the ratio of the areas of the two fitted Gaussians (see Figure 3.16).

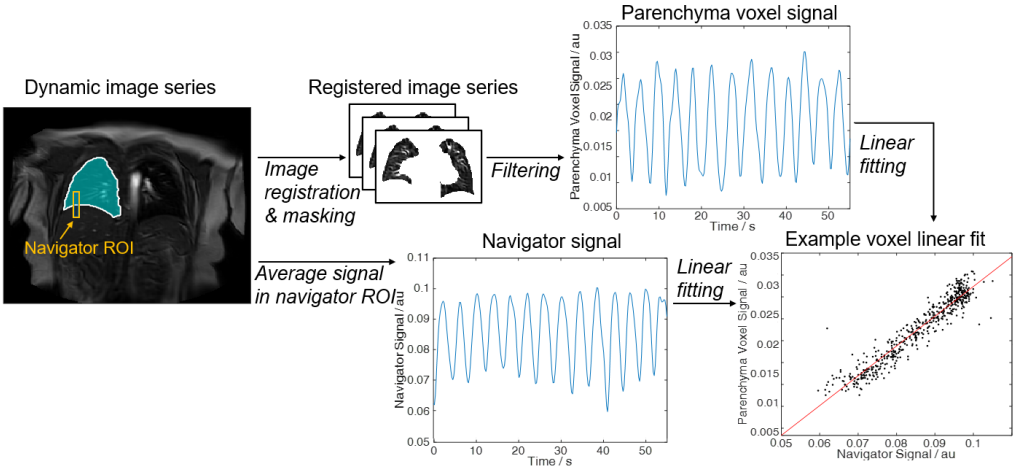


Figure 3.22: Overview of the image processing pipeline for VOLVE analysis. The signal in the lung-diaphragm ROI is averaged to generate the navigator signal over the image time series. Linear regression is carried out voxel-wise between this navigator signal and the registered lung parenchyma signal.

Image analysis is completed automatically without operator input, apart from any required manual corrections to the lung mask segmentation. Processing time for a single data set containing (512-15=) 497 images (240×240 pixels) takes approximately 1 minute on inexpensive hardware (AMD Ryzen 5 5600X CPU 3.7MHz, 16GB RAM), with image registration (utilising parallelisation) accounting for ~ 90% of this time.

3.6 VOLVE vs. PREFUL FV in the Assessment of Resonse to Kaftrio® Therapy in CF

In Section 3.3, it was found that static PREFUL FV, that makes use of only two respiratory states, was insensitive as a measure of response to therapy (Kaftrio®) and showed relatively poor same-day repeatability in CF. This provided motivation for the subsequent methods development in Section 3.4. To assess any potential improvement in sensitivity and repeatability afforded by the developed VOLVE analysis, the same CF data was reanalysed with the VOLVE pipeline. The results of this analysis are compared with the previously determined PREFUL results. CC_V and $Grad_V$ parametric maps and histograms were computed for Visit 1, Visit 2 and Visit 2 repeat.

Figure 3.23 shows boxplots with the CC_V median and skewness, and $Grad_V$ median and PAR in the healthy volunteer and CF groups. For CF, dotted and solid lines show the relation between values for each subject between Visit 1 and Visit 2, and Visit 2 and Visit 2 repeat, respectively. For comparison, the results from Section 3.3 are plotted in the same format in Figure 3.24 — showing fractional ventilation measures, FV = $\frac{S_{exp}-S_{insp}}{S_{exp}}$. Table 3.5 shows p values assessing sensitivity to disease and response to therapy, as well as Pearson correlation values against FEV_1 for CF. Both CC_V median and skewness were significantly different in the CF group compared to HCs. No significant correlations with FEV_1 were found for the VOLVE measures.

The key finding of this comparison is that while PREFUL FV failed to differentiate between CF and HC, VOLVE showed a significant difference (CC_V median $p<0.009$ and CC_V skewness $p<0.02$). This suggests that VOLVE may be more sensitive to lung disease, or more robust in detecting differences in lung function, due to the use of all of the images in the respiratory cycle. The VOLVE metrics tended to increase/decrease in line with hypothesis (e.g. increased VOLVE parameter medians after therapy), whereas the PREFUL FV metrics exhibited no clear trend. The numbers in this pilot study are small and therefore it is not statistically powered; a larger

cohort would enable an appropriately powered study.

It is noteworthy that PREFUL FV ventilation defect percentage (VDP) and skewness did significantly correlate with FEV_1, whereas none of the VOLVE parameters did. This could indicate that VOLVE is evaluating lung physiology in a different way (dynamic ventilation) to FV (static ventilation). While being able to verify that novel MR functional metrics correspond to improvements in conventional PFTs is instructive, it is not necessarily a drawback or weakness that VOLVE does not appear to strongly correlation with FEV_1, as this is a measure of airways obstruction which forms only a part of the overall functional picture in the case of CF. It is even potentially advantageous that these measures do not correlate well, as this could indicate that VOLVE is measuring a different aspect of lung parenchyma function.

Another key difference between PREFUL FV and VOLVE is in the observed within-visit repeatability. In general there was little difference between repeated VOLVE metrics, whereas the PREFUL FV values were more variable. This is reflected by the larger C_v values for PREFUL FV (Table 3.6) and is illustrated in Figures 3.23 and 3.24.

Overall, this preliminary work has shown that VOLVE analysis appears to demonstrate superior sensitivity and repeatability to static approaches such as PREFUL FV. This may indicate an improved robustness to breathing behavior and/or noise in the data for VOLVE. Further work is required to establish VOLVE as a clinically feasible technique, including application in different patient groups.

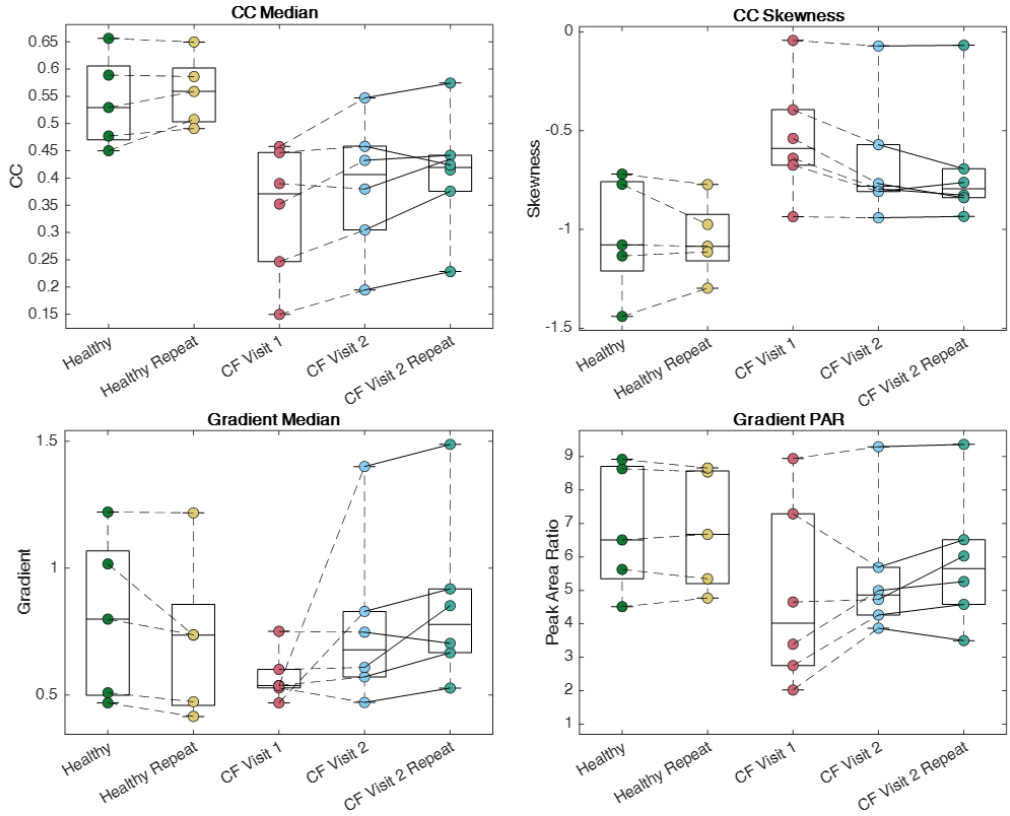


Figure 3.23: Boxplots showing VOLVE metrics.

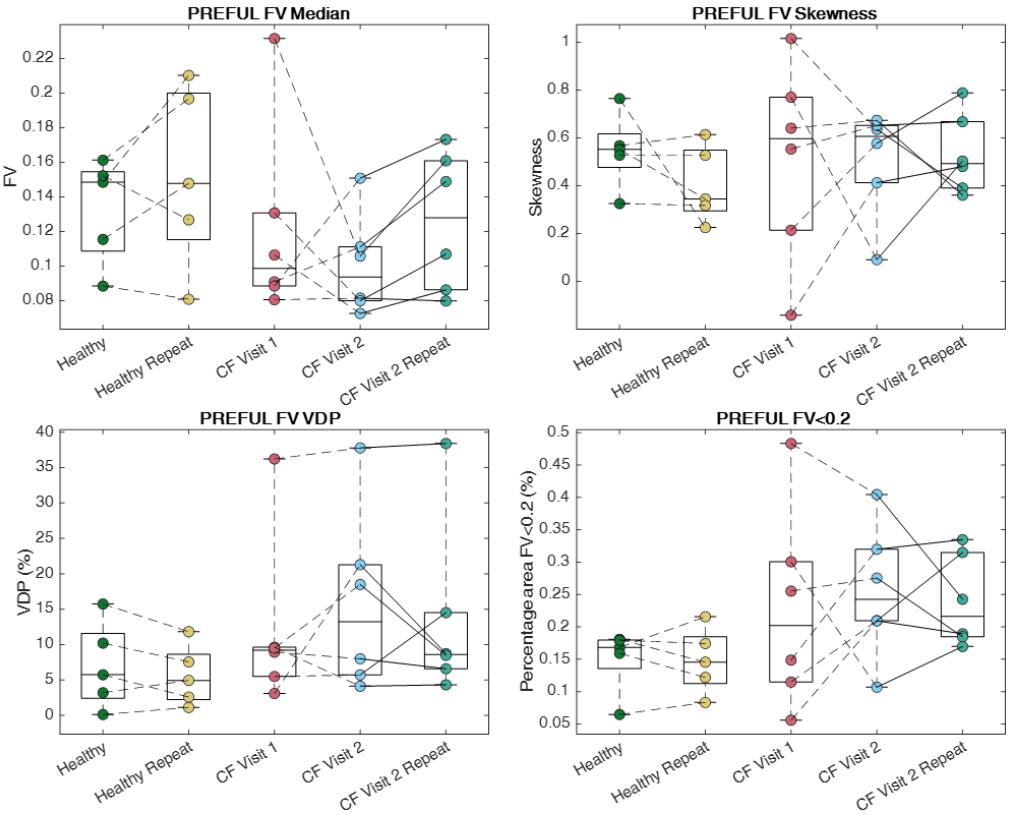


Figure 3.24: Boxplots showing PREFUL FV metrics.

	HC scan 1 vs CF Visit 1 (sensitivity to disease), p	CF Visit 1 vs Visit 2 scan 1 (response to therapy), p	CF Pearson Correlation against FEV_1 Visit 1, r (p)	CF Pearson Correlation against FEV_1 Visit 2, r (p)
PREFUL FV				
Median	0.71	0.80	0.61 (0.19)	0.49 (p=0.32)
VDP (%)	0.61	0.31	-0.81 (p=0.04)*	-0.79 (p=0.02)*
Skewness	0.50	0.50	-0.83 (p=0.04)*	-0.91 (p=0.01)*
%FV<0.2	0.77	0.36	-0.78 (p=0.07)	-0.50 (p=0.3)
VOLVE				
CC Median	0.009*	0.30	0.56 (p=0.25)	0.42 (p=0.41)
CC Skewness	0.02*	0.15	-0.69 (p=0.13)	-0.55 (p=0.27)
Gradient Median	0.62	0.09	0.54 (p=0.27)	0.56 (p=0.25)
Gradient PAR	0.31	0.20	0.40 (p=0.44)	-0.03 (p=0.95)

Table 3.5: Assessment of change between HC and CF patients and in CF patients in response to therapy (two-sample, one-tailed, t-test; *=significant) with both PREFUL FV (from Table 3.3) and VOLVE analysis.

Metric	HC	CF
PREFUL FV		
VDP (%)	0.70	0.38
Skewness	0.41	0.37
%FV<0.2	0.27	0.25
VOLVE		
CC_V Median	0.10	0.13
CC_V Skewness	0.09	0.07
$Grad_V$ Median	0.11	0.10
$Grad_V$ PAR	0.07	0.08

Table 3.6: Assessment of repeatability: within subject coefficient of variation, $C_{v,w}$, for Healthy Controls (HC) and Cystic Fibrosis (CF).

3.7 Conclusion

This chapter has overviewed dynamically acquired functional lung ^{1}H MRI methods, including FD, PREFUL and DMD. PREFUL was used to determined FV-based functional ventilation assessment in a small CF pilot study. It was found that FV was insensitive to presence of disease, was unable to detect functional change associated with therapy, and lacked an acceptable level of repeatability. It was hypothesised that this was largely due to FV as a static ventilation metric only making use of inspiration and expiration phases. This results in inefficient data sampling, introduces bias based on the respiratory cycle phases used in the analysis, and increases sensitivity to irregular breathing patterns.

This motivated the development of a novel image analysis pipeline termed VOxelwise Lung VEntilation (VOLVE). This pipeline uses a lung-diaphragm navigator signal directly to evaluate lung parenchyma MR signal evolution. Functional metrics including the gradient, cross-correlation and lags allow for probing of the MR signal, and may enable novel functional insight. This pipeline was used to re-analyse the CF data, and an improvement for the sensitivity and repeatability of VOLVE metrics was demonstrated. Further work is required to establish VOLVE as a clinically feasible technique, including application in different patient groups. The VOLVE pipeline is now applied in a prospective pilot study entitled Functional And STructural imaging in Chronic Obstructive Pulmonary Disease (FASTCOPD), detailed in Chapter 4.

Chapter 4

Application and Validation of Voxel-wise Lung Ventilation (VOLVE) Assessment in COPD

Abstract

There is a need for sensitive measures of regional lung function in respiratory medicine that can be carried out using standard imaging technology, without the need for inhaled or intravenous contrast agents. The proposed method of analysing free-breathing ^{1}H Magnetic Resonance Imaging (MRI) data extends current methods to provide novel measures of pulmonary ventilation and perfusion.

A prospective pilot study was carried out in which 12 healthy volunteers with no smoking history, 4 healthy volunteers with smoking history (>10 pack-years), and 8 participants with Chronic Obstructive Pulmonary Disease (COPD) due to tobacco exposure were recruited. The VOxel-wise Lung VEntilation (VOLVE) method was evaluated in these subjects to determine the ability of the method to quantify regional lung disease, and to assess the repeatability of the method. The VOLVE method was also compared against other prominent post-processing techniques currently in the literature: Phase REsolved FUnctional Lung (PREFUL) and Dynamic Mode Decomposition (DMD).

Significant differences between the healthy, healthy smoker and COPD groups were found for ventilation and perfusion VOLVE metrics, indicating the sensitivity of the methodology to lung disease.

VOLVE was compared to both PREFUL and DMD postprosessing techniques, and it was found that PREFUL and VOLVE are comparable, although VOLVE had increased sensitivity to smoking-related functional status. DMD was sensitive to perfusion changes, but lacked sensitivity and repeatability for ventilation. Therefore, it was shown that VOLVE provides metrics of function quantification using 3T free breathing proton MRI, via a linear regression-based technique which makes use of all the data in the time series for maximum sensitivity.

A component of this work was presented at the International Society for Magnetic Resonance in Medicine (ISMRM) 32nd Annual Meeting (2023) [167].

Statement of Contribution

Zachary Peggs (ZP) performed all data analysis. ZP, Jonathan Brooke (JB) and Charlotte Bolton (CEB) managed the FASTCOPD study, including ethical approvals, governance and recruitment. ZP, JB and Jan Paul (JP) collected the MR data. ZP, JB, CEB, Susan Francis (SF), Penny Gowland (PG) and Ian Hall (IH) contributed towards the experimental design and interpreted the data. SF, PG, CEB and IH supervised the research.

4.1 Introduction

4.1.1 Precision Imaging in COPD

Chronic Obstructive Pulmonary Disease (COPD) is a progressive, chronic respiratory disease that is characterised by generally irreversible airflow obstruction and an abnormal inflammatory response in the lungs, occurring due to the inhalation of harmful particles and gases – usually tobacco (almost exclusively tobacco in the global north/ western world) [168]. COPD is an umbrella term covering emphysema and chronic bronchitis, with disease manifestation varying greatly between individuals. The symptoms of COPD are non-specific and generally include a chronic cough, sputum production, wheeziness, lack of exercise capacity and, above all else, breathlessness. The generality of these symptoms means that a diagnosis of COPD often comes later on in the disease course, where the insidious onset of symptoms can often be dismissed by patients as normal age-related changes or a 'smoker's cough', rather than a serious medical condition which requires medical attention [169]. Although long-term smoking and exposure to air pollutants are responsible for the majority of COPD diagnoses, there are other cases such as genetic disorders which predispose an individual to COPD. Alpha-1 antitrypsin deficiency (AATD) is a rare genetic disorder (1-3% prevalence in Europe) caused by mutation of the serine-protease inhibitor gene, resulting in a deficiency in the A1AT protein levels [170]. These proteins are needed as protection against proteases such as neutrophil elastase, and their absence leads to the destruction of alveolar walls and causes emphysema [171]. Patients who suffer from AATD tend to develop COPD at a younger age and with severity disproportionate to smoking history [172].

Diagnosis of COPD is typically confirmed in people over the age of 35 years with a history of smoking via spirometry. COPD is generally characterised by a ratio of Forced Expiratory Volume in 1 Second (FEV_1) to Forced Vital Capacity (FVC) of less than 0.7 (presence of airways obstruction), with the percentage FEV_1 (predicted) grading airflow limitation

severity according to the Global Initiative for Chronic Obstructive Lung Disease (GOLD) scale [173]. GOLD grades range from 1 (mild, $FEV_1 \geq 80\%$) to 4 (very severe, $FEV_1 < 30\%$).

Although FEV_1 (predicted) is used as the primary classifier for severity in COPD, this measure correlates weakly to the severity of a patient's symptoms, is effort dependent and so shows relatively poor reproducibility, and is insensitive to regionally localised defects [174]. Pulmonary Function Tests (PFTs) provide additional information relating to functional deficiency/-abnormality, such as air trapping and hyperinflation leading to increased Functional Residual Capacity (FRC), Residual Volume (RV) and Total Lung Capacity (TLC) [175] or measures of reduced gas transfer in the presence of emphysematous destruction of the alveoli, leading to decreased D_{LCO} and K_{CO} [176].

However, in the case of more complex or severe COPD, PFT measures may not elucidate the full extent of functional impairment and are limited to global assessments of lung health. The insensitivity of spirometry is also problematic for younger people who are at risk of COPD but have not yet developed significant clinical symptoms. In this case, where spirometry is unable to provide a diagnostic insight, patient management and classification could be informed by a more sensitive functional assessment with identification of localised lung abnormalities.

Unlike other respiratory diseases, imaging plays a minimal role in the diagnosis and management of COPD. While not generally used in routine care pathways, Computed Tomography (CT) imaging is sometimes used to identify complications or in the assessment of suitability for precision medicine approaches such as Lung Volume Reduction (LVR) procedures. LVR can be performed surgically or endoscopically via an endobronchial valve and aims to reduce hyperinflation in order to improve dyspnoea and exercise tolerance. It has been found that patient selection is critical in LVR, with excess early mortality in some subgroups (especially in subjects

with homogenous emphysema), and significant functional improvements with reduced mortality in others (upper lobe emphysema and low exercise capacity) [177]. Recently it was found that patients with heterogenous emphysema and minimal collateral ventilation, as assessed by quantitative CT, benefitted greatly from LVR, with an increase in FEV_1% of 17% after 12 months [178]. This highlights the importance of patient selection for LVR.

This motivates the use of advanced imaging in the management of COPD. Quantitative CT and MRI approaches could be used in a precision medicine framework, to inform individualised therapy approaches. In particular, MRI could provide a comprehensive imaging modality for safe longitudinal disease monitoring, ultimately enabling more accurate patient-tailored treatments [179]. For example, advanced MRI techniques could play a role in selecting individuals and/or specific subgroups who will gain maximal benefit from interventions such as LVR and inform optimum therapeutic targets for surgical/endoscopic interventions.

4.1.2 Application of VOLVE, PREFUL and DMD in COPD

The relative simplicity of proton (^{1}H) MRI lends itself to rapid clinical translation, but the analysis methods and quantitative metrics used must be validated. This chapter details a pilot study in which the developed VOxel-wise Lung VEntilation (VOLVE) methodology is applied in a COPD cohort. This is compared to control groups of healthy never-smokers and people with smoking history but absence of lung disease/symptoms. Same-day repeatability of VOLVE is investigated. Other other analysis methods were also applied to the same data: Phase REsolved FUnctional Lung (PREFUL) and Dynamic Mode Decomposition (DMD) — details of which are outlined in Chapter 3.1.2 and briefly summarised below.

The PREFUL method has gathered much attention in the ^{1}H pulmonary MRI community in the last few years. PREFUL is currently the forerunner for clinical translation in this field, and has been widely applied across various patient groups, most recently in Chronic Thromboembolic Pulmonary

Hypertension (CTEPH) in the first large ^{1}H lung MRI multi-centre trial (CHANGE-MRI) across 9 sites across Europe [90]. It has been shown that dynamic regional flow-volume PREFUL metrics are sensitive to difference in chronic lung allograft dysfunction (CLAD) stage, whereas the static regional ventilation (RVent) metric is not [144]. The dynamic flow-volume loop PREFUL metric is more similar to VOLVE in that it makes use of images throughout the entire respiratory cycle. Here, VOLVE is compared with both static and dynamic PREFUL.

DMD provides a data-driven method for determining lung function information from the dynamic image series. DMD enables computation of the dominant spatiotemporal features in the form of eigenvalues and eigenvectors corresponding to coherent oscillatory features – ventilation and perfusion in this case. This method has only recently been applied to lung imaging by Ilicak *et al.*, and to date only healthy subjects have been evaluated [89]. Here DMD is applied here in COPD and compared to VOLVE and PREFUL approaches.

4.2 Methods

4.2.1 FASTCOPD: Study Participants

To assess VOLVE as a measure of lung function, a prospective pilot study entitled Functional and STructural imaging in Chronic Obstructive Pulmonary Disease (FASTCOPD) was carried out (ClinicalTrials.gov identifier: NCT04966221, IRAS identifier: 301426, REC Reference: 21/WA/0226). The key aims of this study were to: 1) assess VOLVE lung function metrics in obstructive lung disease, 2) compare and contrast differences in regional ventilation heterogeneity in healthy never-smoker, healthy smoker and COPD groups, 3) assess the repeatability and robustness to different breathing patterns and the absence/presence of hyperinflation in these groups, 4) compare these results with other prominent post-processing techniques (PREFUL and DMD), and 5) to collect pilot structural MRI data

— see Appendix 4A.

Participants with Chronic Obstructive Pulmonary Disease (COPD) due to tobacco smoking and healthy people with a history of smoking were recruited following research ethics approval (Wales REC 4; ethics reference: 21/WA/0266). Participants with COPD were recruited from either a complex COPD NHS out-patient clinic or from a COPD register, held within the NIHR Nottingham Biomedical Research Centre (BRC). Healthy smoker participants were identified by the Nottingham BRC via advert. Healthy people who had never smoked were recruited under a University of Nottingham Faculty of Medicine and Health Sciences local research ethical approval.

The recruitment and screening of participants was carried out by Dr Jonathan Brooke (clinical research fellow) and myself. The screening visit consisted of obtaining oral and written consent after an explanation of the study. Following this, basic clinical measurements were made to ensure that the participant was eligible to be scanned: height, weight, blood pressure, heart/respiratory rate, oxygen saturations and temperature. Relevant medial history and records were reviewed, including retrieval of retrospective spirometry values (taken within 24 months of the screening visit; mean ± standard deviation time between spirometry and MRI exam 10 ± 14 months), as University of Nottingham (UoN) COVID-19 safety measures forbade the acquisition of new pulmonary function data during the initial period of this study.

12 healthy volunteers with no tobacco smoking history or lung disease/symptoms, 4 healthy smokers with >10 pack-year smoking history but no respiratory symptoms nor evidence of airflow limitation or other abnormality on spirometry, and 8 participants with COPD (symptoms consistent with COPD, FEV_1/FVC ratio < 0.7 and > 10 pack years of tobacco smoking) were recruited.

4.2.2 MRI Protocol

All participants underwent a single study visit lasting up to 1 hour. Each participant completed a safety screening questionnaire that was approved by an Sir Peter Mansfield Imaging Centre (SPMIC) MRI radiographer, who then performed the MRI exam on a wide-bore 3 T Philips Ingenia MR scanner (Philips Medical Systems, Best, The Netherlands). A summary of the MRI protocol is shown in Table 4.1; the work in this chapter focuses on the '2D FFE' and '2D FFE Repeat' acquisitions in this protocol. Apart from two short (and optional) breath-holds (BH) at the start and end of the protocol, the entire protocol was carried out during free-breathing (FB), which is beneficial for the COPD patients with compromised lung function. All data collected in the study was anonymised with a participant code (FAST-XXX) and was stored in a secure UoN records store and/or secure UoN data server.

	Parameters	Geometry	Breathing
3D FFE expiration BH	TR/TE=1.9/0.63 ms, α=3°, matrix 240x240, resolution 2x2x2.5mm^3, 80 slices	COR	BH – 12s
3D FFE inspiration BH	TR/TE=1.9/0.63 ms, α=3°, matrix 240x240, resolution 2x2x2.5mm^3, 80 slices	COR	BH – 12s
2D Dynamic FFE	TR/TE=1.9/0.57 ms, α=18°, matrix 240x240, resolution 2x2mm^2, thickness 15 mm, single slice, 512 images, partial Fourier=0.75	COR	FB - 117s

3D Dynamic FFE (CS=10)	TR/TR=1.9/0.58 ms, α=18°, matrix = 192x192, resolution 5x5x12mm^3, 400 dynamic images, 12 slices, compressed SENSE acceleration factor = 10	COR	FB - 116s
M2D Dynamic FFE (CS=4)	TR/TE=1.9/0.62 ms, α=18°, matrix = 192x192, resolution 1.8x1.8x11mm^3, 400 dynamic images, 6 slices, compressed SENSE acceleration factor = 4	SAG	FB - 119s
2D Dynamic FFE Repeat	TR/TE=1.9/0.57 ms, α=18°, matrix 240x240, resolution 2x2mm^2, thickness 15 mm, single slice, 512 images, partial Fourier=0.75	COR	FB - 117s
T_2W MultiVane	TR/TE=2.73 sec/126 ms, α=90°, matrix 268x268, resolution 1.5x1.5mm^2, thickness 5mm, 30 slices	AX	FB - 120s
UTE	TR/TE=2.99/0.136 ms, α=5°, matrix 288x288, resolution 1.5x1.5x2mm^3, 80-100 slices	COR/AX	FB - 8-10mins

T_1 Map (MOLL) expiration	TR/TE=2.8/1.42 ms, α=20°, matrix 192x192, resolution 1.5x1.5x5mm^3, single slice (matched to 2D Dynamic FFE)	COR	BH – 11s
T_1 Map (MOLL) inspiration	TR/TE=2.8/1.42 ms, α=20°, matrix 192x192, resolution 1.5x1.5x5mm^3, single slice (matched to 2D Dynamic FFE)	COR	BH – 11s

Table 4.1: Summary of the FASTCOPD scan protocol. Abbreviations: Fast Field Echo (FFE), T_2-weighted (T_2W), ultrashort echo time (UTE), modified Look-Locker inversion recovery (MOLLI), coronal (COR), sagittal (SAG), axial (AX), free-breathing (FB), and breath-hold (BH).

4.2.3 Image Analysis

Image analysis was performed on the dynamic, single slice, FFE image time series (first acquisition and repeat) with three image analysis pipelines: VOLVE analysis, PREFUL analysis and DMD analysis. Functional metrics were computed for each method, and sensitivity to disease and repeatability were assessed, as outlined below.

4.2.3.1 VOLVE Analysis

Principally, VOLVE analysis was performed using the pipeline detailed in Chapter 3.5. Briefly, this involved automatic computation of a lung-diaphragm navigator signal, and of voxel-wise lung parenchyma signal time courses after non-rigid registration and segmentation. The navigator (global) and parenchyma (local) respiratory signals were compared across the entire time course for each voxel in turn, computing 1) XCC_V maps of the maximum cross-correlation and Lag_V maps of the lag at which this cross-

correlation occurs, and 2) $Grad_V$ maps of the gradient of linear regression via York regression. The Lag_V was converted from units of number of images or timeseries points to a percentage of the respiratory cycle by multiplying by the dominant respiratory frequency as determined by Fourier analysis of the navigator signal. Histogram analysis was performed for each map to compute median and skewness values for XCC_V and Lag_V, and to compute median and Peak Area Ratio (PAR) values for $Grad_V$.

The VOLVE pipeline was extended to assess perfusion, perform retrospective cardiac gating and to segment the lung into quadrants for regional analysis.

4.2.3.2 Extension to Assess Pulmonary Perfusion

While the focus of this work was on ventilation assessment, another key aspect to lung function is pulmonary perfusion. A feature of ^{1}H MRI is that the measured MR signal in the parenchyma has signal contributions from both respiratory and cardiac origins.

To assess perfusion, the same linear regression-based framework was applied with minor modifications. By replacing the lung-diaphragm respiratory navigator signal with an aorta or main pulmonary vessel-based cardiac signal timecourse, a characterisation of cardiac phase rather than respiratory phase is achieved. This cardiac phase can be regressed against the lung parenchyma signal timecourse after application of a high-pass filter (0.8 Hz) to remove respiratory signal contributions (rather than a low-pass in the case of ventilation). In this case, VOLVE analysis is therefore performed to yield perfusion information.

The key modification to enable automatic perfusion quantification is the segmentation of an aorta or main pulmonary vessel ROI (followed by the modification of low-pass (0.6 Hz) to high-pass (0.8 Hz) filter). To ensure consistency in cardiac ROI segmentation, an automatic segmentation algorithm was developed, as is shown in Figure 4.1. This involved automatic

segmentation of the lungs via seeded region growing, followed by the joining on the left and right lung mask to produce a mask of the mediastinum. The standard deviation of the timeseries inside the mediastinum mask was computed to identify the major pulmonary vessels. Seeded region growing was then performed on the standard deviation image to define an aorta ROI, with the initial seed placed at the voxel with maximum standard deviation. The signal within this ROI is then averaged to produce a cardiac signal timecourse.

Maps and histograms for perfusion cross-correlation (XCC_Q) and lag (Lag_Q), and gradient ($Grad_Q$) were created.

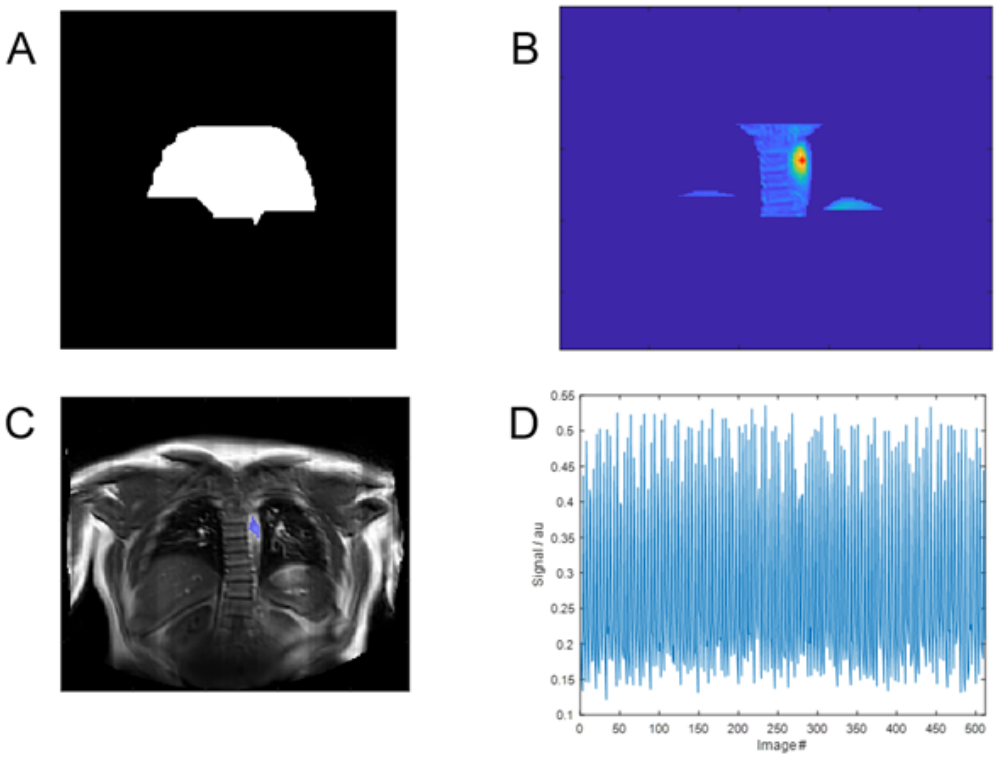


Figure 4.1: Automatic cardiac timecourse generation. A) Joining of the left and right lung masks to cover the mediastinum. B) Standard deviation of the mediastinum mask with maximum standard deviation voxel indicated with a red asterisk. C) Seeded region growing segmentation on the standard deviation image, with initial seed point as the maximum standard deviation (as indicated on B). D) Cardiac signal timecourse generated from averaging the signal in the segmented aorta ROI.

4.2.3.3 Retrospective Cardiac Gating

The ability to characterise the cardiac phase of the images (from the perfusion assessment) enables retrospective cardiac gating of the ventilation parametric maps. Since each image has an associated respiratory and cardiac phase, this enables the separation of ventilation maps at different cardiac phases, such that they can be reconstructed at systole and diastole by subdividing the images accordingly. This may be useful as a means to account for differences in blood volume throughout the cardiac cycle when computing ventilation metrics. Similarly, perfusion maps could in principle also be reconstructed for inspiration and expiration, although respiratory-gated perfusion mapping was not explored in this work.

Retrospectively cardiac-gated ventilation maps were determined by subdividing the data set into systole and diastole by thresholding the cardiac signal timecourse at 80% and 20% of the maximum value, respectively, and performing the VOLVE ventilation analysis on each time series separately.

4.2.3.4 Lung Quadrant Determination For Regional Assessment

The lung mask was split into quadrants for regional analysis. This kind of analysis allows for comparisons to be made between lung regions e.g. basal and apical lung, as done previously [142]. Quadrant segmentation was performed automatically as show in Figure 4.2. The same algorithm was used as to determine the lung-diaphragm ROI, where the height profile was computed by summing the number of voxels within the lung perimeter for each voxel in the left-right direction, thus generating a projection profile in the foot-head direction. Hence the midpoint between the apex and base of the right lung was found and was used to separate the upper and lower lung quadrants. This enabled delineation of 5 lung regions: whole lung, upper right, lower right, upper left and lower left. To investigate regional differences in VOLVE parameters in these regions, VOLVE metric median values were computed for each region.

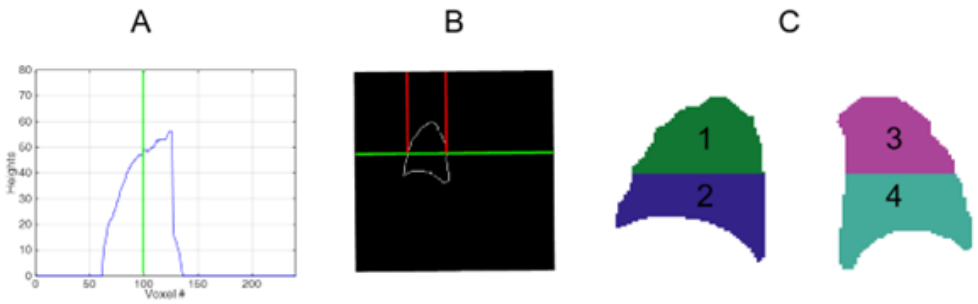


Figure 4.2: Automatic quadrant segmentation algorithm. A) Height projection computation along the left-right axis by summing the voxels within the right lung mask with the 50% point shown in green. B) Plot of lung boundary points (red lines) that intersect the 50% height point. C) Quadrant segmentation using the 50% height projection line. The lung is separated into quadrant 1 (upper right), quadrant 2 (lower right), quadrant 3 (upper left) and quadrant 4 (lower left). Note that left/right refer to anatomical (rather than image) orientation.

4.2.3.5 PREFUL Analysis

In addition to VOLVE, PREFUL analysis was performed. A full explanation of the PREFUL analysis framework is provided in Chapter 3.1.2, and in references [18] and [137]. The PREFUL pipeline used is a modified version of the pipeline of Munidasa *et al.* and focuses on assessment of ventilation [133]. Briefly, the images are resorted into highly temporally resolved respiratory cycles (virtual ventilation cycle), from which functional metrics are computed. RVent was computed according to

$$\text{RVent} = \frac{S_{mid}}{S_{insp}} - \frac{S_{mid}}{S_{exp}} = \frac{S_{exp} - S_{insp}}{S_{exp}} \cdot \frac{S_{mid}}{S_{insp}} \tag{4.1}$$

where S_{mid}, S_{insp} and S_{exp} correspond to signal intensities at mid-respiratory, inspiration and expiration, respectively. Additionally, using the regional ventilation time series RVent(t), defined as

$$\text{RVent(t)} = \frac{S_{exp} - S(t)}{S_{exp}} \cdot \frac{S_{mid}}{S(t)} \tag{4.2}$$

where $S(t)$ is the phase-resolved time series data that spans the entire respiratory cycle. Hence regional flow volume loops (FVL) can be generated, using RVent(t) as a surrogate for volume and the gradient ΔRVent(t) / Δt as a surrogate for flow. This 3D (2D spatial + time) map of voxelwise flow-volume loops is converted to a 2D map by computing the cross-correlation to a reference healthy flow-volume loop curve determined by spatial averaging in a region containing values within the 75^{th} and 95^{th} percentile, to determine the FVL cross-correlation (FVL-CC) metric. This FVL-CC metric provides a measure of regional ventilation dynamics throughout the respiratory cycle, where strong correlation values can be interpreted as areas that are well-ventilated.

Both the static RVent and the dynamic FVL-CC metrics were computed for all subjects. In addition, RVent and FVL-CC ventilation defect maps were generated by a k-means clustering method [133] and by defining a FVL-CC defect threshold of 0.9 [90], respectively.

4.2.3.6 DMD Analysis

Finally, DMD analysis was performed. The pipeline used is detailed in Chapter 3.1.2, following Ilicak *et al.* [89]. Briefly, this involves registration and segmentation as described before, followed by representing the dynamic image series in two time-shifted matrices, X and X', and determining the modes and eigenvalues of the transformation mapping X to X', without having to explicitly compute the transformation, thus being computational efficient/viable. The most dominant modes with the largest eigenvalues capture the dominant spatiotemporal behaviour of the dynamic system; this provides a characterisation of signal fluctuations at the respiratory and cardiac frequencies.

The 15 most dominant modes were identified, and fractional ventilation (referred to as ventilation hereafter) and normalised perfusion (referred to as perfusion hereafter) maps were produced by summing between 0.05 and 0.4 Hz for ventilation, and between 0.75 and 1.45 Hz for perfusion.

The perfusion maps were normalised using the 99th percentile of the main pulmonary vessel timecourse, following Ilicak *et al.*. The associated histograms for the ventilation and perfusion maps were created and the median of the histograms was computed for both repeats.

4.2.4 Statistical Analysis

Statistical analysis was carried out using MATLAB R2022b (MathWorks, Natick, MA, USA) and GraphPad Prism 9.2.0 (GraphPad Software, San Diego, CA, USA). The same statistical tests were carried out for VOLVE, PREFUL and DMD. The MRI-derived parameter data were found to have a non-normal distribution using a Shapiro–Wilk test, and hence nonparametric tests were used. Results were considered statistically significant for $p < 0.05$.

Comparison of functional MRI metrics between the healthy and COPD groups was performed using a Kruskal-Wallis test followed by post-hoc pairwise analysis with Dunn's correction for multiple comparisons. To assess intra-session, intra-subject repeatability, the coefficient of variation (CoV) was computed for all metrics. Bland-Altman analysis was performed and the mean difference and 95% limits of agreement (mean ± 1.96 × SD) was calculated. Repeat values were tested for significance via a Wilcoxon signed rank test.

For VOVLE metrics, differences between lung regions were compared using a Wilcoxon rank sum test. Linear correlation between spirometry-derived and VOLVE parameters was performed using the Spearman correlation coefficient.

4.3 Results

4.3.1 VOLVE: Ventilation Assessment

All participants underwent a single study visit lasting up to 1 hour. The MRI protocol was well tolerated by all study participants. A summary of the

group demographics and derived functional VOLVE parameters is provided in Table 4.2.

Parameter	Healthy (Never Smoker)	Healthy (Smoking History)	COPD	Healthy never smoker vs. smoking history p-value	Healthy never smoker vs. COPD p-value	Healthy smoking history vs. COPD p-value
N	12	4	8	-	-	-
Sex (M:F)	5:7	1:3	4:4	-	-	-
Age (yrs)	30.3 ± 12.5	42.5 ± 18.3	64.1 ± 13.6	0.08	0.0009*	0.03*
GOLD Class						
1	-	-	0	-	-	-
2	-	-	3	-	-	-
3	-	-	5	-	-	-
4	-	-	0	-	-	-
FEV_1 (L/min)	N/A	4.2 ± 1.2	1.3 ± 0.5	-	-	0.01*
FEV_1 % Predicted	N/A	106 ± 9	49 ± 15	-	-	0.01*
FVC (L/min)	N/A	5.1 ± 1.5	2.9 ± 0.8	-	-	0.05*
FVC % Predicted	N/A	103 ± 8	86 ± 18	-	-	0.1
FEV_1/FVC	N/A	0.82 ± 0.01	0.45 ± 0.09	-	-	0.01*
XCC_V Median	0.61 ± 0.07	0.53 ± 0.092	0.40 ± 0.07	0.2	2.5e-04*	0.07

XCC_V Skewness	-0.42 ± 0.24	-0.18 ± 0.31	0.24 ± 0.18	0.1	2.5e-04*	0.07
Lag_V Median	2.45 ± 2.70	6.99 ± 0.59	25.71 ± 8.09	0.002*	2.0e-04*	0.004*
$Grad_V$ Median	0.68 ± 0.26	0.60 ± 0.13	0.19 ± 0.06	0.8	2.5e-04*	0.004*
$Grad_V$ PAR	6.02 ± 1.93	4.62 ± 1.39	1.43 ± 0.72	0.2	2.0e-04*	0.002*

Table 4.2: Summary of Participant Information, Spirometry and MRI Ventilation Parameters. Participant information and MRI data across the groups. Values quoted as mean ± standard deviation. Significant differences ($p<0.05$) marked with an asterisk (*). Abbreviations: Global Initiative for Chronic Obstructive Lung Disease (GOLD), forced expiratory volume in 1 s as a percentage of the predicted value (FEV_1); forced vital capacity (FVC), maximum cross-correlation (XCC) , gradient (grad), not available (N/A).

Example XCC_V, Lag_V and $Grad_V$ maps are shown for a healthy non-smoker and COPD participant in Figure 4.3. VOLVE maps for all study participants are included in Appendix 4B. The XCC_V map for the healthy volunteer is relatively homogenous with XCC values generally > 0.4 (histogram negatively skewed; skewness = -0.78), except for some small regions in, or bordering, vessels. In contrast, the XCC_V map for the COPD participant is heterogeneous (histogram symmetrically distributed with a skewness = -0.02).

The Lag_V map for the healthy volunteer shows that lags < 20% of the respiratory cycle are predominant, with 68% of lung voxels having a < 10% lag. In contrast the Lag_V map for the COPD participant is heterogeneous with many voxels exhibiting a delay – many of which fall between 40% and 70% of the respiratory cycle. These voxels are out of phase with the navigator signal, indicating an increase in MR parenchyma signal on inspiration.

The $Grad_V$ map for the healthy never-smoker displays values generally > 0.5, except for negative values in the main pulmonary vessels; with the histogram displaying a primary peak at 1, and a small secondary peak at -1. In contrast, the $Grad_V$ map for the COPD participant shows a compressed distribution, with a higher proportion of zero values and an enlarged secondary/negative peak, leading to a reduced PAR.

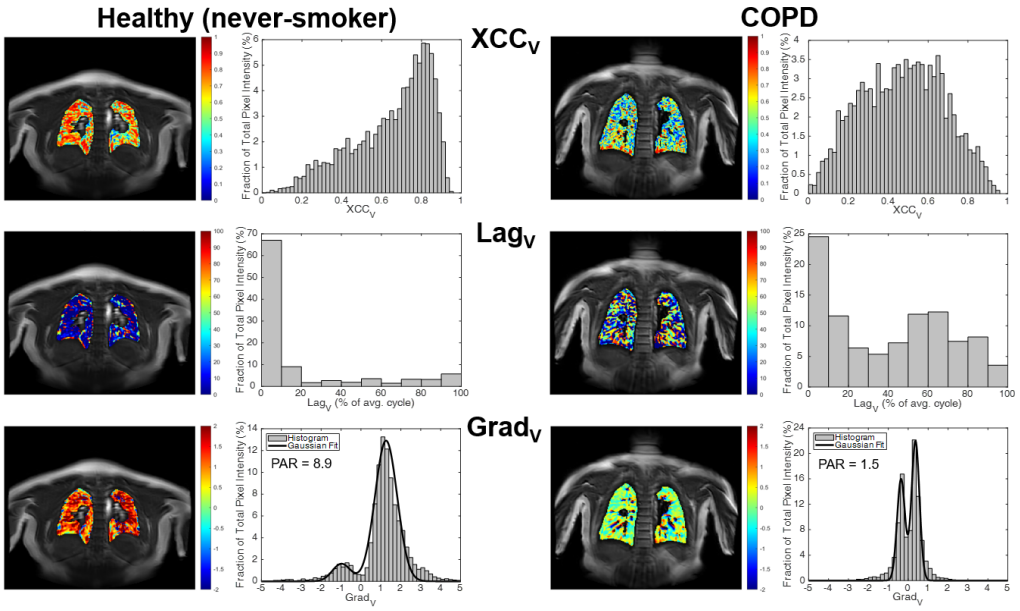


Figure 4.3: Example VOLVE parameter maps and histograms. Maximum cross-correlation maps and histograms (top row); lag maps and histograms (middle row); gradient maps (note the different scales) and histograms with fitted Gaussian mixture model (bottom row); for a healthy never-smoker (age 24, male) and COPD participant (age 66, female, FEV_1=30%, GOLD III).

Figure 4.4 shows boxplots of the median cross-correlation, lag and gradient peak area ratio for each of the three groups. Both the $Grad_V$ and Lag_V metrics were significantly different in the COPD group compared to both the healthy never-smoker group and the healthy smoker group. XCC_V was significantly different between COPD and healthy never-smokers.

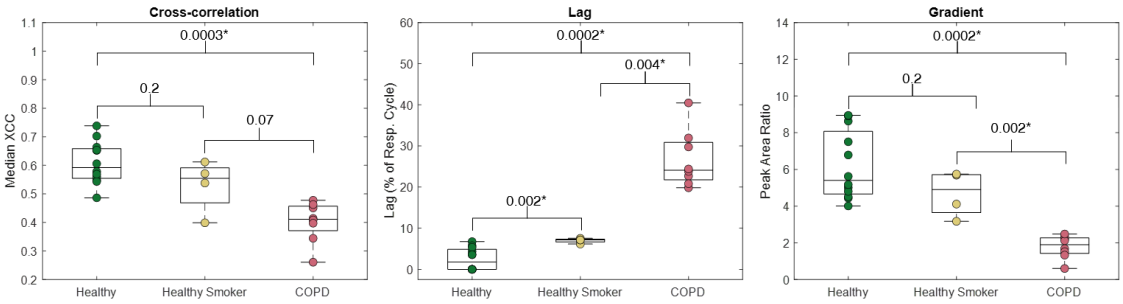


Figure 4.4: Boxplots showing the median cross-correlation (XCC) and lag, and the gradient (fitted peak area ratio) values for the groups. Significant differences ($p<0.05$) between COPD patients and healthy (never-smokers and those with smoking history) are observed in the lag and gradient metrics, and between COPD and healthy never-smokers for XCC; significant results are marked with an asterisk (Kruskal-Wallis test with Dunn's post-hoc test).

Figure 4.5 shows the within-session repeatability of the XCC_V, Lag_V and $Grad_V$ metrics, with repeat scan values plot against one another, Bland-Altman analysis and coefficient of variation (CoV) boxplots. Bland-Altman analysis showed a mean difference of 0.015 (95% confidence interval (CI): ±0.095) for XCC_V median, 0.806 (95% CI: ±4.49) for Lag_V median and -0.051 (95% CI: ±0.529) for $Grad_V$ peak area ratio. All XCC_V median values were within the 95% limits of agreement; and all but 2 of the 24 Lag_V median values (both COPD participants) were within the 95% limits of agreement. For $Grad_V$ peak area ratio, all but 1 of the 24 values (healthy volunteer) was within the 95% limits of agreement. The median CoV value for XCC_V median across the groups was 4.2%, Lag_V median was 8.6% and for $Grad_V$ peak area ratio was 3.9% No significant differences were found between intra-session scans (all $p>0.05$).

Table 4.3 shows that the clinical spirometry measures (FEV_1 and FEV_1/FVC) significantly correlate with VOLVE metrics across the groups.

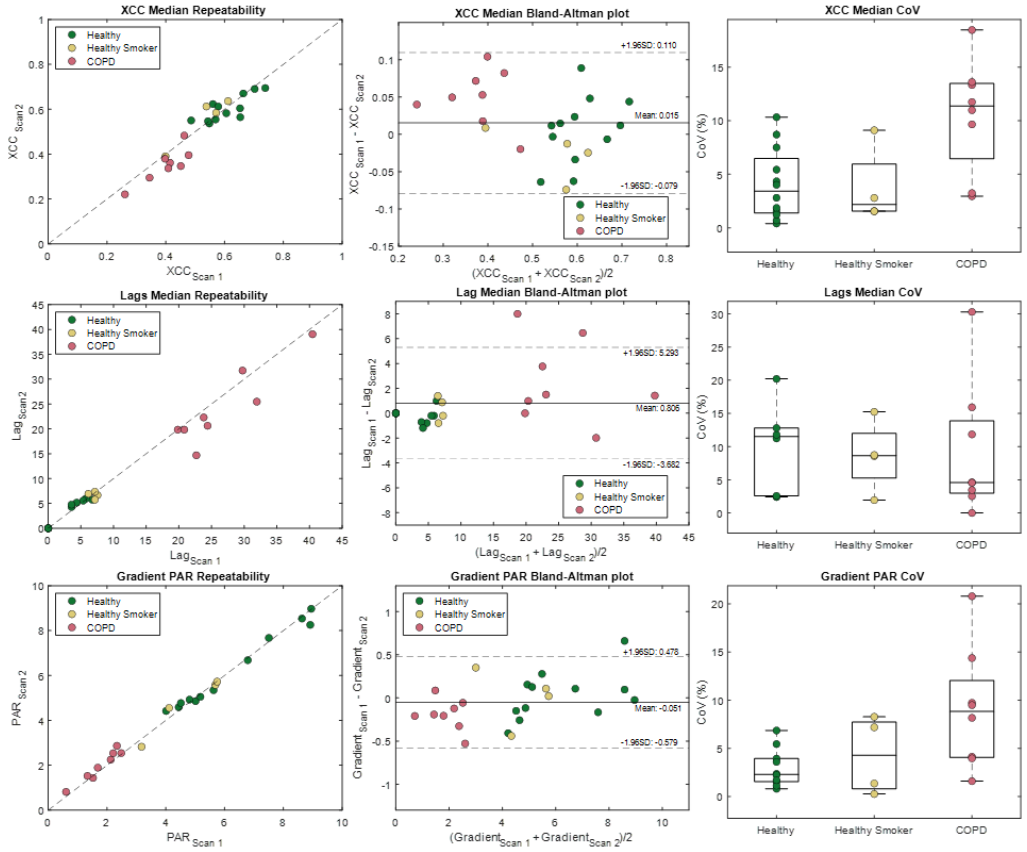


Figure 4.5: Repeatability assessment of VOLVE parameters (median cross-correlation (XCC), lag and gradient peak area ratio). Plots of repeat values, Bland-Altman plots and coefficient of variation (CoV) plots provide an assessment of within-subject repeatability.

	FEV_1 (%)	FVC (%)	FEV_1/FVC
XCC_V Median	0.44 (0.2)	0.29 (0.4)	0.55 (0.08)
XCC_V Skewness	-0.43 (0.2)	-0.18 (0.6)	-0.6 (0.05)
Lag_V Median	-0.57 (0.04)*	-0.25 (0.47)	-0.45 (0.2)
$Grad_V$ Median	0.64 (0.04)*	0.45 (0.2)	0.68 (0.03)*
$Grad_V$ PAR	0.79 (0.004)*	0.52 (0.1)	0.73 (0.01)*

Table 4.3: Spearman Correlation, r, of Spirometry with VOLVE metrics with p-values (given as r (p)), with significant results marked with an asterisk. FEV_1 % predicted, FVC % predicted and the ratio FEV_1/FVC is shown.

Figure 4.6 shows that in both healthy participant groups there was little variation in VOLVE metrics across lung regions (except healthy smoker $Grad_V$ PAR), whereas there tended to be greater relative regional variation in those with COPD, although no significant differences were found between quadrants within groups.

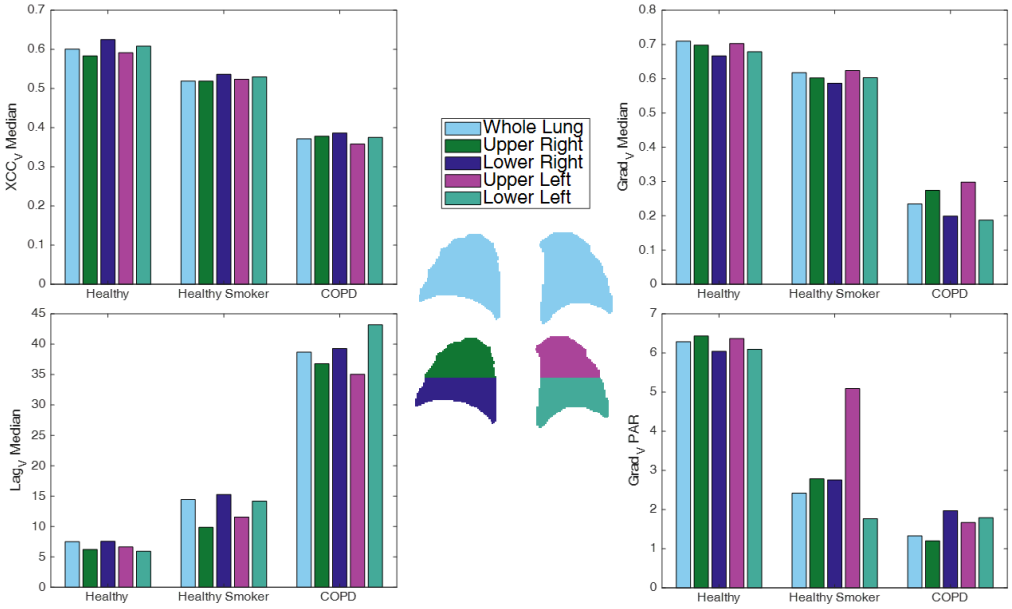


Figure 4.6: VOLVE parameter values shown for different regions across the lung from the quadrant segmentation. Note that left/right refer to anatomical (rather than image) orientation. Abbreviations: cross-correlation (XCC), gradient (grad), peak area ratio (PAR).

4.3.2 VOLVE: Perfusion Assessment

Example VOLVE-perfusion maps are shown in Figure 4.7. Similar to the ventilation maps, the XCC, lag and gradient from the York regression are shown. Strong XCC_Q are observed across the entire lung in the healthy never-smoker participant, whereas weaker XCC_Q is seen in the COPD participant. $Grad_Q$ values show a similar trend, with particularly strong $Grad_Q$ observed in the main pulmonary vessels. All perfusion metrics were significantly different in COPD compared to healthy never-smokers, but only the XCC_Q was significantly different between healthy-smokers and COPD.

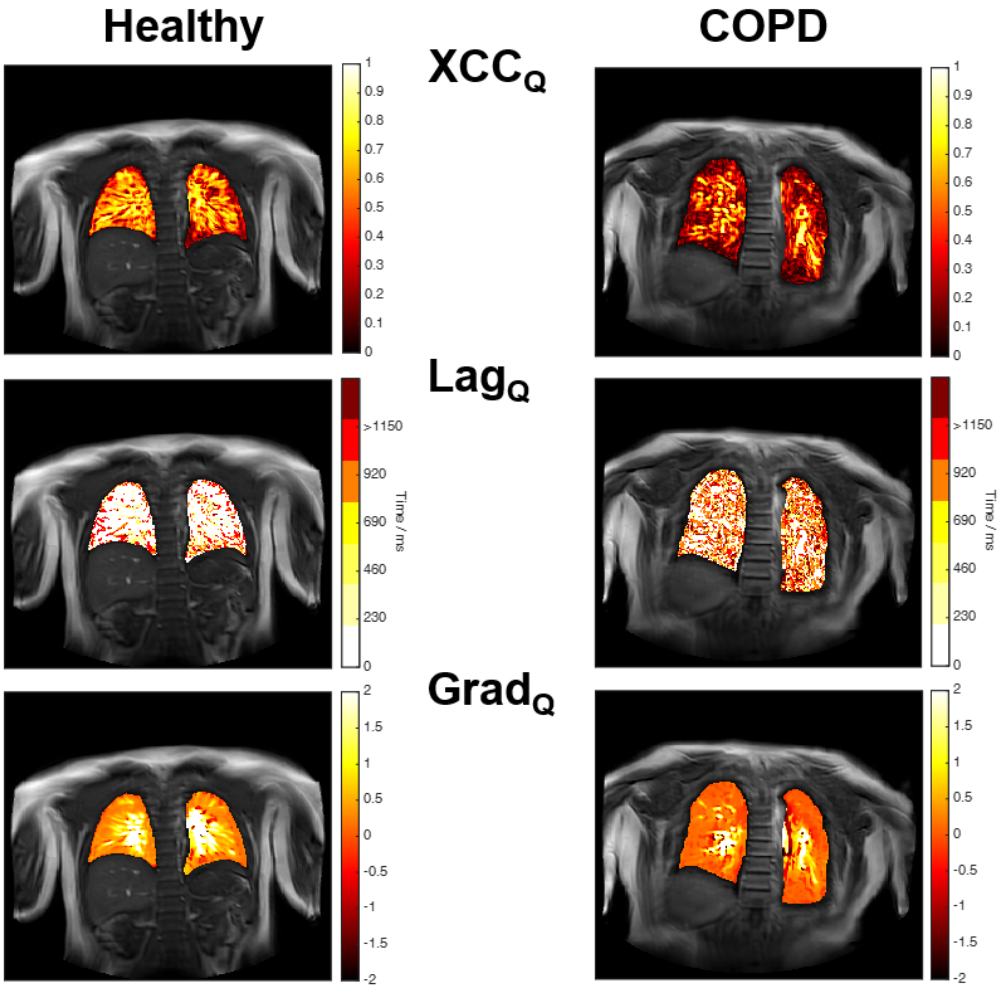


Figure 4.7: Example VOLVE-based perfusion assessment maps. Cross-correlation maps (top row); lag time maps (blood arrival time) (middle row; and gradient maps (bottom row); for a healthy never-smoker (age 23 years, female) and COPD participant (age 79 years, male, FEV_1=61%, GOLD II).

Parameter	Healthy	Healthy Smoker	COPD	Healthy never smoker vs. smoking history p-value	Healthy never-smoker vs. COPD p-value	Healthy smoking history vs. COPD p-value
VOLVE-Perfusion						
XCC_Q Median	0.42 ± 0.07	0.45 ± 0.05	0.29 ± 0.06	0.3	0.002*	0.008*
XCC_Q Skew-ness	0.17 ± 0.25	0.10 ± 0.19	0.70 ± 0.24	0.6	0.001*	0.008*
Lag_Q Median	0.30 ± 1.03	24.60 ± 28.52	30.6 ± 31.65	0.1	0.008*	0.9
$Grad_Q$ Median	0.39 ± 0.23	0.39 ± 0.26	0.16 ± 0.06	0.9	0.01*	0.05
$Grad_Q$ PAR	5.07 ± 5.07	4.748 ± 5.00	1.96 ± 1.54	0.8	0.08	0.5
Cardiac-gated VOLVE-Ventilation						
Systole XCC_V Median	0.44 ± 0.15	0.427 ± 0.16	0.31 ± 0.09	0.9	0.08*	0.4
Diastole XCC_V Median	0.58 ± 0.12	0.478 ± 0.14	0.37 ± 0.11	0.3	0.007*	0.2
Systole XCC_V Skewness	0.056 ± 0.37	0.159 ± 0.45	0.40 ± 0.19	0.9	0.03*	0.6
Diastole XCC_V Skewness	-0.33 ± 0.34	0.03 ± 0.48	0.36 ± 0.35	0.2	0.002*	0.3

Systole Lag_V Median	1.92 ± 6.02	0.5 ± 0.58	2.75 ± 1.67	0.7	0.002*	0.02*
Diastole Lag_V Median	0.42 ± 0.52	1 ± 0.82	3.50 ± 2.67	0.3	6.0e-04*	0.09
Systole $Grad_V$ Median	0.52 ± 0.23	0.457 ± 0.15	0.20 ± 0.066	0.9	4.5e-04*	0.008*
Diastole $Grad_V$ Median	0.61 ± 0.26	0.457 ± 0.13	0.17 ± 0.062	0.4	3.9e-05*	0.006*
Systole $Grad_V$ PAR	4.95 ± 1.88	5.167 ± 2.13	1.56 ± 0.71	1	0.002*	0.004*
Diastole $Grad_V$ PAR	5.73 ± 2.14	3.872 ± 2.26	1.16 ± 0.63	0.3	2.5e-04*	0.03*

Table 4.4: VOLVE-Perfusion and Cardiac-gated VOLVE-Ventilation data across the groups. Values quoted as mean ± standard deviation. Significant results ($p<0.05$) are marked with an asterisk (*).

Table 4.4 shows that the XCC_Q, Lag_Q and $Grad_Q$ perfusion median values were significantly different in COPD than in healthy non-smokers and healthy smokers for all metrics. Also, it can be seen that all ventilation parameters that were significant prior to cardiac gating remain significant for COPD when gated to systole and diastole, except diastole Lag_V median.

4.3.3 PREFUL

Table 4.5 shows the mean ± standard deviation PREFUL metrics across the groups with corresponding p values. Figure 4.8 shows example PREFUL RVent and FVL-CC maps for a healthy non-smoker and COPD participant (the same subjects as for VOLVE analysis in Figure 4.3). The RVent map for the healthy participant displays elevated values which are more homogenous

compared to the COPD participant. The FVL-CC map for the healthy participant shows generally strong correlation values, whereas the COPD participant map is heterogeneous with many areas of low correlation.

Figure 4.9 shows boxplots of the median RVent and FVL-CC for each of the three groups. Both PREFUL metrics were significantly different in the COPD group compared to the healthy never-smoker group, but not the healthy smoker group.

Parameter	Healthy (Never Smoker)	Healthy (Smoking History)	COPD	Healthy never smoker vs. smoking history p-value	Healthy never smoker vs. COPD p-value	Healthy smoking history vs. COPD p-value
RVent Median	0.09 ± 0.04	0.07 ± 0.03	0.02 ± 0.01	0.52	2.47e-04*	0.05*
RVent VDP	23.2 ± 7.6	25.6 ± 8.0	48.9 ± 6.7	0.52	2.47e-04*	0.004*
FVL-CC Median	94.8 ± 2.2	93.6 ± 2.1	70.8 ± 10.4	0.32	2.47e-04*	0.004*
FVL-CC VDP	2.9 ± 1.7	1.7 ± 0.5	6.6 ± 6.8	0.21	0.67	0.68
VTTP Median	55.9 ± 4.5	56.2 ± 5.4	58.7 ± 3.6	1	0.29	0.56
VTTP Skewness	1.1 ± 0.6	1.1 ± 0.4	0.80 ± 0.4	0.86	0.29	0.36

Table 4.5: Summary of PREFUL analysis results. Values quoted as mean ± standard deviation. Significant differences ($p<0.05$) marked with an asterisk (*).

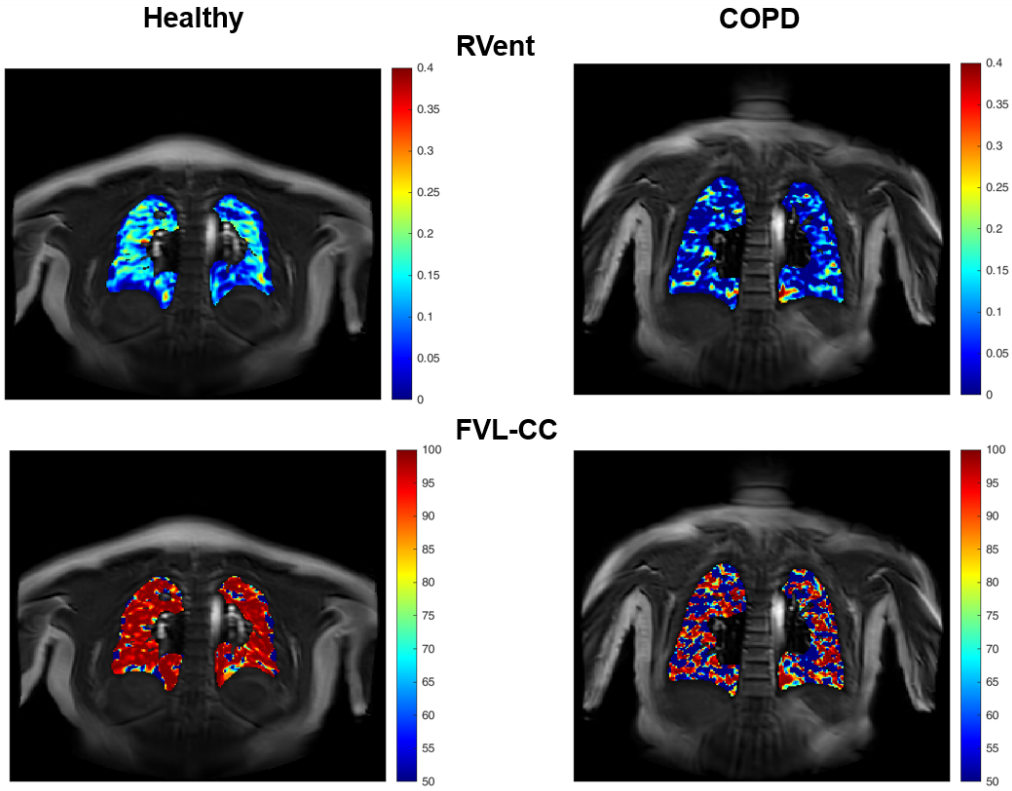


Figure 4.8: Example PREFUL RVent and FVL-CC parameter maps for a healthy never-smoker (age 24 years, male) and COPD participant (age 66 years, female, FEV_1=30%, GOLD III).

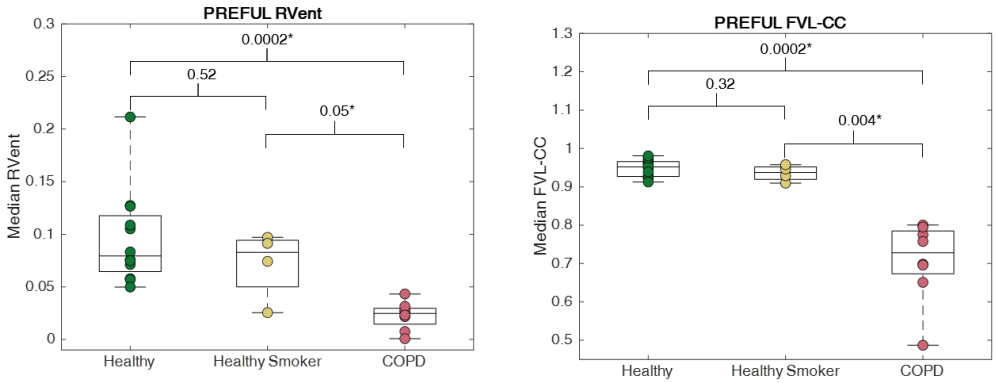


Figure 4.9: Boxplots showing the median RVent and median FVL-CC across the groups. Significant differences ($p<0.05$) between COPD patients and healthy never-smokers are observed in the RVent and FVL-CC metrics.

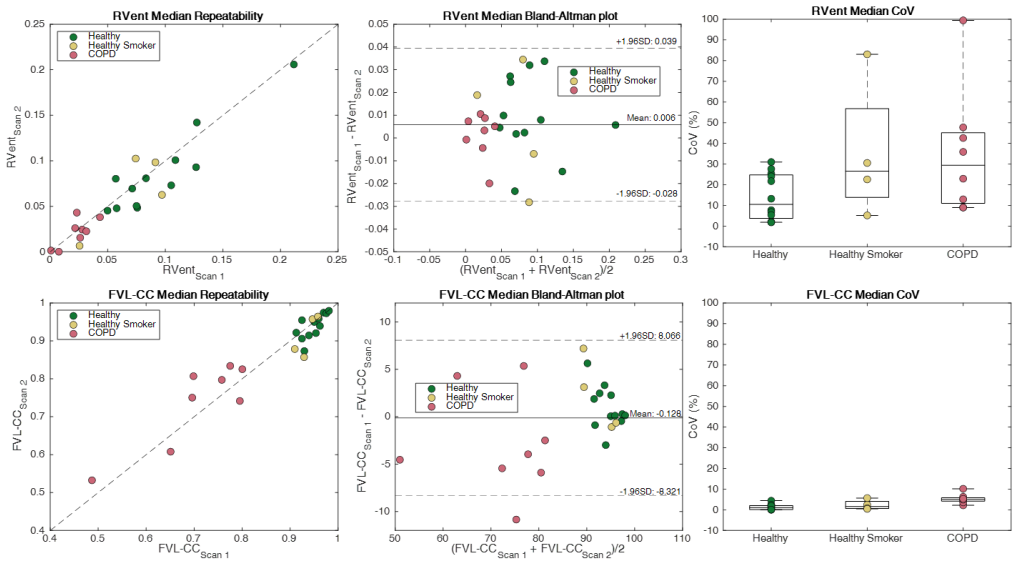


Figure 4.10: Repeatability assessment of PREFUL parameters: median regional ventilation (RVent) and median flow-volume loop cross-correlation (FVL-CC). Plots of repeat values, Bland-Altman plots and coefficient of variation (CoV) plots provide an assessment of within-subject repeatability.

Figure 4.10 shows the within-visit repeatability, with repeat scan values plotted against one another, Bland-Altman analysis and coefficient of variation (CoV) boxplots. Bland-Altman analysis showed a mean difference of 0.006 (95% confidence interval (CI): ±0.033) for RVent and -0.128 (95% CI: ±8.19) for FVL-CC. Both PREFUL metrics were within 95% limits of agreement for all participants except for a single subject each. The median CoV value for RVent across the groups was 22.1% and for FVL-CC was 2.2%. No significant differences were found between intra-session scans (all $p>0.05$).

4.3.4 DMD

Figure 4.11 shows example DMD ventilation and perfusion maps for a healthy non-smoker and COPD participant. The ventilation map for the healthy participant displays elevated values which are more homogenous compared to the COPD participant. Also in the COPD participant there is a clear area of hypoventilation in the right lung. Similarly for perfusion, the healthy map is more homogenous with larger signal values corresponding spa-

tially to the main pulmonary vasculature, whereas in COPD the magnitude of the perfusion signal is reduced.

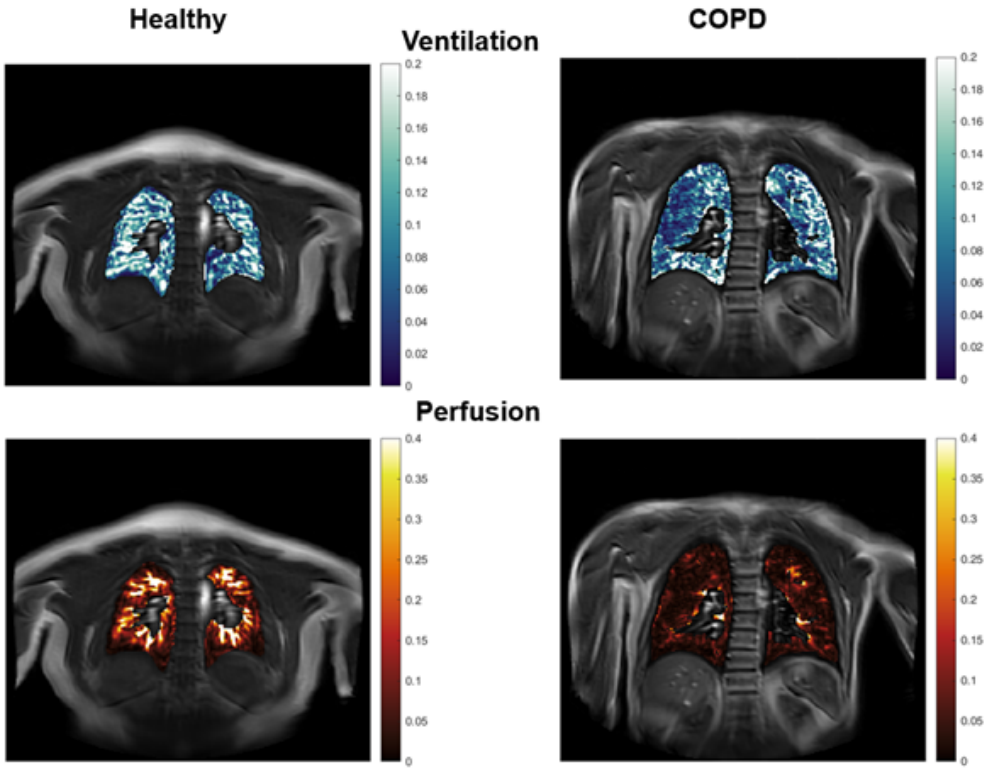


Figure 4.11: Example DMD ventilation and perfusion parameter maps for a healthy never-smoker (age 24 years, male) and COPD participant (age 66 years, female, FEV_1=30%, GOLD III). The COPD participant displays an area of hypoventilation in the right lung.

Figure 4.12 shows boxplots of the median ventilation and perfusion values for each of the three groups, with p values from the Kruskal-Wallis test followed by post-hoc pairwise analysis with Dunn's correction for multiple comparisons. Only DMD perfusion between healthy never-smokers and COPD was significant.

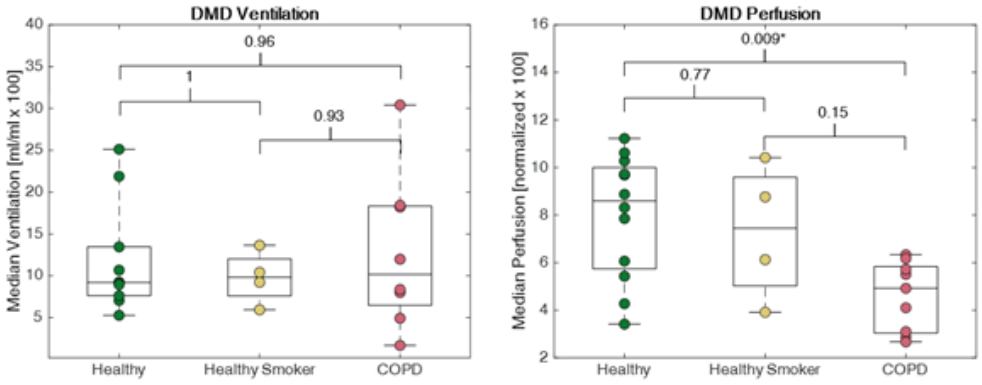


Figure 4.12: Boxplots showing the median DMD ventilation and perfusion across the groups. Significant differences ($p<0.05$) between COPD patients and healthy never-smokers is observed for perfusion.

Figure 4.13 shows the within-visit repeatability, with repeat scan values plotted against one another, Bland-Altman analysis and coefficient of variation (CoV) boxplots. Bland-Altman analysis showed a mean difference of -3.80 (95% confidence interval (CI): ±27.6) for ventilation and -0.139 (95% CI: ±2.8) for perfusion. Both DMD metrics were within 95% limits of agreement for all participants except for one healthy subject for ventilation and two for perfusion. The median CoV value for ventilation across the groups was 32.9% and for perfusion was 7.9%.

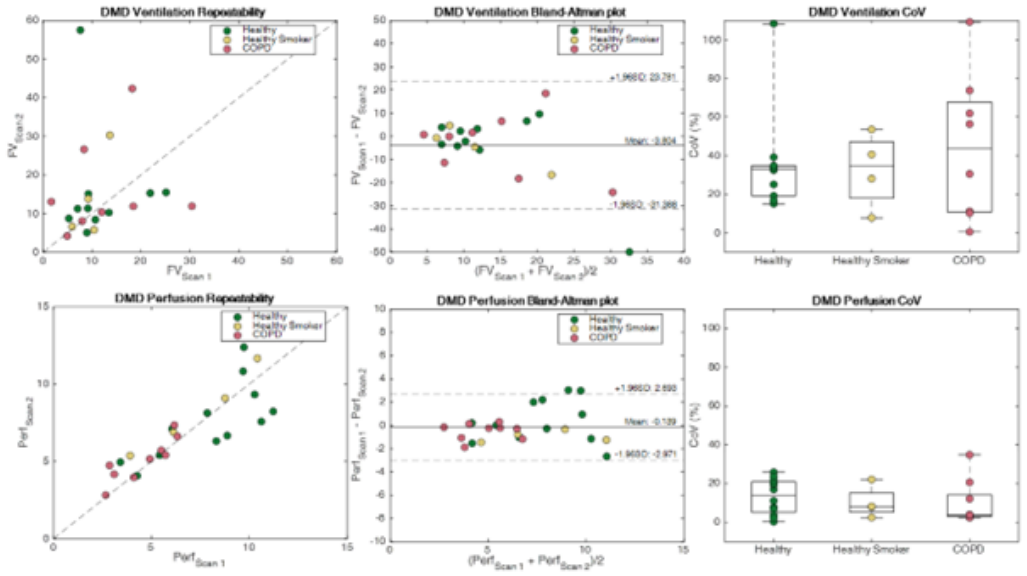


Figure 4.13: Repeatability assessment of DMD parameters: median ventilation and median perfusion. Plots of repeat values, Bland-Altman plots and coefficient of variation (CoV) plots provide an assessment of within-subject repeatability.

4.4 Discussion

This study has applied VOLVE, a novel analysis of widely available free breathing FFE MRI data to assess pulmonary ventilation and perfusion using standard MRI equipment. The feasibility of using linear post-processing that exploits the full respiratory lung signal time course to determine lung ventilation-related information was demonstrated. The method is repeatable and robust as it uses automated analysis to assess lung parenchyma signals from across the entire respiratory cycle of multiple respiratory cycles and requires no sorting or temporal interpolation of signals which is advantageous in situations of low signal-to-noise such as the hyperinflated lung at 3T.

4.4.1 VOLVE Assessment of Entire Timeseries

A significant difference in the $Grad_V$, XCC_V and Lag_V (all VOLVE metrics) between COPD participants and the healthy never-smoker group was observed, and these differences help to elucidate the physical relevance of

the metrics. The cross-correlation XCC_V demonstrates the extent to which the lung parenchyma signal covaries with the navigator signal (and thus lung volume), independent of any lag in response. In the healthy lung, a strong positive cross-correlation, minimal lag and positive gradient was observed, as the alveoli expand and contract with the respiratory cycle, giving rise to the expected tissue density and corresponding MR signal changes. The gradient, $Grad_V$, describes the magnitude of the MR signal change with lung volume and characterises the fundamental MR response to respiration; it is analogous to Fractional Ventilation (FV) but uses data from the entire respiratory cycle.

Participants with COPD demonstrated an altered VOLVE response. It was found that in COPD a greater proportion of voxels exhibited lower cross-correlation indicating a reduction in the linearity of the response. An increase in the number of voxels with longer lag and negative gradient was also observed, suggesting asynchrony or inversion of the expected relationship between the lung parenchymal signal and diaphragm navigator signal. It is suggested that voxels with lower cross-correlation represent areas of alveolar hypoventilation which experience little or no variation in proton density during the respiratory cycle. Regions demonstrating large lags and negative gradients (particularly observed in participants with $FEV_1 < 50\%$ but not for those with milder airflow obstruction) may be indicative of delayed or paradoxical ventilation due to significant expiratory flow limitation [180, 181]. This may reflect severe small airways obstruction, where limitation of expiratory airflow leads either to air trapping or diversion of airflow through collateral channels.

A simpler VOLVE metric is the Pearson correlation coefficient (CC_V, corresponding to XCC_V for zero lag) which provided excellent delineation between the groups, owing to the increased lag observed in COPD that enhanced the difference in the CC_V (see Appendix 4C). However, CC_V cannot distinguish voxels with a lagged response from those that do not exhibit a linear variation with lung volume, whereas the XCC_V can, thus probing the fundamental underlying signal variations. Further work is needed

to investigate these voxels with nonlinear responses, which may be due to hysteresis (i.e. the volume change with respect to navigator signal changes between inspiration and expiration (see 5.2.3)).

A key consideration in COPD is the reduction in SNR due to emphysema and air trapping, caused by a reduction in proton density (minus pathology). ^{1}H MRI signal is inherently low in the lung, and this further pathology-related reduction may bring the measured signal below the MRI noise floor. This may explain the reduction in the cross-correlation in COPD. Whilst this is measuring change in function due to pathophysiological change, this level of assessment does not require advanced/expensive MRI methods. It is difficult to discern whether the spatial distribution of these lower cross-correlation areas corresponds to low SNR pathology without a reference such as a CT image.

4.4.2 Repeatability of Ventilation Metrics

The intra-participant test-retest repeatability was moderate, with particularly good repeatability observed for the $Grad_V$ PAR VOLVE metric, with very narrow limits of agreement (-0.579 to 0.478) relative to the differences between groups. This could be in part due to the $Grad_V$ PAR being robust to asymmetry between respiratory phase and lung volume variation (see Chapter 5.2.1.1). This is a 'best case' repeatability as the subjects were not removed/re-positioned between repeat scans. Repeatability may be impacted by technical factors such as participant motion between scans or imperfect registration, and could potentially be improved with the implementation of a deep-learning segmentation of lung parenchyma [91] in the analysis pipeline.

Lower repeatability in VOLVE metrics was observed overall in the COPD group. The higher CoV values in the COPD group for Lag_V could be in part due to the lag distribution being multimodal in some cases and hence poorly characterised by the median. Since the repeat scans were collected in the same examination, changes are unlikely to be due to genuine changes in lung function. It might reasonably be expected that regional

measures of ventilation are more variable than global measures, such as FEV_1, where defects are averaged across the entire lung volume. Repeatability in COPD participants may also be impacted by prolonged supine posturing and compression of the thorax by the MRI chest coil during scanning, particularly during the approximate 15 minutes between the two scans, which may have led to progressive dynamic hyperinflation, although no systematic change was observed.

4.4.3 Regional Ventilation Analysis

There tended to be relatively greater regional variation in VOLVE ventilation metrics in COPD than healthy participants, as is expected for this heterogeneous disease, although no significant differences were found between lung quadrants within groups. This type of regional analysis may provide clinically relevant information in cases of targeted interventions such as lung volume reduction procedures.

4.4.4 Comparison with Spirometry

Moderate to strong significant relationships were observed between spirometry measures (% predicted FEV_1 and FEV_1/FVC) and XCC_V, Lag_V and $Grad_V$ parameters across the healthy smoker and COPD groups. It is expected that VOLVE measures, similar to other ^{1}H MRI approaches, will not necessarily exhibit strong correlation with spirometry, as these methods evaluate different aspects of lung physiology. MRI methods are sensitive to the presence/absence of ventilation, even at the level of the smallest airways/alveoli, whereas spirometry is mainly a measure of larger airways. For instance, it is well established that substantial small airways disease must be present before FEV_1 values become abnormal. In contrast, VOLVE is likely more sensitive to mild disease, but its ability to measure both the direction and magnitude of ventilation abnormality is also a clear distinction from conventional pulmonary diagnostics and even other lung MRI methods. A limitation of this study was that only retrospective spirometry data was available, which may not have accurately reflected contemporaneous lung

function. This was due to local COVID-19 safety measures during the initial period of data acquisition which forbade the performance of aerosol-generating procedures (this is also the reason for the lack of spirometry data for healthy never-smokers).

4.4.5 VOLVE-Perfusion and Cardiac Gating

The Lag_Q (blood arrival time) map for healthy participants generally showed a short blood arrival time, indicating that the lung was well-perfused. In contrast, in COPD participants exhibited longer blood arrival times and greater heterogeneity. Significant differences between COPD and healthy never-smokers for all VOLVE-perfusion metrics illustrate the sensitivity to perfusion defects and provide the possibility of visualising ventilation/perfusion (V/Q) match and mismatch.

An advantage of the VOLVE approach is that it is possible to separate the time series into both periods of inspiration and expiration, and periods of diastole and systole. This enables VOLVE analysis of cardiac-gated ventilation metrics and respiratory-gated perfusion metrics. Upon retrospective cardiac gating, no significant differences for ventilation was found in these groups of participants. Hence, the implicit perfusion-related information does not seem to have a substantial effect on ventilation assessment. However, there was a trend for VOLVE metrics determined at diastole to be closer to values obtained without cardiac gating, which could be due to reduced blood signal component (and so reduced cardiac 'noise') at diastole compared to systole. Such an approach may be useful in some clinical scenarios such as in patients with cardiac arrhythmia, where cardiac-gated ventilation measures can correct for differences in cardiac cycle variability and the implication this has on the periodic change in blood volume and associated parenchyma signal response.

A potential drawback of retrospective cardiac gating is in the impact this has on determining phase-related metrics. As the well-sampled time series are broken down into two (or more) cardiac states or bins, there may be unequal

time spacing between neighboring images (sampling frequency) within each cardiac bin which may confound the lag computation. It was generally the case that the diastolic state had more images and maintained sufficient sampling to compute the lag, whereas the more undersampled systolic state showed areas of reduced cross-correlation and a more variable lag. There may also be different extents of undersampling if the bins contain differing numbers of images. However, it may still be possible to perform a secondary gating procedure where acceptable cardiac cycles are only chosen when they line up with the respiratory cycle to produce phase-consistent bins between the two cycles, although this would require potentially many more images to be collected, which may increase the scan time by an unacceptable amount. Notwithstanding, it may still be instructive to reconstruct the diastolic state to normalise ventilation measures for blood volume/cardiac noise (without the need for additional sampling).

4.4.6 Limitations and Future Work

The sample size of this pilot study is small, and more data is needed before making more detailed clinical interpretations. A future study should establish quantitative benchmark values in healthy never-smokers which will enable the generation of binary defect maps and ventilation defect percentage (VDP) to facilitate rapid clinical interpretation. The VOLVE response in diseases other than COPD may be different, particularly if diaphragm dynamics are differently affected, or disease manifests as an increase in proton density e.g., fibrosis, and so future studies should consider participants with a range of other respiratory diseases. Even for COPD, the majority of the patients in this study were GOLD stage II and III, which may have altered local alveolar susceptibility profiles to GOLD stage I or IV, and this may vary between phenotypes, and so a larger sample size is needed before these differences can be assessed.

A drawback of the histogram analysis performed is that data is compressed, such that regional maps are reduced to global parameters. Other quantitative

metrics could be explored in future which preserve some regional information, to quantify heterogeneity and distribution of V/Q defects.

This work assumes that the navigator signal is a direct marker of change in lung volume. However, this signal is not a measure of absolute lung volume in a given individual. In some conditions, this relationship between navigator signal and lung volume becomes nonlinear, for example, if there a change in inter-play between the diaphragm and the chest wall. An alternative approach is to measure the relationship between navigator signal and lung volume in an individual if high speed 4D imaging is available (see Chapter 5.2).

A potential source of error is the assumption that respiratory states with equal volume have equal ventilation and MRI signal irrespective of whether they were acquired on inspiration or expiration, and the resulting phase shifts may introduce scatter if a hysteresis effect is present. However, as with the impact of the cardiac phase, fitting over many respiratory cycles is likely to average out this effect. Only the right lung was used to determine the lung-diaphragm navigator signal, which could mischaracterise respiratory phase in the case of asymmetric diaphragm excursion.

As with other studies using a similar acquisition [133, 182], the principal weakness of this approach in characterising the extent of lung disease is that only a single slice is collected. Multiple slices could be collected in future, either by reducing the length of the dynamic data series and scanning different slices consecutively, or by decreasing the dynamic rate and collecting interleaved slices concurrently. Further work is required to determine the optimum temporal resolution and number of dynamic images (see Chapter 6.4). A challenge for whole-lung perfusion quantification in this manner is that peripheral (most anterior/posterior) slices may lack coverage of major pulmonary vasculature and so may not possess a strong vessel signature, which may confound correlation-based analysis. Additionally, the implications of phase differences among various potential reference vessels (e.g., aorta versus pulmonary artery) warrants further investigation.

Alternatively, full lung coverage could be achieved by a single isotropic 3D acquisition. This would enable capturing the full three-dimensional thoracic motion for a direct measurement of lung volume change, as well as functional coverage of the entire lung. Other studies have used multi-slice 2D [93, 183] and 3D [91, 92] acquisitions, although the 3D approach is insensitive to blood inflow due to the requirement of a nonselective hard RF pulse, and is therefore unable to assess perfusion. It would be beneficial to compare different slice positions, especially more anterior slices, to investigate the impact of blood pooling due to supine posturing on the acquired VOLVE metrics. Ultimately to assess lung function in diffuse disease, full lung coverage is key for clinical translation.

This study was conducted at 3 T, and so the methodology presented requires validation at 1.5 T for wider translation. Most recent studies have been carried out at 1.5 T, and while it is not expected that the SNR in the navigator signal will be substantially different at 1.5 T, the change in T_2* could impact the sensitivity to different lung pathology.

4.4.7 PREFUL Discussion

This analysis has shown that PREFUL RVent and FVL-CC metrics are sensitive to lung disease, as significant differences in both PREFUL metrics were observed between both healthy groups and COPD. These results are in concordance with Pöhler *et al.* who found reduced PREFUL RVent and FVL-CC median values in COPD compared to a healthy cohort [184]. However, the median RVent and FVL-CC values found in this study are less than those compared with Pöhler *et al.*, who reported RVent values of 0.18 and 0.12 for healthy and COPD, respectively, and FVL-CC (termed ccVent in their study) values of 0.99 and 0.92 for healthy and COPD, respectively. These differences may be due to differences in participant demographics, including notably different GOLD stage distributions (60% stage II, 40% stage III compared to our 37% stage II, 63% stage III), and difference in sample size. These differences may also be due to technical differences in

the implementation of the PREFUL analysis and/or registration method, although since the Vogel-Claussen Imaging Lab group (Hannover, Germany) implementation of PREFUL is proprietary, is it difficult to ascertain any potential differences. While a direct comparison to another study with this pipeline would be beneficial, this could not be made in this case as this pipeline has only been used by the Hospital for Sick Children, University of Toronto [133], and so has not been used to assess COPD. Indeed, it may be the case that PREFUL is more robust to noise/low SNR data than VOLVE, which may be due to fundamental differences between the methods or in differences in implementation, which requires further investigation.

It was found that FVL-CC achieved better delineation between the groups (Figure 4.9), and better within-subject repeatability (Figure 4.10), than RVent, as expected from a dynamic measure compared to a static measure. RVent had moderate repeatability which did not vary much between groups, whereas FVL-CC had better repeatability overall but poor repeatability in COPD. FVL-CC exhibited small CoV values, whereas RVent CoV was particularly high. This could be due to several COPD subjects' RVent mean values being close to zero, which has the effect of inflating the CoV. At the same time, this could be due to FVL-CC being a secondary metric that is relative to a healthy reference FVL; this self-correlation may artificially improve the repeatability, but inadvertently introduce bias depending on e.g., the spatial position of the healthy reference loop.

A key result from this analysis is that neither PREFUL metric was able to differentiate ventilation status between healthy never-smoker and healthy smoker group. In contrast, VOLVE Lag_{V} was found to be significantly different between these groups. This indicates that while both methods determine dynamic ventilation metrics that are sensitive to established lung disease, the detection of milder, more early-stage functional change is hampered for PREFUL. This could be due to the nature of the complex post-processing steps, involving cycle resorting, interpolation, and lung region classification. This work shows that this complex process may not only

be unnecessary, but that it may potentially impede sensitive functional assessment. In addition, straightforward metrics allow for more rapid clinical interpretation, acceptance, and dissemination, as well as enabling more consistent implementation between sites. Further work is needed to compare differences between VOLVE and PREFUL on a subject-by-subject basis to investigate any potential differences in robustness, sensitivity and repeatability (although a fair comparison would require access to proprietary PREFUL software).

4.4.8 DMD Discussion

This work has shown that is it feasible to carry out functional lung analysis via DMD in healthy and patient groups. Regionally localised maps of lung function depict visual differences between healthy and COPD participants in some cases. Figure 4.11 shows a homogenous ventilation map for the healthy individual, whereas in COPD there is a clear area of hypoventilation in the right lung. Also, the normalised perfusion values are generally smaller for the entire lung in COPD. However, while some visual differences were observed, this analysis has shown that across the groups, the median DMD signal is significantly different for perfusion but not for ventilation (Figure 4.12). The underlying reason of this apparent sensitivity for perfusion and not ventilation is not clear, but must be related to the DMD methodology, as the same data analysed with VOLVE (see 4.3) and PREFUL (see 4.3.3) approaches were both able to determine differences in ventilation between the groups. A possible explanation for the lack of sensitivity is that too many DMD modes were considered. In the case that the ventilation information is characterised by fewer than 15 modes, considering additional modes may have introduced noisy modes which obfuscate the ventilation signal. Further work could be done in determining the optimum number of DMD modes and frequency ranges to consider for maximum sensitivity.

DMD showed moderate repeatability overall, with no systematic differences between the groups. Generally, perfusion showed better repeatable than

ventilation, in spite of the heart rate being more variable than the breathing rate. This could again be related to a suboptimal number of DMD modes. Alternatively, the differences could be due to the perfusion signal remaining linear across the groups, whereas the linearity of the ventilation response is reduced in COPD (as determined by VOLVE, XCC_V reduces relatively more than XCC_Q in COPD) which may hamper the ability of DMD to accurately characterise the dynamics matrix. Similarly to PREFUL, it may be the case that DMD is more robust to noise/low SNR data than VOLVE, where DMD may be able to more accurately extract spatial features, but further investigation of this requires a reference or ground truth.

Overall DMD is feasible for functional pulmonary ^{1}H MRI, but requires further investigation and optimisation, especially for ventilation assessment, before use in determining reliable functional biomarkers or as an endpoint in future clinical trials.

4.5 Conclusion

VOLVE provides a novel method to assess ventilation and perfusion from free-breathing ^{1}H MRI. The linear regression-based approach utilises all images in the respiratory cycle and allows for probing of the underlying signal variations. Healthy volunteers can be discerned from people with COPD.

While dynamic PREFUL measures were found to be sensitive to disease status in the COPD group, they were not sensitive to smoking-related changes in lung function, whereas VOLVE was, indicating potentially increased sensitivity to early-stage disease in VOLVE. Likewise, DMD was sensitive to perfusion changes, but lacked sensitivity and repeatability for ventilation, whereas VOLVE showed superiority in these areas. Therefore VOLVE is a promising candidate for quantification of lung function. While the York gradient has been used to characterise the magnitude signal changes, further work is needed to accurately characterise lung parenchyma voxels that exhibit a nonlinear relationship with global lung expansion.

Chapter 5

Investigating Functional Insights from Lung Motion

Abstract

The ability to exploit both local expansion and global lung motion to provide complimentary information on lung functional assessment (in addition to the signal changes considered in Chapter 3) is an exciting prospect for pulmonary ^{1}H Magnetic Resonance Imaging (MRI). In this chapter, novel registration methods in the context of ventilation imaging are assessed, including assessment of local lung expansion and compression (Section 5.1), and investigation into the potential of dynamic lung imaging to assess diaphragm morphometry and motion (Section 5.2).

Non-rigid image registration is investigated, including the assessment of the impact of different registration methods and algorithms on ventilation quantification. A significant difference in VOxel-wise Lung VEntilation (VOLVE) metrics between healthy and COPD groups was found for all registration methods tested, demonstrating the independence of the VOLVE method from registration method. In addition, it was demonstrated that the voxel-wise Jacobian determinant can be used to assess localised expansion which is sensitive to lung disease (biomechanics). The average Jacobian across both lungs was found to strongly correlate with the lung-diaphragm navigator, and hence could be used as a global measure of respiratory phase that is not dependent on the spatial position of a navigator ROI. Further, utilisation of fast volumetric imaging is demonstrated to determine a correction factor between the 2D navigator-derived respiratory phase and the measured 3D lung volume.

A component of this work was presented at the International Society for Magnetic Resonance in Medicine (ISMRM) 32nd Annual Meeting (2023) [185].

Statement of Contribution

Zachary Peggs (ZP) performed all data analysis. ZP, Susan Francis (SF) and Penny Gowland (PG) interpreted the data. SF, PG, Charlotte Bolton (CEB) and Ian Hall (IH) supervised the research.

5.1 Non-rigid Image Registration: Implications for Ventilation Measures and Prospects for Functional Assessment via the Jacobian Determinant

5.1.1 Introduction

5.1.1.1 Image Registration in ^{1}H Lung MRI

Image registration is a critical step in the analysis of dynamically acquired lung images, as throughout the respiratory cycle the shape of the lungs changes dramatically. For voxel-wise analysis of the lung parenchyma, it is necessary to align the series of images so that the lung boundary is stationary. This requires the use of a non-rigid registration, where the complex nature of the inflation of the lung cannot be accounted for by simpler transformations such as affine transformations. Practically, registration involves a target or fixed image (T), and a number of moving images (M) that are deformed/displaced/distorted to match the target image, as determined by a similarity metric or cost function (S). This can be formulated using the following minimisation problem: minimise the joint energy J with respect to w for

$$J(w) = S(M(y(w)), T) + R(w) \tag{5.1}$$

where $y(w)$ is a parametric transformation with parameter w and $R(w)$ is a regularization term that enables usage of a priori information and/or physical models to constrain the registration to prevent instability in the computed solutions [186]. There are several non-rigid image registration algorithms that can be used, as well as different registration schemes and choices of registration target image. The aim of this work is to explore these registration options and assess their impact on ventilation measures.

For dynamic pulmonary ^{1}H Magnetic Resonance Imaging (MRI), conventional registration (CR) involves selecting a registration target image

of intermediate lung inflation (halfway between end-expiration and end-inspiration) and registering all other images to this target image. The target image can be chosen using the lung-navigator timecourse by finding the image closest to the average of this navigator signal. Once this target image is selected, a deformation field is applied to each image separately in the image series to align them with the target image. The deformation field can be determined with several different regularization terms and constraints, and via several different algorithms and software packages. Previously used algorithms/packages include:

- Advanced Normalization Toolkit (ANTs) [187] as used in [18, 93, 137].
- fMRLung 3.0 (Siemens Corporate Research, Princeton, NJ, USA), as used in [87, 188, 189].
- MATLAB Demons-based registration (implemented by MathWorks according to [148, 149], as used in [132, 133].
- MATLAB Forsberg (implemented by Daniel Forsberg [190]), as used in [92].
- Elastix toolbox [191] as used in [192].
- NiftyReg [193] as used in [53].

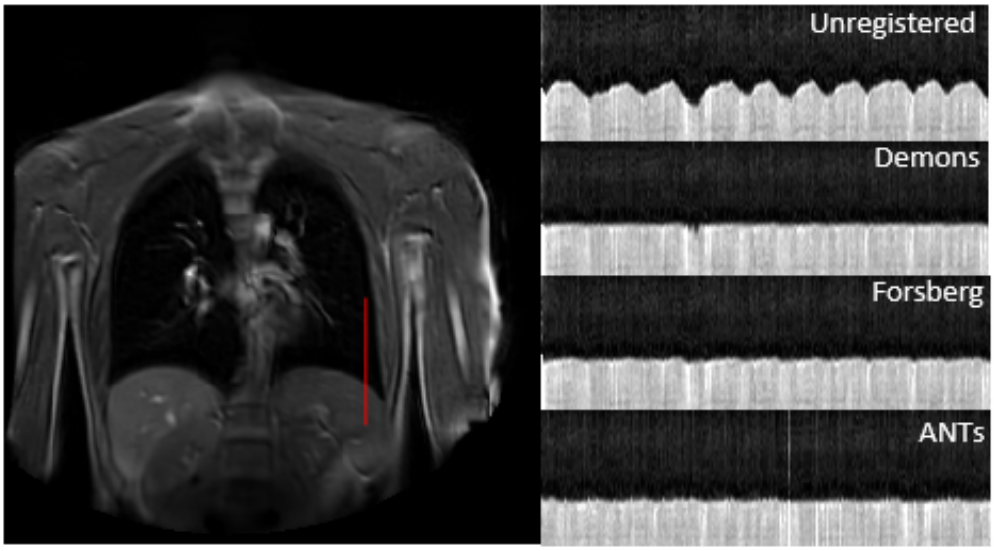


Figure 5.1: Example projection plots for various registration schemes. The LHS shows the anatomical location of the measurement axis. The RHS shows the diaphragmatic movement without motion correction and with MATLAB Demons, MATLAB Forsberg, and ANTs registration algorithms, respectively.

Figure 5.1 shows projection plots along a line crossing the lung-diaphragm boundary in the left lung for unregistered and registered images (for MATLAB Demons, MATLAB Forsberg and ANTs). It can be seen that registration with these algorithms results in a static boundary between the diaphragm and the lung parenchyma as expected. While visual/qualitative assessment of the registration is a useful sanity check, it is important for quantitative analyses that the registration appropriately interpolates the lung signal intensity such that the quantitative maps produced are not a function of the registration algorithm used. The quantitative Jacobian determinant values can also be used as an additional sanity check on the registration, and to extract additional information about local lung expansion and contraction [192].

5.1.1.2 Conventional Registration vs. Group-oriented Registration

Typically, when processing MR images, registration involves a mapping between a single target image and all other images in the timeseries (the

'moving' images). For pulmonary ^{1}H MRI, this involves selecting a target image at an intermediate level of lung inflation, such as the image closest to the mean diaphragm navigator signal. This is chosen so as to reduce the need for large deformations, e.g., registering from end-inspiration to end-expiration. This registration scheme is known as Conventional Registration (CR).

For dynamic lung imaging, an alternative registration scheme has been proposed by Voskrebenzev *et al.*, known as Group-Oriented REGistration (GOREG) [194]. This scheme of registration uses two inherent characteristics of dynamically acquired lung images to aid in registration; firstly, the images are periodic in nature and so neighbouring images will be in similar respiratory states; secondly, the deformation in the image series occurs gradually. GOREG makes use of these traits by grouping and averaging similar images as follows:

1. Divide all images into respiratory states/bins based on navigator signal amplitude and choose a target group for the registration

2. Register images within the bins (similar respiratory state) together (intra-group registration) and save these deformation fields, F_{intra}

3. Average intra-group registered images in each group to determine a representative image for each group

4. Register each group's representative image towards the neighbouring group's representative image in the direction towards the target group, and save these deformation fields, F_{inter}

5. Compose F_{intra} and the required number of F_{inter} deformation fields into a final deformation field, F_{final}

6. Apply F_{final} to each image in the timeseries

As an example, if there are 10 groups and group 5 (M_5) is the middle/target group, the registration of an image in group 8 (M_8) would involve

the application of four separate deformation fields: M_8 -> M_8‘ (intragroup registration, where M_8‘ is the group 8 representative image), M_8‘ -> M_7‘, M_7‘ -> M_6‘, M_6‘ -> M_5‘. Alternatively, an image in group 5 (M_5) undergoes only the intra-group registration, M_5 -> M_5‘.

GOREG has been shown to improve the quality of ventilation-weighted images produced by Fourier Decomposition (FD) [194] and is routinely used in Phase REsolved FUnctional Lung (PREFUL) papers [90, 93, 137]. However, GOREG has only been implemented with the ANTs registration algorithm, and has not been used in any studies computing Jacobian determinants, nor has it been assessed in the context of dynamic ventilation measures. The work presented in this chapter aims to explore the GOREG registration scheme in these circumstances.

5.1.1.3 Jacobian Determinant as a Marker of Ventilation

While image registration is a necessary step in FD-MRI and related approaches, this serendipitously provides additional information relating to lung function. Consider the same simplified two-compartment model used for Fractional Ventilation (FV), where the lung is represented as comprising a variable quantity of air and a fixed quantity of tissue. Then, if the lung undergoes a 10% overall expansion, it implies that 10% more air has entered the lung, meaning that lung expansion equates to ventilation. Applying this concept to the local scale, where the separation or convergence of two points corresponds to an increase or decrease in the intervening airspace, it is possible to measure local air inflow/outflow. Consequently, by discerning pixelwise movement within the lung, we can ascertain local ventilation. This movement is established by the image registration algorithm applied previously in the form of deformation fields. Thus, the outcome of the image registration not only facilitates image alignment but also itself offers an avenue for the quantification of ventilation. This quantification is achieved via the determinant of the Jacobian matrix of the deformation field generated by the image registration.

The Jacobian matrix of a vector-valued function is the matrix of its first-order spatial partial derivatives. The determinant of this matrix, commonly referred to as the Jacobian determinant, is widely used in vector calculus to quantify the local behaviour of a given transformation [195]. The Jacobian determinant represents the extent of volume (or area in 2D) change around a point when the transformation is applied. In 2D the Jacobian matrix, J, of some vector-valued function, u, is defined as

$$J(u) = \begin{pmatrix} \frac{\partial u_x}{\partial x} & \frac{\partial u_x}{\partial y} \\ \frac{\partial u_y}{\partial x} & \frac{\partial u_y}{\partial y} \end{pmatrix} \tag{5.2}$$

and so the Jacobian determinant is given by

$$\det(J(u)) = \begin{vmatrix} \frac{\partial u_x}{\partial x} & \frac{\partial u_x}{\partial y} \\ \frac{\partial u_y}{\partial x} & \frac{\partial u_y}{\partial y} \end{vmatrix} = \frac{\partial u_x}{\partial x}\frac{\partial u_y}{\partial y} - \frac{\partial u_x}{\partial y}\frac{\partial u_y}{\partial x}. \tag{5.3}$$

To illustrate the case of spatial transformation, consider a 2D linear scaling function, $f(x_1, y_1)$, that maps points from one vector space to another and so alters the positions of points in space according to:

$$f(x_1, y_1) = \begin{cases} x_2 = 2x_1 + y_1 + 1 \\ y_2 = x_1 + 2y_1. \end{cases} \tag{5.4}$$

The Jacobian matrix for this transformation is given by

$$J(f) = \begin{pmatrix} \frac{\partial(2x_1+y_1+1)}{\partial x_1} & \frac{\partial(2x_1+y_1+1)}{\partial y_1} \\ \frac{\partial(x_1+2y_1)}{\partial x_1} & \frac{\partial(x_1+2y_1)}{\partial y_1} \end{pmatrix} = \begin{pmatrix} 2 & 1 \\ 1 & 2 \end{pmatrix} \tag{5.5}$$

which has a Jacobian determinant of $(2)(2) - (1)(1) = 3$. Physically, this means that the area is increased three-fold upon application of this transformation. Figure 5.2 illustrates this in the case of the unit square. Hence the resultant area after transformation is equal to the product of the initial area and Jacobian determinant, and so the determinant acts as a percentage expansion parameter.

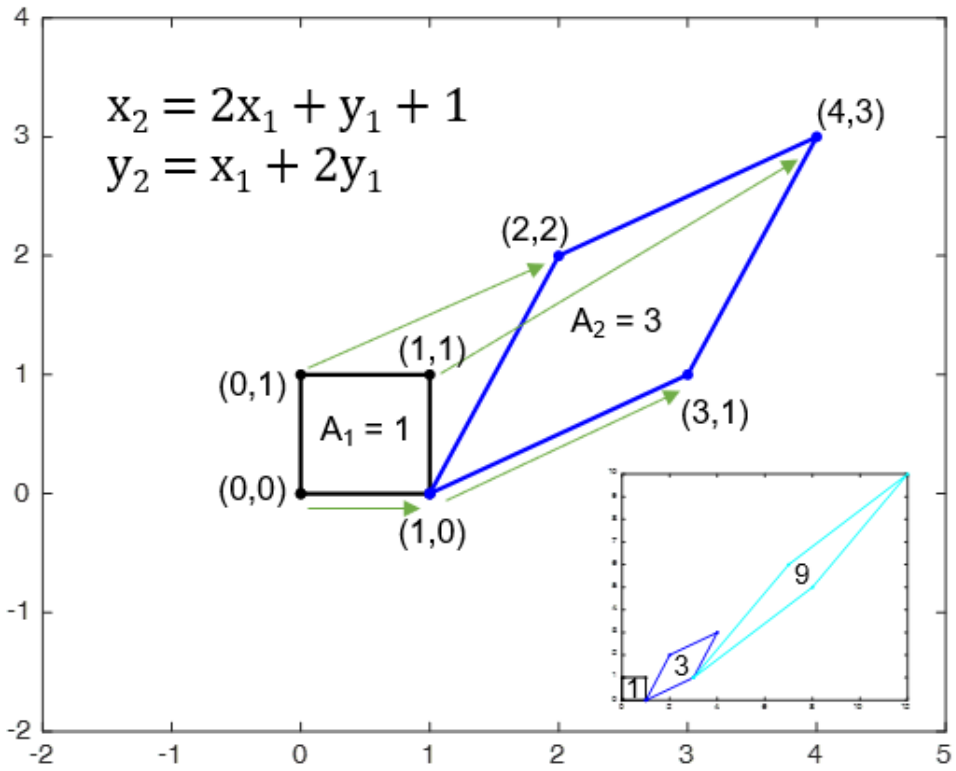


Figure 5.2: Application of a 2D linear transformation on the unit square. The Jacobian determinant of this transformation is 3, resulting in a three-fold increase in enclosed area upon each application of the transformation. The subplot shows an additional application of the transformation resulting in a further three-fold increase in the enclosed area from A_2=3 to A_3=9.

Considering the Jacobian determinant in the context of lung imaging, where the vector field u is given by the diffeomorphic (one-to-one, topology preserving) deformation field from the registration, there are three cases of interest:

1. A Jacobian determinant greater than 1 indicates that the transformation locally expands or dilates space (stretching)

2. A Jacobian determinant greater than 0 but less than 1 indicates local contraction or compression of space (shrinking)

3. A Jacobian determinant equal to 1 represents an isometric transforma-

tion, which preserves local volumes without expansion or contraction.

These are sometimes expressed in the more intuitive logarithmic form, as then stretching is positive, $det(J) > 1 \implies log(det(J)) > 0$, shrinking is negative, $0 < det(J) < 1 \implies log(det(J)) < 0$ and isometry is nil, $det(J) = 1 \implies log(det(J)) = 0$. As discussed previously, as lung expansion can be considered representative of ventilation, these determinant values therefore provide a measure of ventilation. Specifically the Jacobian acts as a pointwise measure of expansion/contraction in the deformation from the moving to the fixed image of registration.

Limited work has been carried out using the Jacobian as a ventilation measure. Kjorstad *et al.* found that the Jacobian showed good agreement with FD in a small cohort (n=10) of healthy volunteers and lung cancer patients (2D dynamic imaging), but with greater homogeneity which was attributed to the Jacobian being not directly dependent on the image signal and so being less susceptible to noise and cardiac frequency interference from smaller vessels [134]. Since then, a handful of other small studies have investigated the Jacobian in 3D. Chassagnon *et al.* used the Jacobian to quantify areas of 'marked shrinkage', where the amount of extreme local compression in the posterior lung was found to be lessened in the presence of fibrosis (n=7) [196]. Boucneau *et al.* used the Jacobian to carry out 3D MR spirometry, where the Jacobian time-derivative was used to generate flow-volume loops which were able to characterise the anisotropic and hysteric regional mechanical behaviour of the lung in a single healthy volunteer (n=1) [192]. Other recent work has applied similar analyses to Computed Tomography (CT) images to quantify biomechanical heterogeneity of the lung in Chronic Obstructive Pulmonary Disease (COPD), where it was found that the average Jacobian and coefficient of variation of the Jacobian correlates with Forced Expiratory Volume in 1 Second (FEV_1) ($p<0.001$) [197]. Other work parametrises lung volume changes using the Jacobian, such as via respiratory-α mapping based on an adapted sponge model [198]. This model has also been used as a tissue density correction factor in oxygen-enhanced MRI [45].

While these pilot studies have shown potential, there is a need for further work in determining robust Jacobian-related measures of ventilation with different registration algorithms, and establishment of how these relate to signal-based ventilation measures.

5.1.1.4 Aims

Using the same data as Chapter 4, Section 5.1 explores the following:

1. The impact of different registration approaches on VOxel-wise Lung VEntilation (VOLVE) parameters, including two registration schemes (conventional registration and group-oriented registration) and two registration algorithms (Demons-based registration and Forsberg registration) — Section 5.1.2.

2. The use of the Jacobian determinant from the registration as a marker of local expansion by incorporating the Jacobian into the VOLVE pipeline (in place of the registered signal) — Section 5.1.3

    - As secondary aims, the impact of registration image target choice and the feasibility of using the average Jacobian determinant across the whole lung as a measure of respiratory phase (in place of a navigator-type signal), were explored.

5.1.2 Investigating the Impact of the Registration Method on the VOLVE Analysis

5.1.2.1 Use of Jacobian to Determine Registration Method Feasibility

The MATLAB Demons (CR) algorithm has been used so far throughout this work, as at the time of commencement of this thesis, this was the only algorithm that had been used in published work for free-breathing ventilation quantification at 3 T [132]. However, recent work has found that an alternative registration package known as the Forsberg registration package leads to an improvement in registration quality and repeatability and

a drastic improvement in computation time compared to other methods for the registration of 3D data [92]. The aim of this work was to compare the performance of the Forsberg package with the Demons algorithm, and to assess any differences in registration quality, as well as any implications on quantitative ventilation parameters derived from VOLVE analysis.

An image registration pipeline was developed for registration of dynamic image series utilising the Forsberg registration package [190]. The polynomial-expansion method was used with the following parameters: elastic regularization (true), fluid regularization (true), start scale parameter = 3, iteration per scale = 6, fluid regularization parameter = 3, elastic regularization parameter = 3. A linear signal model was used with normalised cross-correlation and mean square error as the similarity metric between target and deformed moving images. The registration was performed without the use of a lung mask [92].

As an initial comparison between the registrations, Jacobian determinant maps were computed and visually inspected for both Demons and Forsberg CR. Figure 5.3 shows example Jacobian determinant maps for registration from end-expiration to intermediate lung inflation. Since the lung expands between these states, the Jacobian determinant values are expected to be > 1. The Demons CR registration shows several regions of apparent compression/shrinkage (det(J) < 1), especially in the upper left lung. These likely erroneous Jacobian determinant values may be indicative of inaccurate registration. In contrast, the Forsberg registration results in more physically reasonable Jacobian determinant values, with shrinkage only in areas bordering pulmonary vasculature which feature additional noise due to pulsatile flow. The Forsberg registration also produces more homogenous results, likely due to differences in the regularization parameters between the registrations, although since the MATLAB Demons algorithm used is proprietary and does not allow for regularisation fine-tuning, it is difficult to test this directly.

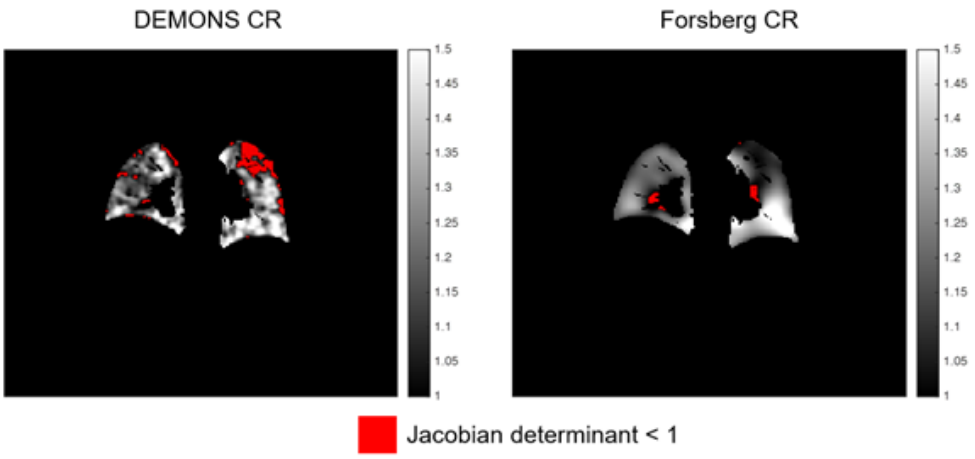


Figure 5.3: Jacobian determinant values for Demons (LHS) and Forsberg (RHS) conventional registration (CR) between end-expiration and mid-inspiratory states. Potentially erroneous shrinkage values are indicated in red.

From this initial assessment, the Forsberg package produced more physically reasonable registration values. This package also allows for flexibility in registration regularization terms and exhibits faster computation times. However, the impact of these different registration methods on quantitative ventilation measures remains unknown. This was therefore explored in this study. It was hypothesised that VOLVE metrics are independent of registration methodology.

5.1.2.2 Methods and Statistical Analysis

An investigation was carried out on the impact of the Demons and Forsberg packages, and the CR and GOREG registration schemes, on VOLVE functional metrics (using the same COPD data as Chapter 4). VOLVE analysis was performed according to Chapter 3.5 separately for Demons CR, Forsberg CR, Demons GOREG and Forsberg GOREG (see Section 5.1.1.2). Image processing (and statistical analysis) was performed in MATLAB R2022b on inexpensive hardware (AMD Ryzen 5 5600X CPU 3.7MHz, 16GB RAM). All registration implementations made use of parallelization across the 6 CPU cores.

The following VOLVE metrics were selected for subsequent statistical analysis: CC_V median and skewness and $Grad_V$ median and Peak Area Ratio (PAR) – see Chapter 3.4.3. Statistical tests were performed to compare the impact of the different registration methods on the VOLVE metrics, and to assess any difference in computation time. Like-registrations were compared, i.e., registrations with the same algorithm or same scheme. Hence, comparisons were made between:

1. Demons CR and Forsberg CR,

2. Demons CR and Demons GOREG,

3. Forsberg CR and Forsberg GOREG,

4. Demons GOREG and Forsberg GOREG.

The VOLVE parameter data were found to have a non-normal distribution using a Shapiro–Wilk test, and hence nonparametric tests were used. A two-sided Friedman's test with post hoc analysis with Tukey-Kramer correction was carried out to assess the extent of differences between the VOLVE parameters. The relation between pairs of VOLVE parameters was assessed via the Pearson correlation coefficient. Bland-Altman analysis was performed to quantify the mean differences. Finally, differences between the groups for each registration method were assessed by a Kruskal-Wallis test followed by post-hoc pairwise analysis with Dunn's correction for multiple comparisons. Since only like-registrations were compared (of the possible C(4,2)=6 combinations, C(4,1)=4 comparisons were made) a Bonferroni-corrected p value of $\frac{0.05}{4}$=0.0125 indicated a statistically significant difference.

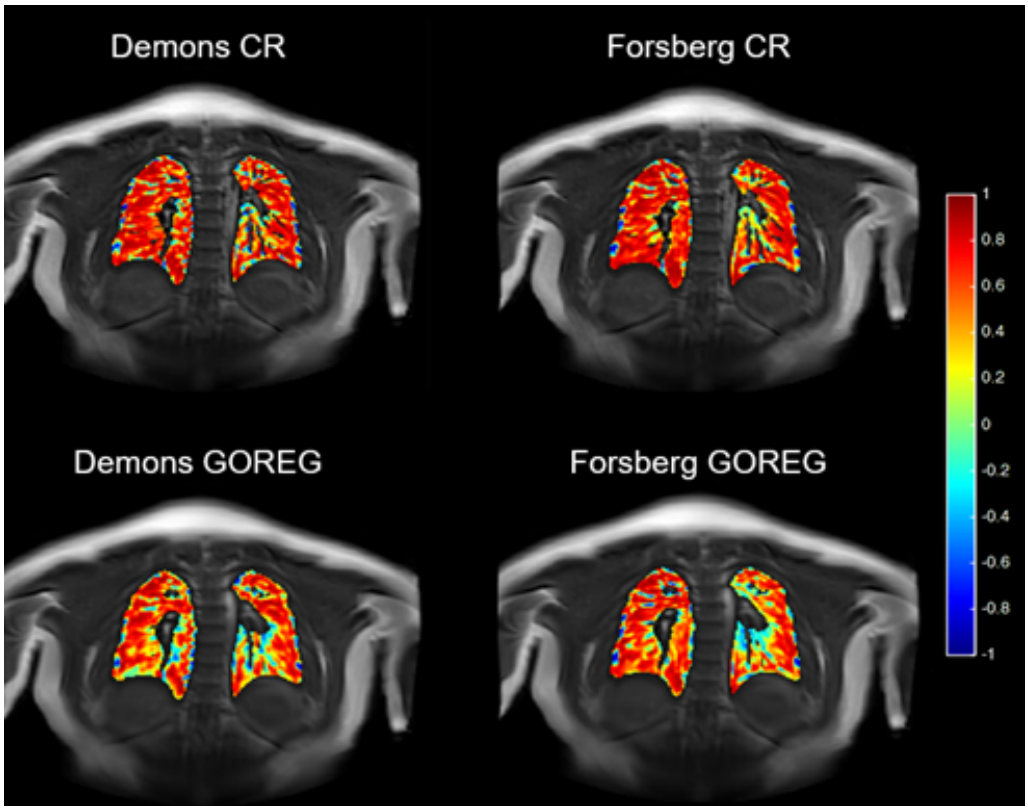


Figure 5.4: Example CC_V maps for a healthy individual (male, age 24) for the 4 compared registration methods. Note the overall similar of the parametric maps, with some reduction in CC_V near the main pulmonary vasculature for both GOREG maps.

5.1.2.3 Results

Figure 5.4 illustrates the visual similarity of CC_V for a healthy individual. Boxplots with VOLVE CC_V and $Grad_V$ metrics are shown in Figures 5.5 and 5.6, respectively, with p values across the groups for each registration method shown in Table 5.1 (within-registration method, across-group assessment of sensitivity to lung disease). All VOLVE metrics were significantly different between the groups for all registration methods. Comparison between registration methods is given in Table 5.2, detailing for each method/group the: median/IQR values, mean bias from the Bland-Altman analysis, and Pearson correlation between each compared pair. Overall, there was little difference in the VOLVE parameters between registration methods. Very strong and significant correlations (r range: 0.956-0.999) were observed

between both the Demons and Forsberg algorithms with the CR scheme. However, comparison between the CR and GOREG schemes revealed varied and generally weaker correlations, although many of these were not significant. Bland-Altman analysis indicated systemic bias in both CC_V and $Grad_V$ median parameters in some groups, but not in CC_V skewness or $Grad_V$ PAR, although these biases were relatively small (maximum relative bias of 14% for $Grad_V$ median).

The median (IQR) computation time in seconds for the different approaches are as follows: 40.7 (2), 29.4 (1), 60.5 (6) and 43.9 (3) for Demons CR, Forsberg CR, Demons GOREG and Forsberg GOREG, respectively. The median overall computation time for the 4 registration methods was significantly different ($p < 0.0001$) between the compared methods.

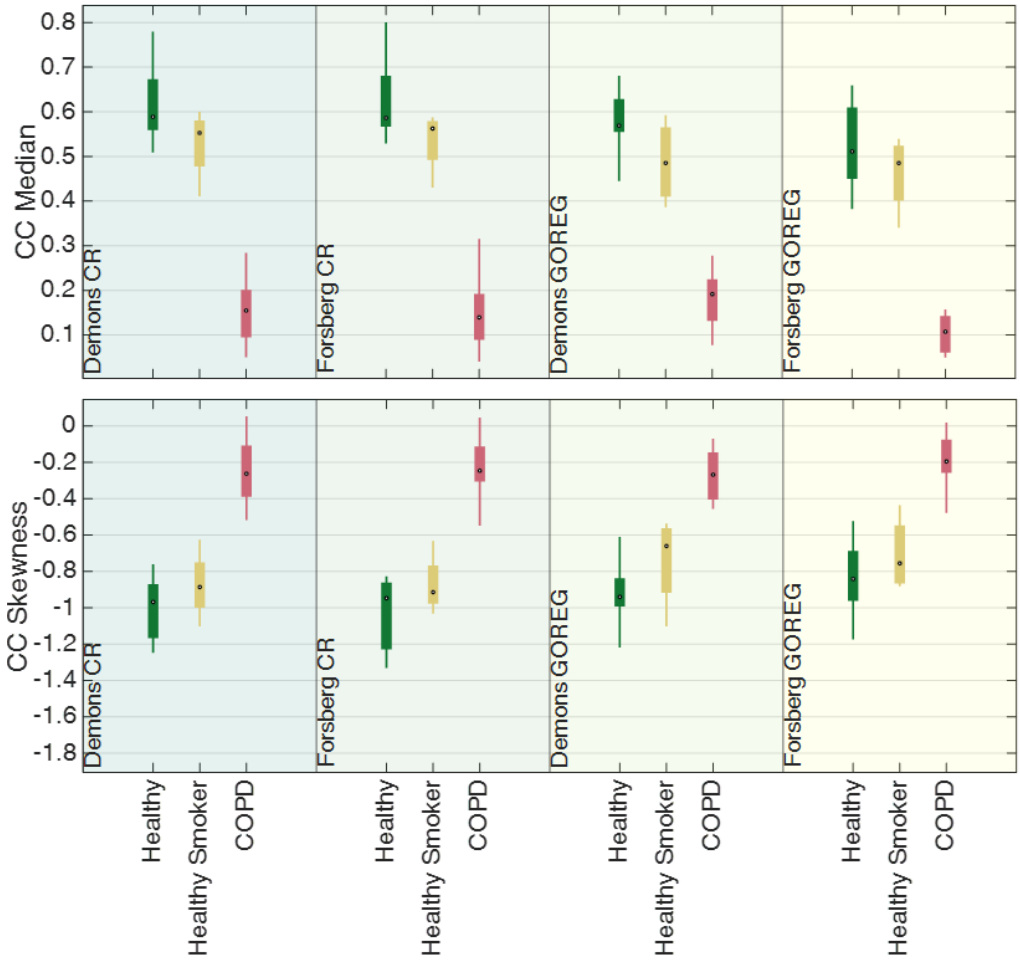


Figure 5.5: Boxplots showing CC_V, for the 4 considered registration methods (Demons CR, Forsberg CR, Demons GOREG, Forsberg GOREG), across the 3 study groups (healthy, healthy smoker and COPD).

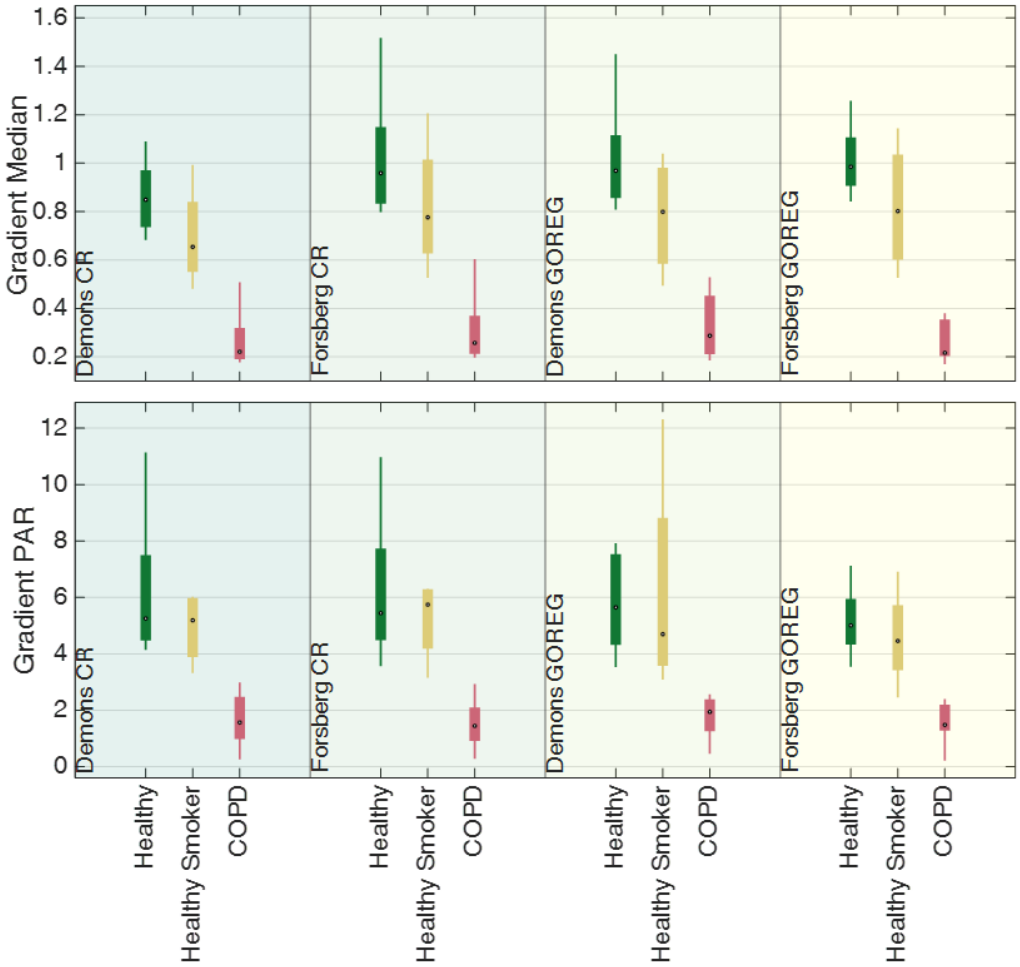


Figure 5.6: Boxplots showing $Grad_V$, for the 4 considered registration methods (Demons CR, Forsberg CR, Demons GOREG, Forsberg GOREG), across the 3 study groups (healthy, healthy smoker and COPD).

	A) Demons CR	B) Forsberg CR	C) Demons GOREG	D) Forsberg GOREG
CC Median	4.44e-04*	4.44e-04*	3.70e-04*	5.79e-04*
CC Skewness	5.49e-04*	5.79e-04*	4.44e-04*	6.36e-04*
Grad Median	8.36e-04*	8.93e-04*	0.0014*	8.92e-04*
Grad PAR	5.79e-04*	6.48e-04*	0.0021*	6.06e-04*

Table 5.1: within-registration method assessment of sensitivity to lung disease. Kruskal-Wallis p values are shown, with significant differences ($p<0.0125$, Bonferroni-corrected) marked with an asterisk (*). CR = conventional registration, GOREG = group-oriented registration.

Median (IQR)	**A) Demons CR**	**B) Forsberg CR**	**C) Demons GOREG**	**D) Forsberg GOREG**
Healthy				
CC Median	0.589 (0.11)	0.586 (0.11)	0.569 (0.07)	0.511 (0.16)
CC Skewness	-0.968 (0.29)	-0.947 (0.37)	-0.940 (0.16)	-0.842 (0.28)
Grad Median	0.849 (0.23)	0.959 (0.32)	0.969 (0.26)	0.985 (0.20)
Grad PAR	5.26 (3.03)	5.45 (3.25)	5.65 (3.22)	5.01 (1.62)
Healthy Smoker				
CC Median	0.552 (0.10)	0.563 (0.09)	0.485 (0.15)	0.485 (0.12)
CC Skewness	-0.886 (0.25)	0.914 (0.21)	-0.660 (0.36)	-0.755 (0.32)
Grad Median	0.654 (0.29)	0.776 (0.39)	0.799 (0.40)	0.802 (0.43)
Grad PAR	5.19 (2.09)	5.75 (2.11)	4.70 (5.25)	4.46 (2.31)
COPD				
CC Median	0.155 (0.11)	0.140 (0.10)	0.192 (0.09)	0.107 (0.08)
CC Skewness	-0.262 (0.28)	-0.246 (0.19)	-0.268 (0.26)	-0.195 (0.18)
Grad Median	0.221 (0.13)	0.258 (0.16)	0.287 (0.24)	0.216 (0.15)
Grad PAR	1.57 (1.49)	1.45 (1.19)	1.95 (1.13)	1.49 (0.92)
Mean bias ± (1.96*SD)	**A vs. B**	**A vs. C**	**B vs. D**	**C vs. D**
Healthy				
CC Median	-0.008±0.04	0.033±0.13	0.096±0.09*	0.056±0.09*
CC Skewness	0.035±0.16	-0.114±0.43	-0.223±0.43	-0.074±0.24
Grad Median	-0.124±0.09*	-0.127±0.10*	-0.042±0.14	-0.039±0.12
Grad PAR	-0.036±0.70	0.421±4.28	1.104±3.66	0.647±1.98
Healthy Smoker				
CC Median	-0.007±0.03	0.042±0.14	0.073±0.06	0.025±0.10
CC Skewness	-0.002±0.09	-0.135±0.53	-0.166±0.15	-0.033±0.39
Grad Median	-0.126±0.14	-0.088±0.20	0.003±0.15	-0.035±0.09
Grad PAR	-0.307±0.74	-1.266±6.56	0.667±2.01	1.626±5.07
COPD				
CC Median	0.005±0.04	-0.027±0.11	0.032±0.05	0.064±0.10*

CC Skewness	-0.019±0.11	0.022±0.25	-0.04±0.13	-0.081±0.26
Grad Median	-0.042±0.06*	-0.059±0.15	0.019±0.07	0.036±0.17
Grad PAR	0.146±0.51	-0.353±1.4	-0.048±1.38	0.451±2.38
Pearson r (p)	**A vs. B**	**A vs. C**	**B vs. D**	**C vs. D**
Healthy				
CC Median	0.973*	0.620	0.868*	0.882*
CC Skewness	0.974*	0.536	0.713*	0.804*
Grad Median	0.991*	0.980*	0.968*	0.972*
Grad PAR	0.989*	0.450	0.669*	0.794*
Healthy Smoker				
CC Median	0.994*	0.661	0.942	0.851
CC Skewness	0.976*	0.297	0.940	0.652
Grad Median	0.999*	0.914	0.963*	0.988*
Grad PAR	0.972*	0.733	0.828	0.924
COPD				
CC Median	0.974*	0.691	0.958*	0.719*
CC Skewness	0.956*	0.729*	0.926*	0.621
Grad Median	0.993*	0.838*	0.966*	0.825*
Grad PAR	0.966*	0.802*	0.616	0.274

Table 5.2: Comparison of the impact of different registration approaches on VOLVE metrics. Significant differences ($p<0.0125$, Bonferroni-corrected) are marked with an asterisk (*).

5.1.2.4 Discussion

These results show that the VOLVE metrics are sensitive to lung disease for all registration methods tested, and that these ventilation parameters are generally independent of registration method. This supports the hypothesis and demonstrates that different registrations can be performed without impacting the overall functional assessment. However, some significant biases were observed for both the CC_V and $Grad_V$ median parameters, implying that these parameters are to some extent a function of the registration method

chosen. This result disagrees with the findings of Ljimani *et al.* [199], who found no significant differences in FD ventilation parameters between image registration methods. Compared to the study presented here, Ljimani *et al.* used a similar image acquisition, but examined the use of different post-processing and different image registration algorithms, which may explain this discrepancy.

A possible explanation for the difference in results between the Demons and Forsberg registrations is the difference in definition of the deformation fields (diffusion model and polynomial expansion, respectively) or in the use of different regularization terms (Gaussian smoothing and elastic/fluid regularisation, respectively).

In terms of computation time, the Forsberg registration was found to be significantly faster than the Demons registration. The Forsberg package also allows for GPU support, which could dramatically reduce the required computation time further. This could be especially desirable for similar analyses in 3D, and for translating these and similar pipelines into clinical practice.

A limitation of this work is that only ventilation parameters have been explored. GOREG bins according to respiratory state, but the impact this has on perfusion quantification is unknown. Visually inspecting Figure 5.4, the GOREG maps appear to exhibit reduced (ventilation) correlation near main pulmonary vasculature in this subject, which could potentially impact perfusion assessment. It may be the case that different registration methods are appropriate for ventilation and perfusion assessment. The optimisation for registration for both V/Q assessment is to be the subject of future work.

Ultimately, any differences between registration methods should be considered through the lens of any clinical impact they impart. Given that the registrations presented all enable the distinction between disease and health, small deviations between these methods may not be clinically relevant. It may instead be more productive for the pulmonary ^{1}H MRI community to

agree on a registration method to be used ubiquitously, as to remove a layer of variability between analysis methods to allow for more of a like for like comparison. Given the results of this study and the study of Klimeš *et al.* [92], the Forsberg registration algorithm appears to be the best candidate in this capacity.

5.1.3 Application of the Jacobian Determinant in VOLVE

5.1.3.1 Assessment of Local Expansion

The primary aim of this work was to perform VOLVE analysis by comparing the Jacobian determinant (deformation-based), rather than the conventional registered parenchyma signal (intensity-based), with the global respiratory phase (navigator). Comparing the respiratory phase directly to the Jacobian, relating to expansion from the deformation field, assesses the motion-related change, rather than motion-induced, density-related signal intensity. This amounts to exploring the local, voxel-wise Jacobian as the dependent variable in VOLVE regression.

A secondary aim of this work was to test the impact of registration target image choice. So far, a registration target image of medium lung inflation has been used throughout this thesis. However, other respiratory states could be chosen, such as the end-expiration state, which is generally more stable in terms of respiratory depth. It was hypothesised that this deformation-based assessment is affected by the respiratory phase of the chosen registration target image. Hence, the choice of target image and the impact this has on the determined Jacobian parameters was explored. The details of this secondary investigation are shown in Appendix 5A.

A further aim of this work was to assess whether the global Jacobian determinant averaged across the lung can be used as a measure of respiratory phase (in place of a navigator-type signal), testing the hypothesis that the average Jacobian determinant across the entire lung corresponds to the lung-diaphragm navigator signal (i.e. exploring the whole-lung average Jacobian as the independent variable in VOLVE regression).

5.1.3.2 Methods and Statistical Analysis

VOLVE analysis was carried out with the Jacobian determinant time-course in place of the registered MR signal timecourse for each lung voxel – this is termed VOLVE-Jacobian analysis. This therefore involved comparison

of the Jacobian determinant timecourse for each voxel with the lung-diaphragm navigator signal. To simplify the comparisons, the VOLVE-Jacobian$_{CC}$, or J-CC$_V$, was chosen as the parameter to compare between registration approaches.

In addition to J-CC$_V$, Jacobian FV values were computed by characterising images as end-inspiration and end-expiration and averaging these states to determine a mean Jacobian map for both inspiration and expiration (as done previously [134]). In this case, since the Jacobian determinant provides a measure of expansion, and expansion is directly proportional to ventilation (rather than MR signal which has inverse proportionality), the fractional ventilation from the Jacobian is given by

$$V_J = \frac{\overline{J_{Insp}} - \overline{J_{Exp}}}{\overline{J_{Insp}}} \tag{5.6}$$

where the inspiration and expiration states in the equation are inverted when compared to the MR signal-based approach.

In this study, both the Demons and Forsberg CR schemes were assessed. In addition to these two registration methods, the impact of registration target image is explored by performing this analysis at both mid-cycle and end-expiration (Appendix 5A).

Statistical analysis was performed to assess the sensitivity of the Jacobian-based metrics to lung disease, and to compare the different registration methods and choices of target image. Sensitivity to lung disease was tested for by a Kruskal-Wallis test. A significance level determined by the Bonferroni-corrected p value of $\frac{0.05}{4}$=0.0125 was used.

Additionally, the mean Jacobian determinant over both lungs was computed and the Pearson correlation coefficient (R) with the lung-diaphragm navigator signal computed. Differences between the subject groups were assessed via Kruskal-Wallis test.

5.1.3.3 Results

A complete account of the metrics investigated is contained within Appendix 5A. Below are the results for the VOLVE parameters with the Forsberg CR registration method, registered to a mid-cycle target image.

Figure 5.7 shows example J-CC_V maps for Forsberg CR. Generally, in healthy subjects the maps are homogenous with very strong correlation values throughout the lung. In COPD participants, some areas show reduced correlation. No direct spatial relationship is seen between J-CC_V and CC_V. Figure 5.8 shows the median J-CC_V values across the lung parenchyma show significant differences between the healthy groups and the COPD group.

J-CC_V skewness was significantly different between groups for all registration methods (Appendix 5A). J-CC_V median and Jacobian-FV median were significantly different in 3/4 cases. Jacobian-FV skewness was not significant. This comparison between groups was repeated pairwise with the Wilcoxon rank-sum test (5A, Table 4) and these observations remained unchanged in the COPD group, but were not significant in the healthy smoker group.

Figure 5.9a shows a strong negative correlation for the mean Jacobian determinant plotted against the lung-diaphragm navigator signal, with this being seen for all subjects across all groups as shown in Figure 5.9b.

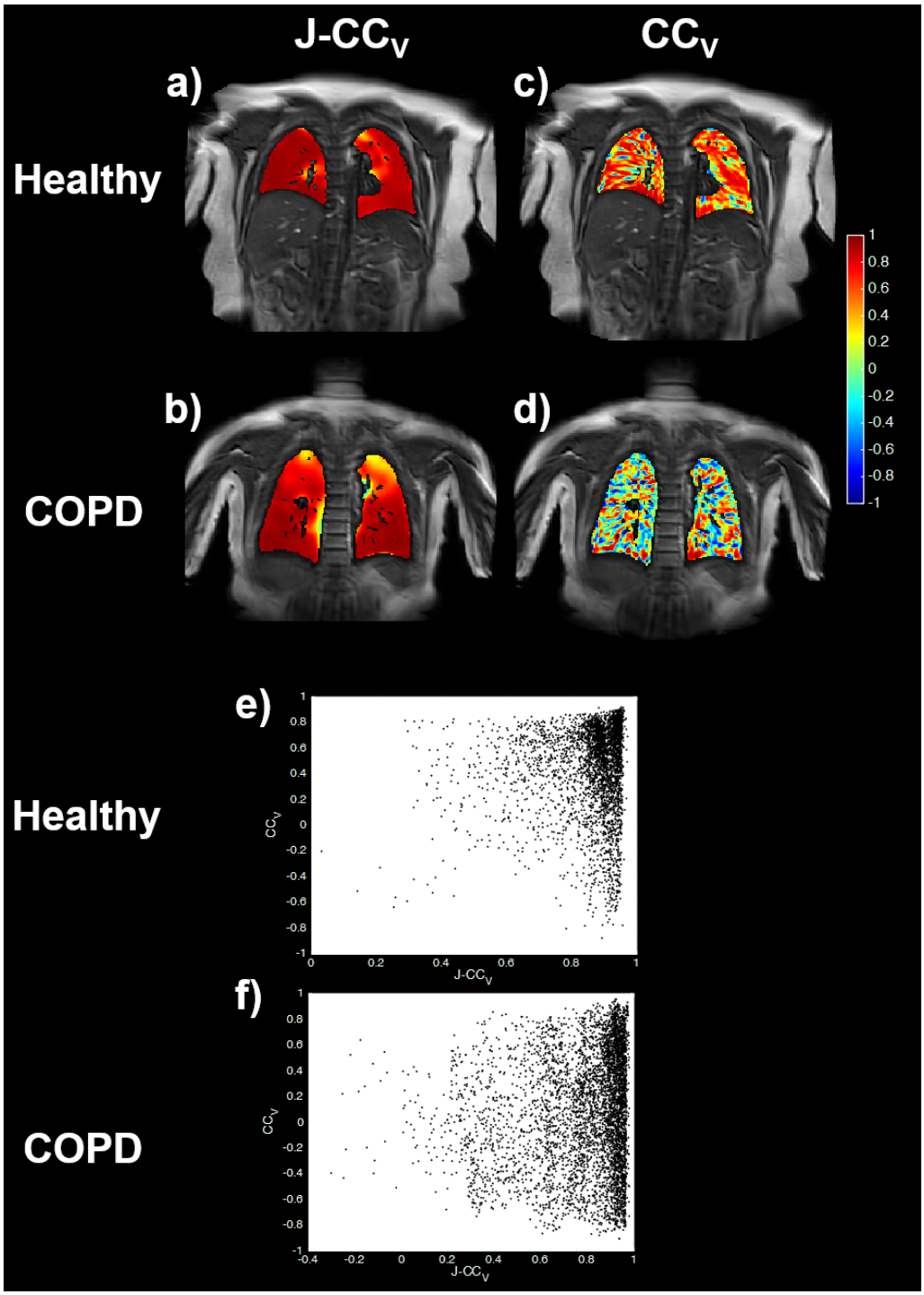


Figure 5.7: Example Jacobian ventilation correlation coefficient (J-CC_V), a)/b), and signal intensity-based CC_V maps, c)/d), in a healthy volunteer (age 24, female) and COPD patient (age 66, female, FEV_1=30%), respectively. J-CC_V was computed as the Pearson correlation coefficient voxel-wise between the navigator signal and the Jacobian determinant timecourse of each lung voxel. Scatter plots, e)/f), indicate no spatial relationship between J-CC_V and CC_V.

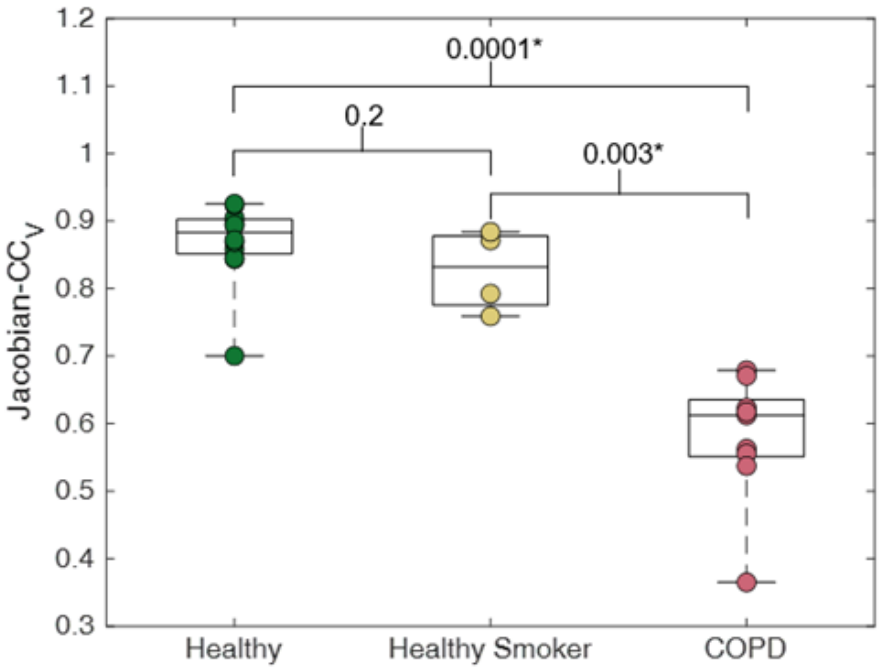


Figure 5.8: Boxplots showing J-CC$_V$ median values. p values (Kruskal-Wallis test) between the groups are shown, with significant differences ($p<0.05$) marked with an asterisk (*).

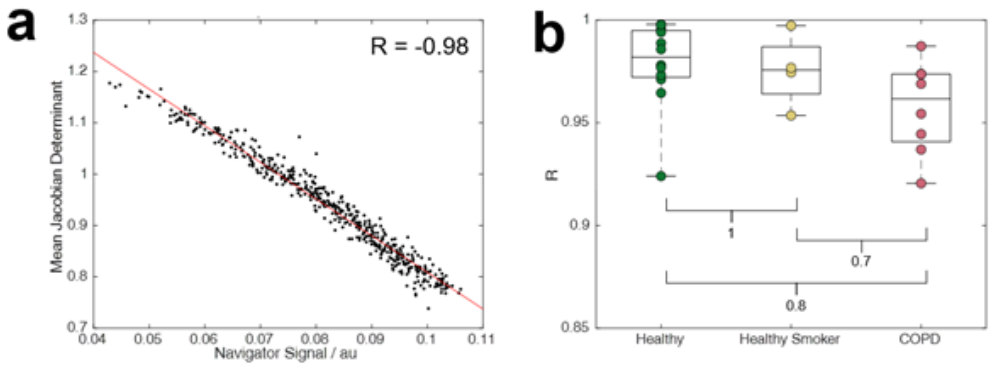


Figure 5.9: a) Scatter plot of the timecourse for the mean Jacobian determinant within the entire lung against the lung-diaphragm navigator signal, derived from an ROI across the right hemidiaphragm, for one healthy subject. A strong Pearson correlation coefficient (R) of -0.98 is shown. b) Boxplots show R for all subjects. p values (Kruskal-Wallis test) between the groups show no differences between the groups. Strong R values across all subjects are observed; R median (IQR) = 0.97 (0.03).

5.1.3.4 Discussion

This work demonstrates the feasibility of using the Jacobian determinant as a functional measure of localised expansion. The J-CC_V maps (Figure 5.7) provide an insight into how local expansion relates to respiratory phase. In healthy participants, there is generally a very strong relationship between the voxel-wise expansion and the lung-diaphragm navigator signal. J-CC_V is close to 1 except near the major pulmonary vessels, which could be due to errors in registration due to cardiac motion. Conversely, in COPD, some lung regions have considerably reduced J-CC_V. A significant difference in J-CC_V is seen between groups (Figure 5.8), indicating sensitivity to lung disease.

The reduced J-CC_V in COPD agrees with the previously presented work in which the intensity-based CC_V is reduced in COPD (Chapter 4.3). The deformation-based J-CC_V may give complimentary information to the intensity-based CC_V (Figure 5.7) and hence this analysis should be carried out in conjunction with signal intensity-based approaches, and structural imaging, to obtain a holistic picture of lung function.

The Jacobian-FV median was found to be sensitive to lung disease also (Appendix 5A), but with larger within-group variance and larger overlap between groups (indicated by larger p values for Jacobian-FV compared to J-CC_V). This can be explained by the FV approach only using two respiratory states and so being prone to bias from variations in respiration pattern, as detailed throughout Chapter 3. Interestingly, the Jacobian-based approaches were only significantly different between healthy never-smokers and COPD groups, whereas the signal-based approaches also delineated healthy never-smoker and healthy smoker groups. This could be due to the expansion-related Jacobian being sensitive to the different respiratory dynamics in the presence of hyperinflation (increased residual volume) in the COPD group.

It was noteworthy that Jacobian measures were generally more spatially uniform. This could be related to reduced sensitivity to noise compared to signal-based methods, where the Jacobian may be more robust to noise from

e.g. vessels or areas of emphysema. Alternatively, the uniformity could be related to signal misalignment due to misregistration resulting in e.g. smooth J-CC_V and heterogeneous/noise-like CC_V, where the Jacobian approach is blind to the registration error. This may be particularly problematic for small, low-signal pathophysiological features of interest that are effectively lost in the registration step.

In the comparison between registration methods and registration target image choice, there were little differences observed overall. All parameters that were significant for COPD with one of the methods was significant for them all, indicating that the sensitivity is not ultimately impacted by these choices. However, there were significant differences between the methods, in particular in the J-CC_V between Demons and Forsberg approaches. This can be explained due to the difference in definition of the deformation fields leading to differences in the computed Jacobian values.

Separately, the average Jacobian determinant across the entire lung area corresponded strongly to the lung-diaphragm navigator signal (Figure 5.9), with all groups showing a similar trend (and no significant differences between groups). The maximum correlation and smaller variance was observed for Fosrberg mid-cycle (Appendix 5A). Nevertheless, there was a tendency for a slightly weaker correlation in COPD, which could be due to the increased reliance on intercostal muscles for breathing effort. Hence the average Jacobian determinant could provide a more accurate measure of respiratory phase, as it is not dependent on the spatial position of a navigator ROI, and so is not biased by breathing style or asymmetric diaphragm excursion.

5.1.4 Conclusion

Using the Jacobian determinant timecourse in VOLVE analysis instead of the registered signal timecourse provides an assessment of local expansion which is sensitive to lung disease. Significant differences in the Jacobian-derived correlation coefficient, J-CC_V, between healthy and COPD groups indicates differences in local expansion, and may provide a lung functional marker. Further investigation is required into the quality of registration of different pathology and how this impacts the uniformity and sensitivity to noise of functional quantification via the Jacobian for robust clinical outcomes. This motivates future work to combine signal intensity-based and deformation-based functional assessments. In addition, the average Jacobian determinant across the lung has been demonstrated as an alternative measure of respiratory phase, which may be more robust in the event of asymmetric diaphragm excursion. Hence the Jacobian determinant is potentially useful as both the dependant and independent variable in VOLVE regression analysis for assessment of local expansion, or global respiratory state, respectively. It was found for both of these purposes that the Forsberg registration algorithm registering to a mid-cycle target image produced results with the least variance.

5.2 Investigating the Relationship between changes in Lung Volume and Lung-Diaphragm Navigator Signal

5.2.1 Introduction

While 3D full lung coverage is desirable for clinical application, especially in the cases of diffuse lung disease, recent methods have largely opted for 2D sequences in order to achieve the required temporal resolution to meet the Nyquist sampling rate for perfusion. Even if ventilation is primarily of interest, it is beneficial to achieve this fast sampling rate to avoid aliased cardiac signals obfuscating the ventilation signal. Although enabling fast enough sampling, the acquisition of 2D slices is somewhat problematic due to through-plane motion and a relatively long time required to acquire the entire lung volume. Another issue with single slice 2D acquisitions is that the ability to characterise lung volume (and change in lung volume) is confounded due to being limited to a single 2D plane, where only the lung slice area can be visualised directly. Single slice datasets therefore provide limited information about changes in the size/shape of the lung across the respiratory cycle. Alternatively, the apical-basal motion of the diaphragm can be used to determine a navigator signal, which provides an estimate of the respiratory phase of each image in the timeseries. This respiratory phase provides a surrogate for lung volume but does not measure it directly. This is problematic when computing functional parameters which rely on accurate characterisation of lung volume changes.

This is especially pertinent to functional assessments that are underpinned by the assumption that lung volume is related linearly to the respiratory phase as determined by this lung-diaphragm navigator signal. This principle was first introduced by Mai *et al.* who demonstrated significant differences in lung parenchyma Signal-to-Noise Ratio (SNR) at inspiration and expiration breath-holds [200]. Bankier *et al.*, then demonstrated a linear relationship

between Magnetic Resonance (MR) signal intensity and lung volume at 10 levels of lung inflation via spirometrically monitored MRI during breath-holds ($r = -0.56$, $p = 0.0001$) [129].

Dynamic 2D imaging or navigator-based approaches that use the apical-basal movement of the diaphragm as a proxy for lung volume change are limited to spatial coverage of a single slice of thickness 10-20mm in typical 2D sequences. During inspiration the lung volume increases and vice-versa on expiration; however, the exact nature of this relationship is important, and the impact of this on MR signal has not previously been explored in the context of free-breathing pulmonary ^{1}H MRI. In particular, the assumption that the lung-diaphragm navigator signal varies linearly with lung volume (e.g., in FV calculations) should be confirmed explicitly. This is especially important in patient groups who may have altered diaphragmatic movement (e.g., hyperinflated COPD patients). Lack of knowledge of the proportionality constant between the navigator signal and lung volume may be a confounder in the comparison of FV values between individuals.

This work aims to explore the relationship between the lung volume and lung-diaphragm navigator signal, assess the implications of this relationship for free-breathing ventilation measures, and presents a method for determining a correction factor between the measured volume and the navigator signal by performing fast volumetric imaging.

5.2.1.1 Motivation: Impact of Diaphragm-Volume Gradient on Diaphragm-Parenchyma Gradient

The diaphragm-volume gradient is the proportionality constant between the relative lung-diaphragm navigator signal change and lung volume change. A diaphragm-volume gradient not equal to 1 indicates that the navigator signal is a mischaracterisation of the volume change. Here, the diaphragm-volume gradient is also referred to as the volume correction factor, as the navigator signal can be transformed to a lung volume signal by multiplication with this proportionality constant, assuming linearity.

To demonstrate the impact of the diaphragm-volume gradient on the diaphragm-parenchyma gradient ($Grad_V$ functional parameter), a proof-of-concept simulation was carried out with an example healthy data set. In this simulation, $Grad_V$ maps were produced for varying diaphragm-volume gradients by multiplication of the navigator signal by a range of scale factors. Gaussian mixture-model fitting was performed and the peak area ratio (PAR) computed. Two sets of five maps were produced: firstly, for volume-gradient correction factors between 0.8 and 1.2 as a 'realistic' value range, and secondly for volume-gradient correction factors between 0.7 and 5 as an 'extreme' value range. Note that the observed values for volume correction factors derived below range between 0.9 and 1.2 (Section 5.2.3.2).

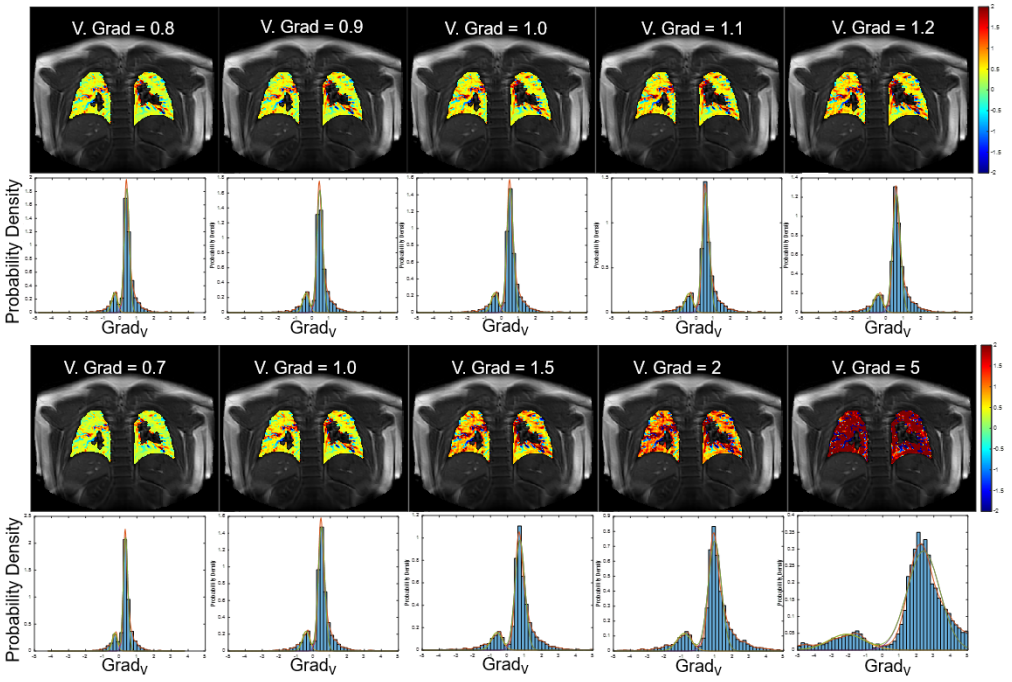


Figure 5.10: $Grad_V$ parametric maps and histograms with Gaussian mixture model fitting. Larger volume correction (lung-volume gradient, V. Grad, indicated on each map) lead to stretching of the $Grad_V$ histogram distribution.

The resultant maps and histograms are shown in Figure 5.10. It can be seen that volume correction values less than 1 compressed the gradient histogram, and values greater than 1 stretch the histogram. This broadening is clear for the larger values, e.g., correction factor = 5. It was found that

the PAR was independent of volume gradient, as show in Figure 5.11. This parameter therefore serves as a useful comparator between individuals and in groups with altered diaphragm mechanics as it is robust to asymmetry between respiratory phase and lung volume variation.

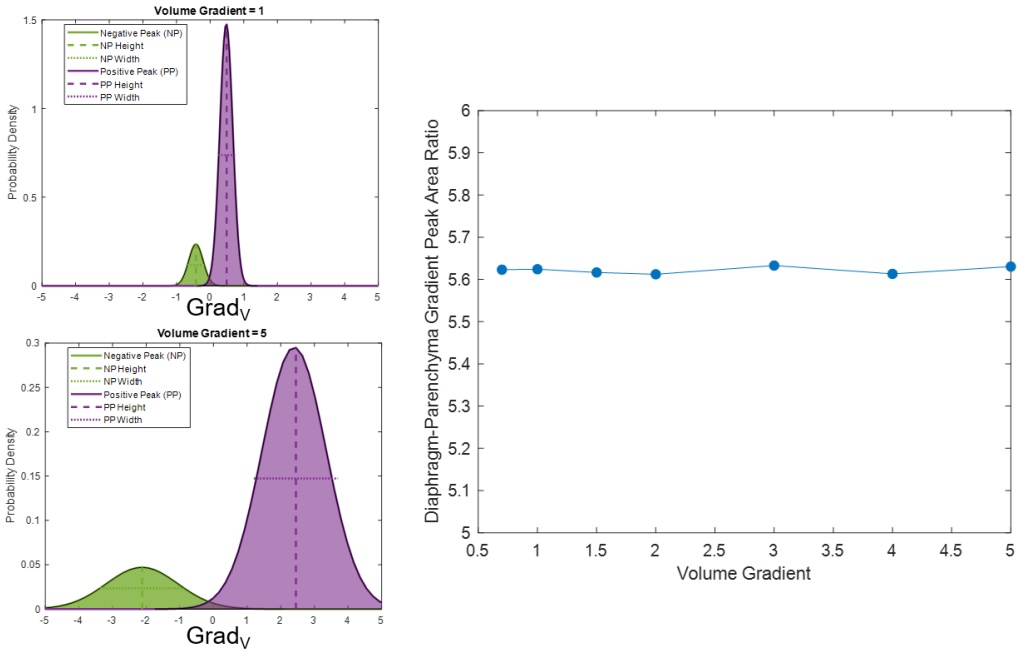


Figure 5.11: Illustration of Grad$_V$ histogram fits for volume gradient (correction factor) = 1 and 5, and independence of Grad$_V$ peak area ratio (PAR) of volume gradient.

While the gradient PAR is independent of volume gradient, the demonstrated change in the VOLVE parameter histogram distribution is problematic if a 1:1 relation is assumed between the navigator signal and the lung volume, as this will skew any subsequent quantitative histogram analysis. The following section details a method for measuring the relation between lung-diaphragm navigator and lung volume directly.

5.2.2 Aims

This section explores:

1. The use of 3D fast volumetric imaging to dynamically image respiratory cycles throughout free-breathing to investigate the relationship between

lung volume and the lung-diaphragm navigator signal — Section 5.2.3.

2. The use of multi-slice fast volumetric imaging to determine a lung volume correction factor (diaphragm-volume gradient) for use in VOLVE analysis — Section 5.2.4.

5.2.3 3D Dynamic Volumetric Acquisition Pilot Study [Adapted from Peggs *et al.* Proc. ISMRM; 2023; #4661]

It is hypothesised that measuring dynamic volumetric data will allow more systematic analysis of regional FV maps based on variations in proton density signal, as performed in PREFUL/FD analysis. To investigate this, a small pilot study was carried out in which fast volumetric monitoring of the lung was performed after optimisation of 3D Fast Field Echo (FFE) sequence. The purpose of this was to (1) monitor dynamic changes in lung morphometry and (2) investigate the relationship between lung volume changes and the lung-diaphragm navigator signal (which is used to characterise respiratory phase in e.g. PREFUL and VOLVE).

5.2.3.1 Methods

Data in this pilot study was collected as part of the FASTCOPD study (see Chapter 4.2.1), including a small additional subgroup of COPD patients diagnosed with alpha-1 antitrypsin deficiency (AATD). A subset of the study participants underwent additional fast volumetric scans with 12 people with COPD (of which n=5 diagnosed with AATD) and 4 healthy smokers (>10 pack-years smoking history but no respiratory symptoms or abnormal spirometry). All participants underwent ^{1}H MRI on a 3T Philips Ingenia scanner. A dynamic 3D Fast Field Echo acquisition (12 coronal slices, spatial resolution 1.8x1.8x14mm^3, TR/TE=1.9/0.58ms) was accelerated by compressed sensing (CS-factor=10) to achieve a dynamic scan time of 3.3 images/second. 400 dynamic images were acquired during 137 s of free-breathing.

Image analysis was performed using custom-written scripts in MATLAB R2022b (Figure 5.12). The lungs were segmented using a semi-automatic Chan-Vese active contours algorithm to determine a lung volume time course throughout tidal breathing [201]. The lung-diaphragm navigator signal was calculated by averaging the MR signal in an automatically segmented ROI spanning the right hemidiaphragm and peripheral right lung of a slice at the level of the descending aorta, matching the previous 2D single slice acquisition. Lowpass filtering (0.6 Hz) was applied to the navigator timecourse to remove cardiac signal fluctuations. The segmented lung volume and the lung-diaphragm signal were expressed as a percentage change relative to their median value, in order to evaluate relative change. A linear least-squares fit was performed on all time points to determine the gradient between lung volume and navigator signal, assuming a linear model.

Since in some cases the data demonstrated hysteresis, datapoints were characterised as either inspiration or expiration by the sign of the instantaneous gradient of the lung volume timeseries. Polynomial regression was performed separately for inspiration and expiration datapoints, and the difference in lung-diaphragm navigator signal at 50% lung volume between maximum inspiration and expiration during tidal breathing (representing functional residual capacity (FRC) plus half tidal volume) computed to assess the extent of hysteresis. Also, the maximum lung volumes from the fits were extracted and compared to Total Lung Capacity (TLC) values from Pulmonary Function Tests (PFTs) where available in COPD and AATD (full PFTs available for 7/12 patients) via the Pearson correlation.

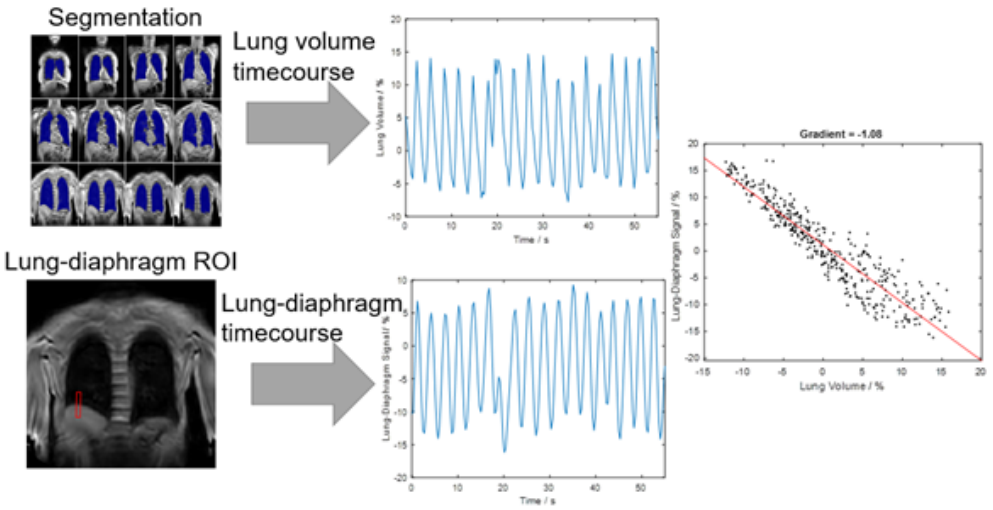


Figure 5.12: Overview of image analysis pipeline. A lung volume time course is generated by segmentation of a 3D scan with full-lung coverage dynamically acquired during free breathing. A lung-diaphragm time course is generated by averaging MR signal in a lung-diaphragm ROI. A scatter plot of the percentage change in these metrics is computed, and a linear least-squares fit performed to determine the gradient.

5.2.3.2 Results

Figure 5.13 shows the gradient from the linear least-squares fit between lung-diaphragm signal and segmented lung volume. A gradient of -1 corresponds to an equal percentage change between lung-diaphragm signal and lung volume. A gradient that is <-1 indicates an overestimation of the lung volume change, e.g., a gradient of -1.5 indicates that a lung-diaphragm signal change of 10% indicates a lung volume change of 15%. The median gradient values for the healthy smoker, COPD and AATD groups were -0.99, -1.38 and -1.45, respectively.

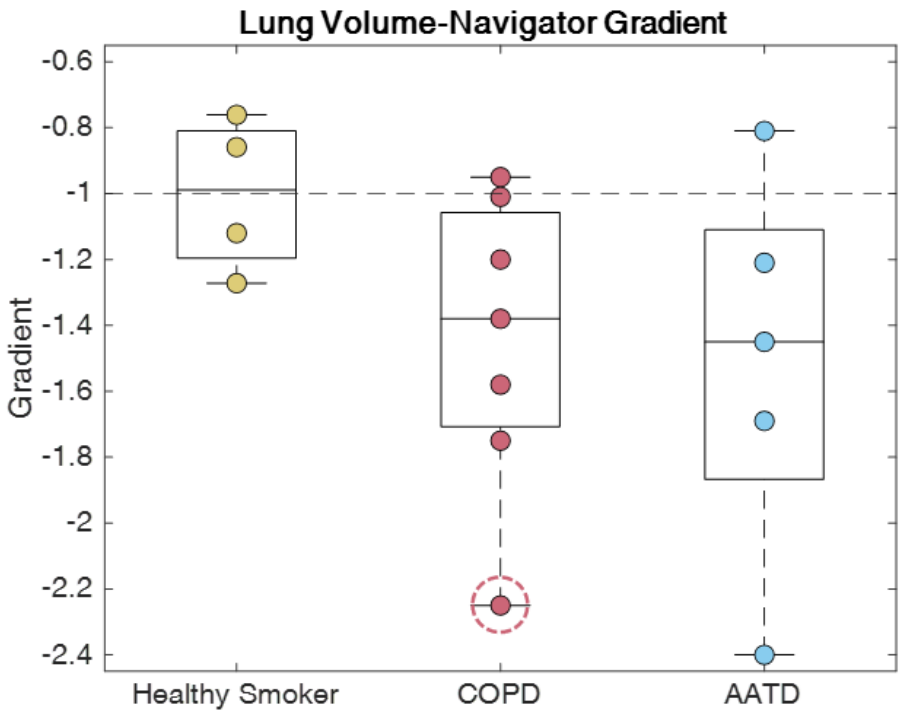


Figure 5.13: Boxplot showing the gradient of percentage change in lung-diaphragm signal versus lung volume for healthy smokers, COPD and AATD. The COPD patient displaying hysteresis in Figure 5.14A is indicated with a dashed circle.

Figure 5.14A shows an example plot showing the separation of inspiration and expiration phases for a participant with COPD, with corresponding polynomial fits for all subjects shown in 5.14B. 5.14C shows the difference in lung-diaphragm signal at 50% lung volume (Functional Residual Capacity (FRC) plus half tidal volume) between end-inspiration and end-expiration during tidal breathing, derived from the hysteresis fits. Median values close to zero are observed in all groups, with notable outliers in the COPD group. The MRI-dervied lung volumes correlated strongly with TLC values from clinical PFTs in the 7 patients that had this data available (r=0.95, p=0.012*).

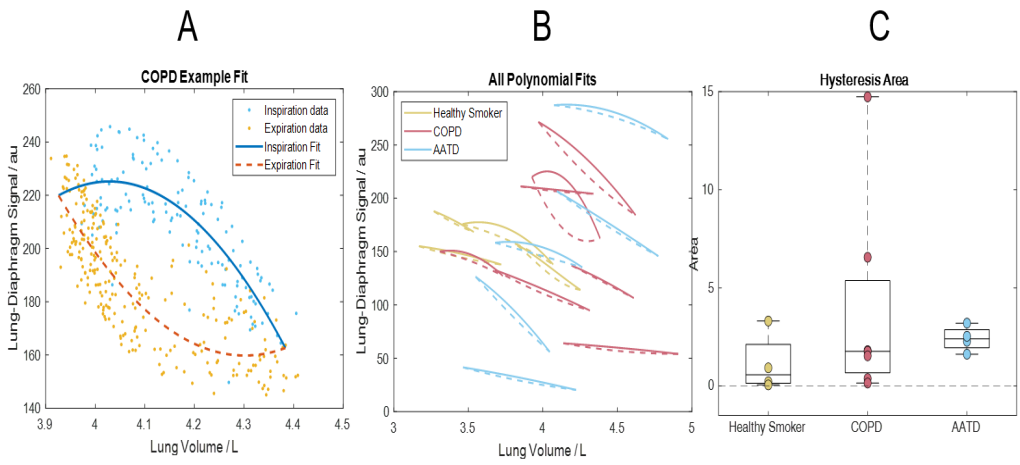


Figure 5.14: A) Example scatter plot of inspiration-expiration hysteresis for a participant with COPD. B) Plot of polynomials fits (quadratic and quartic) between lung-diaphragm signal and lung volume for each participant. Fits to inspiration datapoints are shown in solid lines and expiration with dotted lines. C) Boxplot showing the difference in diaphragm signal at 50% lung volume between inspiration and expiration during tidal breathing, derived from polynomial fitting to hysteresis.

5.2.3.3 Discussion: Implications for Ventilation Measures

Figure 5.13 shows that the navigator signal does not always accurately reflect the change in lung volume, especially in the COPD groups. The healthy group has a median gradient close to -1, but this deviates in some participants, particularly patients. In this situation, use of the diaphragm navigator signal when determining FV could result in mis-characterisation of volume changes, leading to variability in the estimates of regional ventilation. However, the gradient between the navigator and lung volume could be used as a correction factor to convert the navigator signal to lung volume for more accurate and repeatable analysis of ^{1}H lung ventilation (where an additional calibration scan would be required per individual).

Figure 5.14 also shows that assuming a linear relationship is inaccurate in some participants, and the presence and extent of hysteresis is variable between participants. In obstructive lung disease, conventional pressure/-

volume hysteresis loops are widened by a combination of airflow obstruction, decreased lung compliance, positive end-expiratory pressure and expiratory flow limitation. This results in shallow pressure/volume gradients during tidal breathing and in cases of more severe disease, active expiration is then required to complete the expiratory manoeuvre [202]. In the MRI data, the extreme hysteresis observed in one COPD subject may represent this effect. However, this was not demonstrated in other patients and further work is required to determine how this MRI-derived measure of hysteresis relates to conventional pressure/volume loops.

While the MRI-derived lung volumes measured via segmentation correlated strongly with TLC determined from PFTs, the MRI-derived volumes tended to slightly underestimate the volumes. This could be due to small errors with the lung segmentation, especially in the most anterior and posterior slices where some partial volume artefacts with the ribs occurred in some cases. The image segmentation could be improved in future by use of a deep-learning segmentation approach.

In conclusion, in some cases where the diaphragm movement does not relate directly to the lung volume, the presented methodology could be used to determine a correction factor to convert the navigator signal to lung volume, and itself be a functional biomarker of diaphragmatic mechanics.

5.2.4 Lung Volume Correction for VOLVE

As an alternative to the 3D acquisition presented in Section 5.2.3, a Multi-Slice 2D (M2D) sequence can be also used for volume quantification. This is potentially advantageous because the acquisition parameters can be aligned with the quantitative 2D single slice acquisition used throughout this work.

An M2D FFE acquisition was optimised, comprising of six sagittal slices (three in each lung with a slice gap of 10 mm) collected with a temporal resolution of 297 ms, with a total of 400 dynamic images acquired in 119 s. Sequence parameters were: TE/TR=0.62/1.9 ms, flip angle=18°, slice

thickness 11 mm, FOV = 350x350 mm, matrix = 192x192, phase partial Fourier = 0.75, and bandwidth 1528 (0.28 pixels) Hz/pixel, compressed sensing (CS-factor=4).

To obtain the conversion factor between the respiratory phase signal and lung volume for the 2D single slice FFE acquisition, image analysis was carried out similarly to the previously presented 3D approach (Section 5.2.3.1). The following post-processing steps were carried out:

1. Automated segmentation of the lungs (Chan-Vese active contours) throughout tidal breathing was used to generate a lung volume timecourse.

2. As for the 2D coronal time series, an automatically determined ROI spanning the right hemidiaphragm and peripheral right lung was used to determine a lung-diaphragm timecourse to measure the phase of respiration in a central slice. In this case, segmentation of the lungs to produce a binary mask was performed before averaging within the ROI, to ensure that the signals can be compared between the 2D and multi-slice 2D acquisitions (since the histograms then exhibit the same distribution), as shown in Figure 5.15.

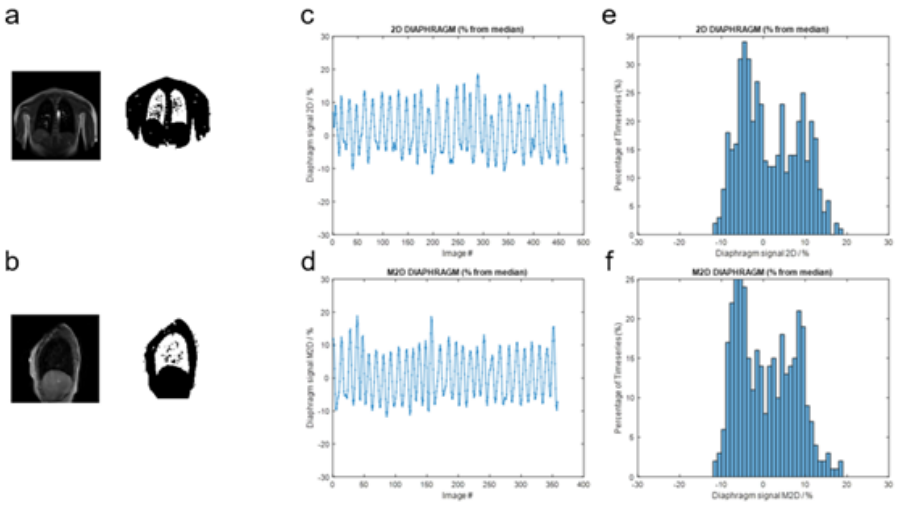


Figure 5.15: Schematic showing 2D coronal FFE (top) and multi-slice 2D sagittal FFE (bottom) acquisitions and signals. (a-b) shows an example image with and without thresholding, (c-d) shows the lung-diaphragm signal timecourses, and (e-f) shows the lung-diaphragm signal histograms.

3. The M2D navigator (respiratory phase) timecourse was then plotted against the lung volume timecourse, with both timecourses expressed as a percentage change relative to their own median. This step was important as it allows arbitrary signal intensity values to be comparable between acquisitions; the percentage change in navigator signal is compared to the percentage change in lung volume. A linear least-squares fit was used to determine the gradient between these quantities, assuming a linear model. This gradient was then used as the proportionality constant between the lung-diaphragm navigator signal and the lung volume.

The resultant gradients from the M2D sequence are shown for each group in Figure 5.16. It was found that for healthy participants, the average gradient was approximately -1 (median=-0.990, μ=-1.002, σ=0.085), showing that the diaphragm navigator is a good proxy for relative lung volume change. The COPD participants display a slightly decreased gradient, possibly owing to changes in diaphragm mechanics due to hyperinflation. Still, the lung-diaphragm signal provides a good approximation lung volume in this case (up

to 20% error in this data). For each subject, this gradient value can be used as a conversion factor to convert the lung-diaphragm navigator signal to a lung volume signal, when expressed as percentage change from the median volume. If the navigator signal is converted to volume using this relationship, and the parenchyma signals are normalised, then the VOLVE metrics may provide quantitative MR markers of lung function (as opposed to weighted parameters) that can be compared between individuals.

An alternative approach is to perform histogram matching by fitting a suitable function to both navigator histograms and subsequently applying a series of linear transformations to map the volumetric navigator signal to the 2D quantitative acquisition navigator signal. This was attempted with both gamma and Weibull functions, but the volumetric distributions were not well characterised by these functions which limited the accuracy of the fits and therefore the ability to match the histograms. It is therefore suggested that the correction factor is determined via the M2D lung volume-navigator gradient.

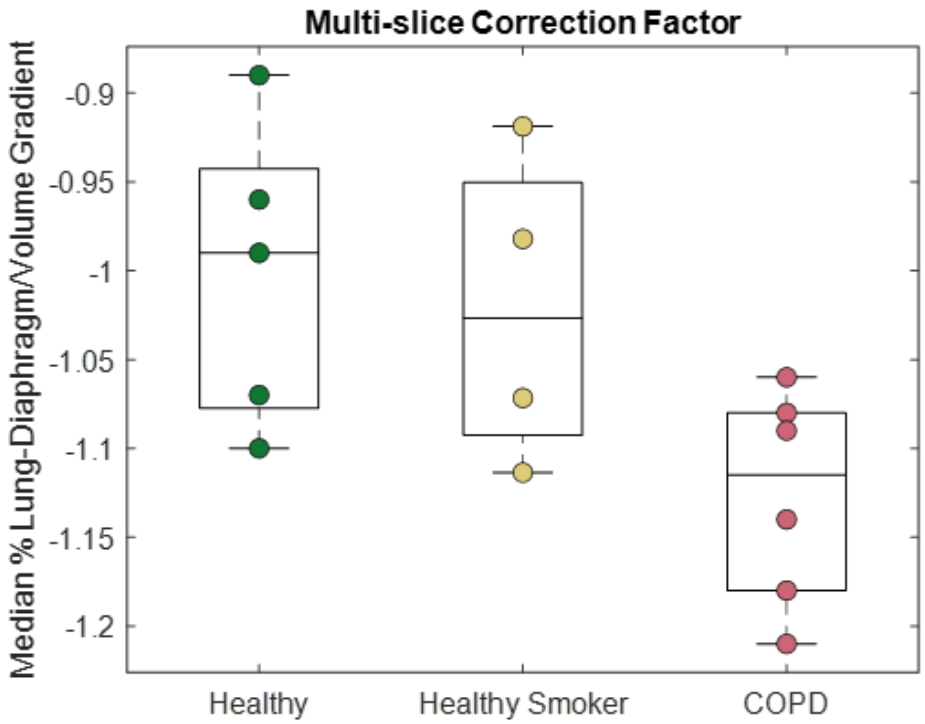


Figure 5.16: Boxplot showing the gradient of linear fit between percentage change in lung-diaphragm signal and percentage change in lung volume for healthy volunteers (median=-0.99, [25th,75th percentile]=[-1.08 -0.94]), healthy smokers (-1.03, [-1.09 -0.95]) and patients with COPD (-1.16, [-1.18 -1.08]). Note: this plot is analogous to Figure 5.13, but using an M2D acquisition in a different participant cohort.

5.2.5 Conclusion

This fast volumetric imaging approach provides methodology for conversion of the lung-diaphragm navigator signal to lung volume, potentially allowing for more accurate and repeatable analysis of ^{1}H lung ventilation. This also enables investigation into diaphragmatic mechanics, where hysteresis between change in lung volume and diaphragm motion is demonstrated in some cases. This could be used to quantify changes in inter-play between the diaphragm and chest wall, and forms an additional avenue through which probing of respiratory mechanics is possible.

5.3 Conclusion

This chapter has explored lung motion, with investigations into functional insights from image registration and the impact on registration method used on VOLVE-derived ventilation metrics. In addition, an investigation into the relationship between lung volume and the lung-diaphragm navigator signal was performed.

It was found that VOLVE metrics were generally independent of the image registration method used, with no significant differences in VOLVE metrics observed when using different registrations. The Jacobian determinant was incorporated into the VOLVE pipeline, and this was shown to produce measures that are sensitive to lung disease. Significant differences in the Jacobian-derived correlation coefficient between healthy and COPD groups indicated differences in local expansion that may provide a lung functional marker more directly related to deformation rather than density-related changes. Future work is needed to combine signal intensity-based and deformation-based functional assessments. In addition, the average Jacobian determinant across the lung was demonstrated as an alternative measure of respiratory phase. It was suggested that the Forsberg registration algorithm is a good candidate for future work, as it produces physically reasonable Jacobian values, has good repeatability and is computationally efficient.

The lung volume and lung-diaphragm navigator signal did not always exhibit a 1:1 relationship, especially in COPD patients. Generally a gradient of <-1 between these two quantities was observed, which indicates that the navigator signal overestimates the lung volume change. The presented fast volumetric imaging approach provides methodology for computation of a conversion factor, which could be used to quantify changes in inter-play between the diaphragm and chest wall, and forms an additional avenue through which probing of respiratory mechanics is possible.

Chapter 6

Investigation and Optimisation of VOLVE Acquisition

Abstract

This chapter investigates aspects of data acquisition for functional respiratory signals, including the evaluation and optimisation of VOLVE image acquisition parameters. Specifically, four factors are studied:

1. The effect of coil placement (with a device used to support the weight of the coil) on VOLVE metrics was investigated. It was found that the support device did not significantly impact the measured ventilation signals.
2. The impact of flip angle on the measured ventilation and perfusion signals. It was found that a flip angle larger than the Ernst angle may be optimal for the joint assessment of ventilation and perfusion.
3. The impact of temporal undersampling was investigated, where aliasing is demonstrated for temporal undersampling below the Nyquist limit.
4. The number of dynamic acquisitions required for adequate Signal-to-Noise Ratio (SNR) was also investigated. It was found that a reduction by half ($\frac{512}{2} = 256$ dynamic images) in the image timeseries gives rise to minimal changes in the obtained VOLVE ventilation parameters.
   4.1. This motivated a small pilot study in Cystic Fibrosis (CF) participants. Full lung coverage was obtained in a clinically feasible time period by reducing the number of acquired dynamic images of the 2D Fast Field Echo (FFE) sequence to allow an increase in the number of acquired slices.

Statement of Contribution

Zachary Peggs (ZP) performed all data analysis and collected the MR data. ZP, Susan Francis (SF) and Penny Gowland (PG) interpreted the data. SF, PG, Charlotte Bolton (CEB) and Ian Hall (IH) supervised the research.

6.1 Introduction

This chapter considers the optimization of the lung MRI scanning protocol for VOLVE data. The two key motivations for this were to enhance patient comfort and to minimise scan time for the efficient utilization of healthcare resources.

For individuals with established lung disease, extended periods of lying supine during conventional scans can be physically demanding and emotionally taxing. The optimisation of scanning protocols is not just a technical refinement, but minimises discomfort, reduces scan duration, and enhances the overall experience for patients. In minimising the time a patient is required to stay in a specific position, this will not only provide a more comfortable and tolerable imaging experience, but also reduce the likelihood of motion artefact. In parallel, a growing burden on radiology departments is manifested through extended scan times, leading to reduced throughput and increased demand on valuable resources. As the demand for lung MRI continues to grow, optimised scanning protocols are imperative for clinical translation. In particular, reducing scan duration contributes to a more streamlined and resource-efficient delivery of pulmonary imaging services.

The following chapter is composed of 4 sections, which investigate:

1. The impact of a coil support on the measured MR ventilation signal.

2. The optimum flip angle for the simultaneous assessment of ventilation and perfusion.

3. The impact of undersampling the VOLVE image timeseries, both temporally and by reducing the length of the dynamic image series.

4. The feasibility of acquiring full lung coverage, which is then tested in a small CF cohort using a shortened acquisition in a clinically feasible timeframe.

6.2 Impact of Coil Support and Relative Coil Displacement on Ventilation Signal

6.2.1 Introduction

The lung imaging in this thesis has been collected using the Philips integrated dStream FlexCoverage anterior transmit coil (flex coil in conjunction with the in-built posterior receive coils (Philips Medical Systems, Best, The Netherlands). The flex coil is 60 cm wide and easily covered the thorax of all examined participants. However, for some participants, such as those with compromised lung function who may be dyspneic, the additional pressure on the thorax/abdomen due to the weight of the coil may cause discomfort and exasperate breathlessness. A solution to this might be to use a plastic coil support that can be placed over a participant to support the weight of the coil. While this aids with participant comfort, it has the effect of keeping the coil stationary in space, and so it does not move in the anterior-posterior direction with thoracic cavity expansion. There is therefore the possibility of relative motion between the flex coil and the lungs during tidal breathing which may impact VOLVE analysis.

Relative motion between the flex coil and the lung could be problematic for functional assessments based on proton density measurements such as VOLVE. These assessments assume that local proton density reduces on inspiration and increases on expiration. However, if there is relative motion towards and away from the coil, such as movement towards the coil on inspiration and away from the coil on expiration, this could have the effect of increasing/decreasing the measured MR signal due to proximity to the coil, and impact the coil sensitivity profile, potentially confounding the proton density-based functional assessment. While this motion occurs in three dimensions, a simplifying assumption will be made that the anterior-posterior thoracic motion is predominant for breathing effort while supine.

6.2.2 Methods

To investigate the impact of using the plastic coil support (shown in Figure 6.1) on the MR signal of the lung, an experiment was conducted with three healthy volunteers with a gadolinium-based reference phantom placed next to their lungs. The gadolinium phantom was made by diluting 0.5 ml of Gd (0.1 mM) in 1 L of distilled water, following local laboratory standard operating procedures and risk assessments. This solution was contained within a bottle of dimensions L=8 x W=8 x H=24 cm which was placed under the right arm of the volunteer. 2D dynamic Fast Field Echo (FFE) datasets were acquired with the anterior receive coil with the plastic coil support and without the coil support, and also without the anterior receive coil (instead using only the in-built transmit/receive coils). Since the phantom had constant MR properties, and was stationary throughout the image acquisition, this provided a reference signal against which the lung-diaphragm navigator signal can be compared.

To investigate whether relative coil motion occurring due to respiration had any impact on MR signal, the following image analysis steps were performed:

1. The lung-diaphragm navigator signal was estimated to determine the phase of respiration, and act as a proxy for the relative distance from the coil in the presence of the coil support.

2. An ROI within the reference phantom was segmented and subsequent averaging performed to determine the reference phantom signal timecourse.

3. The Pearson correlation coefficient (CC) was calculated between the navigator signal and phantom reference signal on the data from three healthy participants and for each of the three experiments: with coil support, without coil support and without anterior receive coil.



Figure 6.1: Plastic coil support which can be used to support the weight of the anterior receive coil.

6.2.3 Results

Scatter plots of the reference signal timecourse from the phantom plot against the lung-diaphragm navigator signal are shown for the three volunteers for the three setups in Figure 6.2.

The mean ± standard deviation of the CC for the three setups is as follows: with coil holder, CC = -0.08 ± 0.2; without coil holder, CC = 0.09 ± 0.1; without flex coil, CC = 0.06 ± 0.1.

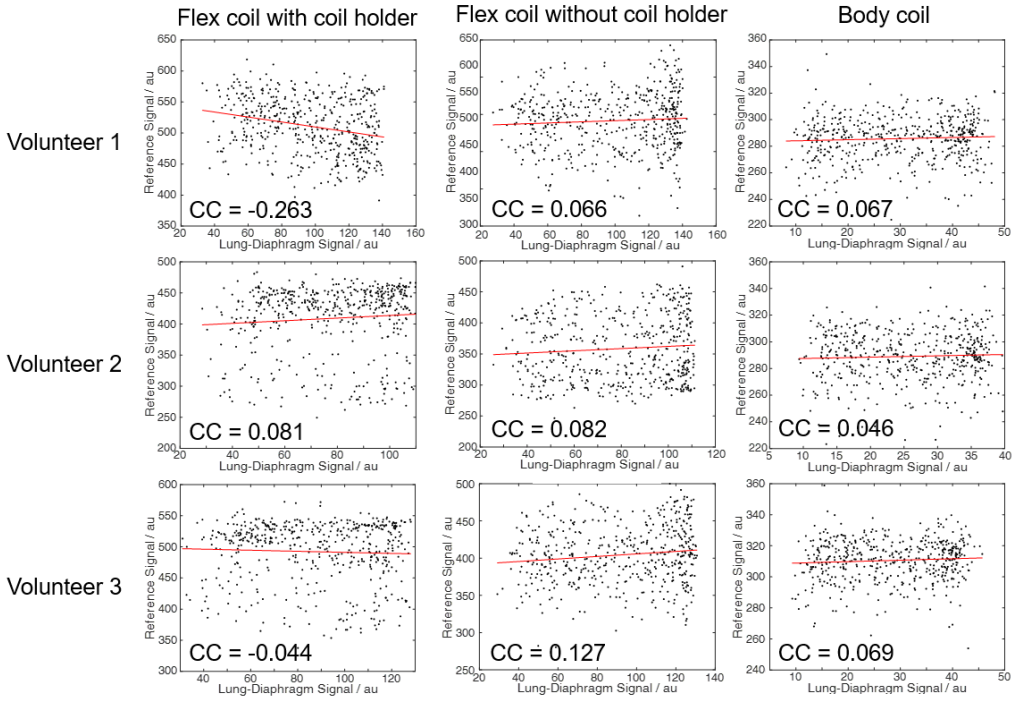


Figure 6.2: Scatter plots for the plastic coil holder investigation, showing the phantom reference signal plot against the lung-diaphragm navigator signal with linear fit (red line) and correlation coefficient (CC) in subplot titles. The LHS column shows plots with the plastic coil holder (with anterior FlexCoverage coil), the middle column shows without the coil holder (with anterior FlexCoverage coil), and the RHS column shows plots using only the built-in body receive coil rather than the FlexCoverage reciever coil and/or coil holder.

6.2.4 Discussion

There was no correlation between the phase of respiration and the reference phantom. Relative motion between the volunteer and the coil in the presence of the coil support did not appear to significantly impact the MR signal. The strongest CC value (-0.263) was observed in Volunteer 1 with the coil holder; this may suggest that depending on coil loading and subject

size, there could be a weak interaction owing to the presence of the coil holder (Volunteer 1 was smaller in the anterior-posterior dimension). This effect is small and does not account for the signal changes used for the quantification of lung function, as motion towards the coil (increasing sensitivity to signal) during inspiration (decreasing proton density-based signal) – and vice versa on expiration – have opposite implications for the MR signal. Hence any effect of relative motion will lead to a small reduction in the estimated ventilation. This could potentially be corrected for by obtaining a phantom-based reference signal as shown here. Further work could investigate the impact of coil sensitivity profiles varying over the respiratory cycle due to this relative motion and the impact this has on parallel imaging techniques.

In conclusion, the presence of a coil holder does not have a large impact on the obtained MR signal. There is potential for a weak coupling depending on participant size, which could be further investigated before widespread application in populations with smaller anterior-posterior size such as pediatrics.

6.3 Flip Angle Optimisation for Quantitative Assessment of Pulmonary Ventilation and Perfusion

6.3.1 Introduction

A major advantage of ^{1}H functional pulmonary MRI is the ability to simultaneously obtain lung ventilation and perfusion information in a single scan. Ventilation metrics are calculated from the local proton density variations in the lung parenchyma during respiration, while the time-of-flight effect provides signal from which to infer perfusion-related information.

The time-of-flight effect arises due to the flow of unsaturated blood into the imaging slice. This effect can be explained by considering an imaging volume to which a train of RF-pulses are applied during the imaging sequence, flipping the longitudinal magnetisation, M_z, into the transverse plane. For sequences with a long TR (generally TR>5xT_1), the longitudinal magnetisation recovers completely to its initial state, M_0. However, in the case of a sequence with a shorter TR the longitudinal magnetisation is tipped again before it has recovered to full/initial magnetisation, M_0. This creates a new steady-state magnetisation level, M_{SS}, lower than that of M_0. Hence the tissues contained within the imaging volume are partially saturated, with a reduced tissue Magnetic Resonance (MR) signal compared to blood outside of the slab which has fully recovered magnetisation [203]. This difference in magnetisation gives rise to the time-of-flight effect, where unsaturated (i.e. fully magnetised) 'fresh' blood from outside of the partially saturated slab flows into the imaging volume. This is known as flow-related enhancement [204]. Figure 6.3 shows an exemplar plot of MR signal against flip angle for spins that are unsaturated (i.e. 'fresh' blood) and that are in steady-state (i.e. lung tissue within imaging slice) for a spoiled gradient echo (FFE) sequence.

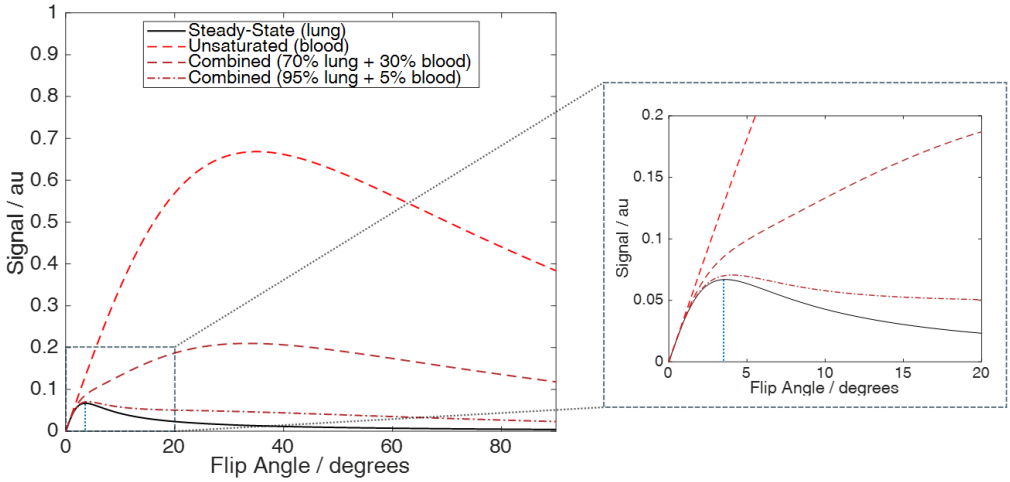


Figure 6.3: Exemplar plot for a spoiled gradient echo sequence of MR signal against flip angle. The tissue in the imaging slice has steady-state magnetisation (partially saturated) and so possesses a lower MR signal than the in-flowing, unsaturated blood. For increasing flip angle, the difference between the steady-state and unsaturated signals increases up to 35°. The Ernst angle for the steady-state is shown at 3.5° (blue line). Two combined curves with weighting 70% lung and 30% blood, and 95% lung and 5% blood, are shown to illustrate voxels containing both saturated lung tissue and unsaturated blood. Example plotted using Eqn. 2.30 with parameters matched to the FFE acquisition outlined in Section 3.2, and relaxation times from Table 1.1: T_1=1000 ms, T_2*=0.7 ms, TE=0.6 ms and TR=2 ms for steady-state and TR=200 ms for unsaturated.

This work investigated the impact of flip angle on lung ventilation and perfusion signals. Generally in steady-state, the flip angle that produces the maximum signal intensity for a given T_1 and TR is the Ernst angle, α_{Ernst}, which is given by Eqn. 2.31, $\alpha_{Ernst} = \cos^{-1}(\exp^{-TR/T_1})$.

Hence, for a typical 2D fast field echo (FFE) sequence with TR ≈ 2ms, and a relatively long lung parenchyma T_1 of ≈1000ms at 3T [205], α_{Ernst} ≈3.5°. Therefore typically low flip angles close to the Ernst angle of 3-5° are used. However, a low flip angle reduces the contrast between the lung tissue and the pulmonary vasculature, as the unsaturated blood has relatively lower signal

at these lower flip angles and hence the contrast is reduced (Figure 6.3). At very small flip angles this may impede the segmentation of the pulmonary vasculature from the parenchyma. By increasing the flip angle, the perfusion-weighting of the data can be increased due to a greater magnetisation of the unsaturated inflowing blood relative to the parenchymal steady-state magnetisation. The effect of flip angle on quantification of ventilation and perfusion from free-breathing proton MRI at 3 T was assessed in healthy individuals using VOLVE analysis.

6.3.2 Methods

5 healthy volunteers were recruited to undergo ^{1}H lung MRI on a 3T Philips Ingenia scanner. Images were acquired during free-breathing using a 2D fast field echo (FFE) sequence (TR/TE=1.9/0.57ms, 4.37 images/second) at a range of flip angles (α: 3°, 5°, 7°,10°, 14° and 18° with an additional α=12° collected for 2 of the 5 volunteers). A single coronal slice placed approximately 1 cm posterior to the heart was imaged, with 512 images collected in 117s. Three repeats were collected for each flip angle.

VOLVE analysis was performed in MATLAB (R2022b) for each flip angle dataset as described previously (Chapter 3.5). All images were registered to a mid-ventilation image using demons-based registration [149]. The thoracic cavity was segmented for each image series via seeded region growing to generate a whole lung mask. The whole-lung masks for each flip angle were split into parenchyma and vessel masks via adaptive thresholding with manual corrections if needed, and common masks across all flip angles were generated. To determine how well the masks could be created for the datasets at each flip angle, the Sørensen–Dice coefficient was computed to assess the spatial overlap between whole lung, parenchyma and vessel masks generated at each flip angle.

The mean signal, S_{Avg}, was computed voxelwise and averaged across the segmented masks (parenchyma, vessel and whole-lung) for each flip angle. The VOLVE ventilation correlation coefficient (CC_V) and perfusion

correlation coefficient (CC_Q) were computed by comparing the registered parenchyma timeseries values to a lung-diaphragm navigator signal, and an aorta or major pulmonary vessel-based cardiac signal timecourse, respectively. Median CC_V and CC_Q values were computed within each mask for each flip angle. For each subject, the median and interquartile range (IQR) of S_{Avg}, CC_V and CC_Q across the 3 repeats were computed and a linear model fit across all subjects.

6.3.3 Results

Figure 6.4 shows maps of S_{Avg}, CC_V and CC_Q. A trend for S_{Avg} and CC_V to decrease, and CC_Q to increase in the parenchyma with increasing flip angle was observed.

Figure 6.5 shows the CC_V and CC_Q within the parenchyma mask for all volunteers. For CC_V, the maximum correlation was seen at 3° and this decreased with increasing flip angle. CC_Q increased with increasing flip angle until reaching a plateau at ≈10°-14°.

Figure 6.6 shows the matrix of Dice coefficients between each of the masks generated at each flip angle. Spatial overlap was generally >0.9 for the parenchyma (mean ± std = 0.95 ± 0.03) and whole lung (0.97 ± 0.02) masks, with the vessel (0.82 ± 0.1) masks showing slightly lower overlap. Figure 6.7 shows the mean MR signal, S_{Avg}, as a function of flip angle for the parenchyma and vessel masks. Signal within the parenchyma decreased with increasing flip angle (Spearman r=-0.99, p=0.003), whilst the vessel signal was relatively constant for $\alpha \leq 10°$.

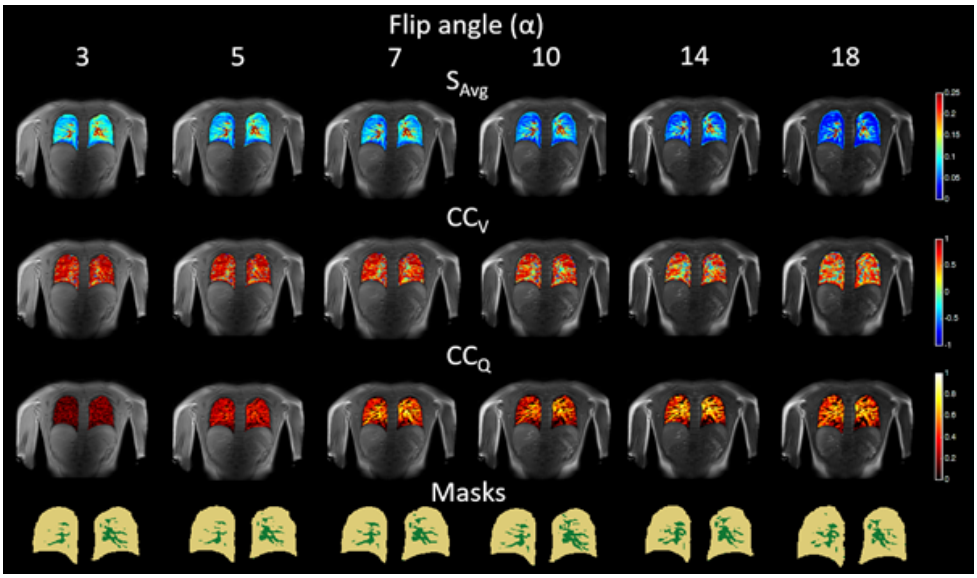


Figure 6.4: Example maps of S_{Avg}, CC_V (ventilation correlation coefficient), and CC_Q (perfusion correlation coefficient) for a healthy volunteer (age 24, female) across flip angles, and associated parenchyma (yellow) and vessel masks (green). On increasing the flip angle, S_{Avg} and CC_V tend to decrease, while CC_Q increases.

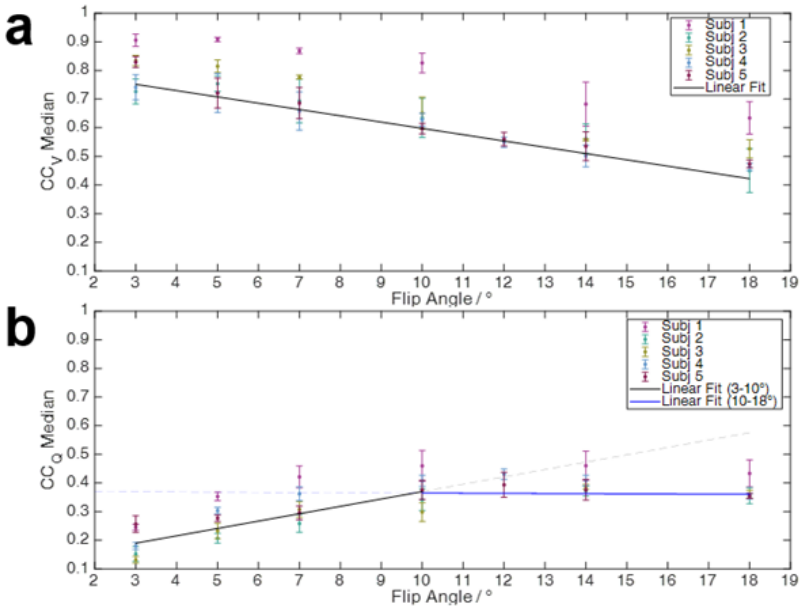


Figure 6.5: Median and interquartile range (IQR) values for a) CC_V (fit R^2 = 0.95) and b) CC_Q (fit R^2 = 0.89 between 3° and 10° and fit R^2 = 0.68 between 10° and 18°) computed within the lung parenchyma mask. CC_Q is approximately 50% lower than CC_V. NB =12° was only collected for 2/5 subjects.

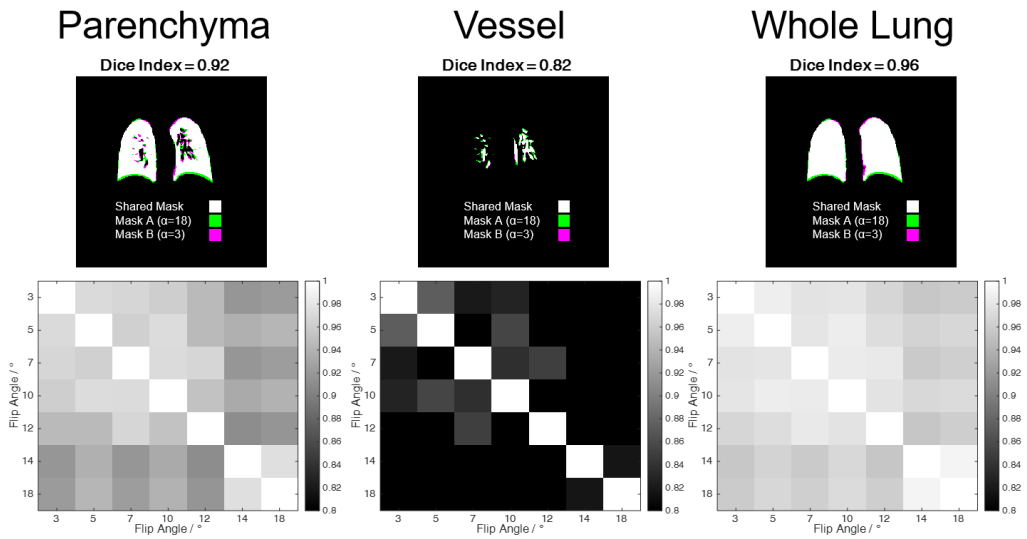


Figure 6.6: Spatial overlap of the masks is shown between flip angle α = 3° and 18° (top) with small deviations at the boundary of the main pulmonary vessels or at the level of the diaphragm due to small differences in respiratory phase in the chosen registration target images. Dice coefficients of the parenchyma, vessel and whole lung masks are shown (bottom). Agreement of 0.9 or greater is observed for the parenchyma and whole lung masks, and of 0.8 or greater for the vessel masks. Note the top row of images corresponds to the bottom left / top right element of the below matrix.

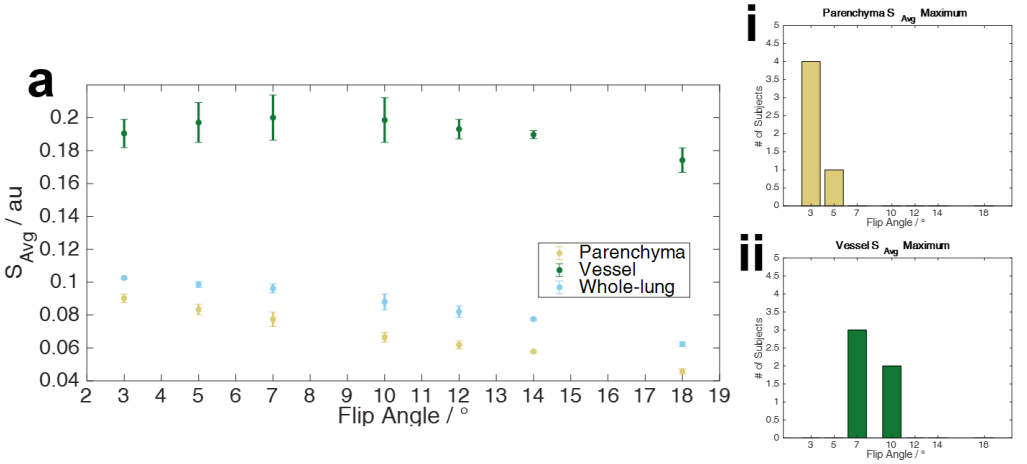


Figure 6.7: a) Average signal in whole-lung, parenchyma, and vessel masks for a single volunteer. Flip angle of maximum S_{Avg} across all subjects for the i) parenchyma mask and ii) vessel mask. The maximum S_{Avg} in the parenchyma and vessel masks occurred at 3-5° and 7-10°, respectively.

6.3.4 Discussion

This work explored the impact of flip angle on ventilation and perfusion signals obtained from free-breathing proton lung MRI. While low flip angles close to the Ernst angle for the parenchyma elicit a strong CC_V, this results in a lower CC_Q (Figures 6.4 & 6.5). To trade-off the estimation of both parenchyma ventilation and perfusion signals a flip angle higher than the Ernst angle (α_E =3.5°) of α=7-12° may be appropriate.

The reduced contrast between lung parenchyma and pulmonary vasculature at lower flip angles did not impede the segmentation of the vessel/parenchyma ROIs (Figure 6.6) using adaptive thresholding (this could alternatively be achieved using the voxel-wise cardiac power spectrum). The reduced Dice coefficient observed in the vessel mask is likely due to the registration target images having different cardiac phases. S_{Avg} in the vessel mask was generally more variable than the parenchyma masks for all values of α (Figure 6.7), since as expected the vessels had a larger dynamic signal range. S_{Avg} in parenchyma was consistent between repeats for all volunteers.

The need for a trade-off between obtaining a strong ventilation signal whilst not suppressing the parenchyma perfusion signal is demonstrated. Overall a flip angle α=7° is recommended for a strong V/Q signal and high S_{Avg} across the lung. Verification in lung disease is required, such as in diseases where parenchyma T_1 may be increased [22].

6.4 Temporal Undersampling and Length of Dynamic Image Series

6.4.1 Introduction

It is important to acquire dynamic images with adequate temporal resolution as to avoid aliasing of the cardiac signals. The Nyquist frequency varies between individuals, dependent on heart rate. The temporal resolution of the acquired image series throughout this work is 229 ms, equivalent to 4.3 Hz, and so is able to resolve cardiac signal variations occurring at 2.15 Hz (130 Beats per Minute (BPM)). The aim of this section is to investigate the feasibility of temporal undersampling and reducing the length of the dynamic image series in order to either collect multiple slices concurrently, or reduce the image acquisition time, respectively, without jeopardising the sensitivity of the VOLVE functional assessment.

6.4.2 Methods

The impact of sampling at a reduced frequency is investigated here by retrospectively temporally undersampling the data by a factor of 2, and thus resolving signal variations at approximately 1.075 Hz (65 BPM). This is referred to as the 'undersampled' dataset. In addition to temporal undersampling, the impact of halving the number of time points analysed (while maintaining sampling rate) was investigated. This reduces the number of respiratory (and cardiac) cycles sampled, but requires a shorter image acquisition time, which may be beneficial in a clinical setting. This is referred to as the 'short' dataset. Figure 6.8 illustrates the sampling schemes for the undersampled and short datasets. Both the datasets contain half the amount of data (256 images) compared to the fully sampled data.

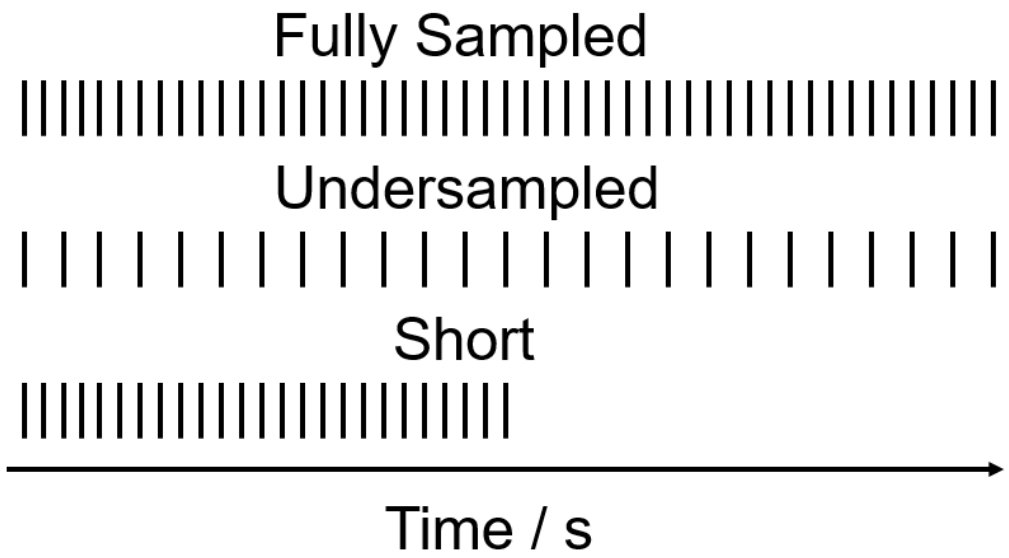


Figure 6.8: Sampling schemes for the undersampled and short datasets. The fully sampled dataset has a temporal resolution of 4.3 Hz and is made up of 512 images. The undersampled data is temporally undersampled by a factor of 2, reducing the temporal resolution to approximately 2.15 Hz. The short data has only the first half of the dynamic image series and so is made up of the first 256 images.

VOLVE analysis was performed on the FASTCOPD data presented in Chapter 4. The first 10 images were discarded to ensure the signal had reached steady state, then VOLVE analysis was performed to determine the ventilation correlation values, CC_V. Within-group comparisons were made between fully sampled VOLVE metric distributions and each undersampled method (e.g. healthy CC_V fully sampled was compared to healthy CC_V undersampled and the healthy CC_V short dataset separately) via the Wilcoxon rank-sum test.

6.4.3 Results

Figure 6.9 shows the CC_V for fully sampled data, and temporal undersampling factors of 2 and 3. Visual inspection of these maps reveals little change between full sampling and undersampling by 2, but marked reduced correlation values when undersampling by 3. This can by explained by

aliasing of the MR signal since a sampling frequency of 1.4 Hz is below the Nyquist limit for the cardiac frequency of this subject (70 BPM = 1.17 Hz, requires sampling rate of 2.34 Hz). Given that many subjects will have a faster heart rate than this, necessitating even faster sampling, 3x undersampling was not investigated further.

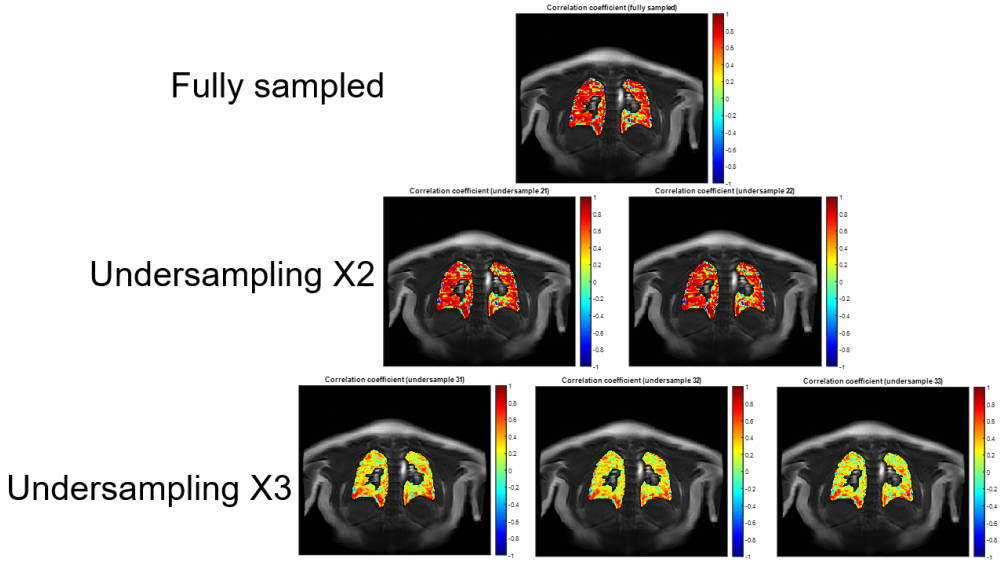


Figure 6.9: Example VOLVE CC_V maps for fully sampled data (acquisition rate 4.30 Hz), x2 undersampling (acquisition rate 2.15 Hz) and x3 undersampling (acquisition rate 1.43 Hz). Visual similarity is observed between fully sampled and x2 undersampled data, but not for x3 undersampled data.

Figures 6.10 & and 6.11 show boxplots of CC_V and $Grad_V$ for both temporal and dynamic undersampling. The general trend across the VOLVE metrics is that the short datasets (half the number of dynamic acquisitions) produces VOLVE metric distributions similar to the fully sampled data. In contrast, the temporally undersampled data (half the image acquisition rate) showed generally altered distributions. In particular, the spread of the metric distributions is increased (e.g. healthy CC median IQR is similar between fully sampled (0.093) and short datasets (0.088), but increases in the case of temporal undersampling (0.154)), suggesting increased variability and reduced sensitivity. This is unsurprising given the extent of aliasing that occurs at this reduced temporal resolution. However, the observed

distributions were not significantly different from the fully sampled data within groups for either undersampling scheme (Table 6.1).

It can be concluded that while halving the number of dynamics has little impact on VOLVE metrics, halving the temporal resolution increases variability due to aliased cardiac signals. This suggests that fewer dynamic acquisitions could be collected to reduce image acquisition time. Further work is required to determine the optimum number of images required for reliable convergence of VOLVE metrics, and how this is impacted by temporal and spatial sampling schemes, as well as other acquisition parameters such as flip angle. A potential downside in reducing acquisition time in this manner is that if the participant moves, coughs or undergoes any bulk motion which corrupts the acquired data and so needs to be discarded, only a small number of respiratory cycles may remain for the VOLVE fitting routine. Acquiring more data allows for a level of sampling redundancy to avoid this. Further work is needed to explore the impact of reduced dynamic sampling in a disease group — this is explored in the following section.

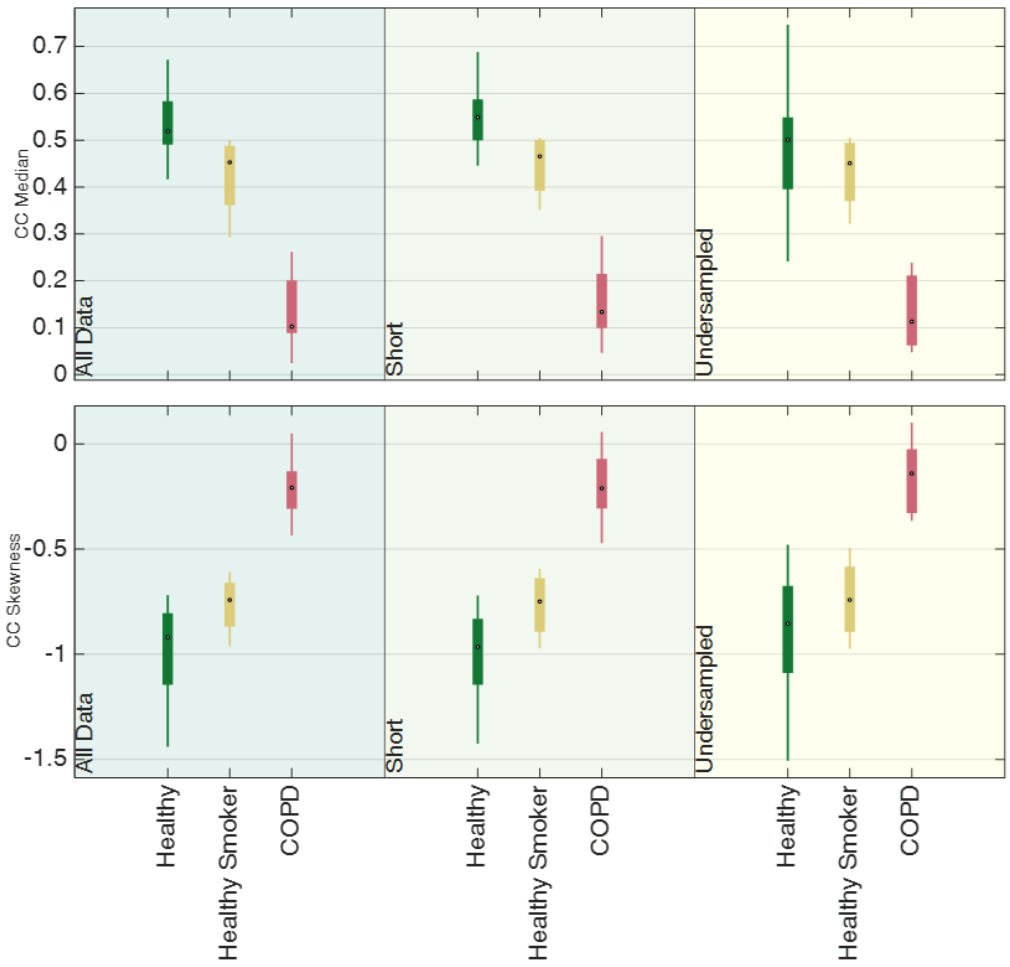


Figure 6.10: Boxplots showing VOLVE ventilation correlation coefficient (CC_V) median (top row) and skewness (bottom row). Shown are results for all data (full 512 image series), 'half dyns' where the second half of the 512 image timeseries was discarded, and 'undersample' where every other image in the timeseries was discarded (2X temporal undersampling).

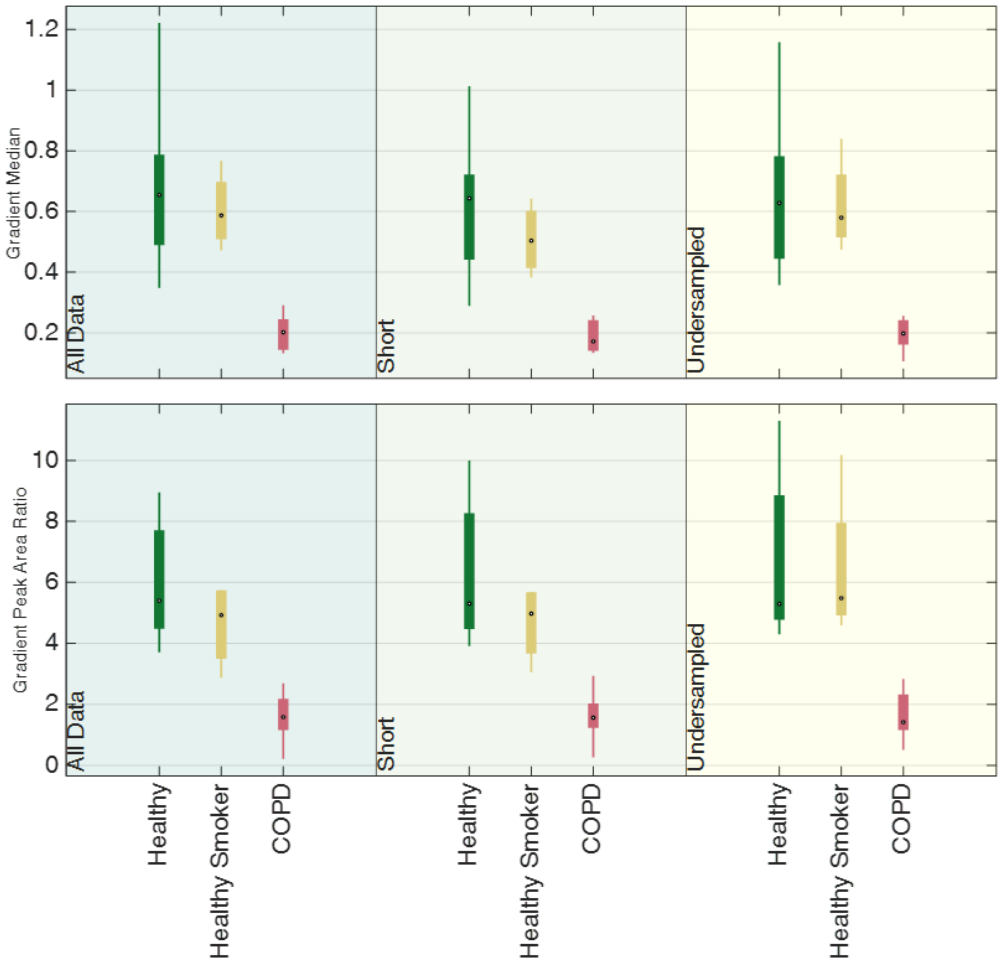


Figure 6.11: Boxplots showing VOLVE ventilation York gradient ($Grad_Y$) median (top row) and peak area ratio (bottom row). Shown are results for all data (full 512 image series), 'half dyns' where the second half of the 512 image timeseries was discarded, and 'undersample' where every other image in the timeseries was discarded (2X temporal undersampling).

	Healthy	Healthy Smoker	COPD
Undersampled			
CC_V Median	0.34	0.89	0.34
CC_V Skewness	0.24	1	0.39
$Grad_V$ Median	0.80	0.89	0.80
$Grad_V$ PAR	0.67	0.69	0.86
Short			
	Healthy	Healthy Smoker	COPD
CC_V Median	0.54	0.69	0.54
CC_V Skewness	0.75	1	1
$Grad_V$ Median	0.47	0.49	0.47
$Grad_V$ PAR	0.89	0.89	1

Table 6.1: p values from the Wilcoxon rank-sum test for within-group comparisons to the fully sampled distributions.

6.5 Pilot Study: Whole Lung Coverage in Cystic Fibrosis

6.5.1 Introduction

In Section 6.4 it was established that VOLVE metrics, in particular the CC_V and $Grad_V$, are not significantly impacted by reducing the number of dynamic acquisitions from 512 to 256, which reduces the image acquisition time of a single 15 mm slice from ~2 minutes to ~1 minute. This reduction in image acquisition time enables the acquisition of multiple slices covering the entire lung volume in a reasonable time period. This motivated a small pilot study in which full lung coverage was achieved in patients with Cystic Fibrosis (CF) with multiple 2D slices. While some 3D acquisitions to enable ventilation quantification across the entire lung have been recently published [91], no study to date has attempted to cover the entire lung volume with multiple 2D slices, enabling both ventilation and perfusion quantification.

6.5.2 Methods

5 adult patients with CF were recruited by my co-investigator Dr Jonathan Brooke (ethics reference: 19/NE/0330), to undergo MRI examination on a Philips 3 T Ingenia scanner. The same 2D FFE sequence, as described in 3.2, was used but with 256 (instead of 512) dynamic acquisitions. Full lung coverage was achieved by repeating this acquisition without a slice gap several times (between 16 and 22 slices (mean ± standard deviation (SD) = 17.4±2.8 slices) depending on the participant's anterior-posterior dimensions). The central 15 slices of each participant were extracted for further analysis to avoid partial volume artefacts in the most anterior/posterior slices.

VOLVE analysis was applied to each slice separately. CC_V and CC_Q were determined. To illustrate the clinical utility of this whole-lung functional assessment, thresholding was used to obtain maps of 'normal' and 'defect' ventilation and perfusion. Threshold values were chosen according to the literature to determine ventilation defect percentage (VDP) and perfusion

defect percentage (QDP) for each slice [206]. For ventilation, the median value–1.75*SD was used, and for perfusion the median value–0.75*SD. These thresholds were chosen by Glandorf *et al.* to maintain a VDP and QDP of less than 10% and 20%, respectively, in healthy subjects. The VPD/QDP were computed as the percentage of voxels within the lung mask below these threshholds, and these thresholded maps used to generate V/Q mismatch plots.

6.5.3 Results

The imaging was well-tolerated by all participants and the image quality was good — in particular there were no artefacts apparent in slices containing the heart, due to the fast acquisition rate.

VDP and QDP values for all participants are shown in Figure 6.15. Variation across participants and across slices within participants was observed. The minimum/maximum values observed for VDP and QDP were 11.7/31.5% and 5.1/17.9%, respectively.

Figure 6.16 shows example respiratory/cardiac navigator signals for a single CF participant. Example maps for the 12 central slices of the lung are shown for the same CF participant for CC_V (Figure 6.12), CC_Q (Figure 6.13) and V/Q match (Figure 6.14).

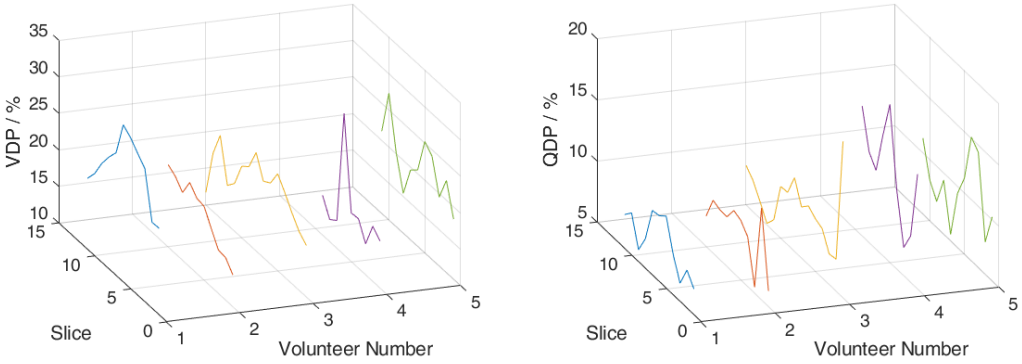


Figure 6.15: Plots showing the ventilation defect percentage (VDP) and perfusion defect percentage (QDP) for the 5 study participants with CF. The example maps shown in Figures 6.12, 6.13 and 6.14 are for volunteer number 3.

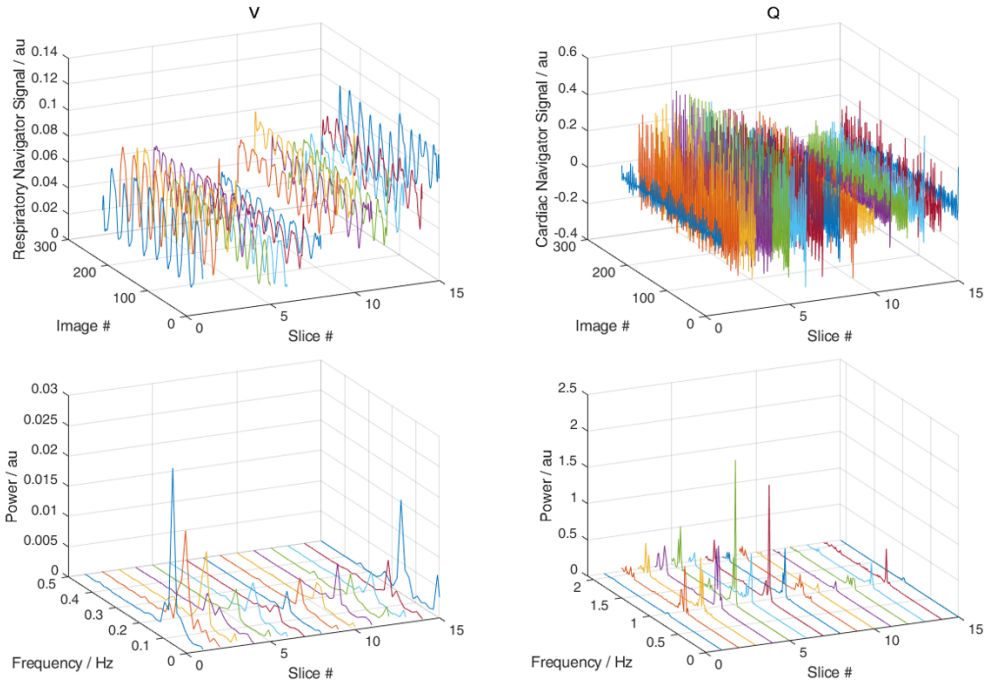


Figure 6.16: Plots showing the respiratory (LHS) and cardiac (RHS) navigator signals for volunteer number 3, with corresponding respiratory and cardiac power spectra below. A strong respiratory trace is obtained for all slices, but the quality of the cardiac navigator signal is reduced in the peripheral (most anterior/posterior) slices.

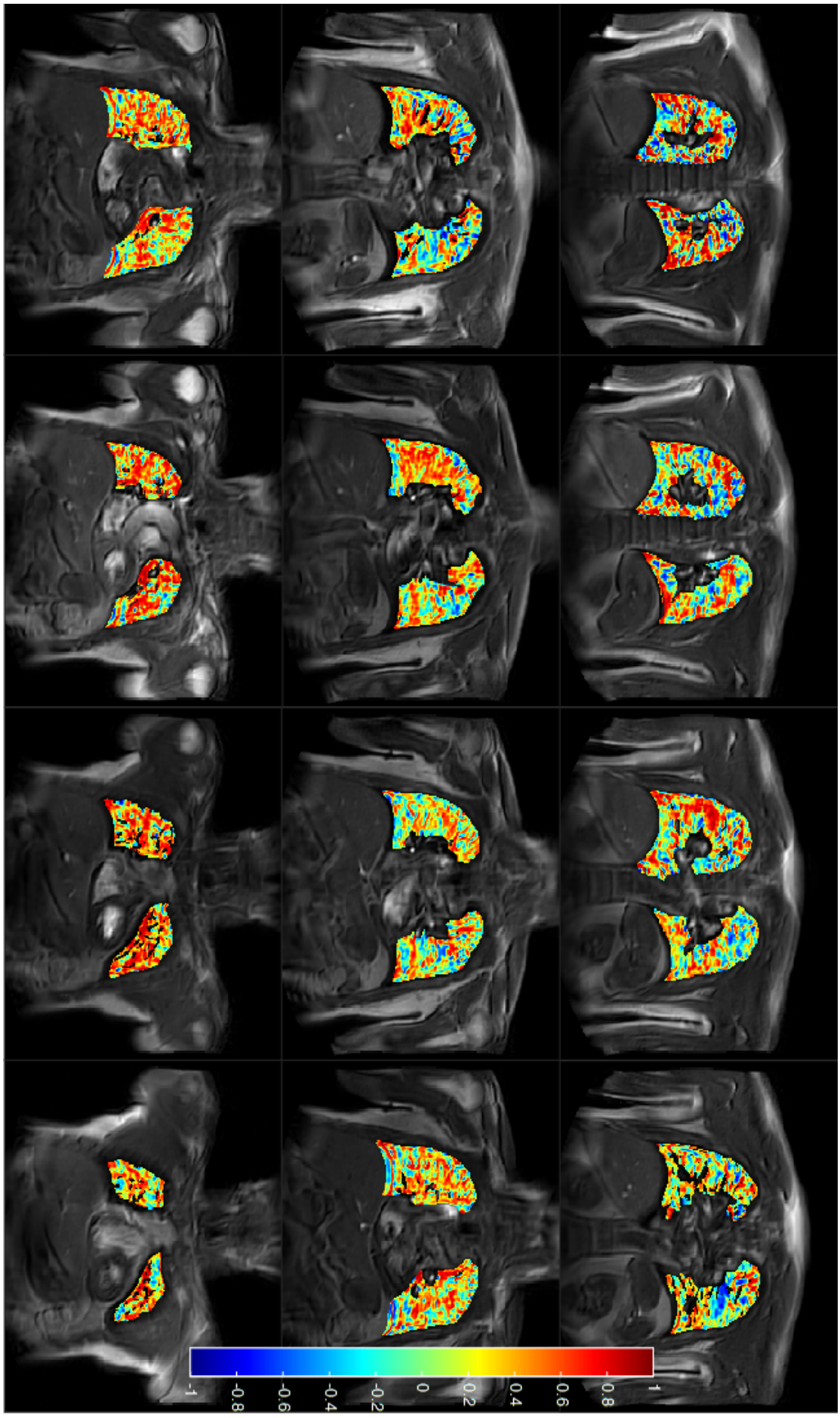


Figure 6.12: Multi-slice maps of ventilation correlation coefficient (CC_V) for a single CF participant.

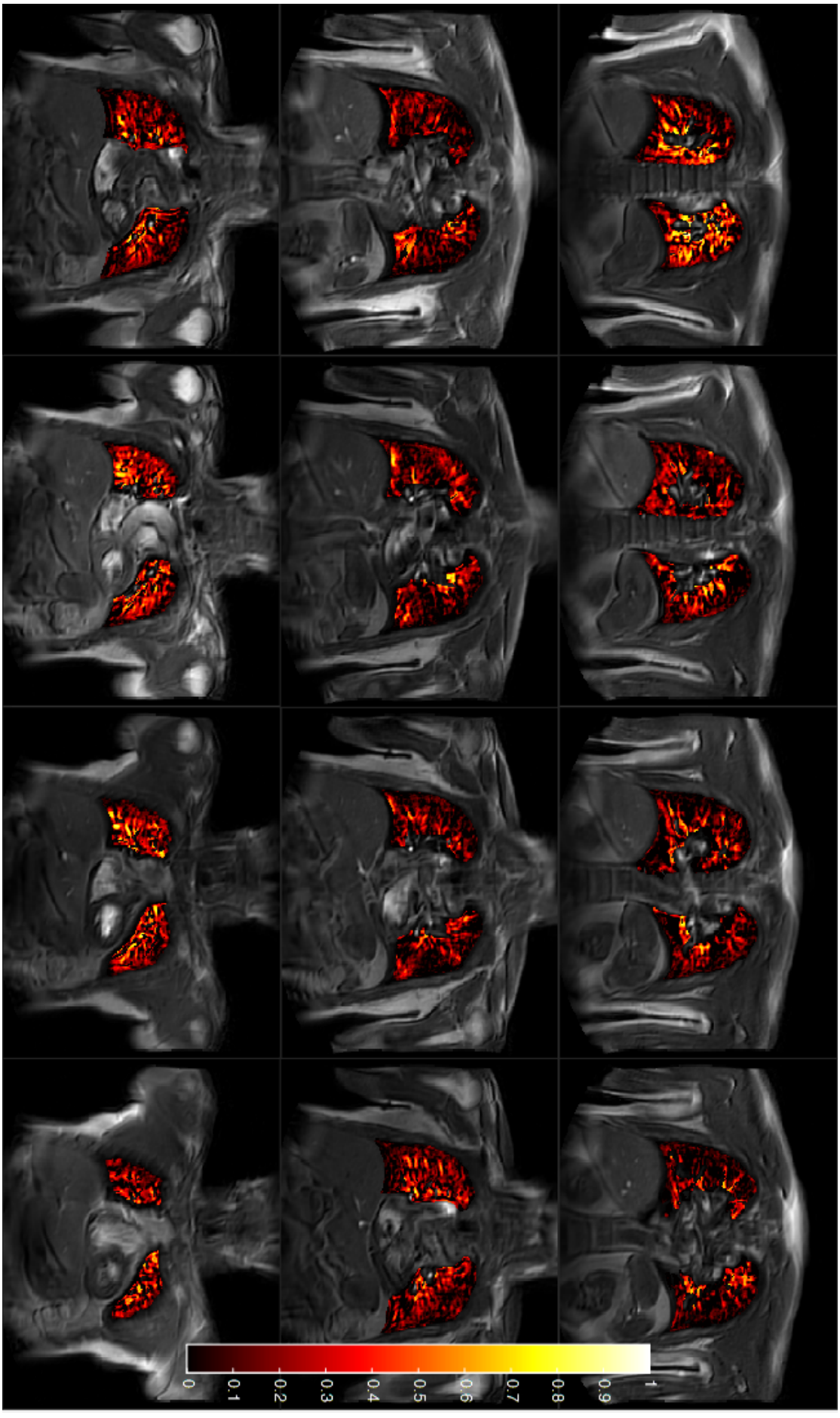


Figure 6.18: Multi-slice maps of perfusion correlation coefficient (CC_Q) for a single CF participant.

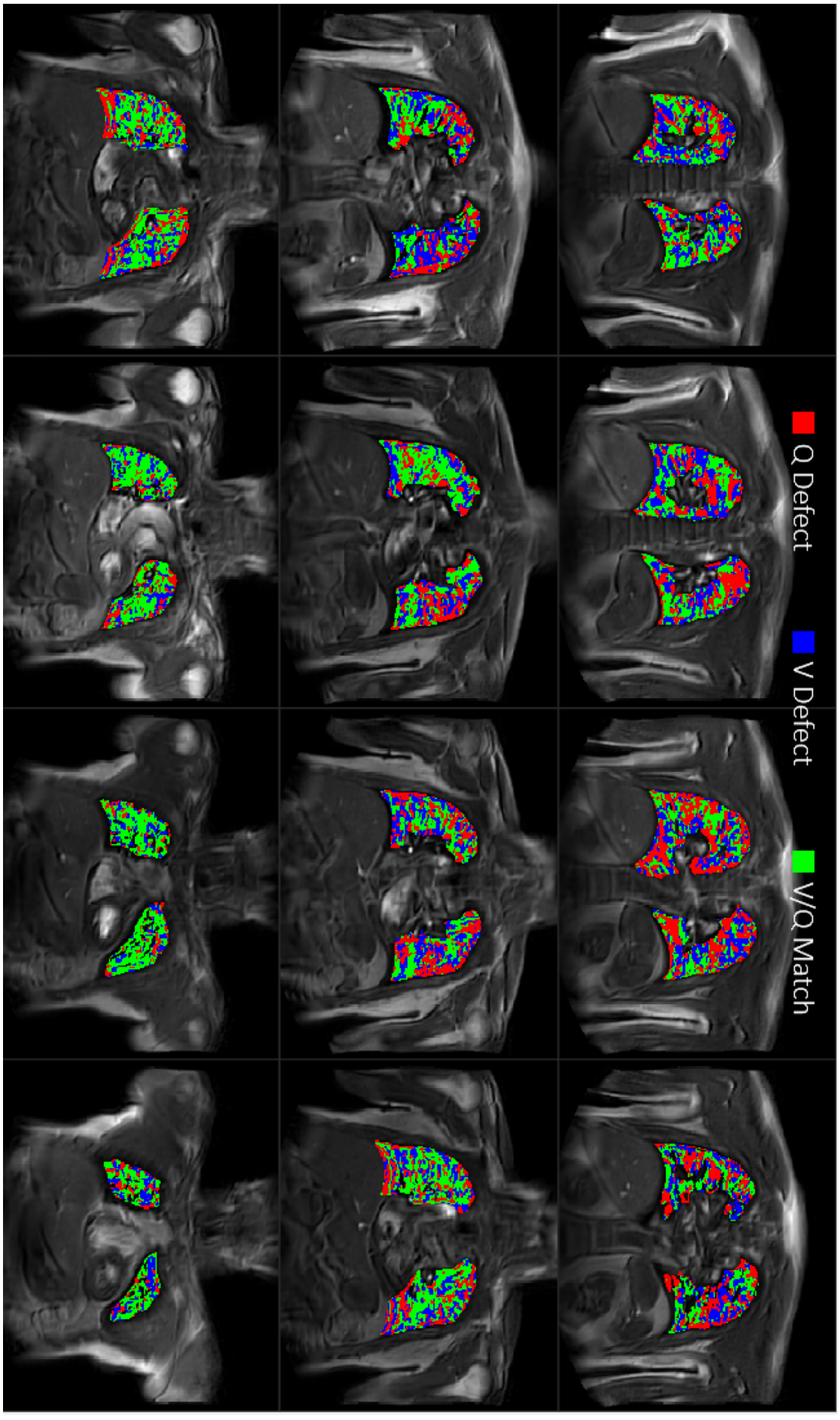


Figure 6.14: Multi-slice V/Q match/mismatch maps for a single CF participant.

6.5.4 Discussion

This work has demonstrated the feasibility of acquiring multiple 2D slices to obtain functional information across the entire lung in a feasible timeframe (~17 minutes). This is important for assessment of diffuse disease such as CF for which the heterogeneity of disease across the lung is clearly demonstrated (Figure 6.15).

The main limitation of this method is that each slice is collected at a different time and so the the breathing pattern and heart rate could vary between scans. While the VOLVE method is designed to be robust to this, verification that extreme breathing patterns do not influence the VOLVE metrics would be beneficial. There is also the possibility for motion to occur between slice acquisitions, although this can be at least partially compensated for by registration. Another issue with collecting slices individually is that peripheral (the most anterior/posterior) slices that do not contain major pulmonary vasculature may have a weaker navigator/reference vessel signature as shown in Figure 6.16, which may confound correlation-based analysis. Further, the implications of phase and oxygenation differences between different possible reference vessels (e.g. aorta versus pulmonary artery) requires further investigation, which could be achieved by high-resolution MRI-compatible physiological monitoring.

The lack of healthy control data means it is difficult to discern between the inherent ventilation spatial distribution across the supine lung and variations due to diffuse lung disease. It is also challenging to discern the impact of the quality of the signal across the lung volume without a healthy reference.

Concurrently collecting interleaved slices could be explored, but a reduction in sampling frequency below the Nyquist limit leads to a reduction in sensitivity as demonstrated in Section 6.4 — although this could be mitigated by e.g. exploiting parallel imaging techniques. Future work could also involve comparing this 2D approach to a 3D radial acquisition (at least for ventilation assessment). Also, while the thresholds chosen in this work are in accordance

with previous studies, these were determined for Phase REsolved FUnctional Lung (PREFUL) and so may not be optimum for VOLVE. Further work is required to determine optimum threshold values for defect ventilation and perfusion VOLVE metrics in the presence of different pathophysiology — necessitating more healthy data and application across additional patients groups.

In conclusion, an imaging protocol such as that demonstrated here allows for the assessment of diffuse lung disease, which is crucial for clinical assessment of diseases with a heterogeneous presentation.

6.6 Conclusion

This chapter has detailed several aspects relating to the VOLVE scanning methodology, including considerations relating to the MR receive coil positioning and MRI parameters used.

It has been demonstrated that suspending the coil above the participant with a coil support does not have a large impact on the obtained MR signal, although further investigation in a pediatric population (with smaller anterior-posterior dimensions) could be beneficial.

The need for careful flip angle choice to simultaneously obtain strong ventilation and perfusion signals was demonstrated. A flip angle higher than the Ernst may be optimum for the assessment of ventilation and perfusion. α=7° is recommended, although this requires verification in lung disease where parenchyma T_1 may be increased.

The detrimental impact of temporal undersampling was demonstrated, where greater variability in VOLVE metrics due to cardiac signal aliasing was observed. Conversely, halving the length of the dynamic image series from 512 to 256 was shown to have little impact on the computed VOLVE metrics.

It was therefore shown that halving the length of the dynamic image

series, and so the image acquisition time per slice, enables full lung coverage via multiple 2D slices in a clinically feasible time period. This multi-slice approach should be compared to a 3D acquisition, but has been shown to be a feasible method for fitting into clinical routine.

Chapter 7

Conclusion

This thesis introduced advances in pulmonary Magnetic Resonance Imaging (MRI). This includes novel methods for quantifying periodic Magnetic Resonance (MR) signal changes in the lung, with methods applied in healthy individuals, and participants with Cystic Fibrosis (CF) and Chronic Obstructive Pulmonary Disease (COPD). The key aim of this work was to develop readily clinically translatable methods of lung function assessment using widely available MRI sequences.

Chapter 3 explored the assessment of respiratory induced ^{1}H signal changes in the lung, where the assessment of ventilation was found to have poor repeatability and sensitivity when only considering isolated respiratory states (static measures such as Fractional Ventilation (FV)). This motivated the development of the VOxel-wise Lung VEntilation (VOLVE) method, in which the entire respiratory cycle is used to determine dynamic measures of ventilation. This was found to have superior sensitivity and repeatability to FV in a small CF cohort. The VOLVE framework allows for underlying signal variations to be probed, including the linearity, magnitude and delay of the local parenchyma MR signal response to respiration.

The VOLVE method was extended in Chapter 4 to assess pulmonary perfusion, retrospectively cardiac-gated ventilation and quadrant-wise regional metrics. This analysis was then applied in healthy individuals, healthy smokers and participants with COPD. The Phase REsolved FUnctional Lung (PREFUL) and Dynamic Mode Decomposition (DMD) methods were also applied to this data. Sensitivity to disease, repeatability, regional variations and correlation to spirometry were investigated. It was shown that VOLVE metrics were sensitive to lung disease and smoking-related functional status, and showed good levels of repeatability, whereas PREFUL and DMD had lower sensitivity to smoking-related changes and ventilation sensitivity, respectively. It was shown that VOLVE is potentially sensitive to paradoxical ventilation, where an inversion of the expected parenchyma signal relationship with lung volume was observed in COPD patients with significant airflow obstruction, which has not been demonstrated in other non-contrast-

based techniques.

In Chapter 5 the effects of lung motion and image registration were explored. The impact of different registration methods on VOLVE including Conventional Registration (CR), Group-Oriented REGistration (GOREG) and Demons and Forsberg registration algorithms was investigated. It was shown that VOLVE metrics were not largely impacted by the choice of registration approach. Metrics that were sensitive to disease (significantly different between healthy control and lung disease groups) for one registration method were sensitive for all registration methods tested. The least variance in VOLVE measures was observed with the Forsberg algorithm, in agreement with a previous PREFUL study. This work also explored the use of the Jacobian determinant to assess local expansion of the lung, which was incorporated into the VOLVE pipeline. The VOLVE-Jacobian analysis was found to be sensitive to lung disease, where differences in local expansion may provide an additional lung functional marker. The average Jacobian determinant across the lung was shown to be a viable alternative to a navigator signal as a measure of respiratory phase that is not dependant on the spatial positioning of a navigator Region of Interest (ROI).

A method for dynamically measuring lung volume with fast volumetric imaging was also presented, enabled by high levels of Compressed Sensing (CS). Segmentation of this dynamically acquired lung volume allowed for a direct comparison between the lung-diaphragm navigator signal used in PREFUL/VOLVE-type analyses. It was found that there was not always a direct relation between relative lung volume change and relative navigator signal change, and in some cases hysteresis was observed. The presented method was used to compute a conversion factor between a 2D-derived navigator signal and a measured lung volume for more accurate and repeatable analysis of ^{1}H lung ventilation.

In Chapter 6 various aspects of the data acquisition of the free-breathing Fast Field Echo (FFE) sequence were investigated. This included demon-

stration that the respiratory MR signal was not adversely impacted by a coil support used for patient comfort to suspend the receive RF coil above the thorax (hence impacting the relative distance between coil and thorax) during MRI examination. Then, the FFE sequence parameters were investigated, specifically the flip angle, temporal resolution and the length of the dynamic image series. For the flip angle, the need for a trade-off between obtaining a strong ventilation signal without suppressing the perfusion signal was demonstrated. For the sequence used, a flip angle of α=7° (higher than the Ernst angle) was suggested to be optimum for the dual assessment of ventilation and perfusion. When considering the temporal resolution, it was found that temporal undersampling beyond the Nyquist limit led to reduced sensitivity due to cardiac signal aliasing. It was found that reducing the number of dynamic images in the image series by 50% had little impact on the VOLVE metrics considered, but halved the image acquisition time. This motivated a pilot study in CF in which functional assessment of the entire lung was achieved by collecting multiple 2D slices consecutively in a clinically feasible time period.

There are several areas of future work required to establish VOLVE as a clinically feasible technique as a quantitative measure of lung function. The analysis pipeline could be further improved with the implementation of a deep-learning segmentation of the lung so that image processing is automated and operator independent. This makes the technique less labour intensive to use, increasing throughput and decreasing cost in the setting of widespread clinical adoption, as well as making the quantitative measures more repeatable and reproducible across sites. Future work is required to determine optimum threshold values for defect ventilation and perfusion VOLVE metrics in the presence of different pathophysiology, necessitating more healthy data and application across additional patients groups. Since VOLVE ventilation/perfusion maps can be cardiac/respiratory gated, future work could investigate patient groups where this may be clinically relevant such as in patients with cardiac arrhythmia. Further work is needed to accurately characterise lung parenchyma voxels that exhibit a nonlinear

relationship with global lung expansion. This could potentially be achieved by using Principal Component Analysis (PCA). It would also be beneficial to validate the VOLVE method against another technique such as oxygen-enhanced (OE) MRI for ventilation, hyperpolarized gas MRI for ventilation and sensitivity to paradoxical ventilation or dynamic-contrast-enhanced (DCE) MRI for perfusion.

Extending the single slice acquisition used for VOLVE to a multi-slice acquisition to allow greater coverage of the lung would be beneficial for applications in heterogeneous lung disease. For this, a compromise between SNR, temporal resolution, lung coverage and scan time must be reached, whilst considering in-flow and flip angle optimisation. This could be achieved by parallel imaging techniques, although it should be verified that the coil sensitivity profiles do not vary over the respiratory cycle. Parallel imaging such as SENSE could be used to collect two slices more rapidly, or more advanced techniques such as MultiBand could be used in which two slices can be collected simultaneously. Alternatively a 3D FFE/UTE acquisition could be used with a appropriate respiratory state k-space re-binning, although this is highly dependent on the re-binning process as both the image reconstruction and respiratory phase sorting steps are essentially combined.

In Chapter 5, the Jacobian determinant from the image registration was used to quantify the interplay between the global respiratory phase and local deformations of the lung. Further work is required in exploiting the Jacobian determinant to investigate the biomechanics of the lung, which could make use of a physiological/mathematical lung model. Differences in deformation-based and signal intensity-based assessments should be further explored. These different approaches may be able to delineate functional changes from pathology relating to lung expansion (e.g. hyperinflation or musculoskeletal deformity) and pathology relating to reduced alveolar density (e.g. emphysema).

Overall, the various lung MRI approaches in this work serve as a foundation in progress towards a comprehensive understanding of lung health and disease. In particular, the VOLVE method, with additional assessments including lung perfusion, cardiac-gating, localised expansion via the Jacobian determinant and respiratory mechanics via fast volumetric imaging, all contribute complimentary information to an assessment of pulmonary function. These methods can now be employed in multiparametric pulmonary MRI studies in patient groups, including longitudinal observational studies and assessment of response to various therapeutic options. Such multiparametric assessments could make use of e.g. the Grad_{V}, XCC_{V} and Lag_{V}, combined with J-CC_{V} and MR signal intensity on a voxelwise basis to provide a map of ventilation abnormality, where areas of normal, reduced, minimal, delayed and paradoxial ventilation could be identified, and linked to disease-specific pathophysiology.

While historically lung MRI been neglected due to the challenges associated with low proton density and short T_2^* in the lung, the work presented in this thesis demonstrates the richness of ^{1}H lung MRI data, that remains largely unprobed, which contains information relating to ventilation, perfusion and biomechanics. As we continue to assemble these different facets, together with advancements in morphological imaging, our efforts culminate in a more holistic and nuanced comprehension of lung pathology and function, laying the groundwork for advancements in diagnostic accuracy to inform individualised patient care.

Chapter 8

Appendices

2A Determining Lung Volume, Structure and Function via Retrospective 4D Reconstruction

While this work is focused on readily clinically translatable methods, there are emerging options for retrospective image reconstruction that make use of advanced reconstruction techniques, such as parallel imaging/compressed sensing, respiratory hard/soft gating and artificial intelligence-based reconstructions. This, for example, enables continuous 4D (3D spatial + time) imaging that can be retrospectively gated or binned to different respiratory states. This enables high resolution structural imaging, which could be exploited to obtain both lung volume information and ventilation information – all from a single acquisition. In particular, golden angle sampling allows for continuous data sampling whilst ensuring good k-space coverage in time (any consecutive Fibonacci number of spokes has uniform k-space coverage), enabling dynamic imaging with flexible temporal resolution. Exemplar uniform and golden angle trajectories are shown in Figure 1.

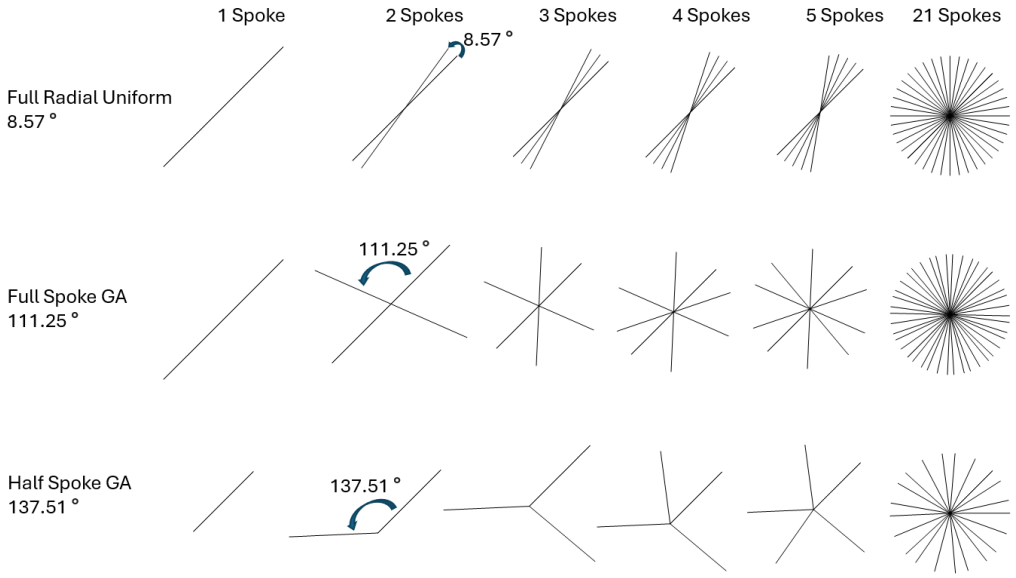


Figure 1: Exemplar trajectories for full radial, 180°/21 spokes = 8.57°; full golden angle (GA), (360 – ($^{360}/_{1.618}$ = 137.51)); and half GA (centre-out), $^{180}/_{1.618}$ = 111.25.

The following details a proof-of-concept study in which a single phantom

and in vivo dataset were collected and retrospectively reconstructed. Image reconstruction was performed using the Berkeley Advanced Reconstruction Toolkit (BART) [207]. The following subsection will detail the image acquisition and reconstruction, which provides a foundation for further work in implementing this method in vivo for further optimisation.

The image acquisition was performed with a 3D FFE radial stack-of-stars sequence with the following acquisition parameters: TR/TE = 3/1.5 ms, flip angle = 5°, number of slices = 57, radial percentage = 800%, FOV = 300x300x200 mm^3, matrix = 240x240, resolution = 1.25x1.25x3.5 mm^3. No slice oversampling, partial Fourier or parallel acceleration techniques were used. Three separate radial trajectories were collected: uniform, golden angle, and pseudo-golden angle. Images were reconstructed in the coronal orientation in MATLAB R2022b.

For image reconstruction, the k-space data was exported in the Philips raw data format (.data/.list), which was then loaded into MATLAB. This was then converted into the BART data format (.cfl/.hdr). The following image reconstruction process was then followed: FFT in the slice dimension (3D cartesian phase encoding), and density compensation function (DCF) determination by computing the root sum squared (RSS) of the k-space trajectory (Ram-Lak filter), followed by adjoint non-uniform Fourier transform (NUFFT) of the density-compensated k-space for re-gridding and final image reconstruction. The density-compensated k-space can be split into respiratory state e.g., by using a respiratory bellows signal – in this case each k-space line is assigned to a time point in the respiratory bellows signal which has associated respiratory phase, and so can then be binned or grouped with like states.

This binning procedure was carried out for two example respiratory states (inspiration and expiratory phases), as shown in Figure 2. In the phantom data no respiratory motion is present and so the two binned states are identical – and so should only be different due to noise/sampling differences. A low-resolution in vivo data set is shown as a proof-of-concept, with visible

difference between the expiration (bin 1) and inspiration (bin 2) states. As shown, this methodology can be used to generate motion-resolved states from continuous 4D imaging. Alternative methods for binning the k-space data are available, such as self-navigation where the k-space centre (DC) is used to determine the average signal of the excitation volume [25], or more recently image-based self-navigation where low spatial but high temporal resolution images are reconstructed to characterise motion directly [208]. Further work is required to investigate the impact of interpolation error accumulation for functional measures that require interpolation for re-gridding, registration and cycle resorting.

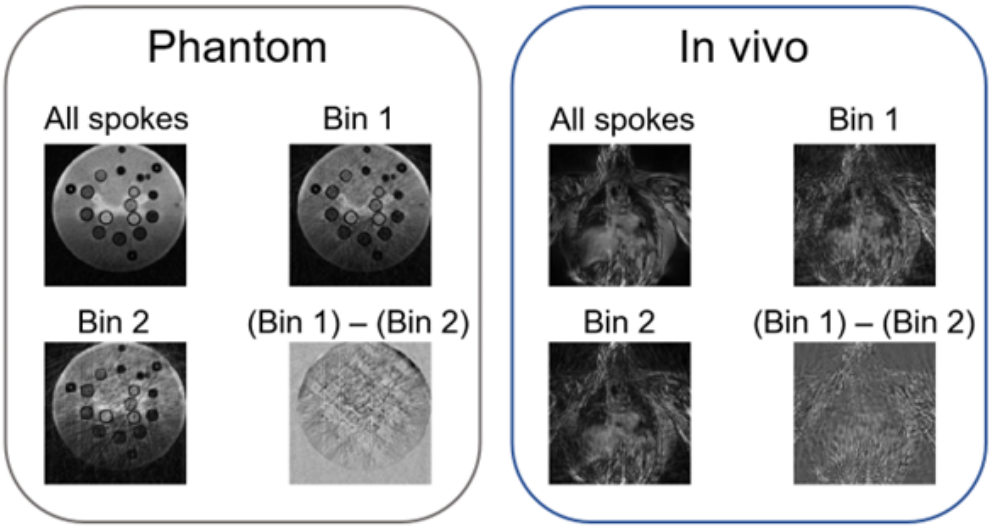


Figure 2: Image reconstruction example with golden angle trajectory for phantom (LHS) and in vivo (RHS) applications. The radial spokes are split into two bins/states based on an artificial respiratory signal (phantom) and a respiratory bellows signal (in vivo).

4A Quantification of Emphysema via Low Signal Volume Assessment

While this thesis has focused on the VOLVE functional imaging pipeline in COPD, it is also possible to ascertain a quantitative assessment of emphysema via structural imaging. Currently densitometry-based Computed Tomography (CT) is the gold standard for emphysema quantification, with the percentage of voxels below the -950 Hounsfield Units (HU) threshold commonly being used [209]. In analogy to this, recent work has attempted to achieve similar emphysema quantification with ultrashort echo time (UTE) MRI [210]. Similarly to the reduced HU values observed in CT, the MR signal intensity is reduced in areas of emphysema due to reduced proton density in these regions which can be quantified via the so-called low-signal-intensity volume, referred to here as low signal volume (LSV). MRI could be advantageous as a replacement for CT for longitudinal monitoring and assessment of neonates, children and pregnant people.

To date, only nonsmokers and patients with Chronic Obstructive Pulmonary Disease (COPD) and Cystic Fibrosis (CF) have been evaluated via this LSV approach [210], and so here a small proof-of-concept study is presented in healthy people with a smoking history (HS), COPD and Alpha-1-antitrypsin deficiency (AATD). As part of the FASTCOPD study (HS, n=3; COPD, n=8; AATD, n=7), structural scans were acquired (prospectively gated T_2-weighted MultiVane and Ultrashort Echo Time (UTE); acquisition parameters in Table 1) which were analysed following the approach of Benlala *et al.* [210] with minor modifications. Subsequent image analysis involved semiautomatic 3D segmentation of the lung parenchyma via Chan-Vese active contours, followed by normalization of the segmented parenchyma by dividing by the mean signal in a soft-tissue ROI (chest wall). An overview of the analysis pipeline is shown in Figure 3A. The LSV was then computed based on a low-signal threshold of 0.05 ($\%LSV_{0.05}$), as defined in the literature, and is shown in Figure 3B. Anatomically matched axial slices from the two

acquisitions are shown in Figure 3C. A Kruskal-Wallis test followed by post-hoc pairwise analysis with Dunn's correction for multiple comparisons was performed to assess any differences in LSV between the groups.

	Parameters	Geometry	Breathing
T_2W MultiVane	TR/TE=2.73 sec/126 ms, α=90°, matrix 268x268, resolution 1.5x1.5mm^2, thickness 5mm, 30 slices	AX	FB - ~120s
UTE	TR/TE=2.99/0.136 ms, α=5°, matrix 288x288, resolution 1.5x1.5x2mm^3, 80-100 slices	COR/AX	FB - 8-10mins

Table 1: Summary of the structural imaging parameters for the T2-weighted MultiVane and ultrashort echo time (UTE) acquisitions.

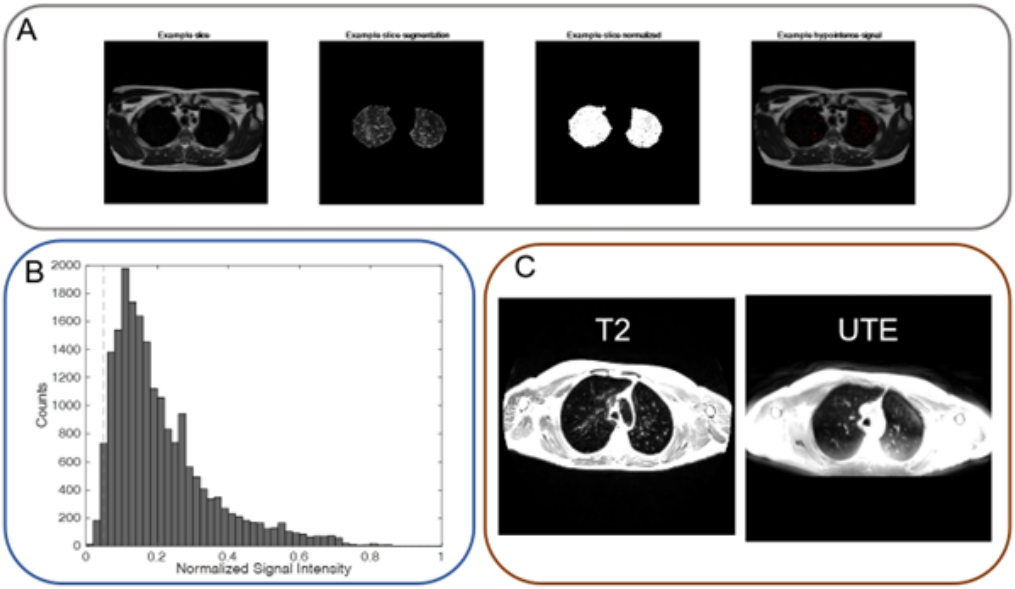


Figure 3: A) Overview of the image analysis pipeline: the segmented lung parenchyma is normalized via the chest wall signal, followed by hypointense low-signal-volume determination based on the 0.05 threshold value. B) Example normalized lung parenchyma signal histogram. C) Anatomically matched axial slices for the T_2 MultiVane and UTE acquisitions.

The computed LSV values are shown in Figure 4. Significant differences between the healthy smoker group and the COPD/AATD groups were found for both the T_2 MultiVane and UTE acquisitions, indicating sensitivity of this approach to emphysema detection/quantification. No significant differences between COPD and AATD were found, as to be expected due to the likely presence of emphysema in both groups. A limitation of the image reconstruction employed is that when prospectively gating, changes in breathing behaviour can lead to blurring as the gating delay is preset for the entire acquisition period. This can be avoided with the previously described continuous acquisition and retrospective respiratory state re-binning. Further work is ongoing in developing more sophisticated re-binning algorithms.

These structural scans should also be compared directly for validation against CT images for assessment of spatial agreement of areas with hypointense signal. In future once validated, a more sophisticated assessment could be achieved by utilising information from these structural scans and from functional assessments of ventilation and perfusion abnormalities.

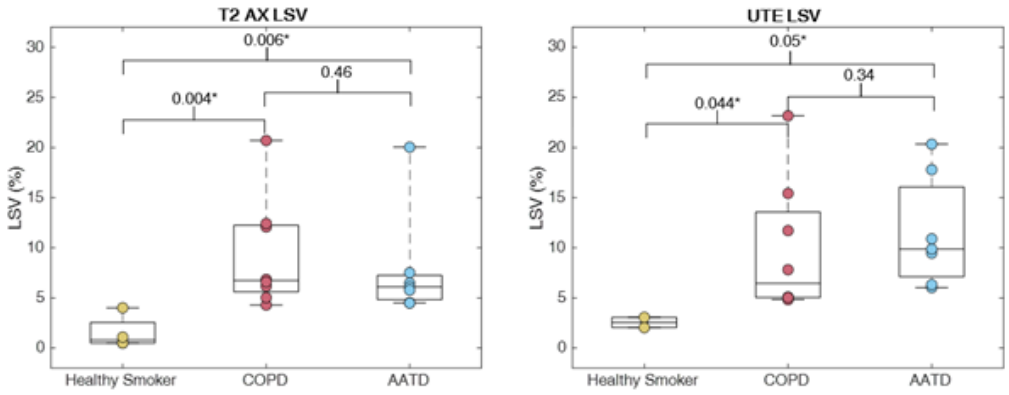


Figure 4: Boxplots showing the low signal volume (LSV) % for the healthy smoker, COPD and AATD groups for the T2 (LHS) and UTE (RHS) sequences. p values between the groups are shown, with significant ($p<0.05$) differences marked with an asterisk (*).

4B All Subject VOLVE Maps

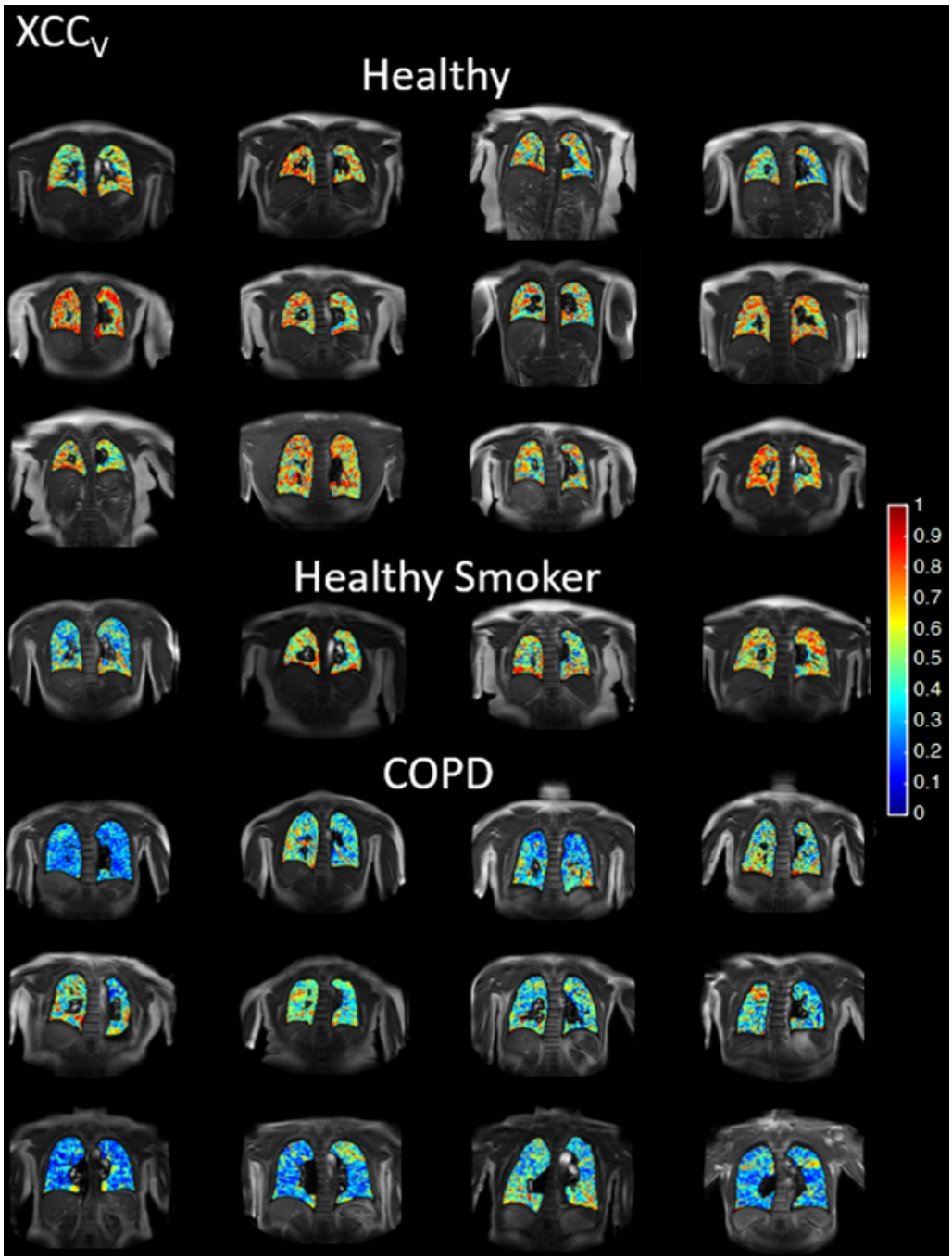


Figure 5: All subject VOLVE maps for XCC$_V$.

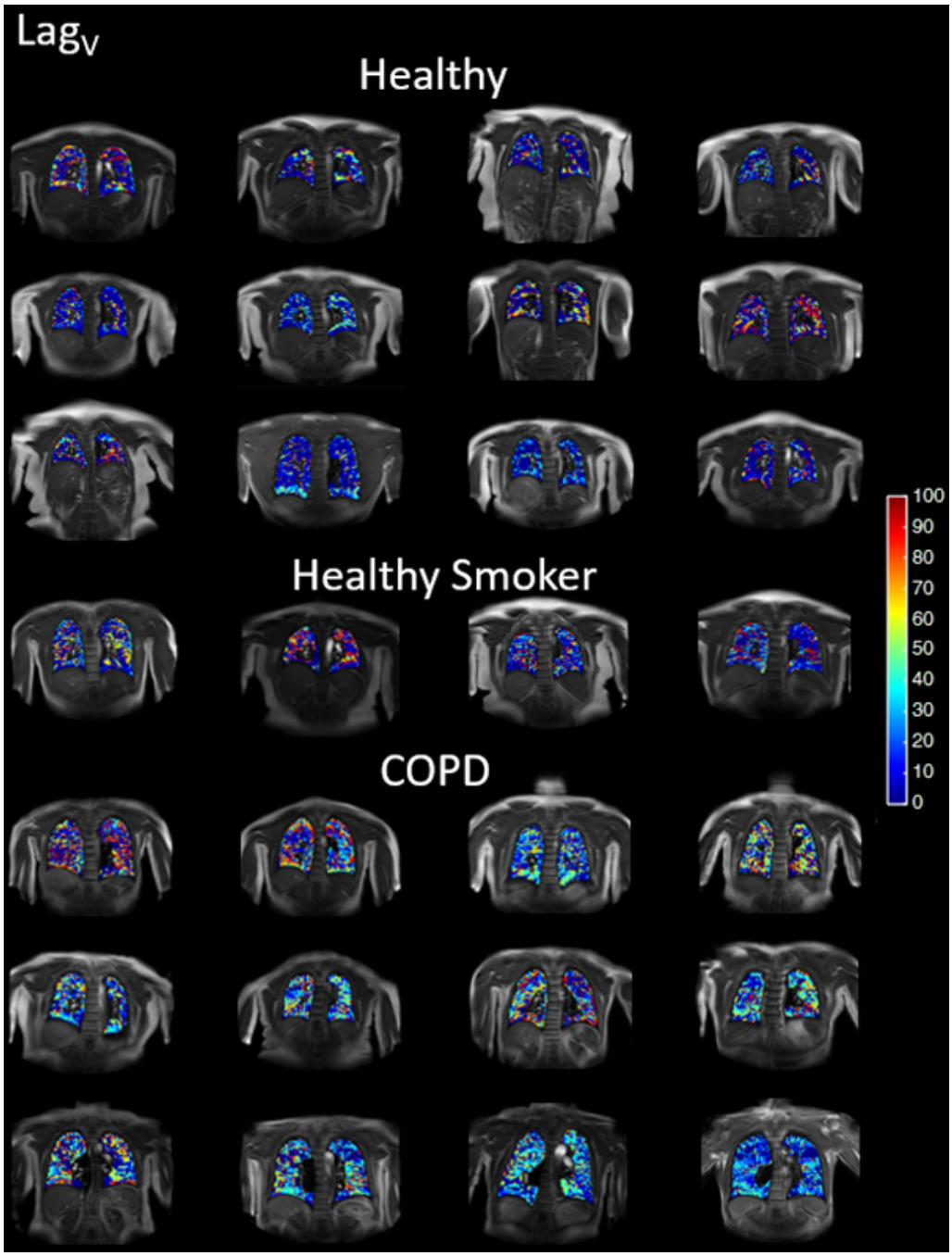


Figure 6: All subject VOLVE maps for Lag$_V$.

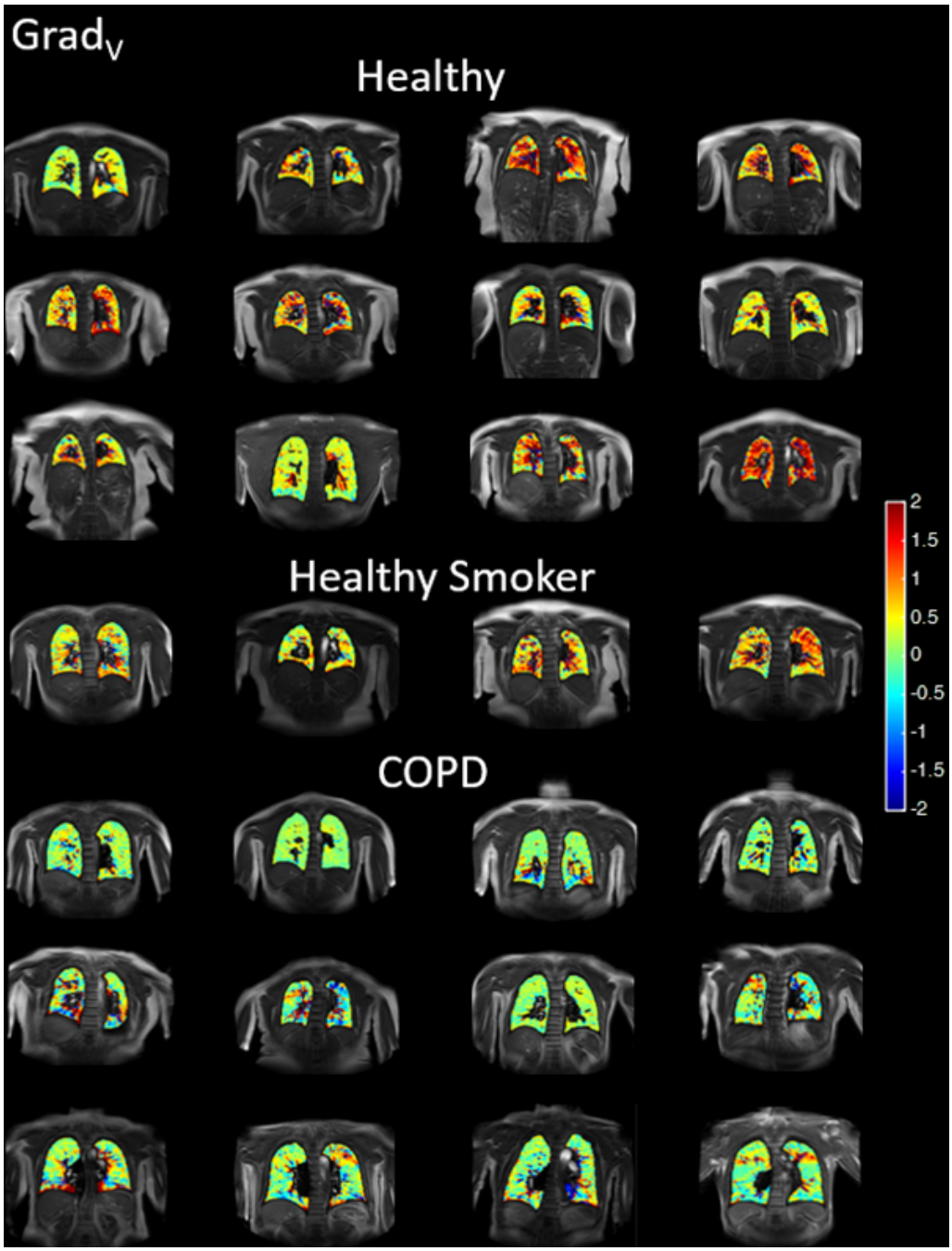


Figure 7: All subject VOLVE maps for Grad$_V$.

4C Pearson Correlation Coefficient

As an alternative to using the cross-correlation (XCC), lags and gradient to characterise the local parenchyma signal changes with respect to the global navigator signal, a simplified approach involves using the Pearson correlation coefficient (CC) which reflects both the XCC and the lag. The CC_V demonstrates the extent to which the signals from individual lung voxels covary in-phase with the navigator. Example maps and histograms are shown in Figure 8. Similarly to the cross-correlation (XCC_V shown for these subjects in Figure 4.3), the CC_V map for the healthy volunteer is relatively homogenous with CC_V values > 0.7 (histogram negatively skewed; skewness = -1.44), except for some small regions in, or bordering, vessels. In contrast, the CC_V map for the COPD participant is heterogeneous (histogram symmetrically distributed with a skewness = -0.04), with a substantial proportion of lung parenchyma voxels displaying a CC_V of 0 or less, a lower correlation compared to the XCC_V values, where a negative correlation coefficient indicates an increase in MR parenchyma signal on inspiration. In this case the CC_V is picking up those voxels that have a large lag/phase shift as well as magnitude change. Figure 9 shows boxplots of the CC_V median and skewness which were significantly different between the groups.

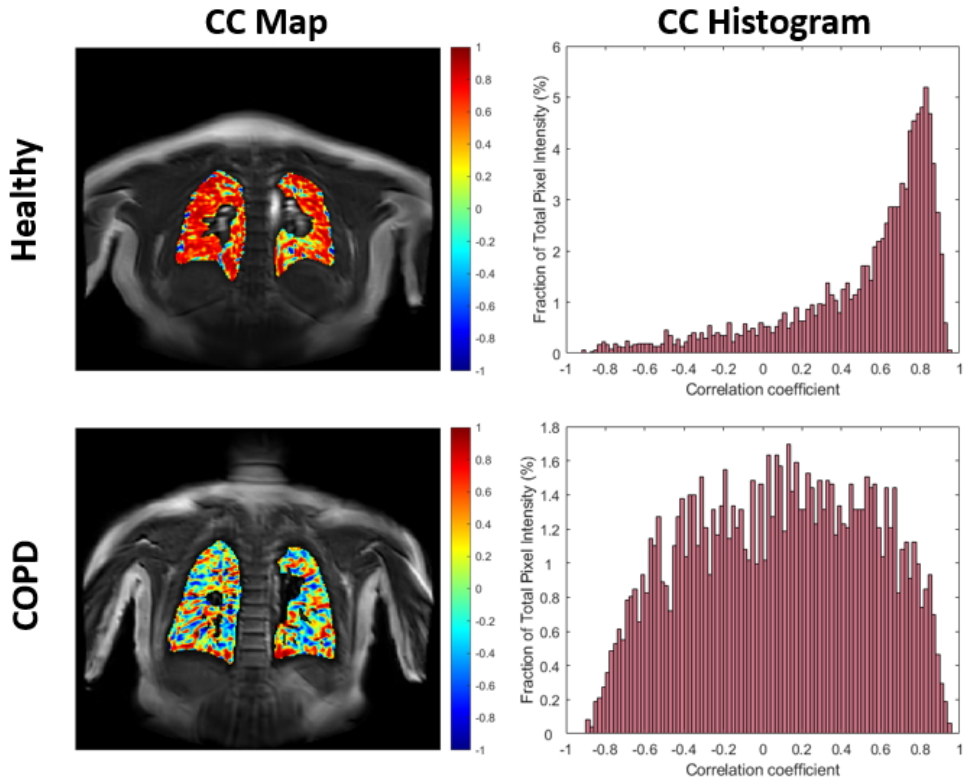


Figure 8: Example correlation coefficient (CC) map and histogram for a healthy never-smoker (age 24 years, male) and COPD participant (age 66 years, female, FEV1=30%, GOLD III).

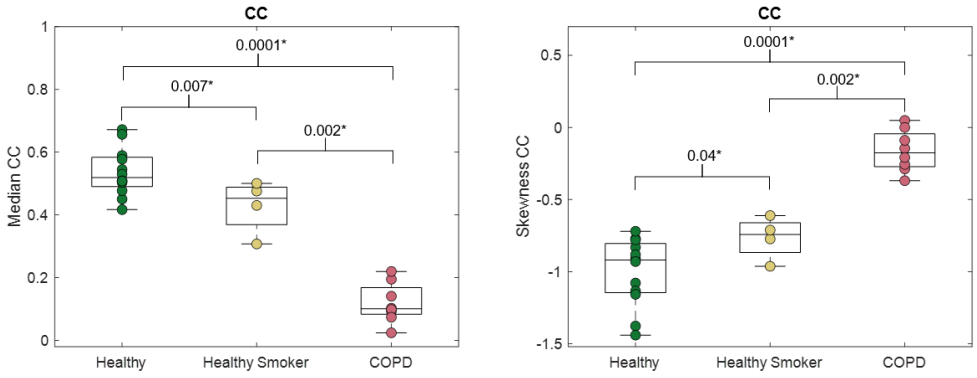


Figure 9: Boxplots showing correlation coefficient (CC) median and skewness for the groups. Significant differences ($p<0.05$) between the groups is observed for both metrics; significant results are marked with an asterisk.

The XCC is an informative measure as the quantification of the delay (lags) along with the linearity (XCC) and magnitude (gradient) of the

response provides a holistic description of the MR signal variations of the lung parenchyma. However, the CC effectively combines the information available in the XCC and lag and provides a measure which gives clear delineation between the groups.

5A Impact of Choice of Registration Target Image on Jacobian Measures

This appendix outlines a component of the investigation into application of the Jacobian determinant in VOLVE analysis, involving different image registration target images. This is presented separately here for clarity as this was not the primary aim of the study.

5A.1 Introduction

In this study, the impact of registration target image was explored by performing the VOLVE-Jacobian and Jacobian-FV analysis with both mid-cycle and end-expiration target image choices. End-inspiration was avoided as this is the most variable respiratory state in terms of respiration depth. This appendix details all metrics tested for each registration method and target image choice — the same analysis and metrics as detailed above, but with additional target image choices.

The respiratory phase of the target image shifts the Jacobian determinant around unity, depending on the choice of target state. For example, for a mid-cycle target image choice, (moving) images in expiratory states are stretched by the registration and so have a $\det(J)>1$ (and have $\det(J)<1$ for inspiration). Conversely, for an end-expiration target image choice, all registered images undergo compression and so have $\det(J)<1$. Hence for these examples, the Jacobian determinant timecourse is either centred on 1, or has a global maximum of 1, respectively. So far, an image of medium lung inflation (closest to the mean respiratory phase as determined by the lung-diaphragm navigator signal) has been used in all previous registrations to reduce the need for large deformation fields (e.g., registering from end-expiration to end-inspiration). However, other respiratory states could be chosen, such as the end-expiration state, which is generally more stable in terms of respiratory depth. The choice of target image and the impact this has on the determined Jacobian parameters is therefore explored.

5A.2 Methods

Image analysis was performed as described in Section 5.1.3. Sensitivity to lung disease was tested for by a Kruskal-Wallis test. Additionally, a Wilcoxon rank-sum test was performed to compare Demons end-expiration (DE), Forsberg end-expiration (FE) and Forsberg mid-cycle (FM) (the 'new' registrations) with Demons mid-cycle (DM) (which has been used throughout this work) for healthy never-smoker individuals.

5A.3 Results

For the assessment between different target image choices, Table 2 shows the p values for the DE, FM and FE methods against the DM method for healthy controls only. No significant differences were found between Demons methods (all DE vs. DM $p > 0.05$), whereas some significant differences were observed between DM and Forsberg approaches.

Figures 10 and 11 show the Jacobian-CC_V and Jacobian-FV metrics across the groups for the Demons and Forsberg CR registration approaches, with p-values between groups shown in Table 3 (Kruskal-Wallis).

Parameter	DE p-value	FE p-value	FM p-value
CC Median	0.0885	0.0029*	0.0014*
CC Skewness	0.1749	0.0166*	0.0007*
FV Median	0.1572	0.8399	0.7950
FV Skewness	0.0885	0.0051*	0.0531

Table 2: between-registration method assessment of choice of target image. p-values from the Wilcoxon rank sum test for healthy controls for each registration scheme (DE, FS, FM) against DM. Significant values ($p < 0.05$) are marked with an asterisk (*).

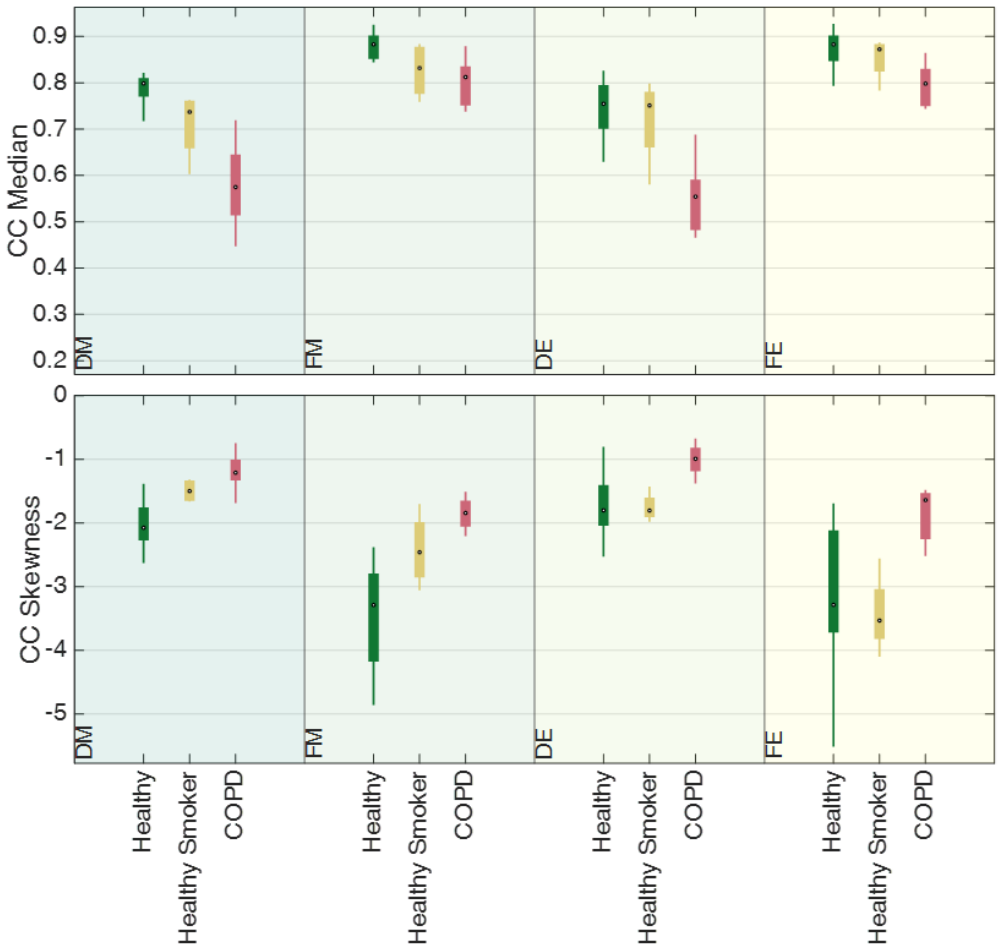


Figure 10: Boxplots showing the Jacobian-CC_V median and skewness for the 4 considered registration methods (Demons mid-cycle (DM), Forsberg mid-cycle (FM), Demons end-expiration (DE), Forsberg end-expiration (FE)), across the 3 study groups (healthy, healthy smoker and COPD).

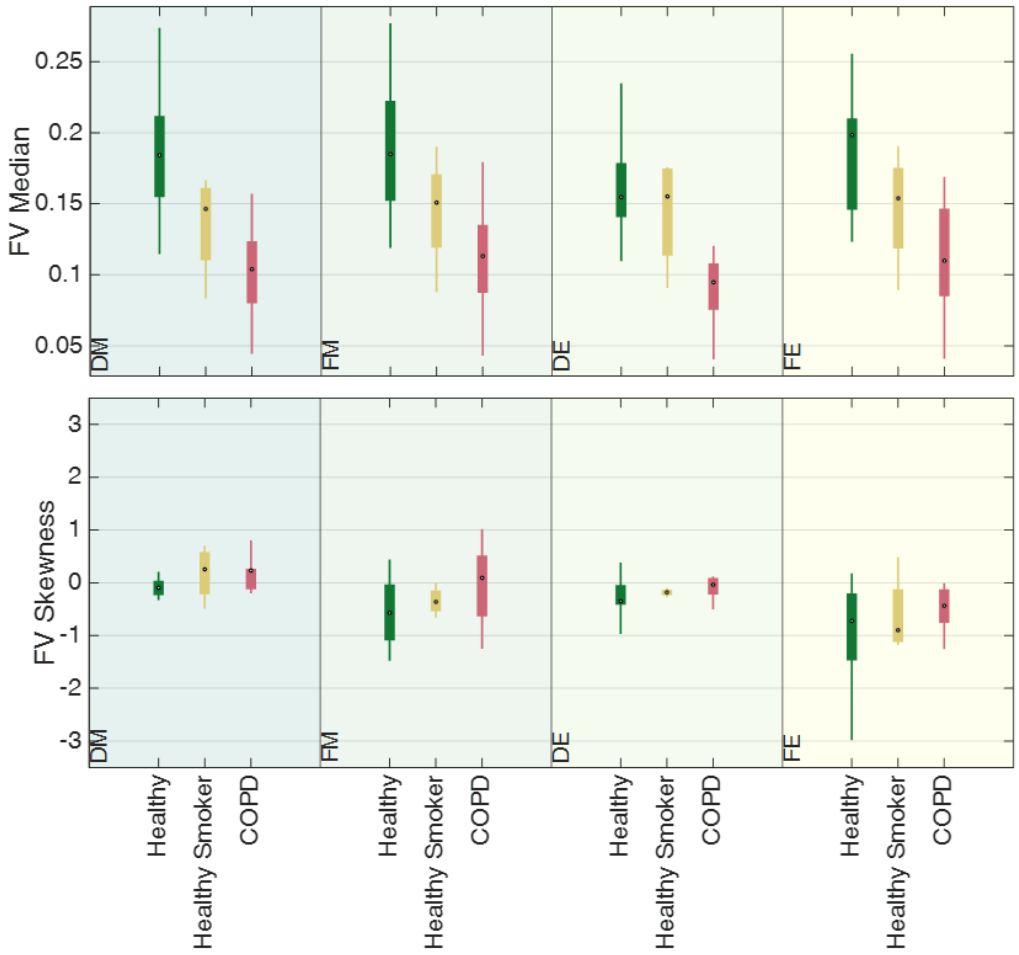


Figure 11: Boxplots showing the Jacobian FV median and skewness for the 4 considered registration methods (Demons mid-cycle (DM), Forsberg mid-cycle (FM), Demons end-expiration (DE), Forsberg end-expiration (FE)), across the 3 study groups (healthy, healthy smoker and COPD).

Parameter	DM p-value	FM p-value	DE p-value	FE p-value
CC Median	3.1804e-04*	0.0241	0.0020*	0.0113*
CC Skewness	1.7616e-04*	6.1314e-04*	0.0021*	0.0035*
FV Median	0.0017*	0.0040*	0.0016*	0.0149
FV Skewness	0.1470	0.2448	0.2548	0.4195

Table 3: within-registration method assessment of sensitivity to lung disease. Kruskal-Wallis p values are shown, with significant differences ($p<0.0125$, Bonferroni-corrected) marked with an asterisk (*).

	DM HS	DM COPD	DE HS	DE COPD	FE HS	FE COPD	FM HS	FM COPD
CC Median	0.0198	0.0003*	0.7703	0.0009*	0.4462	0.0062*	0.2121	0.0095*
CC Skewness	0.0044	0.0002*	0.9527	0.0020*	0.5209	0.0050*	0.1033	0.0025*
FV Median	0.0780	0.0007*	0.7703	0.0004*	0.2615	0.0050*	0.1703	0.0016*
FV Skewness	0.3165	0.0597	0.5989	0.1265	0.6835	0.2136	0.3165	0.1265

Table 4: within-registration method assessment of sensitivity to lung disease. p-values from the Wilcoxon rank sum test for each group (HS, n=4; COPD, n=12) and each registration scheme (DM,DE, FS, FM) against healthy controls. Significant values ($p < 0.05$) are marked with an asterisk (*). Abbreviations: DM = Demons mid-cycle, DE = Demons end-expiration, FM = Forsberg mid-cycle, FE = Forsberg end-expiration, HS = healthy smoker, COPD = chronic obstructive pulmonary disease, CC = correlation coefficient, FV = fractional ventilation.

Very strong correlations (median (LQ-UQ) = 0.95 (0.93-0.97)) were found between the average Jacobian and the navigator signal for all methods (Figure 12). No significant differences were found between the groups, although the correlations tended to be weaker in the healthy smoker and weaker again in COPD. The within-group variance tended to be smaller when registering to mid-cycle compared to end-expiration. The maximum correlation and smaller variance was observed for FM.

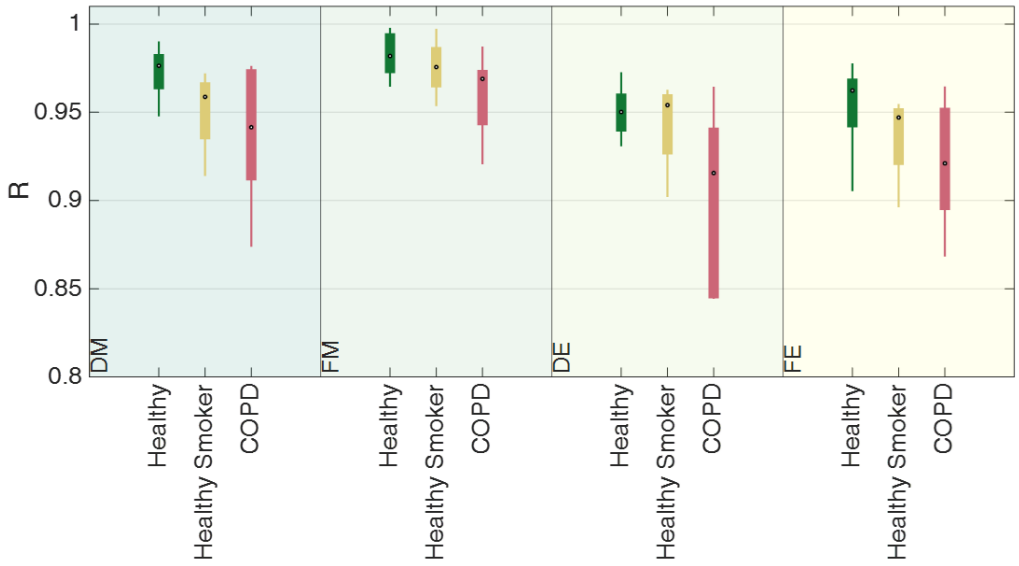


Figure 12: Boxplot showing the Pearson correlation coefficient between whole-lung mean Jacobian determinant and the lung-diaphragm navigator signal for the 4 considered registration methods (Demons mid-cycle (DM), Forsberg mid-cycle (FM), Demons end-expiration (DE), Forsberg end-expiration (FE)), across the 3 study groups (healthy, healthy smoker and COPD).

5A.4 Discussion

When considering these 4 registration approaches, there was little difference overall for sensitivity to disease — all parameters that were significant for COPD with one of the methods was significant for them all, indicating that the sensitivity is not ultimately impacted by the specifics of the registration approach. The discussion of the main work (Section 5.1.3) is therefore

applicable to this additional investigation.

Overall, the mid-cycle target image choices exhibited the strongest correlations with average Jacobian, with the Forsberg package delivering the smallest variance. The larger variations when registering from end-expiration could be due to the large spatial deformation required between the end-inspiration and end-expiration states. This together with sensitivity to disease, and sensitivity of Jacobian-FV makes the FM method stand out as the best candidate of those investigated for registration method choice.

Bibliography

[1] Nicholas J Kassebaum, Megha Arora, Ryan M Barber, Zulfiqar A Bhutta, Jonathan Brown, Austin Carter, Daniel C Casey, Fiona J Charlson, Matthew M Coates, Megan Coggeshall, Leslie Cornaby, Lalit Dandona, and Christopher J L Murray. Global, regional, and national disability-adjusted life-years (DALYs) for 315 diseases and injuries and healthy life expectancy (HALE), 1990–2015: a systematic analysis for the Global Burden of Disease Study 2015. *The Lancet*, 388(10053):1603–1658, oct 2016. ISSN 0140-6736. doi: 10.1016/S0140-6736(16)31460-X. URL http://www.thelancet.com/article/S014067361631460X/fulltext.

[2] The top 10 causes of death in the world. URL https://www.who.int/news-room/fact-sheets/detail/the-top-10-causes-of-death.

[3] Peter G.J. Burney, Jaymini Patel, Roger Newson, Cosetta Minelli, and Mohsen Naghavi. Global and regional trends in COPD mortality, 1990-2010, may 2015. ISSN 13993003. URL http://ow.ly/I66ND.

[4] David Allan Cook and Paul D. Scanlon. Pulmonary Function Tests. *The Ulster Medical Journal*, 80(2):84, jan 2011. ISSN 2046-4207. doi: 10.1201/b14283-51. URL /pmc/articles/PMC3229853/.

[5] Sanja Stanojevic, Stephanie D. Davis, George Retsch-Bogart, Hailey Webster, Miriam Davis, Robin C. Johnson, Renee Jensen, Maria Ester Pizarro, Mica Kane, Charles C. Clem, Leah Schornick, Padmaja

Subbarao, and Felix A. Ratjen. Progression of lung disease in preschool patients with cystic fibrosis. *American Journal of Respiratory and Critical Care Medicine*, 195(9):1216–1225, may 2017. ISSN 15354970. doi: 10.1164/RCCM.201610-2158OC/SUPPL_FILE/DISCLOSURES.PDF. URL www.atsjournals.org.

[6] Aishwarya Gulati and Rashmi Balasubramanya. Lung Imaging. *Respiratory Monitoring in Mechanical Ventilation: Techniques and Applications*, pages 127–176, may 2023. doi: 10.1007/978-981-15-9770-1_3. URL https://www.ncbi.nlm.nih.gov/books/NBK558976/.

[7] Sebastian Ley. Lung imaging. *European Respiratory Review*, 24(136): 240–245, jun 2015. ISSN 16000617. doi: 10.1183/16000617.00011214. URL http://ow.ly/KbVtd.

[8] Paul J. Roach, Dale L. Bailey, and Benjamin E. Harris. Enhancing Lung Scintigraphy With Single-Photon Emission Computed Tomography. *Seminars in Nuclear Medicine*, 38(6):441–449, nov 2008. ISSN 0001-2998. doi: 10.1053/J.SEMNUCLMED.2008.06.002.

[9] Selene Capitanio, Abdul Jalil Nordin, Abdul Rahim Noraini, and Claudio Rossetti. PET/CT in nononcological lung diseases: current applications and future perspectives. *European Respiratory Review*, 25 (141):247, sep 2016. ISSN 16000617. doi: 10.1183/16000617.0051-2016. URL /pmc/articles/PMC9487216/.

[10] Dale L. Bailey and Kathy P. Willowson. An Evidence-Based Review of Quantitative SPECT Imaging and Potential Clinical Applications. *Journal of Nuclear Medicine*, 54(1):83–89, jan 2013. ISSN 0161-5505. doi: 10.2967/JNUMED.112.111476. URL https://jnm.snmjournals.org/content/54/1/83.

[11] Stephen J. (Respiratory physician) Chapman. *Oxford handbook of respiratory medicine*. Oxford University Press, 2014. ISBN

0198703864. URL https://books.google.com/books/about/Oxford{_}Handbook{_}of{_}Respiratory{_}Medicine.html?id=hLqXAwAAQBAJ.

[12] M. Puderbach, C. Hintze, S. Ley, M. Eichinger, H. U. Kauczor, and J. Biederer. MR imaging of the chest: A practical approach at 1.5 T. *European Journal of Radiology*, 64(3):345–355, dec 2007. ISSN 0720048X. doi: 10.1016/j.ejrad.2007.08.009. URL https://pubmed.ncbi.nlm.nih.gov/17900843/.

[13] J. M. Wild, H. Marshall, M. Bock, L. R. Schad, P. M. Jakob, M. Puderbach, F. Molinari, E. J. R. Van Beek, and J. Biederer. MRI of the lung (1/3): methods. *Insights into Imaging 2012 3:4*, 3(4):345–353, jun 2012. ISSN 1869-4101. doi: 10.1007/S13244-012-0176-X. URL https://insightsimaging.springeropen.com/articles/10.1007/s13244-012-0176-x.

[14] John P. Mugler and Talissa A. Altes. Hyperpolarized 129Xe MRI of the human lung. *Journal of Magnetic Resonance Imaging*, 37(2):313–331, feb 2013. ISSN 1522-2586. doi: 10.1002/JMRI.23844. URL https://onlinelibrary.wiley.com/doi/full/10.1002/jmri.23844.

[15] James T. Grist, Guilhem J. Collier, Huw Walters, Minsuok Kim, Mitchell Chen, Gabriele Abu Eid, Aviana Laws, Violet Matthews, Kenneth Jacob, Susan Cross, Alexandra Eves, Marianne Durrant, Anthony McIntyre, Roger Thompson, Rolf F. Schulte, Betty Raman, Peter A. Robbins, Jim M. Wild, Emily Fraser, and Fergus Gleeson. Lung Abnormalities Detected with Hyperpolarized 129Xe MRI in Patients with Long COVID. *Radiology*, 305(3):709–717, dec 2022. ISSN 15271315. doi: 10.1148/RADIOL.220069/ASSET/IMAGES/LARGE/RADIOL.220069.FIG6.JPEG. URL https://pubs.rsna.org/doi/10.1148/radiol.220069.

[16] David J. Roach, Yannick Crémillieux, Robert J. Fleck, Alan S. Brody, Suraj D. Serai, Rhonda D. Szczesniak, Stephanie Kerlakian, John P. Clancy, and Jason C. Woods. Ultrashort echo-time magnetic resonance imaging is a sensitive method for the evaluation of early cystic fibrosis lung disease. *Annals of the American Thoracic Society*, 13(11):1923–1931, nov 2016. ISSN 23256621. doi: 10.1513/ANNALSATS.201603-203OC/SUPPL_FILE/DISCLOSURES.PDF. URL /pmc/articles/PMC5122478/.

[17] Grzegorz Bauman, Michael Puderbach, Michael Deimling, Vladimir Jellus, Christophe Chefd'hotel, Julien Dinkel, Christian Hintze, Hans-Ulrich Kauczor, and Lothar R. Schad. Non-contrast-enhanced perfusion and ventilation assessment of the human lung by means of fourier decomposition in proton MRI. *Magnetic Resonance in Medicine*, 62(3):656–664, sep 2009. ISSN 1522-2594. doi: 10.1002/MRM.22031. URL https://onlinelibrary.wiley.com/doi/full/10.1002/mrm.22031.

[18] Andreas Voskrebenzev, Gutberlet M, Klimeš F, Kaireit TF, Schönfeld C, Rotärmel A, Wacker F, and Vogel-Claussen J. Feasibility of quantitative regional ventilation and perfusion mapping with phase-resolved functional lung (PREFUL) MRI in healthy volunteers and COPD, CTEPH, and CF patients. *Magnetic resonance in medicine*, 79 (4):2306–2314, apr 2018. ISSN 1522-2594. doi: 10.1002/MRM.26893. URL https://pubmed.ncbi.nlm.nih.gov/28856715/.

[19] Ye Tian and Krishna S. Nayak. New clinical opportunities of low-field MRI: heart, lung, body, and musculoskeletal. *Magnetic Resonance Materials in Physics, Biology and Medicine 2023*, pages 1–14, oct 2023. ISSN 1352-8661. doi: 10.1007/S10334-023-01123-W. URL https://link.springer.com/article/10.1007/s10334-023-01123-w.

[20] Olaf Dietrich, Thomas Gaass, and Maximilian F. Reiser. T1 relaxation

time constants, influence of oxygen, and the oxygen transfer function of the human lung at 1.5 T—A meta-analysis. *European Journal of Radiology*, 86:252–260, jan 2017. ISSN 18727727. doi: 10.1016/j.ejrad.2016.11.027. URL http://www.ejradiology.com/article/S0720048X16303783/fulltext.

[21] Jiangsheng Yu, Yiqun Xue, and Hee Kwon Song. Comparison of Lung T2* During Free-Breathing at 1.5T and 3.0T with Ultrashort Echo Time (UTE) Imaging. *Magnetic resonance in medicine : official journal of the Society of Magnetic Resonance in Medicine / Society of Magnetic Resonance in Medicine*, 66(1):248, 2011. ISSN 15222594. doi: 10.1002/MRM.22829. URL /pmc/articles/PMC3122137/.

[22] Saeed Mirsadraee, Matthew Tse, Lucy Kershaw, Scott Semple, Nicola Schembri, Calvin Chin, John T. Murchison, Nik Hirani, and Edwin J.R. Van Beek. T1 characteristics of interstitial pulmonary fibrosis on 3T MRI—a predictor of early interstitial change? *Quantitative Imaging in Medicine and Surgery*, 6(1):42, 2016. ISSN 22234306. doi: 10.3978/J.ISSN.2223-4292.2016.02.02. URL /pmc/articles/PMC4775244/.

[23] Richard B. Buxton, Robert R. Edelman, Bruce R. Rosen, Gary L. Wismer, and Thomas J. Brady. Contrast in rapid MR imaging: T1- and T2-weighted imaging. *Journal of computer assisted tomography*, 11(1):7–16, 1987. ISSN 0363-8715. doi: 10.1097/00004728-198701000-00003. URL https://pubmed.ncbi.nlm.nih.gov/3805431/.

[24] C J Bergin, J M Pauly, and A Macovski. Lung parenchyma: projection reconstruction MR imaging. *https://doi.org/10.1148/radiology.179.3.2027991*, 179(3):777–781, jun 1991. doi: 10.1148/RADIOLOGY.179.3.2027991. URL https://pubs.rsna.org/doi/abs/10.1148/radiology.179.3.2027991.

[25] Nara S. Higano, Andrew D. Hahn, Jean A. Tkach, Xuefeng Cao, Laura L. Walkup, Robert P. Thomen, Stephanie L. Merhar, Paul S. Kingma, Sean B. Fain, and Jason C. Woods. Retrospective respiratory self-gating and removal of bulk motion in pulmonary UTE MRI of neonates and adults. *Magnetic Resonance in Medicine*, 77(3):1284–1295, mar 2017. ISSN 1522-2594. doi: 10.1002/MRM.26212. URL https://onlinelibrary.wiley.com/doi/10.1002/mrm.26212.

[26] Julius F. Heidenreich, Simon Veldhoen, Corona Metz, Lenon Mendes Pereira, Thomas Benkert, Josef Pfeuffer, Thorsten A. Bley, Herbert Köstler, and Andreas M. Weng. Functional MRI of the Lungs Using Single Breath-Hold and Self-Navigated Ultrashort Echo Time Sequences. *Radiological Society of North America*, 2(3):e190162, jun 2020. doi: 10.1148/RYCT.2020190162. URL https://pubs.rsna.org/doi/abs/10.1148/ryct.2020190162.

[27] Li Feng. Golden-Angle Radial MRI: Basics, Advances, and Applications. *Journal of Magnetic Resonance Imaging*, 56(1):45–62, jul 2022. ISSN 1522-2586. doi: 10.1002/JMRI.28187. URL https://onlinelibrary.wiley.com/doi/full/10.1002/jmri.28187.

[28] Üstün Aydıngöz, Adalet Elçin Yıldız, and F. Bilge Ergen. Zero Echo Time Musculoskeletal MRI: Technique, Optimization, Applications, and Pitfalls. *Radiographics*, 42(5):1398–1414, sep 2022. ISSN 15271323. doi: 10.1148/RG.220029/ASSET/IMAGES/LARGE/RG.220029.FIG18.JPEG. URL https://pubs.rsna.org/doi/10.1148/rg.220029.

[29] Kyungsoo Bae, Kyung Nyeo Jeon, Moon Jung Hwang, Joon Sung Lee, Ji Young Ha, Kyeong Hwa Ryu, and Ho Cheol Kim. Comparison of lung imaging using three-dimensional ultrashort echo time and zero echo time sequences: preliminary study. *European Radiology 2018 29:5*, 29(5):2253–2262, dec 2018. ISSN 1432-1084. doi: 10.1007/S00330-018-5889-X. URL https://link.springer.com/

article/10.1007/s00330-018-5889-x.

[30] Sedat Alibek, Mika Vogel, Wei Sun, David Winkler, Christopher A. Baker, Michael Burke, and Hubertus Gloger. Acoustic noise reduction in MRI using Silent Scan: An initial experience. *Diagnostic and Interventional Radiology*, 20(4):360–363, 2014. doi: 10.5152/DIR.2014.13458.

[31] Brian Sgard, Maya Khalifé, Arthur Bouchut, Brice Fernandez, Marine Soret, Alain Giron, Clara Zaslavsky, Gaspar Delso, Marie Odile Habert, and Aurélie Kas. ZTE MR-based attenuation correction in brain FDG-PET/MR: performance in patients with cognitive impairment. *European Radiology*, 30(3):1770–1779, mar 2020. ISSN 14321084. doi: 10.1007/S00330-019-06514-Z/FIGURES/4. URL https://link.springer.com/article/10.1007/s00330-019-06514-z.

[32] Emil Ljungberg, Nikou L. Damestani, Tobias C. Wood, David J. Lythgoe, Fernando Zelaya, Steven C.R. Williams, Ana Beatriz Solana, Gareth J. Barker, and Florian Wiesinger. Silent zero TE MR neuroimaging: Current state-of-the-art and future directions. *Progress in Nuclear Magnetic Resonance Spectroscopy*, 123:73–93, apr 2021. ISSN 0079-6565. doi: 10.1016/J.PNMRS.2021.03.002.

[33] Markus Weiger, David O. Brunner, Benjamin E. Dietrich, Colin F. Müller, and Klaas P. Pruessmann. ZTE imaging in humans. *Magnetic Resonance in Medicine*, 70(2):328–332, aug 2013. ISSN 1522-2594. doi: 10.1002/MRM.24816. URL https://onlinelibrary.wiley.com/doi/10.1002/mrm.24816.

[34] Markus Weiger, Mingming Wu, Moritz C. Wurnig, David Kenkel, Andreas Boss, Gustav Andreisek, and Klaas P. Pruessmann. ZTE imaging with long-T2 suppression. *NMR in Biomedicine*, 28(2):247–254, feb 2015. doi: 10.1002/NBM.3246.

[35] Fabio Gibiino, Laura Sacolick, Anne Menini, Luigi Landini, and Florian Wiesinger. Free-breathing, zero-TE MR lung imaging. *Magnetic Resonance Materials in Physics, Biology and Medicine 2014 28:3*, 28(3):207–215, sep 2014. ISSN 1352-8661. doi: 10.1007/S10334-014-0459-Y. URL https://link.springer.com/article/10.1007/s10334-014-0459-y.

[36] Kyungsoo Bae, Kyung Nyeo Jeon, Moon Jung Hwang, Joon Sung Lee, Sung Eun Park, Ho Cheol Kim, and Anne Menini. Respiratory motion–resolved four-dimensional zero echo time (4D ZTE) lung MRI using retrospective soft gating: feasibility and image quality compared with 3D ZTE. *European Radiology 2020 30:9*, 30(9):5130–5138, apr 2020. ISSN 1432-1084. doi: 10.1007/S00330-020-06890-X. URL https://link.springer.com/article/10.1007/s00330-020-06890-x.

[37] R. Edward Hendrick and E. Mark Haacke. Basic physics of MR contrast agents and maximization of image contrast. *Journal of Magnetic Resonance Imaging*, 3(1):137–148, jan 1993. ISSN 1522-2586. doi: 10.1002/JMRI.1880030126. URL https://onlinelibrary.wiley.com/doi/10.1002/jmri.1880030126.

[38] N. Bloembergen and L. O. Morgan. Proton Relaxation Times in Paramagnetic Solutions. Effects of Electron Spin Relaxation. *The Journal of Chemical Physics*, 34(3):842, aug 2004. ISSN 0021-9606. doi: 10.1063/1.1731684. URL https://aip.scitation.org/doi/abs/10.1063/1.1731684.

[39] N. Bloembergen, E. M. Purcell, and R. V. Pound. Relaxation Effects in Nuclear Magnetic Resonance Absorption. *Physical Review*, 73(7):679, apr 1948. doi: 10.1103/PhysRev.73.679. URL https://journals.aps.org/pr/abstract/10.1103/PhysRev.73.679.

[40] Stanley J. Kruger, Scott K. Nagle, Marcus J. Couch, Yoshiharu Ohno,

Mitchell Albert, and Sean B. Fain. Functional imaging of the lungs with gas agents. *Journal of Magnetic Resonance Imaging*, 43(2):295–315, feb 2016. ISSN 1522-2586. doi: 10.1002/JMRI.25002. URL https://onlinelibrary.wiley.com/doi/full/10.1002/jmri.25002.

[41] Klaus W Stock, Qun Chen, Martina Morrin, Hiroto Hatabu, and Robert R Edelman. Oxygen-Enhanced Magnetic Resonance Ventilation Imaging of the Human Lung at 0.2 and 1.5 T. *JOURNAL OF MAGNETIC RESONANCE IMAGING*, 9:838–841, 1998. doi: 10.1002/(SICI)1522-2586(199906)9:6.

[42] Eberhard D. Pracht, Johannes F.T. Arnold, Tungte Wang, and Peter M. Jakob. Oxygen-enhanced proton imaging of the human lung using T2*. *Magnetic Resonance in Medicine*, 53(5):1193–1196, may 2005. ISSN 1522-2594. doi: 10.1002/MRM.20448. URL https://onlinelibrary.wiley.com/doi/full/10.1002/mrm.20448.

[43] M. J. Silvennoinen, C. S. Clingman, X. Golay, R. A. Kauppinen, and Peter C.M. Van Zijl. Comparison of the dependence of blood R2 and R on oxygen saturation at 1.5 and 4.7 Tesla. *Magnetic Resonance in Medicine*, 49(1):47–60, jan 2003. ISSN 1522-2594. doi: 10.1002/MRM.10355. URL https://onlinelibrary.wiley.com/doi/full/10.1002/mrm.10355.

[44] Bastiaan Driehuys, Santiago Martinez-Jimenez, Zackary I. Cleveland, Gregory M. Metz, Denise M. Beaver, John C. Nouls, S. Sivaram Kaushik, Rafael Firszt, Christine Willis, Kevin T. Kelly, Jan Wolber, Monica Kraft, and H. Page McAdams. Chronic obstructive pulmonary disease: Safety and tolerability of hyperpolarized 129Xe MR imaging in healthy volunteers and patients. *Radiology*, 262(1):279–289, jan 2012. ISSN 00338419. doi: 10.1148/RADIOL.11102172/-/DC1. URL /pmc/articles/PMC3244666/.

[45] Mina Kim, Josephine H. Naish, Sarah H. Needleman, Marta Tibiletti,

Yohn Taylor, James P.B. O'Connor, and Geoff J.M. Parker. Feasibility of dynamic T2*-based oxygen-enhanced lung MRI at 3T. *Magnetic Resonance in Medicine*, 91(3):972–986, mar 2024. ISSN 1522-2594. doi: 10.1002/MRM.29914. URL https://onlinelibrary.wiley.com/doi/full/10.1002/mrm.29914.

[46] Simon M.F. Triphan, Felix A. Breuer, Daniel Gensler, Hans-Ulrich Kauczor, and Peter M. Jakob. Oxygen enhanced lung MRI by simultaneous measurement of T1 and T2* during free breathing using ultrashort TE. *Journal of Magnetic Resonance Imaging*, 41(6):1708–1714, jun 2015. ISSN 1522-2586. doi: 10.1002/JMRI.24692. URL https://onlinelibrary.wiley.com/doi/10.1002/jmri.24692.

[47] Kathrin R. F. Hemberger, Peter M. Jakob, and Felix A. Breuer. Multiparametric oxygen-enhanced functional lung imaging in 3D. *Magnetic Resonance Materials in Physics, Biology and Medicine 2014 28:3*, 28(3):217–226, oct 2014. ISSN 1352-8661. doi: 10.1007/S10334-014-0462-3. URL https://link.springer.com/article/10.1007/s10334-014-0462-3.

[48] Stanley J. Kruger, Sean B. Fain, Kevin M. Johnson, Robert V. Cadman, and Scott K. Nagle. Oxygen-enhanced 3D radial ultrashort echo time magnetic resonance imaging in the healthy human lung. *NMR in Biomedicine*, 27(12):1535–1541, dec 2014. ISSN 1099-1492. doi: 10.1002/NBM.3158.

[49] Wei Zha, Stanley J. Kruger, Kevin M. Johnson, Robert V. Cadman, Laura C. Bell, Fang Liu, Andrew D. Hahn, Michael D. Evans, Scott K. Nagle, and Sean B. Fain. Pulmonary ventilation imaging in asthma and cystic fibrosis using oxygen-enhanced 3D radial ultrashort echo time MRI. *Journal of Magnetic Resonance Imaging*, 47(5):1287–1297, may 2018. ISSN 1522-2586. doi: 10.1002/JMRI.25877. URL https://onlinelibrary.wiley.com/doi/10.1002/jmri.25877.

[50] Pengfei Xu, Jichang Zhang, Zhen Nan, Thomas Meersmann, and Chengbo Wang. Free-Breathing Phase-Resolved Oxygen-Enhanced Pulmonary MRI Based on 3D Stack-of-Stars UTE Sequence. *Sensors 2022, Vol. 22, Page 3270*, 22(9):3270, apr 2022. ISSN 1424-8220. doi: 10.3390/S22093270. URL https://www.mdpi.com/1424-8220/22/9/3270/htm.

[51] Yoshiharu Ohno, Masao Yui, Takeshi Yoshikawa, Shinichiro Seki, Daisuke Takenaka, Yoshimori Kassai, Hidekazu Hattori, Kazuhiro Murayama, and Hiroshi Toyama. 3D Oxygen-Enhanced MRI at 3T MR System: Comparison With Thin-Section CT of Quantitative Capability for Pulmonary Functional Loss Assessment and Clinical Stage Classification of COPD in Smokers. *Journal of Magnetic Resonance Imaging*, 53(4):1042–1051, apr 2021. ISSN 1522-2586. doi: 10.1002/JMRI.27441. URL https://onlinelibrary.wiley.com/doi/full/10.1002/jmri.27441.

[52] S. F. Thieme, O. Dietrich, D. Maxien, K. Nikolaou, S. O. Schoenberg, M. Reiser, and C. Fink. Oxygen-enhanced MRI of the lungs: Intraindividual comparison between 1.5 and 3 tesla. *RoFo*, 183(4):358–364, 2011. ISSN 14389029. doi: 10.1055/S-0029-1245808.

[53] Sarah H Needleman, Mina Kim, Jamie R McClelland, Josephine H Naish, Marta Tibiletti, James P B O, Geoff J M Parker, and Correspondence J Geoff M Parker. Independent component analysis (ICA) applied to dynamic oxygen-enhanced MRI (OE-MRI) for robust functional lung imaging at 3 T. *Magnetic Resonance in Medicine*, nov 2023. ISSN 1522-2594. doi: 10.1002/MRM.29912. URL https://onlinelibrary.wiley.com/doi/full/10.1002/mrm.29912.

[54] Geon Ho Jahng, Ka Loh Li, Leif Ostergaard, and Fernando Calamante. Perfusion Magnetic Resonance Imaging: A Comprehensive Update on Principles and Techniques. *Korean Journal of Radiology*, 15(5):554–577, oct 2014. ISSN 1229-6929. doi: 10.3348/KJR.2014.

15.5.554. URL https://doi.org/10.3348/kjr.2014.15.5.554.

[55] Moshe Rogosnitzky and Stacy Branch. Gadolinium-based contrast agent toxicity: a review of known and proposed mechanisms. *Biometals*, 29(3):365, jun 2016. ISSN 15728773. doi: 10.1007/S10534-016-9931-7. URL /pmc/articles/PMC4879157/.

[56] J. Biederer, M. Beer, W. Hirsch, J. Wild, M. Fabel, M. Puderbach, and E. J.R. van Beek. MRI of the lung (2/3). Why … when … how? *Insights into Imaging*, 3(4):355, aug 2012. ISSN 18694101. doi: 10.1007/S13244-011-0146-8. URL /pmc/articles/PMC3481084/.

[57] Christina Amaxopoulou, Ralph Gnannt, Kai Higashigaito, Andreas Jung, and Christian J. Kellenberger. Structural and perfusion magnetic resonance imaging of the lung in cystic fibrosis. *Pediatric Radiology 2017 48:2*, 48(2):165–175, nov 2017. ISSN 1432-1998. doi: 10.1007/S00247-017-4021-8. URL https://link.springer.com/article/10.1007/s00247-017-4021-8.

[58] Mark O. Wielpütz, Michael Puderbach, Annette Kopp-Schneider, Mirjam Stahl, Eva Fritzsching, Olaf Sommerburg, Sebastian Ley, Migle Sumkauskaite, Jürgen Biederer, Hans-Ulrich Kauczor, Monika Eichinger, and Marcus A. Mall. Magnetic Resonance Imaging Detects Changes in Structure and Perfusion, and Response to Therapy in Early Cystic Fibrosis Lung Disease. *https://doi.org/10.1164/rccm.201309-1659OC*, 189(8):956–965, apr 2014. doi: 10.1164/RCCM.201309-1659OC. URL www.atsjournals.org.

[59] Michael Ingrisch, Daniel Maxien, Felix G. Meinel, Maximilian F. Reiser, Konstantin Nikolaou, and Olaf Dietrich. Detection of pulmonary embolism with free-breathing dynamic contrast-enhanced MRI. *Journal of Magnetic Resonance Imaging*, 43(4):887–893, apr 2016. ISSN 1522-2586. doi: 10.1002/JMRI.25050. URL https://onlinelibrary.wiley.com/doi/full/10.1002/jmri.25050.

[60] Maria TA Buzan, Andreas Wetscherek, Christopher M Rank, Michael Kreuter, Claus Peter Heussel, Marc Kachelrieß, and Julien Dinkel. Delayed contrast dynamics as marker of regional impairment in pulmonary fibrosis using 5D MRI - a pilot study. *https://doi.org/10.1259/bjr.20190121*, 93(1113), jul 2020. doi: 10.1259/BJR.20190121. URL https://www.birpublications.org/doi/abs/10.1259/bjr.20190121.

[61] Lea Behrendt, Laurie J. Smith, Andreas Voskrebenzev, Filip Klimeš, Till F. Kaireit, Gesa H. Pöhler, Agilo L. Kern, Cristian Crisosto Gonzalez, Anna Maria Dittrich, Helen Marshall, Katharina Schütz, Paul J.C. Hughes, Pierluigi Ciet, Harm A.W.M. Tiddens, Jim M. Wild, and Jens Vogel-Claussen. A dual center and dual vendor comparison study of automated perfusion-weighted phase-resolved functional lung magnetic resonance imaging with dynamic contrast-enhanced magnetic resonance imaging in patients with cystic fibrosis. *Pulmonary Circulation*, 12(2):e12054, apr 2022. ISSN 2045-8940. doi: 10.1002/PUL2.12054. URL https://onlinelibrary.wiley.com/doi/full/10.1002/pul2.12054.

[62] Luis A. Torres, Kristine E. Lee, Gregory P. Barton, Andrew D. Hahn, Nathan Sandbo, Mark L. Schiebler, and Sean B. Fain. Dynamic Contrast Enhanced MRI for the Evaluation of Lung Perfusion in Idiopathic Pulmonary Fibrosis. *European Respiratory Journal*, 60(4), mar 2022. ISSN 0903-1936. doi: 10.1183/13993003.02058-2021. URL https://erj.ersjournals.com/content/early/2022/03/02/13993003.02058-2021.

[63] Marilisa Schiwek, Simon M.F. Triphan, Jürgen Biederer, Oliver Weinheimer, Monika Eichinger, Claus F. Vogelmeier, Rudolf A. Jörres, Hans Ulrich Kauczor, Claus P. Heußel, Philip Konietzke, Oyunbileg von Stackelberg, Frank Risse, Bertram J. Jobst, and Mark O. Wielpütz. Quantification of pulmonary perfusion abnormalities using DCE-MRI

in COPD: comparison with quantitative CT and pulmonary function. *European Radiology*, 32(3):1879–1890, mar 2022. ISSN 14321084. doi: 10.1007/S00330-021-08229-6/FIGURES/4. URL https://link.springer.com/article/10.1007/s00330-021-08229-6.

[64] Yu Sen Huang, Jenny Ling Yu Chen, Feng Ming Hsu, Jei Yie Huang, Wei Chun Ko, Yi Chang Chen, Fu Shan Jaw, Ruoh Fang Yen, and Yeun Chung Chang. Response assessment of stereotactic body radiation therapy using dynamic contrast-enhanced integrated MR-PET in non-small cell lung cancer patients. *Journal of Magnetic Resonance Imaging*, 47(1):191–199, jan 2018. ISSN 1522-2586. doi: 10.1002/JMRI.25758. URL https://onlinelibrary.wiley.com/doi/full/10.1002/jmri.25758.

[65] Jean Philip Daniel Weber, Judith Eva Spiro, Matthias Scheffler, Jürgen Wolf, Lucia Nogova, Marc Tittgemeyer, David Maintz, Hendrik Laue, and Thorsten Persigehl. Reproducibility of dynamic contrast enhanced MRI derived transfer coefficient Ktrans in lung cancer. *PLOS ONE*, 17(3):e0265056, mar 2022. ISSN 1932-6203. doi: 10.1371/JOURNAL.PONE.0265056. URL https://journals.plos.org/plosone/article?id=10.1371/journal.pone.0265056.

[66] Lihua Chen, Daihong Liu, Jiuquan Zhang, Bing Xie, Xiaoyue Zhou, Robert Grimm, Xuequan Huang, Jian Wang, and Li Feng. Free-breathing dynamic contrast-enhanced MRI for assessment of pulmonary lesions using golden-angle radial sparse parallel imaging. *Journal of Magnetic Resonance Imaging*, 48(2):459–468, aug 2018. ISSN 1522-2586. doi: 10.1002/JMRI.25977. URL https://onlinelibrary.wiley.com/doi/10.1002/jmri.25977.

[67] Grzegorz Bauman, Kevin M. Johnson, Laura C. Bell, Julia V. Velikina, Alexey A. Samsonov, Scott K. Nagle, and Sean B. Fain. 3D pulmonary perfusion MRI with radial ultra-short echo time and spatial-temporal constrained reconstruction. *Magnetic resonance in medicine : official*

journal of the Society of Magnetic Resonance in Medicine / Society of Magnetic Resonance in Medicine, 73(2):555, feb 2015. doi: 10.1002/MRM.25158. URL https://www.ncbi.nlm.nih.gov/pmc/articles/PMC4156934/.

[68] Agilo Luitger Kern and Jens Vogel-Claussen. Hyperpolarized gas MRI in pulmonology. *https://doi.org/10.1259/bjr.20170647*, 91(1084), jan 2018. doi: 10.1259/BJR.20170647. URL https://www.birpublications.org/doi/abs/10.1259/bjr.20170647.

[69] Justus E. Roos, Holman P. McAdams, S. Sivaram Kaushik, and Bastiaan Driehuys. Hyperpolarized Gas MRI: Technique and Applications. *Magnetic resonance imaging clinics of North America*, 23(2):217, may 2015. doi: 10.1016/J.MRIC.2015.01.003. URL https://www.ncbi.nlm.nih.gov/pmc/articles/PMC4428591/.

[70] Joseph W. Plummer, Kiarash Emami, Andrew Dummer, Jason C. Woods, Laura L. Walkup, and Zackary I. Cleveland. A Semi-empirical Model to Optimize Continuous-Flow Hyperpolarized 129Xe Production under Practical Cryogenic-Accumulation Conditions. *Journal of magnetic resonance (San Diego, Calif. : 1997)*, 320:106845, nov 2020. ISSN 10960856. doi: 10.1016/J.JMR.2020.106845. URL /pmc/articles/PMC7655637/.

[71] Jonathan R. Birchall, Robert K. Irwin, Panayiotis Nikolaou, Aaron M. Coffey, Bryce E. Kidd, Megan Murphy, Michael Molway, Liana B. Bales, Kaili Ranta, Michael J. Barlow, Boyd M. Goodson, Matthew S. Rosen, and Eduard Y. Chekmenev. XeUS: A second-generation automated open-source batch-mode clinical-scale hyperpolarizer. *Journal of Magnetic Resonance*, 319:106813, oct 2020. ISSN 1090-7807. doi: 10.1016/J.JMR.2020.106813.

[72] I. C. Ruset, S. Ketel, and F. W. Hersman. Optical pumping system design for large production of hyperpolarized Xe129. *Physical*

Review Letters, 96(5):053002, feb 2006. ISSN 10797114. doi: 10.1103/PHYSREVLETT.96.053002/FIGURES/3/MEDIUM. URL https://journals.aps.org/prl/abstract/10.1103/PhysRevLett.96.053002.

[73] M. A. Bouchiat, T. R. Carver, and C. M. Varnum. Nuclear Polarization in He3 Gas Induced by Optical Pumping and Dipolar Exchange. *Physical Review Letters*, 5(8):373, oct 1960. doi: 10.1103/PhysRevLett.5.373. URL https://journals.aps.org/prl/abstract/10.1103/PhysRevLett.5.373.

[74] WILLIAM HAPPER. Optical Pumping. *Reviews of Modern Physics*, 44 (2):169, apr 1972. doi: 10.1103/RevModPhys.44.169. URL https://journals.aps.org/rmp/abstract/10.1103/RevModPhys.44.169.

[75] Thad G. Walker and William Happer. Spin-exchange optical pumping of noble-gas nuclei. *Reviews of Modern Physics*, 69(2):629–642, 1997. doi: 10.1103/REVMODPHYS.69.629.

[76] Sean B. Fain, Frank R. Korosec, James H. Holmes, Rafael O'Halloran, Ronald L. Sorkness, and Thomas M. Grist. Functional lung imaging using hyperpolarized gas MRI. *Journal of Magnetic Resonance Imaging*, 25(5):910–923, may 2007. ISSN 1522-2586. doi: 10.1002/JMRI.20876. URL https://onlinelibrary.wiley.com/doi/10.1002/jmri.20876.

[77] S. Sivaram Kaushik, Matthew S. Freeman, Suk W. Yoon, Maria G. Liljeroth, Jane V. Stiles, Justus E. Roos, W. Michael Foster, Craig R. Rackley, H. P. McAdams, and Bastiaan Driehuys. Measuring diffusion limitation with a perfusion-limited gas-Hyperpolarized 129Xe gas-transfer spectroscopy in patients with idiopathic pulmonary fibrosis. *Journal of Applied Physiology*, 117(6):577–585, sep 2014. ISSN 15221601. doi: 10.1152/JAPPLPHYSIOL.00326.2014/ASSET/IMAGES/LARGE/ZDG0181411370007.JPEG. URL

https://journals.physiology.org/doi/10.1152/japplphysiol.00326.2014.

[78] Lukas Ebner, Mu He, Rohan S. Virgincar, Timothy Heacock, Suryanarayanan S. Kaushik, Matthew S. Freemann, H. Page McAdams, Monica Kraft, and Bastiaan Driehuys. Hyperpolarized 129Xenon Magnetic Resonance Imaging to Quantify Regional Ventilation Differences in Mild to Moderate Asthma: A Prospective Comparison between Semiautomated Ventilation Defect Percentage Calculation and Pulmonary Function Tests. *Investigative Radiology*, 52(2):120–127, feb 2017. ISSN 15360210. doi: 10.1097/RLI.0000000000000322. URL https://journals.lww.com/investigativeradiology/fulltext/2017/02000/hyperpolarized{_}129xenon{_}magnetic{_}resonance{_}imaging.7.aspx.

[79] Tahreema N. Matin, Najib Rahman, Annabel H. Nickol, Mitchell Chen, Xiaojun Xu, Neil J. Stewart, Tom Doel, Vicente Grau, James M. Wild, and Fergus V. Gleeson. Chronic obstructive pulmonary disease: Lobar analysis with hyperpolarized 129Xe MR imaging. *Radiology*, 282(3):857–868, mar 2017. ISSN 15271315. doi: 10.1148/RADIOL.2016152299/ASSET/IMAGES/LARGE/RADIOL.2016152299.FIG6.JPEG. URL https://pubs.rsna.org/doi/10.1148/radiol.2016152299.

[80] Marcus J. Couch, Robert Thomen, Nikhil Kanhere, Raymond Hu, Felix Ratjen, Jason Woods, and Giles Santyr. A two-center analysis of hyperpolarized 129Xe lung MRI in stable pediatric cystic fibrosis: Potential as a biomarker for multi-site trials. *Journal of Cystic Fibrosis*, 18(5):728–733, sep 2019. ISSN 1569-1993. doi: 10.1016/J.JCF.2019.03.005.

[81] Jennifer M. Wang, Scott H. Robertson, Ziyi Wang, Mu He, Rohan S. Virgincar, Geoffry M. Schrank, Rose Marie Smigla, Thomas G.

O'Riordan, John Sundy, Lukas Ebner, Craig R. Rackley, Page McAdams, and Bastiaan Driehuys. Using hyperpolarized 129Xe MRI to quantify regional gas transfer in idiopathic pulmonary fibrosis. *Thorax*, 73(1):21–28, jan 2018. ISSN 0040-6376. doi: 10.1136/THORAXJNL-2017-210070. URL https://thorax.bmj.com/content/73/1/21.

[82] Talal Dahhan, Shiv S. Kaushik, Mu He, Joseph G. Mammarappallil, Victor F. Tapson, Holman P. McAdams, Thomas A. Sporn, Bastiaan Driehuys, and Sudarshan Rajagopal. Abnormalities in hyperpolarized 129Xe magnetic resonance imaging and spectroscopy in two patients with pulmonary vascular disease. *Pulmonary Circulation*, 6(1):126–131, mar 2016. ISSN 20458940. doi: 10.1086/685110/ASSET/IMAGES/LARGE/10.1086_685110-FIG4.JPEG. URL https://journals.sagepub.com/doi/full/10.1086/685110.

[83] S. Sivaram Kaushik, Zackary I. Cleveland, Gary P. Cofer, Gregory Metz, Denise Beaver, John Nouls, Monica Kraft, William Auffermann, Jan Wolber, H. Page McAdams, and Bastiaan Driehuys. Diffusion-weighted hyperpolarized 129Xe MRI in healthy volunteers and subjects with chronic obstructive pulmonary disease. *Magnetic Resonance in Medicine*, 65(4):1154–1165, apr 2011. ISSN 1522-2594. doi: 10.1002/MRM.22697. URL https://onlinelibrary.wiley.com/doi/full/10.1002/mrm.22697.

[84] Miranda Kirby, Sarah Svenningsen, Amir Owrangi, Andrew Wheatley, Adam Farag, Alexei Ouriadov, Giles E. Santyr, Roya Etemad-Rezai, Harvey O. Coxson, David G. McCormack, and Grace Parraga. Hyperpolarized 3He and 129Xe MR imaging in healthy volunteers and patients with chronic obstructive pulmonary disease. *Radiology*, 265(2):600–610, nov 2012. ISSN 00338419. doi: 10.1148/RADIOL.12120485/ASSET/IMAGES/LARGE/120485FIG03.JPEG. URL https://pubs.rsna.org/doi/10.1148/radiol.12120485.

[85] S. Sivaram Kaushik, Scott H. Robertson, Matthew S. Freeman, Mu He, Kevin T. Kelly, Justus E. Roos, Craig R. Rackley, W. Michael Foster, H. Page McAdams, and Bastiaan Driehuys. Single-breath clinical imaging of hyperpolarized 129xe in the airspaces, barrier, and red blood cells using an interleaved 3D radial 1-point Dixon acquisition. *Magnetic Resonance in Medicine*, 75(4):1434–1443, apr 2016. ISSN 1522-2594. doi: 10.1002/MRM.25675. URL https://onlinelibrary.wiley.com/doi/full/10.1002/mrm.25675.

[86] Grzegorz Bauman and Oliver Bieri. Matrix pencil decomposition of time-resolved proton MRI for robust and improved assessment of pulmonary ventilation and perfusion. *Magnetic Resonance in Medicine*, 77(1):336–342, jan 2017. ISSN 1522-2594. doi: 10.1002/MRM.26096. URL https://onlinelibrary.wiley.com/doi/full/10.1002/mrm.26096.

[87] David Bondesson, Moritz J. Schneider, Thomas Gaass, Bernd Kühn, Grzegorz Bauman, Olaf Dietrich, and Julien Dinkel. Nonuniform Fourier-decomposition MRI for ventilation- and perfusion-weighted imaging of the lung. *Magnetic Resonance in Medicine*, 82(4):1312–1321, oct 2019. ISSN 1522-2594. doi: 10.1002/MRM.27803. URL https://onlinelibrary.wiley.com/doi/10.1002/mrm.27803.

[88] André Fischer, Stefan Weick, Christian O. Ritter, Meinrad Beer, Clemens Wirth, Helge Hebestreit, Peter M. Jakob, Dietbert Hahn, Thorsten Bley, and Herbert Köstler. SElf-gated Non-Contrast-Enhanced FUnctional Lung imaging (SENCEFUL) using a quasi-random fast low-angle shot (FLASH) sequence and proton MRI. *NMR in Biomedicine*, 27(8):907–917, aug 2014. ISSN 1099-1492. doi: 10.1002/NBM.3134. URL https://analyticalsciencejournals.onlinelibrary.wiley.com/doi/10.1002/nbm.3134.

[89] Efe Ilicak, Safa Ozdemir, Jascha Zapp, Lothar R. Schad, and Frank G.

Zöllner. Dynamic mode decomposition of dynamic MRI for assessment of pulmonary ventilation and perfusion. *Magnetic Resonance in Medicine*, 90(2):761–769, aug 2023. ISSN 1522-2594. doi: 10.1002/MRM.29656. URL https://onlinelibrary.wiley.com/doi/10.1002/mrm.29656.

[90] Tawfik Moher Alsady, Andreas Voskrebenzev, Lea Behrendt, Karen Olsson, Claus Peter Heußel, Ekkehard Gruenig, Henning Gall, Ardeschir Ghofrani, Fritz Roller, Sebastian Harth, Helen Marshall, Paul J.C. Hughes, Jim Wild, Andrew J. Swift, David G. Kiely, Jürgen Behr, Julien Dinkel, Dietrich Beitzke, Irene M. Lang, Kai Helge Schmidt, Karl Friedrich Kreitner, Thomas Frauenfelder, Silvia Ulrich, Okka W. Hamer, and Jens Vogel-Claussen. Multicenter Standardization of Phase-Resolved Functional Lung MRI in Patients With Suspected Chronic Thromboembolic Pulmonary Hypertension. *Journal of Magnetic Resonance Imaging*, 2023. ISSN 1522-2586. doi: 10.1002/JMRI.28995. URL https://onlinelibrary.wiley.com/doi/full/10.1002/jmri.28995.

[91] Filip Klimeš, Andreas Voskrebenzev, Marcel Gutberlet, Agilo Luitger Kern, Lea Behrendt, Robert Grimm, Hendrik Suhling, Cristian Gonzales Crisosto, Till Frederick Kaireit, Gesa Helen Pöhler, Julian Glandorf, Frank Wacker, and Jens Vogel-Claussen. 3D phase-resolved functional lung ventilation MR imaging in healthy volunteers and patients with chronic pulmonary disease. *Magnetic Resonance in Medicine*, 85(2):912–925, feb 2021. ISSN 1522-2594. doi: 10.1002/MRM.28482. URL https://onlinelibrary.wiley.com/doi/full/10.1002/mrm.28482.

[92] Filip Klimeš, Andreas Voskrebenzev, Marcel Gutberlet, Robert Grimm, Frank Wacker, and Jens Vogel-Claussen. Evaluation of image registration algorithms for 3D phase-resolved functional lung ventilation magnetic resonance imaging in healthy volunteers and

chronic obstructive pulmonary disease patients. *NMR in Biomedicine*, 36(3):e4860, mar 2023. ISSN 1099-1492. doi: 10.1002/NBM.4860. URL https://analyticalsciencejournals.onlinelibrary.wiley.com/doi/10.1002/nbm.4860.

[93] Andreas Voskrebenzev, Till F. Kaireit, Filip Klimeš, Gesa H. Pöhler, Lea Behrendt, Heike Biller, Korbinian Berschneider, Frank Wacker, Tobias Welte, Jens M. Hohlfeld, and Jens Vogel-Claussen. PREFUL MRI Depicts Dual Bronchodilator Changes in COPD: A Retrospective Analysis of a Randomized Controlled Trial. *Radiology: Cardiothoracic Imaging*, 4(2), apr 2022. ISSN 26386135. doi: 10.1148/RYCT.210147/ASSET/IMAGES/LARGE/RYCT.210147.FIG5.JPEG. URL https://pubs.rsna.org/doi/10.1148/ryct.210147.

[94] John Burnard West. *Respiratory Physiology: The Essentials*. Wolters Kluwer Health/Lippincott Williams & Wilkins, Philadelphia, PA, 10th edition, 2015. ISBN 978-1-4963-1011-8.

[95] Wikimedia Commons. Major Respiratory Organs, 2013. URL https://commons.wikimedia.org/wiki/File:2301{_}Major{_}Respiratory{_}Organs.jpg.

[96] Wikimedia Commons. Respiratory System Complete, 2007. URL https://commons.wikimedia.org/wiki/File:Respiratory{_}system{_}complete{_}en.svg.

[97] A. Wanner, M. Salathe, and T. G. O'Riordan. Mucociliary clearance in the airways. *American Journal of Respiratory and Critical Care Medicine*, 154(6):1868–1902, dec 2012. ISSN 1073449X. doi: 10.1164/AJRCCM.154.6.8970383.

[98] T. J. Hixon, M. D. Goldman, and J. Mead. Kinematics of the Chest Wall during Speech Production: Volume Displacements of the Rib

Cage, Abdomen, and Lung. *Journal of Speech and Hearing Research*, 16 (1):78–115, 1973. ISSN 00224685. doi: 10.1044/JSHR.1601.78. URL https://pubs.asha.org/doi/10.1044/jshr.1601.78.

[99] Ewald R. Weibel. *Morphometry of the Human Lung*. Springer Berlin Heidelberg, 1963. ISBN 9781483225791. doi: 10.1007/978-3-642-87553-3.

[100] E R Weibel. What makes a good lung? *Swiss Medical Weekly*, 139(2728 SE - Review article: Biomedical intelligence):375–386, jul 2009. doi: 10.4414/smw.2009.12270. URL https://smw.ch/index.php/smw/article/view/994.

[101] Connie C.W. Hsia, Dallas M. Hyde, and Ewald R. Weibel. Lung Structure and the Intrinsic Challenges of Gas Exchange. *Comprehensive Physiology*, 6(2):827, apr 2016. ISSN 20404603. doi: 10.1002/CPHY.C150028. URL /pmc/articles/PMC5026132/.

[102] Wikimedia Commons. Pulmonary Circuit, 2013. URL https://commons.wikimedia.org/wiki/File:2119{_}Pulmonary{_}Circuit.jpg.

[103] Susan R. Hopkins. Ventilation/Perfusion Relationships and Gas Exchange: Measurement Approaches. *Comprehensive Physiology*, 10(3):1155, jul 2020. ISSN 20404603. doi: 10.1002/CPHY.C180042. URL /pmc/articles/PMC8274320/.

[104] V. C. Moore. Spirometry: step by step. *Breathe*, 8(3):232–240, mar 2012. ISSN 1810-6838. doi: 10.1183/20734735.0021711. URL https://breathe.ersjournals.com/content/8/3/232.

[105] Jeffrey M. Haynes. Basic spirometry testing and interpretation for the primary care provider. *Canadian Journal of Respiratory Therapy*, 54(4):92–98, 2018. ISSN 23686820. doi: 10.29390/CJRT-2018-017. URL /pmc/articles/PMC6516140/.

[106] Wikimedia Commons. Lung Volumes Updated, 2014. URL https://commons.wikimedia.org/wiki/File:Lungvolumes{_}Updated.png.

[107] Joseph Feher. Lung Volumes and Airway Resistance. *Quantitative Human Physiology*, pages 563–571, jan 2012. doi: 10.1016/B978-0-12-382163-8.00061-X.

[108] Susan R. Hopkins and G. Kim Prisk. Lung Perfusion Measured Using Magnetic Resonance Imaging: New Tools for Physiological Insights Into the Pulmonary Circulation. *Journal of Magnetic Resonance Imaging*, 32(6):1287, dec 2010. ISSN 10531807. doi: 10.1002/JMRI.22378. URL /pmc/articles/PMC3359842/.

[109] Susan R. Hopkins, A. Cortney Henderson, David L. Levin, Kei Yamada, Tatsuya Arai, Richard B. Buxton, and G. Kim Prisk. VERTICAL GRADIENTS IN REGIONAL LUNG DENSITY AND PERFUSION IN THE SUPINE HUMAN LUNG: THE SLINKY® EFFECT. *Journal of applied physiology (Bethesda, Md. : 1985)*, 103(1): 240, jul 2007. ISSN 87507587. doi: 10.1152/JAPPLPHYSIOL.01289.2006. URL /pmc/articles/PMC2399899/.

[110] Rui Carlos Sá, Matthew V. Cronin, A. Cortney Henderson, Sebastiaan Holverda, Rebecca J. Theilmann, Tatsuya J. Arai, David J. Dubowitz, Susan R. Hopkins, Richard B. Buxton, and G. Kim Prisk. Vertical distribution of specific ventilation in normal supine humans measured by oxygen-enhanced proton MRI. *Journal of Applied Physiology*, 109(6): 1950, dec 2010. ISSN 87507587. doi: 10.1152/JAPPLPHYSIOL.00220.2010. URL /pmc/articles/PMC3006418/.

[111] Zechariah S. Gardner, Gregg L. Ruppel, and David A. Kaminsky. Grading the Severity of Obstruction in Mixed Obstructive-Restrictive Lung Disease. *Chest*, 140(3):598–603, sep 2011. ISSN 0012-3692. doi: 10.1378/CHEST.10-2860.

[112] Rodrigo Athanazio. Airway disease: similarities and differences between asthma, COPD and bronchiectasis. *Clinics*, 67(11):1335, nov 2012. ISSN 18075932. doi: 10.6061/CLINICS/2012(11)19. URL /pmc/articles/PMC3488995/.

[113] Nina Saxena. Restrictive lung disease. In *The Perioperative Medicine Consult Handbook*, pages 199–202. Springer International Publishing, jan 2015. ISBN 9783319093666. doi: 10.1007/978-3-319-09366-6_32/COVER. URL https://link.springer.com/chapter/10.1007/978-3-319-09366-6{_}32.

[114] Naomi B. Bishop, Pawel Stankiewicz, and Robin H. Steinhorn. Alveolar Capillary Dysplasia. *American Journal of Respiratory and Critical Care Medicine*, 184(2):172, jul 2011. ISSN 1073449X. doi: 10.1164/RCCM.201010-1697CI. URL /pmc/articles/PMC3172887/.

[115] Mark Wielpütz and Hans Ulrich Kauczor. MRI of the lung: state of the art. *Diagnostic and interventional radiology (Ankara, Turkey)*, 18(4):344–353, jul 2012. ISSN 1305-3612. doi: 10.4261/1305-3825.DIR.5365-11.0. URL https://pubmed.ncbi.nlm.nih.gov/22434450/.

[116] R. J. Allgood, W. G. Wolfe, P. A. Ebert, and D. C. Sabiston. Effects of carbon dioxide on bronchoconstriction after pulmonary artery occlusion. *American Journal of Physiology*, 214(4):772–775, 1968. ISSN 00029513. doi: 10.1152/AJPLEGACY.1968.214.4.772. URL https://journals.physiology.org/doi/10.1152/ajplegacy.1968.214.4.772.

[117] Charles P. Slichter. *Principles of Magnetic Resonance*. Springer Series in Solid-State Sciences. Springer Berlin Heidelberg, Berlin, Heidelberg, 3rd edition, 1990. ISBN 978-3-642-08069-2. doi: 10.1007/978-3-662-09441-9. URL http://link.springer.com/10.1007/978-3-662-09441-9.

[118] Daniel. Canet. *Nuclear magnetic resonance : concepts and methods*. Wiley, 1996. ISBN 978-0-471-96145-1. URL https://www.wiley.com/en-us/Nuclear+Magnetic+Resonance{%}3A+Concepts+and+Methods-p-9780471961451.

[119] Matt A. Bernstein, Kevin F. King, and Xiaohong Joe Zhou. *Handbook of MRI Pulse Sequences*. Academic Press, 2004. ISBN 9780120928613. URL http://www.sciencedirect.com:5070/book/9780120928613/handbook-of-mri-pulse-sequences.

[120] A Elster. Questions and Answers in MRI, feb 2024.

[121] I. I. Rabi, J. R. Zacharias, S. Millman, and P. Kusch. A New Method of Measuring Nuclear Magnetic Moment. *Physical Review*, 53(4):318, feb 1938. ISSN 0031899X. doi: 10.1103/PhysRev.53.318. URL https://journals.aps.org/pr/abstract/10.1103/PhysRev.53.318.

[122] F. Bloch. Nuclear Induction. *Physical Review*, 70(7-8):460, oct 1946. ISSN 0031899X. doi: 10.1103/PhysRev.70.460. URL https://journals.aps.org/pr/abstract/10.1103/PhysRev.70.460.

[123] E. M. Purcell, H. C. Torrey, and R. V. Pound. Resonance absorption by nuclear magnetic moments in a solid [7]. *Physical Review*, 69(1-2):37–38, jan 1946. ISSN 0031899X. doi: 10.1103/PHYSREV.69.37/FIGURE/1/THUMB. URL https://journals.aps.org/pr/abstract/10.1103/PhysRev.69.37.

[124] Michael Lustig, David Donoho, and John M. Pauly. Sparse MRI: The application of compressed sensing for rapid MR imaging. *Magnetic Resonance in Medicine*, 58(6):1182–1195, dec 2007. ISSN 07403194. doi: 10.1002/mrm.21391. URL https://onlinelibrary.wiley.com/doi/10.1002/mrm.21391.

[125] Damian J. Tyler, Matthew D. Robson, R. Mark Henkelman, Ian R. Young, and Graeme M. Bydder. Magnetic resonance imaging with

ultrashort TE (UTE) PULSE sequences: Technical considerations. *Journal of Magnetic Resonance Imaging*, 25(2):279–289, feb 2007. ISSN 1522-2586. doi: 10.1002/JMRI.20851. URL https://onlinelibrary.wiley.com/doi/full/10.1002/jmri.20851.

[126] Zachary Peggs, Jonathan Brooke, Shahidehalsadat Safavi, Andrew Prayle, Christabella Ng, Jan Paul, Christopher Bradley, Andrew Cooper, Samal Munidasa, Brandon Zanette, Giles Santyr, Alan Smyth, Helen Harr, Ian Hall, Susan Francis, and Penny Gowland. Use of phase resolved functional lung imaging (PREFUL) to assess response to Kaftrio therapy in Cystic Fibrosis. In *Proceedings of the Thirty-First Meeting of the International Society for Magnetic Resonance in Medicine. London, UK: International Society for Magnetic Resonance in Medicine; 1480.*, London, 2022.

[127] Zachary Peggs, Jonathan Brooke, Andrew Cooper, Charlotte Bolton, Ian Hall, Susan Francis, and Penny Gowland. Variation of Proton Lung Signal with Ventilation at 3T. In *Proceedings of the Thirty-First Meeting of the International Society for Magnetic Resonance in Medicine. London, UK: International Society for Magnetic Resonance in Medicine; 1399.*, London, 2022.

[128] Maren Zapke, Hans-Georg Topf, Martin Zenker, Rainer Kuth, Michael Deimling, Peter Kreisler, Manfred Rauh, Christophe Chefd'hotel, Bernhard Geiger, and Thomas Rupprecht. Magnetic resonance lung function – a breakthrough for lung imaging and functional assessment? A phantom study and clinical trial. *Respiratory Research 2006 7:1*, 7(1):1–9, aug 2006. ISSN 1465-993X. doi: 10.1186/1465-9921-7-106. URL https://respiratory-research.biomedcentral.com/articles/10.1186/1465-9921-7-106.

[129] Alexander A. Bankier, Carl R. O'Donnell, Vu M. Mai, Pippa Storey, Viviane De Maertelaer, Robert R. Edelman, and Qun Chen. Impact of lung volume on MR signal intensity changes of the lung parenchyma.

Journal of Magnetic Resonance Imaging, 20(6):961–966, dec 2004. ISSN 1522-2586. doi: 10.1002/JMRI.20198. URL https://onlinelibrary.wiley.com/doi/full/10.1002/jmri.20198.

[130] C. Chefd'hotel, G. Hermosillo, and O. Faugeras. Flows of diffeomorphisms for multimodal image registration. *Proceedings - International Symposium on Biomedical Imaging*, 2002-Janua:753–756, 2002. doi: 10.1109/ISBI.2002.1029367.

[131] M Deimling, V Jellus, B Geiger, and C Chefd'hotel. Time Resolved Lung Ventilation Imaging by Fourier Decomposition. In *ISMRM*, 2008.

[132] Marcus J. Couch, Samal Munidasa, Jonathan H. Rayment, Andreas Voskrebenzev, Ravi Teja Seethamraju, Jens Vogel-Claussen, Felix Ratjen, and Giles Santyr. Comparison of Functional Free-Breathing Pulmonary 1H and Hyperpolarized 129Xe Magnetic Resonance Imaging in Pediatric Cystic Fibrosis. *Academic Radiology*, 28(8):e209–e218, aug 2021. ISSN 1076-6332. doi: 10.1016/J.ACRA.2020.05.008.

[133] Samal Munidasa, Brandon Zanette, Marcus Couch, Robert Grimm, Ravi Seethamraju, Marie Pier Dumas, Wallace Wee, Jacky Au, Sharon Braganza, Daniel Li, Jason Woods, Felix Ratjen, and Giles Santyr. Inter- and intravisit repeatability of free-breathing MRI in pediatric cystic fibrosis lung disease. *Magnetic Resonance in Medicine*, 89(5):2048–2061, may 2023. ISSN 1522-2594. doi: 10.1002/MRM.29566. URL https://onlinelibrary.wiley.com/doi/10.1002/mrm.29566.

[134] Åsmund Kjørstad, Dominique M. R. Corteville, Thomas Henzler, Gerald Schmid-Bindert, Erlend Hodneland, Frank G. Zöllner, and Lothar R. Schad. Quantitative lung ventilation using Fourier decomposition MRI; comparison and initial study. *Magnetic Resonance Materials in Physics, Biology and Medicine 2014 27:6*, 27

(6):467–476, feb 2014. ISSN 1352-8661. doi: 10.1007/S10334-014-0432-9. URL https://link.springer.com/article/10.1007/s10334-014-0432-9.

[135] Tatsuya J. Arai, Felix C. Horn, Rui Carlos Sá, Madhwesha R. Rao, Guilhem J. Collier, Rebecca J. Theilmann, G. Kim Prisk, and Jim M. Wild. Comparison of quantitative multiple-breath specific ventilation imaging using colocalized 2D oxygen-enhanced MRI and hyperpolarized 3He MRI. *Journal of Applied Physiology*, 125(5):1526–1535, nov 2018. ISSN 15221601. doi: 10.1152/JAPPLPHYSIOL.00500.2017/ASSET/IMAGES/LARGE/ZDG0101827820005.JPEG. URL https://journals.physiology.org/doi/10.1152/japplphysiol.00500.2017.

[136] Rui Carlos Sá, Amran K. Asadi, Rebecca J. Theilmann, Susan R. Hopkins, G. Kim Prisk, and Chantal Darquenne. Validating the distribution of specific ventilation in healthy humans measured using proton MR imaging. *Journal of Applied Physiology*, 116(8):1048–1056, apr 2014. ISSN 15221601. doi: 10.1152/JAPPLPHYSIOL.00982.2013/ASSET/IMAGES/LARGE/ZDG0081409990004.JPEG. URL https://journals.physiology.org/doi/10.1152/japplphysiol.00982.2013.

[137] F. Klimeš, A. Voskrebenzev, M. Gutberlet, A. Kern, L. Behrendt, T. F. Kaireit, C. Czerner, J. Renne, F. Wacker, and J. Vogel-Claussen. Free-breathing quantification of regional ventilation derived by phase-resolved functional lung (PREFUL) MRI. *NMR in Biomedicine*, 32(6):e4088, jun 2019. ISSN 1099-1492. doi: 10.1002/NBM.4088. URL https://analyticalsciencejournals.onlinelibrary.wiley.com/doi/10.1002/nbm.4088.

[138] Anthony E. Lujan, Edward W. Larsen, James M. Balter, and Randall K. Ten Haken. A method for incorporating organ motion due to breathing into 3D dose calculations. *Medical Physics*, 26(5):715–720,

may 1999. ISSN 2473-4209. doi: 10.1118/1.598577. URL https://aapm.onlinelibrary.wiley.com/doi/10.1118/1.598577.

[139] Barry Hill; Sarah H Annesley. Monitoring respiratory rate in adults. *British Journal of Nursing*, 29(1):12–16, jan 2020. doi: 10.12968/BJON.2020.29.1.12. URL https://www.magonlinelibrary.com/doi/abs/10.12968/bjon.2020.29.1.12.

[140] Giorgio Quer, Pishoy Gouda, Michael Galarnyk, Eric J. Topol, and Steven R. Steinhubl. Inter- and intraindividual variability in daily resting heart rate and its associations with age, sex, sleep, BMI, and time of year: Retrospective, longitudinal cohort study of 92,457 adults. *PLOS ONE*, 15(2):e0227709, feb 2020. ISSN 1932-6203. doi: 10.1371/JOURNAL.PONE.0227709. URL https://journals.plos.org/plosone/article?id=10.1371/journal.pone.0227709.

[141] Åsmund Kjørstad, Dominique M.R. Corteville, Andre Fischer, Thomas Henzler, Gerald Schmid-Bindert, Frank G. Zöllner, and Lothar R. Schad. Quantitative lung perfusion evaluation using fourier decomposition perfusion MRI. *Magnetic Resonance in Medicine*, 72(2):558–562, aug 2014. ISSN 1522-2594. doi: 10.1002/MRM.24930. URL https://onlinelibrary.wiley.com/doi/10.1002/mrm.24930.

[142] Lea Behrendt, Andreas Voskrebenzev, Filip Klimeš, Marcel Gutberlet, Hinrich B. Winther, Till F. Kaireit, Tawfik Moher Alsady, Gesa H. Pöhler, Thorsten Derlin, Frank Wacker, and Jens Vogel-Claussen. Validation of Automated Perfusion-Weighted Phase-Resolved Functional Lung (PREFUL)-MRI in Patients With Pulmonary Diseases. *Journal of Magnetic Resonance Imaging*, 52(1):103–114, jul 2020. ISSN 1522-2586. doi: 10.1002/JMRI.27027. URL https://onlinelibrary.wiley.com/doi/10.1002/jmri.27027.

[143] Till F. Kaireit, Andreas Voskrebenzev, Marcel Gutberlet, Julia Freise, Bertram Jobst, Hans-Ulrich Kauczor, Tobias Welte, Frank Wacker,

and Jens Vogel-Claussen. Comparison of quantitative regional perfusion-weighted phase resolved functional lung (PREFUL) MRI with dynamic gadolinium-enhanced regional pulmonary perfusion MRI in COPD patients. *Journal of Magnetic Resonance Imaging*, 49 (4):1122–1132, apr 2019. ISSN 1522-2586. doi: 10.1002/JMRI.26342. URL https://onlinelibrary.wiley.com/doi/10.1002/jmri.26342.

[144] Tawfik Moher Alsady, Andreas Voskrebenzev, Mark Greer, Lena Becker, Till F. Kaireit, Tobias Welte, Frank Wacker, Jens Gottlieb, and Jens Vogel-Claussen. MRI-derived regional flow-volume loop parameters detect early-stage chronic lung allograft dysfunction. *Journal of Magnetic Resonance Imaging*, 50(6):1873–1882, dec 2019. ISSN 1522-2586. doi: 10.1002/JMRI.26799. URL https://onlinelibrary.wiley.com/doi/10.1002/jmri.26799.

[145] P J Schmid, L Li, M P Juniper, and O Pust. Applications of the dynamic mode decomposition. *Comput. Fluid Dyn*, 25:249–259, 2011. doi: 10.1007/s00162-010-0203-9.

[146] J. Nathan Kutz, Steven L. Brunton, Bingni W. Brunton, and Joshua L. Proctor. Dynamic Mode Decomposition. *Dynamic Mode Decomposition*, nov 2016. doi: 10.1137/1.9781611974508.

[147] D. M.R. Corteville, A. Kjørstad, T. Henzler, F. G. Zöllner, and L. R. Schad. Fourier decomposition pulmonary MRI using a variable flip angle balanced steady-state free precession technique. *Magnetic Resonance in Medicine*, 73(5):1999–2004, may 2015. ISSN 1522-2594. doi: 10.1002/MRM.25293. URL https://onlinelibrary.wiley.com/doi/full/10.1002/mrm.25293.

[148] J. P. Thirion. Image matching as a diffusion process: an analogy with Maxwell's demons. *Medical Image Analysis*, 2(3):243–260, sep 1998. ISSN 1361-8415. doi: 10.1016/S1361-8415(98)80022-4.

[149] Tom Vercauteren, Xavier Pennec, Aymeric Perchant, and Nicholas Ayache. Diffeomorphic demons: Efficient non-parametric image registration. *NeuroImage*, 45(1):S61–S72, mar 2009. ISSN 1053-8119. doi: 10.1016/J.NEUROIMAGE.2008.10.040.

[150] Miranda Kirby, Mohammadreza Heydarian, Sarah Svenningsen, Andrew Wheatley, David G. McCormack, Roya Etemad-Rezai, and Grace Parraga. Hyperpolarized 3He magnetic resonance functional imaging semiautomated segmentation. *Academic radiology*, 19(2):141–152, feb 2012. ISSN 1878-4046. doi: 10.1016/J.ACRA.2011.10.007. URL https://pubmed.ncbi.nlm.nih.gov/22104288/.

[151] Alejandro F. Frangi, Wiro J. Niessen, Koen L. Vincken, and Max A. Viergever. Multiscale vessel enhancement filtering. *Lecture Notes in Computer Science (including subseries Lecture Notes in Artificial Intelligence and Lecture Notes in Bioinformatics)*, 1496:130–137, oct 1998. doi: 10.1007/BFB0056195. URL https://link.springer.com/chapter/10.1007/BFb0056195.

[152] Sean A. Aspinall, Kelly A. Mackintosh, Denise M. Hill, Bethany Cope, and Melitta A. McNarry. Evaluating the Effect of Kaftrio on Perspectives of Health and Wellbeing in Individuals with Cystic Fibrosis. *International Journal of Environmental Research and Public Health 2022, Vol. 19, Page 6114*, 19(10):6114, may 2022. ISSN 1660-4601. doi: 10.3390/IJERPH19106114. URL https://www.mdpi.com/1660-4601/19/10/6114.

[153] Wei Zha, David J. Niles, Stanley J. Kruger, Bernard J. Dardzinski, Robert V. Cadman, David G. Mummy, Scott K. Nagle, and Sean B. Fain. Semiautomated Ventilation Defect Quantification in Exercise-induced Bronchoconstriction Using Hyperpolarized Helium-3 Magnetic Resonance Imaging: A Repeatability Study. *Academic Radiology*, 23(9):1104–1114, sep 2016. ISSN 18784046. doi: 10.1016/j.acra.2016.04.005. URL http://www.academicradiology.org/article/

S1076633216300733/fulltext.

[154] Mathieu Lederlin, Grzegorz Bauman, Monika Eichinger, Julien Dinkel, Mathilde Brault, Jürgen Biederer, and Michael Puderbach. Functional MRI using Fourier decomposition of lung signal: Reproducibility of ventilation- and perfusion-weighted imaging in healthy volunteers. *European Journal of Radiology*, 82(6):1015–1022, jun 2013. ISSN 0720-048X. doi: 10.1016/J.EJRAD.2012.12.003.

[155] Andreas Voskrebenzev, Marcel Gutberlet, Lena Becker, Frank Wacker, and Jens Vogel-Claussen. Reproducibility of fractional ventilation derived by Fourier decomposition after adjusting for tidal volume with and without an MRI compatible spirometer. *Magnetic Resonance in Medicine*, 76(5):1542–1550, nov 2016. ISSN 1522-2594. doi: 10.1002/MRM.26047. URL https://onlinelibrary.wiley.com/doi/10.1002/mrm.26047.

[156] Jeong Il Kang, Dae Keun Jeong, and Hyun Choi. Correlation between diaphragm thickness and respiratory synergist muscle activity according to severity of chronic obstructive pulmonary disease. *Journal of Physical Therapy Science*, 30(1):150, 2018. ISSN 09155287. doi: 10.1589/JPTS.30.150. URL https://www.ncbi.nlm.nih.gov/pmc/articles/PMC5788796/.

[157] Derek York, Norman M. Evensen, Margarita López Martınez, and Jonás De Basabe Delgado. Unified equations for the slope, intercept, and standard errors of the best straight line. *American Journal of Physics*, 72(3):367, feb 2004. ISSN 0002-9505. doi: 10.1119/1.1632486. URL https://aapt.scitation.org/doi/abs/10.1119/1.1632486.

[158] Felicia Seemann, Ahsan Javed, Rachel Chae, Rajiv Ramasawmy, Kendall O'Brien, Scott Baute, Hui Xue, Robert J. Lederman, and Adrienne E. Campbell-Washburn. Imaging gravity-induced lung water redistribution with automated inline processing at 0.55 T

cardiovascular magnetic resonance. *Journal of Cardiovascular Magnetic Resonance*, 24(1):35, dec 2022. ISSN 1532429X. doi: 10.1186/S12968-022-00862-4. URL /pmc/articles/PMC9172183/.

[159] Gene H. Golub and Charles F. van Loan. An Analysis of the Total Least Squares Problem. *SIAM Journal on Numerical Analysis*, 17(6): 883–893, jul 2006. ISSN 0036-1429. doi: 10.1137/0717073. URL https://epubs.siam.org/doi/10.1137/0717073.

[160] Edwards W Deming. *Statistical Adjustment Of Data*. Wiley, New York, 1943.

[161] R. J. Carroll and David Ruppert. The Use and Misuse of Orthogonal Regression in Linear Errors-in-Variables Models. *American Statistician*, 50(1):1–6, 1996. ISSN 15372731. doi: 10.1080/00031305.1996.10473533.

[162] Richard Wehr and Scott R. Saleska. The long-solved problem of the best-fit straight line: Application to isotopic mixing lines. *Biogeosciences*, 14(1):17–29, jan 2017. ISSN 17264189. doi: 10.5194/BG-14-17-2017.

[163] C A Cantrell. Atmospheric Chemistry and Physics Discussions. *European Geosciences Union*, 8(2):6409–6436, 2008. URL www.atmos-chem-phys-discuss.net/8/6409/2008/.

[164] Derek York. LEAST-SQUARES FITTING OF A STRAIGHT LINE. *https://doi.org/10.1139/p66-090*, 44(5):1079–1086, may 2011. ISSN 0008-4204. doi: 10.1139/P66-090. URL https://cdnsciencepub.com/doi/10.1139/p66-090.

[165] HáKon Gudbjartsson and Samuel Patz. The rician distribution of noisy mri data. *Magnetic Resonance in Medicine*, 34(6):910–914, dec 1995. ISSN 1522-2594. doi: 10.1002/MRM.1910340618. URL https://onlinelibrary.wiley.com/doi/10.1002/mrm.1910340618.

[166] Douglas E. Prah, Eric S. Paulson, Andrew S. Nencka, and Kathleen M. Schmainda. A simple method for rectified noise floor suppression: Phase-corrected real data reconstruction with application to diffusion-weighted imaging. *Magnetic Resonance in Medicine*, 64(2):418–429, aug 2010. ISSN 1522-2594. doi: 10.1002/MRM.22407. URL https://onlinelibrary.wiley.com/doi/10.1002/mrm.22407.

[167] Zachary Peggs, Jonathan Brooke, Jan Paul, Christopher Bradley, Andrew Cooper, Charlotte Bolton, Ian Hall, Susan Francis, and Penny Gowland. Functional Pulmonary Proton MRI: Voxel-wise Linear-fitting Ventilation (VOLVE) Assessment in Chronic Obstructive Pulmonary Disease (COPD). In *Proceedings of the Thirty-Second Meeting of the International Society for Magnetic Resonance in Medicine. Toronto, ON: International Society for Magnetic Resonance in Medicine; 4662.*, Toronto, 2023.

[168] William MacNee. Pathogenesis of chronic obstructive pulmonary disease. *Proceedings of the American Thoracic Society*, 2(4):258–266, 2005. ISSN 1546-3222. doi: 10.1513/PATS.200504-045SR. URL https://pubmed.ncbi.nlm.nih.gov/16267346/.

[169] Stephen Gundry. COPD 1: pathophysiology, diagnosis and prognosis, 2019. URL https://www.nursingtimes.net/clinical-archive/respiratory-clinical-archive/copd-1-pathophysiology-diagnosis-and-prognosis-23-03-2020/.

[170] Joan B. Soriano and Ravi Mahadeva. α1-Antitrypsin deficiency: count me in please! *European Respiratory Journal*, 49(1), jan 2017. ISSN 0903-1936. doi: 10.1183/13993003.01941-2016. URL https://erj.ersjournals.com/content/49/1/1601941.

[171] Kalfopoulos M, Wetmore K, and ElMallah MK. Pathophysiology of Alpha-1 Antitrypsin Lung Disease. *Methods in molecular biology (Clifton, N.J.)*, 1639:9–19, 2017. ISSN 1940-6029. doi: 10.1007/

978-1-4939-7163-3_2. URL https://pubmed.ncbi.nlm.nih.gov/28752442/.

[172] Mario Cazzola, Daiana Stolz, Paola Rogliani, and Maria Gabriella Matera. α1-Antitrypsin deficiency and chronic respiratory disorders. *European Respiratory Review*, 29(155), mar 2020. ISSN 0905-9180. doi: 10.1183/16000617.0073-2019. URL https://err.ersjournals.com/content/29/155/190073.

[173] Jane Kirkby, Raffaella Nenna, and Aisling McGowan. Changes in FEV1 over time in COPD and the importance of spirometry reference ranges: the devil is in the detail. *Breathe*, 15(4):337–339, dec 2019. ISSN 1810-6838. doi: 10.1183/20734735.0252-2019. URL https://breathe.ersjournals.com/content/15/4/337.

[174] Global Initiative for Chronic Obstructive Lung Disease. GOLD Report 2020. *Global Initiative for Chronic Obstructive Lung Disease*, page 141, 2020. URL https://goldcopd.org/wp-content/uploads/2019/12/GOLD-2020-FINAL-ver1.2-03Dec19{_}WMV.pdf.

[175] Sotirios Kakavas, Ourania S. Kotsiou, Fotis Perlikos, Maria Mermiri, Georgios Mavrovounis, Konstantinos Gourgoulianis, and Ioannis Pantazopoulos. Pulmonary function testing in COPD: looking beyond the curtain of FEV1. *NPJ Primary Care Respiratory Medicine*, 31(1), dec 2021. ISSN 20551010. doi: 10.1038/S41533-021-00236-W. URL https://www.ncbi.nlm.nih.gov/pmc/articles/PMC8105397/.

[176] Silvestro Ennio D'Anna, Roberto Asnaghi, Gaetano Caramori, Lorenzo Appendini, Manfredi Rizzo, Carmelo Cavallaro, Giorgio Marino, Francesco Cappello, Bruno Balbi, and Antonino Di Stefano. High-Resolution Computed Tomography Quantitation of Emphysema Is Correlated with Selected Lung Function Values in Stable COPD. *Respiration*, 83(5):383–390, may 2012. ISSN 0025-7931. doi: 10.1159/000329871. URL https://dx.doi.org/10.

1159/000329871.

[177] Alfred Fishman, Fernando Martinez, Steven Piantadosi, Robert Wise, Johns Hopkins Uni-versity, and Andrew Ries. A Randomized Trial Comparing Lung-Volume–Reduction Surgery with Medical Therapy for Severe Emphysema. *New England Journal of Medicine*, 348(21):2059–2073, may 2003. ISSN 0028-4793. doi: 10.1056/NEJMOA030287/SUPPL_FILE/PIANTADOSI_SA1-8.PDF. URL https://www.nejm.org/doi/10.1056/NEJMoa030287.

[178] Gerard J. Criner, Richard Sue, Shawn Wright, Mark Dransfield, Hiram Rivas-Perez, Tanya Wiese, Frank C. Sciurba, Pallav L. Shah, Momen M. Wahidi, Hugo Goulart De Oliveira, Brian Morrissey, Paulo F.G. Cardoso, Steven Hays, Adnan Majid, Nicholas Pastis, Lisa Kopas, Mark Vollenweider, P. Michael McFadden, Michael Machuzak, David W. Hsia, Arthur Sung, Nabil Jarad, Malgorzata Kornaszewska, Stephen Hazelrigg, Ganesh Krishna, Brian Armstrong, Narinder S. Shargill, and Dirk Jan Slebos. A multicenter randomized controlled trial of Zephyr Endobronchial Valve treatment in heterogeneous emphysema (LIBERATE). *American Journal of Respiratory and Critical Care Medicine*, 198(9):1151–1164, nov 2018. ISSN 15354970. doi: 10.1164/RCCM.201803-0590OC/SUPPL_FILE/DISCLOSURES.PDF. URL www.clinicaltrials.gov.

[179] Francesca Polverino, Erik B. Hysinger, Nishant Gupta, Matt Willmering, Tod Olin, Steven H. Abman, and Jason C. Woods. Lung MRI as a Potential Complementary Diagnostic Tool for Early COPD. *The American Journal of Medicine*, 133(6):757–760, jun 2020. ISSN 0002-9343. doi: 10.1016/J.AMJMED.2019.12.009.

[180] Helen Marshall, Juan Parra-Robles, Martin H. Deppe, David A. Lipson, Rod Lawson, and Jim M. Wild. 3He pO2 mapping is limited by delayed-ventilation and diffusion in chronic obstructive pulmonary disease. *Magnetic Resonance in Medicine*, 71(3):1172–1178, mar 2014.

ISSN 1522-2594. doi: 10.1002/MRM.24779. URL https://onlinelibrary.wiley.com/doi/full/10.1002/mrm.24779.

[181] D. E. O'Donnell and P. Laveneziana. Physiology and consequences of lung hyperinflation in COPD. *European Respiratory Review*, 15 (100):61–67, dec 2006. ISSN 0905-9180. doi: 10.1183/09059180.00010002. URL https://err.ersjournals.com/content/15/100/61.

[182] Brandon Zanette, Eric M. Schrauben, Samal Munidasa, Datta S. Goolaub, Anuradha Singh, Ailish Coblentz, Elaine Stirrat, Marcus J. Couch, Robert Grimm, Andreas Voskrebenzev, Jens Vogel-Claussen, Ravi T. Seethamraju, Christopher K. Macgowan, Mary Louise C. Greer, Emily W.Y. Tam, and Giles Santyr. Clinical Feasibility of Structural and Functional MRI in Free-Breathing Neonates and Infants. *Journal of Magnetic Resonance Imaging*, 55(6):1696–1707, jun 2022. ISSN 1522-2586. doi: 10.1002/JMRI.28165. URL https://onlinelibrary.wiley.com/doi/full/10.1002/jmri.28165.

[183] Helen Marshall, Andreas Voskrebenzev, Laurie J. Smith, Alberto M. Biancardi, Agilo L. Kern, Guilhem J. Collier, Piotr A. Wielopolski, Pierluigi Ciet, Harm A.W.M. Tiddens, Jens Vogel-Claussen, and Jim M. Wild. 129Xe and Free-Breathing 1H Ventilation MRI in Patients With Cystic Fibrosis: A Dual-Center Study. *Journal of Magnetic Resonance Imaging*, 57(6):1908–1921, jun 2023. ISSN 1522-2586. doi: 10.1002/JMRI.28470. URL https://onlinelibrary.wiley.com/doi/full/10.1002/jmri.28470.

[184] Gesa H. Pöhler, Filip Klimeš, Lea Behrendt, Andreas Voskrebenzev, Cristian Crisosto Gonzalez, Frank Wacker, Jens M. Hohlfeld, and Jens Vogel-Claussen. Repeatability of Phase-Resolved Functional Lung (PREFUL)-MRI Ventilation and Perfusion Parameters in Healthy Subjects and COPD Patients. *Journal of Magnetic Resonance Imaging*, 53(3):915–927, mar 2021. ISSN 1522-2586. doi: 10.1002/

JMRI.27385. URL https://onlinelibrary.wiley.com/doi/full/10.1002/jmri.27385.

[185] Zachary Peggs, Jonathan Brooke, Jan Paul, Christopher Bradley, Andrew Cooper, Charlotte Bolton, Ian Hall, Susan Francis, and Penny Gowland. Investigating the Relationship between Lung Volume and the Lung-Diaphragm Signal at 3T: Implications for Ventilation Measures. In *Proceedings of the Thirty-Second Meeting of the International Society for Magnetic Resonance in Medicine. Toronto, ON: International Society for Magnetic Resonance in Medicine; 4661.*, 2023.

[186] Aurelie Akossi, Fusheng Wang, George Teodoro, and Jun Kong. IMAGE REGISTRATION WITH OPTIMAL REGULARIZATION PARAMETER SELECTION BY LEARNED AUTO ENCODER FEATURES. *Proceedings. IEEE International Symposium on Biomedical Imaging*, 2021:702, apr 2021. ISSN 19458452. doi: 10.1109/ISBI48211.2021.9434161. URL https://www.ncbi.nlm.nih.gov/pmc/articles/PMC8975123/.

[187] Brian B. Avants, Nicholas J. Tustison, Gang Song, Philip A. Cook, Arno Klein, and James C. Gee. A reproducible evaluation of ANTs similarity metric performance in brain image registration. *NeuroImage*, 54(3):2033–2044, feb 2011. ISSN 1053-8119. doi: 10.1016/J.NEUROIMAGE.2010.09.025.

[188] Åsmund Kjørstad, Dominique M.R. Corteville, Thomas Henzler, Gerald Schmid-Bindert, Frank G. Zöllner, and Lothar R. Schad. Non-invasive quantitative pulmonary V/Q imaging using Fourier decomposition MRI at 1.5T. *Zeitschrift für Medizinische Physik*, 25(4):326–332, dec 2015. ISSN 0939-3889. doi: 10.1016/J.ZEMEDI.2015.02.002.

[189] Artur Wujcicki, Dominique Corteville, Andrzej Materka, and Lothar R. Schad. Perfusion and ventilation filters for Fourier-

decomposition MR lung imaging. *Zeitschrift für Medizinische Physik*, 25 (1):66–76, mar 2015. ISSN 0939-3889. doi: 10.1016/J.ZEMEDI.2014.10.002.

[190] Daniel Forsberg. fordanic/image-registration, 2016. URL https://github.com/fordanic/image-registration.

[191] Stefan Klein, Marius Staring, Keelin Murphy, Max A. Viergever, and Josien P.W. Pluim. Elastix: A toolbox for intensity-based medical image registration. *IEEE Transactions on Medical Imaging*, 29(1):196–205, jan 2010. ISSN 02780062. doi: 10.1109/TMI.2009.2035616.

[192] Tanguy Boucneau, Brice Fernandez, Peder Larson, Luc Darrasse, and Xavier Maître. 3D Magnetic Resonance Spirometry. *Scientific Reports 2020 10:1*, 10(1):1–12, jun 2020. ISSN 2045-2322. doi: 10.1038/s41598-020-66202-7. URL https://www.nature.com/articles/s41598-020-66202-7.

[193] Caroline A. Schneider, Wayne S. Rasband, and Kevin W. Eliceiri. NIH Image to ImageJ: 25 years of image analysis. *Nature Methods 2012 9:7*, 9(7):671–675, jun 2012. ISSN 1548-7105. doi: 10.1038/nmeth.2089. URL https://www.nature.com/articles/nmeth.2089.

[194] Andreas Voskrebenzev, Marcel Gutberlet, Till F. Kaireit, Frank Wacker, and Jens Vogel-Claussen. Low-pass imaging of dynamic acquisitions (LIDA) with a group-oriented registration (GOREG) for proton MR imaging of lung ventilation. *Magnetic Resonance in Medicine*, 78(4):1496–1505, oct 2017. ISSN 1522-2594. doi: 10.1002/MRM.26526. URL https://onlinelibrary.wiley.com/doi/10.1002/mrm.26526.

[195] Shuangzhe Liu, Víctor Leiva, Dan Zhuang, Tiefeng Ma, and Jorge I. Figueroa-Zúñiga. Matrix differential calculus with applications in the

multivariate linear model and its diagnostics. *Journal of Multivariate Analysis*, 188:104849, mar 2022. ISSN 0047-259X. doi: 10.1016/J.JMVA.2021.104849.

[196] Guillaume Chassagnon, Charlotte Martin, Rafael Marini, Maria Vakalopolou, Alexis Régent, Luc Mouthon, Nikos Paragios, and Marie Pierre Revel. Use of elastic registration in pulmonary MRI for the assessment of pulmonary fibrosis in patients with systemic sclerosis. *Radiology*, 291(2):487–492, may 2019. ISSN 15271315. doi: 10.1148/RADIOL.2019182099/ASSET/IMAGES/LARGE/RADIOL.2019182099.FIG5.JPEG. URL https://pubs.rsna.org/doi/10.1148/radiol.2019182099.

[197] Surya P. Bhatt, Sandeep Bodduluri, John D. Newell, Eric A. Hoffman, Jessica C. Sieren, Meilan K. Han, Mark T. Dransfield, and Joseph M. Reinhardt. CT-derived Biomechanical Metrics Improve Agreement Between Spirometry and Emphysema. *Academic radiology*, 23(10):1255, oct 2016. ISSN 18784046. doi: 10.1016/J.ACRA.2016.02.002. URL https://www.ncbi.nlm.nih.gov/pmc/articles/PMC5026854/.

[198] Orso Pusterla, Grzegorz Bauman, Mark O. Wielpütz, Sylvia Nyilas, Philipp Latzin, Claus P. Heussel, and Oliver Bieri. Rapid 3D in vivo 1H human lung respiratory imaging at 1.5T using ultra-fast balanced steady-state free precession. *Magnetic Resonance in Medicine*, 78(3):1059–1069, sep 2017. ISSN 1522-2594. doi: 10.1002/MRM.26503. URL https://onlinelibrary.wiley.com/doi/full/10.1002/mrm.26503.

[199] Alexandra Ljimani, Malte Hojdis, Julia Stabinska, Birte Valentin, Miriam Frenken, Elisabeth Appel, Gerald Antoch, and Hans Jörg Wittsack. Analysis of different image-registration algorithms for Fourier decomposition MRI in functional lung imaging. *https://doi.org/10.1177/0284185120944902*, 62(7):875–881, jul 2020.

ISSN 16000455. doi: 10.1177/0284185120944902. URL https://journals.sagepub.com/doi/10.1177/0284185120944902.

[200] Vu M Mai, Qun Chen, Wei Li, Hiroto Hatabu, and Robert R Edelman. Effect of Respiratory Phases on MR Lung Signal Intensity and Lung Conspicuity Using Segmented Multiple Inversion Recovery Turbo Spin Echo (MIR-TSE). *Magnetic Resonance in Medicine*, 43:760–763, 2000. doi: 10.1002/(SICI)1522-2594(200005)43:5. URL https://onlinelibrary.wiley.com/doi/10.1002/.

[201] Tony F. Chan and Luminita A. Vese. Active contours without edges. *IEEE Transactions on Image Processing*, 10(2):266–277, feb 2001. ISSN 10577149. doi: 10.1109/83.902291.

[202] D. Papandrinopoulou, V. Tzouda, and G. Tsoukalas. Lung Compliance and Chronic Obstructive Pulmonary Disease. *Pulmonary Medicine*, 2012, 2012. ISSN 20901836. doi: 10.1155/2012/542769. URL https://www.ncbi.nlm.nih.gov/pmc/articles/PMC3486437/.

[203] E. M. Haacke, T. J. Masaryk, P. A. Wielopolski, F. R. Zypman, J. A. Tkach, S. Amartur, J. Mitchell, M. Clampitt, and C. Paschal. Optimizing blood vessel contrast in fast three-dimensional MRI. *Magnetic Resonance in Medicine*, 14(2):202–221, may 1990. ISSN 1522-2594. doi: 10.1002/MRM.1910140207. URL https://onlinelibrary.wiley.com/doi/full/10.1002/mrm.1910140207.

[204] Ed X. Wu, Edward S. Hui, and Jerry S. Cheung. TOF-MRA using multi-oblique-stack acquisition (MOSA). *Journal of Magnetic Resonance Imaging*, 26(2):432–436, aug 2007. ISSN 1522-2586. doi: 10.1002/JMRI.20954. URL https://onlinelibrary.wiley.com/doi/full/10.1002/jmri.20954.

[205] Neville D. Gai, Ashkan A. Malayeri, and David A. Bluemke. Three-dimensional T1 and T2* mapping of human lung parenchyma using

interleaved saturation recovery with dual echo ultrashort echo time imaging (ITSR-DUTE). *Journal of Magnetic Resonance Imaging*, 45 (4):1097–1104, apr 2017. ISSN 1522-2586. doi: 10.1002/JMRI.25487. URL https://onlinelibrary.wiley.com/doi/full/10.1002/jmri.25487.

[206] Julian Glandorf, Filip Klimeš, Andreas Voskrebenzev, Marcel Gutberlet, Lea Behrendt, Cristian Crisosto, Frank Wacker, Pierluigi Ciet, Jim M. Wild, and Jens Vogel-Claussen. Comparison of phase-resolved functional lung (PREFUL) MRI derived perfusion and ventilation parameters at 1.5T and 3T in healthy volunteers. *PLOS ONE*, 15(12):e0244638, dec 2020. ISSN 1932-6203. doi: 10.1371/JOURNAL.PONE.0244638. URL https://journals.plos.org/plosone/article?id=10.1371/journal.pone.0244638.

[207] Martin Uecker, Frank Ong, Jonathan Tamir, Dara Bahri, Patrick Virtue, Joseph Cheng, Tao Zhang, and Michael Lustig. Berkeley Advanced Reconstruction Toolbox. In *International Society for Magnetic Resonance in Medicine*, Toronto, 2015.

[208] Xucheng Zhu, Marilynn Chan, Michael Lustig, Kevin M. Johnson, and Peder E.Z. Larson. Iterative motion-compensation reconstruction ultra-short TE (iMoCo UTE) for high-resolution free-breathing pulmonary MRI. *Magnetic Resonance in Medicine*, 83(4):1208–1221, apr 2020. ISSN 1522-2594. doi: 10.1002/MRM.27998. URL https://onlinelibrary.wiley.com/doi/10.1002/mrm.27998.

[209] Annemarie M. den Harder, Erwin de Boer, Suzanne J. Lagerweij, Martijn F. Boomsma, Arnold M.R. Schilham, Martin J. Willemink, Julien Milles, Tim Leiner, Ricardo P.J. Budde, and Pim A. de Jong. Emphysema quantification using chest CT: influence of radiation dose reduction and reconstruction technique. *European Radiology Experimental*, 2(1), dec 2018. ISSN 25099280. doi: 10.1186/S41747-018-0064-3. URL https://www.ncbi.nlm.nih.gov/pmc/

articles/PMC6220000/.

[210] Ilyes Benlala, Sophie Point, Cédric Leung, Patrick Berger, Jason C. Woods, Chantal Raherison, François Laurent, Julie Macey, and Gaël Dournes. Volumetric quantification of lung MR signal intensities using ultrashort TE as an automated score in cystic fibrosis. *European Radiology*, 30(10):5479–5488, oct 2020. ISSN 14321084. doi: 10.1007/S00330-020-06910-W/TABLES/4. URL https://link.springer.com/article/10.1007/s00330-020-06910-w.